

REPORT DOCUMENTATION PAGEForm Approved
OMB No. 074-0188

Public reporting burden for this collection of information is estimated to average 1 hour per response, including the time for reviewing instructions, searching existing data sources, gathering and maintaining the data needed, and completing and reviewing this collection of information. Send comments regarding this burden estimate or any other aspect of this collection of information, including suggestions for reducing this burden to Washington Headquarters Services, Directorate for Information Operations and Reports, 1215 Jefferson Davis Highway, Suite 1204, Arlington, VA 22202-4302, and to the Office of Management and Budget, Paperwork Reduction Project (0704-0188), Washington, DC 20503

1. AGENCY USE ONLY (Leave blank)**2. REPORT DATE**
10/15/2004**3. REPORT TYPE AND DATES COVERED**

Final Technical, 11/01/1999 to 10/31/2002

4. TITLE AND SUBTITLE

Microwave-Driven Air Plasma Studies for Drag Reduction and Power Extraction in Supersonic Air

5. FUNDING NUMBERS

G - F49620-00-1-0034

6. AUTHOR(S)

Richard B. Miles and Sergey Macheret

7. PERFORMING ORGANIZATION NAME(S) AND ADDRESS(ES)Dept. of Mechanical & Aerospace Engineering, Princeton University
Princeton, NJ 08544**8. PERFORMING ORGANIZATION
REPORT NUMBER****9. SPONSORING / MONITORING AGENCY NAME(S) AND ADDRESS(ES)**Air Force Office of Scientific
Research/NA (John Schmisser, Program
Manager)
801 N. Randolph St., Room 732
Arlington, VA 22203-1977**10. SPONSORING / MONITORING
AGENCY REPORT NUMBER****11. SUPPLEMENTARY NOTES**

The views, opinions and/or findings contained in this report are those of the author(s) and should not be construed as an official Department of the Army position, policy or decision, unless so designated by other documentation.

12a. DISTRIBUTION / AVAILABILITY STATEMENT

Approved for public release, distribution unlimited

12b. DISTRIBUTION CODE**13. ABSTRACT (Maximum 200 Words)**

Program involving modeling and experiment to explore the utility of plasmas and magnetohydrodynamics (MHD) for aerodynamic applications. Anomalous behavior of shocks on weakly ionized plasmas has been explained in terms of conventional gas dynamics with temperature gradients. Theoretical and computational models have been developed for plasma aerodynamics and nonequilibrium MHD. Models include a new theory of nonequilibrium dissociation and vibrational relaxation and kinetics of plasmas generated by electron beams and high-voltage nanosecond pulses. Aerodynamic steering using plasma energy addition has been explored using the newly developed microwave-driven supersonic plasma wind tunnel. Potential performance of hypersonic MHD devices with electron beam ionization has been outlined. Plasma and MHD control of hypersonic flows and scramjet inlets was studied. On-ramp MHD device with ionization by electron beams was shown to be capable of maintaining the shock-on-lip condition at Mach numbers higher than the design one, while generating net power. For mass capture increase at Mach numbers lower than the design one, a new concept of "virtual cowl" was proposed and tentatively studied. In preparation for experimental studies of MHD control of cold-air high-speed flows, ionization by repetitive high-voltage nanosecond pulses was studied theoretically, and a plasma sustained by such pulses was made operational.

BEST AVAILABLE COPY**20041108 081****14. SUBJECT TERMS**

Plasmas, Magnetohydrodynamics (MHD), Aerodynamic Applications

15. NUMBER OF PAGES

121

16. PRICE CODE**17. SECURITY CLASSIFICATION
OF REPORT**

Unclassified

**18. SECURITY CLASSIFICATION
OF THIS PAGE**

Unclassified

**19. SECURITY CLASSIFICATION
OF ABSTRACT**

Unclassified

20. LIMITATION OF ABSTRACT

UL

TABLE OF CONTENTS
"Microwave-Driven Air Plasma Studies for Drag Reduction and Power Extraction in Supersonic Air"
AFOSR Grant #F49620-00-1-0034 Final Technical Report

Abstract	1
Chapter 1: Shock Propagation and Dispersion in Glow Discharge Plasmas.....	1
I. Introduction.....	2
II. Experiments on Shock Propagation in Steady-State Flow Discharges.....	2
III. Results of Shock Propagation Studies in Steady-State Discharges and Comparison with CFD Axisymmetric Modeling.....	5
IV. Experiments on Shock Propagation in Pulsed Discharges.....	6
V. Conclusions.....	8
References	8
Chapter 2: Theoretical Analysis of MHD and EHD Effects in Weakly Ionized Gas Flows.....	27
I. Introduction	30
II. Theoretical Analysis of MHD and EHD Effects in Weakly Ionized Gas Flows	30
III. Electrodeless MHD Flow Control: A Magneto-Thermal Funnel.....	36
IV. Conclusions	40
References	40
Chapter 3: Nonequilibrium MHD Control of SCRAMJET Inlets.....	50
I. Introduction	50
II. The Model	51
III. Computed Cases	52
IV. Mass Capture Increase by Off-Body Energy Addition: A Virtual Cowl.....	55
V. Conclusions.....	56
References.....	56
Chapter 4: Development of a Supersonic Plasma Wind Tunnel.....	73
I. Introduction	73
II. Wind Tunnel Design	73
III. Microwave Field Distribution	73
IV. Numerical Simulations	75
V. Breakdown Measurements	75
VI. Conclusions	75
References	76
Chapter 5: Studies of Electron Beam-Initiated, Microwave-Driven Plasma Discharges for Aerodynamic Control.....	84
I. Introduction	84
II. Apparatus	84
III. Experiment	86
IV. Results	87
V. Conclusions	91
References	91
Chapter 6: Efficient Plasma Generation by Repetitive High-Voltage Nanosecond Pulses for MHD Flow Control.....	91
I. Introduction	91
References	94
Chapter 7: Semiclassical Modeling of State-Specific Dissociation Rates in Diatomic Gases	
I. Introduction	95
II. The FHO-Based Dissociation Model.....	95
III. Results and Discussion	101
IV. Conclusions	104
V. References	104

TABLE OF CONTENTS (CONTINUED)

PERSONNEL SUPPORTED	111
PUBLICATIONS	111
INTERACTIONS/TRANSITIONS	115
INVITED PRESENTATIONS AND SEMINARS	118
NEW DISCOVERIES, INVENTIONS, and PATENT DISCLOSURES	119
HONORS/AWARDS	119
ACKNOWLEDGEMENT/DISCLAIMER	120

FINAL TECHNICAL REPORT—October 15, 2004

**“MICROWAVE-DRIVEN AIR PLASMA STUDIES FOR DRAG REDUCTION AND POWER
EXTRACTION IN SUPERSONIC AIR”**

**AFOSR GRANT #F49620-00-1-0034
(150-6776)**

**Richard B. Miles and Sergey O. Macheret
Department of Mechanical & Aerospace Engineering
Princeton University
Princeton, New Jersey 08544**

ABSTRACT

A program involving both modeling and experiment has been underway at Princeton for several years in an effort to explore the utility of plasmas and magnetohydrodynamics (MHD) for aerodynamic applications. Early in the program, “anomalous” behavior of shocks on weakly ionized plasmas has been explained in terms of conventional gas dynamics with temperature gradients. Then, theoretical and computational models have been developed for plasma aerodynamics and nonequilibrium MHD. The models include a new theory of nonequilibrium dissociation and vibrational relaxation and kinetics of plasmas generated by electron beams and high-voltage nanosecond pulses. Aerodynamic steering using plasma energy addition has been explored both computationally and experimentally, using the newly developed microwave-driven supersonic plasma wind tunnel. Potential performance of hypersonic MHD devices with electron beam ionization has been outlined. In the last year of the program, plasma and MHD control of hypersonic flows and scramjet inlets was studied. On-ramp MHD device with ionization by electron beams was shown to be capable of maintaining the shock-on-lip condition at Mach numbers higher than the design one, while generating net power, although at the expense of some losses of total pressure. For mass capture increase at Mach numbers lower than the design one, a new concept of “virtual cowl” was proposed and tentatively studied. In preparation for experimental studies of MHD control of cold-air high-speed flows, ionization by repetitive high-voltage nanosecond pulses was studied theoretically, and a plasma sustained by such pulses was made operational. This plasma is to be used for MHD studies at Mach 4 with a 6.5 Tesla superconducting magnet. Advanced optical diagnostic techniques, including Filtered Rayleigh Scattering, filtered Thomson scattering, coherent Rayleigh scattering, and coherent Rayleigh-Brillouin scattering, have been developed and applied to studies of weakly ionized plasmas.

**CHAPTER 1
SHOCK PROPAGATION AND DISPERSION IN GLOW DISCHARGE PLASMAS**

Summary

Spark-generated shock waves were studied in glow discharges in argon and argon-nitrogen mixtures. UV Filtered Rayleigh Scattering was used to measure radial profiles of gas temperature, and laser schlieren method was used to measure shock arrival times and axial density gradients. Time accurate, inviscid, axisymmetric CFD computations were run and results compared with the experiments. Our simulation show that changes in shock structure and velocity in weakly ionized gases are explained by classical gas dynamics, with critical role of thermal and multi-dimensional effects (transverse gradients, shock curvature, etc.). A direct proof of the thermal mechanism was obtained by pulsing the discharge. With sub-millisecond delay between starting the discharge and shock launch, plasma parameters reach their steady-state values, but the temperature is still low, laser schlieren signals are virtually identical to those without the discharge, differing dramatically from the signals in discharges with fully established temperature profiles.

I. Introduction

Weakly ionized gases (plasmas) could potentially have an impact on high-speed aerodynamics. Using plasmas for shock wave control, drag reduction, vehicle steering, sonic boom attenuation, ignition of combustion in engines, and MHD power extraction and enthalpy by-pass is being actively discussed. Of course, fundamental issues have to be resolved prior to any practical applications.

Propagation of shock waves in weakly ionized plasmas was studied in Russia,^{1-11, 15, 16} and, later, in the U.S.¹²⁻¹⁴ Shock acceleration, broadening, and "splitting" was observed in various d.c., RF, and pulsed discharges, in inert as well as molecular gases. Some researchers^{1-11, 12-14} attributed experimental observations to various plasma-specific phenomena, from electric double layers to ion-acoustic waves to new long-range interactions or microscopic structure formed in gas discharges. However, other Russian researchers^{15, 16} found that their data can be adequately explained by conventional thermal phenomena. Gas heating, temperature inhomogeneity, and vibrational relaxation were theoretically shown to result in "anomalous" behavior of shocks in gas discharges.¹⁷⁻¹⁹

In Refs. 20 and 21, analysis of various physical mechanisms resulted in a conclusion that the "broadening", "splitting", and acceleration of shocks in gas discharges could hardly be explained by plasma-specific effects. This is due ultimately to the very low ionization fraction in the discharges, which leads to small fraction of the total gas energy stored in ionized and excited states, to very inefficient energy and momentum transfer from electrons and ions to the bulk neutral gas, and to very long times of these transfer processes.

In 1997, two research groups simultaneously and independently showed, based on inviscid CFD modeling,^{22, 23} that transverse and longitudinal temperature and density gradients present in gas discharges due to Joule heating can be responsible for the observed "anomalous" shock profiles. The inviscid modeling of Ref. 22, extended in Ref. 24, emphasized that transverse gradients result in multi-dimensional nature of shock propagation, and that attempts to interpret the phenomena in one-dimensional terms can be misleading. For example, shock curvature could be misinterpreted as a "broadened" or "split" 1D structure. The inviscid results were confirmed in Navier-Stokes computations.²⁵ Additionally, as demonstrated in Ref. 25, in the case of very weak shocks (with Mach number very close to 1) or very long propagation distances (many meters) wall shear could also result in an apparent "splitting" of laser schlieren signals even in a cold gas.

In this chapter, we describe a combined experimental and computational effort to clarify mechanisms of shock propagation in weakly ionized plasmas. Experiments were done in well-characterized positive column of glow discharge in Ar and Ar-N₂ mixtures. Shock velocity and structure was measured using laser schlieren method, similar to experiments of Refs. 12-14. Since temperature and its gradients could play a critical role in shock propagation, radial temperature profiles in our experiments were measured with Filtered Rayleigh Scattering. Axisymmetric CFD modeling gives a very good agreement with experimental data, thus proving that it is classical, but multi-dimensional, gas dynamics can explain for the "anomalous" effects.

In order to study shock propagation in weakly ionized plasma with very small or absent temperature gradients, pulsed discharge experiments were carried out. Those experiments prove again the thermal nature of shock propagation in gas discharges.

II. Experiments on shock propagation in steady-state glow discharges

II.1. Experimental setup and procedures

The experimental setup at Princeton University^{26, 27} is basically similar to that of Refs. 12-14. The plasmas studied were created by longitudinal continuous or pulsed glow discharge. The discharge tube, 3.8 cm i.d. and 120 cm full length, was made of quartz. Shock waves were generated by a spark discharge at the one end of the tube. The spark circuit parameters are: capacitor 0.2 μ F, voltage 15 – 20 kV. The capacitor discharge was controlled by a triggering spark gap. The shock wave entered the discharge through a narrow (2 mm wide and 0.1 mm thick) ring electrode made of stainless steel foil mounted adjacent to (almost flush with) the wall. The electrode nearest to the spark was always the anode, in order to prevent the incoming shock wave from passing by the hot cathode and through the cathode fall of the discharge. The cathode in all pulse and most steady-state experiments was identical in size and material to the anode. In some experimental runs, where shock profiles deep inside the plasma, far from the

cathode, were studied, another cathode was used: a 25 mm diameter hollow cylinder with the axis perpendicular to the tube axis. This cathode was used only when it was far enough downstream of the shock and could not affect shock propagation. Both the cathode and anode could be placed at different location in the tube, so that the distance between the spark and the anode could be 20 or 40 cm, and the length of discharge could be 20, 40, or 60 cm. The flexibility in changing the discharge length was used for measuring the electric field in the plasma (see below).

Similarly to Refs. 12-14, we used a laser schlieren method²⁸ for detecting the shock wave front (Fig.1). A He-Ne laser beam crossed the discharge horizontally along the diameter and was then focused onto the plane of a knife by a lens ($f=50$ cm). The beam 1/e diameter was about 0.3 mm. A photodiode with a response time of 20 ns measured the light intensity after the knife edge. The signal was recorded by a digital oscilloscope with 1 k Ω resistor at the input, and a time resolution $\approx 0.1 \mu\text{s}$. In some measurements a miniature pressure sensor was also used.

To measure the instantaneous shock wave velocity we used an approach similar to that proposed in Ref. 29. After the laser beam crossed the discharge it was retro-reflected from a small 90° prism and passed through the discharge once more with the spatial offset and then focused onto the knife edge. This produced two closely separated schlieren signals of opposite signs. Shock wave velocity was found by dividing the distance between the two beam passages (12 to 21 mm) by the time gap between the schlieren signals. This method provided an accuracy of absolute velocity near 3 per cent (≈ 10 m/s) and that of relative velocity about 0.5 per cent (2 m/s).

Experiments were performed in an Ar-N₂ mixture (1% of N₂). Addition of nitrogen substantially improved the radial uniformity of the discharge. A pure argon discharge contracted at currents $i > 30 - 40$ mA (for pressures $p \geq 30$ Torr). With nitrogen the discharge was not contracted at all conditions studied ($p \leq 100$ Torr, $i \leq 100$ mA). To prevent electrophoresis and accumulation of impurities, the gas mixture was pumped through the discharge with a rate of 300 sccm, which corresponded to 5 - 10 cm/s linear speed in the tube. Control measurements with the gas flow turned off for a short time gave shock velocities and schlieren profiles identical to those with the flow on.

As was already mentioned, the flexibility in changing the discharge length allowed us to measure an electric field E in a positive column of the discharge (cathode voltage drop V_c could also be found in these measurements). For $p=30-50$ Torr, $i=30-100$ mA the E value was from 8 to 14 V/cm. Assuming a Bessel radial profile for gas temperature, we calculated the reduced electric field E/N (N is the gas number density) and electron number density n_e . Averaged over the tube cross section, these values are $E/N=1.2-1.4$ Td, $n_e=(1.2-4) \cdot 10^{10} \text{ cm}^{-3}$ for the condition range mentioned above.

II.2. Measurements of temperature profiles

We have used Ultraviolet Filtered Rayleigh Scattering (UV FRS)^{30, 31} to measure temperature profiles of the discharges studied. A summary of these measurements is presented here. A narrow linewidth laser is used to illuminate the sample gas and the scattered light is imaged through a narrow band absorption filter onto a detector, as shown schematically in Fig.2. The laser should be tunable so that it may be tuned within an absorption notch, and narrow linewidth so that the elastic background (due to windows, particulates etc.) is narrow compared to the spectral width of an absorption notch. The amount of scattered light measured by the detector depends on the spectral overlap of the scattered light and the filter absorption profile. The filter offers very nearly 100% transmission outside of the absorption notches, yet is extremely optically thick (suppression modeled as 10^5 and higher) within the absorption notches. The light scattered by the atoms and/or molecules in the flow is thermally and collisionally broadened, and is therefore spectrally wider than the laser and background. When the laser is tuned to overlap an absorption notch, the filter serves to suppress the background while transmitting a large fraction of the light scattered from the flow. By appropriate selection of filter conditions, and laser frequency, one may obtain very strong background suppression (greater than 10^5) while transmitting close to half of the scattered light.

Depending on the conditions of a specific measurement, slightly different approaches may be used. In cases of constant (known) pressure we use a method which precludes the need for background subtraction. The approach is to ratio the FRS signal at a temperature to be measured, T_M , to the signal at a known temperature, T_{ref} . Both measurements are taken at the same frequency within an absorption notch so that any background is strongly suppressed in both cases. At constant pressure there is a one-to-one correspondence of temperature and density so that the measured ratio uniquely defines the unknown temperature T_M . The signal ratio is primarily determined by the density ratio, with a smaller opposing contribution from lineshape effects.

Modeling results for the present measurements are shown in Figs. 3 and 4. Fig. 3 shows the modeled filter transmission profile and FRS signal levels as functions of frequency. The filter has a length of 5 cm, a mercury vapor pressure of 0.0030 torr, and a temperature of 315K. In this spectral region, mercury has six absorption notches due to hyperfine splitting and different isotopic contributions. Fig. 3 is a closer view of the highest frequency absorption notch – the one used in the current work. The nominal location of the lines is at 253.7 nm. The modeled FRS signal levels are for a scatterer of 50 Torr of argon at various temperatures. The Rayleigh scattering cross-section is not affected by the weak ionization and so the curves describe both argon gases and the plasmas used in these experiments. The signals are normalized to 300 K (by the ideal gas law) so that their relative magnitude scales as would be measured by a detector. In the absence of the filter the signal is linear with density (or $1/T$), while within the absorption features there is also a weaker effect from the variation of scattering linewidth with temperature. From such modeling one may find the relationship between the experimentally measured FRS signal ratio,

$$\text{Ratio} = \text{FRS signal } (T=T_M) / \text{FRS signal } (T=T_{\text{ref}}),$$

and the unknown temperature T_M . Fig. 4 is such a curve. In this case the unknown temperature, T_M , corresponds to the “plasma on” temperature while the reference temperature, T_{ref} , corresponds to the “plasma off” temperature – in this case $T_{\text{ref}}=308$ K.

The experimental configuration for FRS temperature measurements is illustrated in Fig.2. A high power, tunable, narrow linewidth Titanium Sapphire laser³² was used as the excitation source. The frequency-tripled output was delivered to the plasma tube through several anti-reflection coated beam-shaping optics. For these experiments pulse energies of ~ 10 mJ in the ultraviolet (254 nm) were used. The beam passed through a quarter wave plate to ensure the correct orientation of the linearly polarized beam, and through a half-wave plate to correct for the slight elliptical polarization introduced at the tube windows. Several irises were used to reduce stray light carried with beam. A long focal length lens (~90 cm) was used to weakly focus the beam to a waist of ~200 microns at the sample volume. The sample volume was within the discharge tube and was defined by the laser beam waist and an iris located between the discharge tube and imaging lens ($f\# = 2.4$). The geometry was such that the sample volume had a length of about 1mm. The scattered light was collected at a scattering angle of 90 degrees with the imaging lens and imaged through the mercury vapor filter. The filter had length 5 cm and had two temperature controllers yielding a vapor pressure of 0.003 Torr, and a filter temperature of 315 K. After the mercury filter, the light passed through a monochromator, which acted as a broad passband filter, while rejecting plasma luminosity and other colors of light from the laser. Finally, the scattered light signal was collected with a Hamamatsu R960 photomultiplier tube. After propagation through the discharge tube a quartz flat was used to pick off a fraction of the beam for power normalization as well as a frequency reference. The picked off beam illuminated a diffuser, and the elastically scattered light was detected through a second mercury filter (frequency reference), as well as measured by a photodiode (power reference). The latter two measurements used thin film interference filters (CORION G25-254-F) for spectral filtering. The three signals were collected with a Stanford Research System boxcar onto a computer.

In plasma temperature profile measurements, a thermocouple was used to measure the wall temperature. Two 1-D translation stages were used to translate the discharge tube horizontally relative to the laser beam. Radial profiles along the horizontal axis were found by translating the discharge tube. Profiles were obtained in the argon plasma as well as the argon plus 1% nitrogen mixture, both at a pressure of 50 Torr, at several different values of electric current.

For the range of experimental conditions studied, $p=30 - 50$ Torr, $i=30 - 100$ mA, the steady-state centerline temperature range was found to be from 440 ± 30 K to 830 ± 70 K. Fig. 5 shows the experimental profile of an argon plasma at pressure 50 Torr and current 20 mA. Figures 6 and 7 are experimental profiles of an argon + 1% nitrogen mixture at a pressure of 50 Torr, and currents of 10 and 40 mA respectively. The experimental points are in good agreement with computation.³¹ We have plotted them here with fitted Gaussian curves:

$$\frac{T(r)}{T_w} = \frac{T_c}{T_w} \exp \left[-\ln \frac{T_c}{T_w} \cdot \left(\frac{r}{R} \right)^2 \right], \quad (1)$$

where T_c and T_w are the centerline and wall temperature, respectively; r is the radial variable; and R is the tube radius.

III. Results of shock propagation studies in steady-state discharges and comparison with CFD axisymmetric modeling

In our earlier work^{22, 24}, we performed a 2D inviscid modeling of shock propagation through a discharge-heated gas and concluded that transverse gradient and multi-dimensionality play a crucial role in shock propagation in glow discharges, and that multi-peak laser schlieren signals are simply due to the shock curvature. For better comparison with experiments, in this work we developed an axisymmetric version of our code. The code solves the axisymmetric conservative form of the Euler equations on unstructured, triangular, adaptive meshes. The flux balance and shock capturing were carried out by extending the BGK solver developed and validated in Ref. 33 to axisymmetric problems. The grid adaption technique was identical to the one used for the two-dimensional code. The "driven" gas was initially at rest, and a shock wave of prescribed strength separated initially the "driven" gas from the "driver". The state of the "driver" gas was specified according to the Rankine-Hugoniot conditions.

The subsequent development of the flow field was computed by solving time-dependent Euler equations in conservation form. Thus, no additional care was required to satisfy the Rankine-Hugoniot conditions, and the correct shock propagation and jump conditions across shocks and other discontinuities were captured by the solution.

As found in the earlier work,²⁴ to model shock structure on a 10-microsecond time scale, simple computations of a "piston-driven", or "step" shock would suffice. This is due to the fact that the initial spark-generated shock broadens so much in its 20-40 cm path to the discharge entrance or a measurement point that on the 5-mm distance (or 10 μ s time interval) from the shock front the shock is very close to a "step" shock.²⁴ This simplification, while being quite accurate, saved us from running extremely CPU-intensive full computations of the spark-generated pulse shocks. The plasma region between the infinitely thin electrodes was considered uniform along the tube axis (x), and to have a symmetric radial temperature profile described by the analytical fit (1) to the experimentally measured profile. Both wall temperature and the gas temperature outside the discharge were set equal to room temperature. Thus, there was a sharp thermal diaphragm between the cold and hot regions. In absence of diffusion (both physical and numerical) this diaphragm will remain fixed with respect to a quiescent gas until the incident shock impinges upon it. The initial position of the incident shock in the calculations reported here was one tube radius to the left from the boundary between the cold and the discharge-heated gases. Mach numbers of the incident shock were selected so as to give the shock velocity in the uniform room-temperature gas at a given location close to that measured experimentally with the discharge off.

For comparison with laser schlieren measurements, the density gradient integrated in x direction across the narrow "laser beam" and averaged in the radial direction across the tube was computed. The "laser beam" width in the computations was adjusted once to match the experimentally determined width of the schlieren signal with the discharge off. The result of this calibration is shown in Fig.8. As seen in the Figure, computations reproduce the shape of the experimental peak very well.

Note that in the experiments time was measured from the moment of spark firing, while the computations started with the shock located at a distance of one tube radius to the left of the discharge region. Thus, computational time is shifted with respect to the experimental one by a constant. This is reflected in Figs. 8 – 11. For example, in Fig. 9, the experimental signals are plotted versus $(t - 700 \mu\text{s})$, where t is the time from the spark firing, and the computational results are plotted against $(t - 420 \mu\text{s})$, with the computational time t counted from the moment when the shock was located at a distance of one tube radius to the left of the discharge region. The constant shift of t obviously does not affect differential measurements or computations of shock velocity.

Figures 9 – 11 show measured and computed schlieren signals in pure argon (Fig.9) and Ar+1%N₂ (Figs. 10 and 11). In each figure, upper plots correspond to the discharge-off case, while lower plots correspond to the discharge current of 20 mA (Fig. 9), and 10 and 40 mA in Figs. 10 and 11. Figs. 10 and 11 differ in that the schlieren measurement point in Fig. 11 is about 11 cm downstream of that in Fig. 10. Measured and computed velocities of shock waves are shown near all the signals in Figs. 9 – 11. As seen in the figures, agreement between the computations and experiments, in both shock velocities and the two-peak signal shapes, is excellent. As discussed in Ref. 24, the two-peak structure of the laser schlieren signals is due to the curvature of the shock front in a region with transverse temperature gradient. This is illustrated in Fig.12 (a-d), where lines of constant density are shown in 4 moments of time, as the shock propagated from the room-temperature gas into the plasma. Note that

flow perturbations upstream of the moving shock, such as the distortion of the boundary between hot and cold regions seen in Figs. 12 (c) and (d), do not affect shock propagation. The first peak in the schlieren signal comes from the portion of the shock that propagates through the hot centerline region. The high temperature and low density in this region result in both higher shock speed and lower intensity of the peak compared with those corresponding to colder near-wall regions. The portion of the shock moving through the cold near-wall region lags behind and produces a strong peak in the signal due to the high density near the wall. (Note that in Fig. 12d, a well-resolved Mach stem is discernible near the wall). The decrease in the schlieren signal following the first peak is due to the curvature of the shock. Indeed, the signal is proportional to the axial component of the density gradient. Therefore, with the decrease of the shock angle with the tube axis from 90° to lower values (Fig. 12d), the signal weakens substantially.

Although in Figs. 9 – 11 the agreement between computed and experimentally measured parameters is excellent, it is not perfect. Specifically, computed shock velocities and distances between two peaks in schlieren signals agree very well with experimental values. On the other hand, computed height of both peaks in the signals relative to the signal strength between the peaks is higher than that in experiments. One of the principal uncertainties in computations is due to the use of Gaussian fit (1) to the experimentally measured temperature profile, especially since temperature measurements have their own errors. Next, neither experimental nor computational (the latter – due to the mesh size) resolution is perfect. Still another factor is the use of inviscid model that disregards viscosity and heat conduction. According to the data of Ref. 34, kinematic viscosity of Ar at 50 Torr, 300 K, is $\nu = 2.1 \text{ cm}^2/\text{s}$, and at 50 Torr, 600 K, it is $\nu = 7.1 \text{ cm}^2/\text{s}$. Thermal diffusivity values are, of course, comparable with those of viscosity.³⁴ The total width of the signal (that is, the distance between the peaks) in Figs. 9 – 11 is about $t = 10 \text{ } \mu\text{s}$. During this time, viscosity and heat conduction can smear velocity and density profiles on a length scale of $\delta \approx \sqrt{6\nu t} = 0.1 - 0.2 \text{ mm}$. Since the width of each peak, converted into the length scale, is about 0.5 mm, and the distance between the peaks – about 5 mm, viscosity and heat conduction cannot change the overall structure of the schlieren signals, which reaffirms the validity of inviscid modeling; however, some smearing of the signals can occur, helping to fill the “trough” between the peaks.

Note that since the linear velocity of the gas downstream of the shock is extremely low, 5-10 cm/s, boundary layer is virtually nonexistent prior to the shock arrival. Behind the shock, boundary layer thickness growth with distance x can be estimated, similar to the previous paragraph, as $\delta \approx \sqrt{6\nu t}$, where $t = x/u$, and u is the gas velocity behind the shock. On the time scale of 1-10 μs after the shock passage, the boundary layer will grow to only $\delta = 0.03 - 0.09 \text{ mm}$ in our experimental conditions. Thus, the boundary layer is very thin in the vicinity of the shock and does not affect schlieren signals. As to the boundary layer farther upstream, it has no effect on the shock propagation.

For further quantitative comparison between computational and experimental results, Figures 13 and 14 show the width of schlieren signals versus centerline temperature (Fig.13) and the shock velocity versus average temperature in the discharge (Fig.14), using the same set of shock propagation data. The average temperature was determined in a standard way:

$$T_{av} = \frac{\int_0^R T(r) \cdot 2\pi r dr}{\pi R^2} \quad (2)$$

Again, Figure 13 and 14 show excellent agreement between computations and experimental data. This provides a strong evidence of conventional, thermal mechanism of shock propagation in weakly ionized plasmas.

IV. Experiments on shock propagation in pulsed discharges

To distinguish between thermal and plasma-specific mechanisms of shock propagation, it would be desirable to eliminate temperature effects while maintaining plasma with the same density of charged particles, electric field, etc. Unfortunately, conventional steady-state discharge is a system where thermal effects are coupled with electric fields and electron density. However, in pulsed discharges, a relatively long time interval can exist when electron, ion, and excited molecule densities are quite high while the temperature is low. Indeed, gas heating

and cooling occurs on time scale orders of magnitude longer than the time scale for ionization/recombination/excitation processes.³⁵

In this work, the pulsed mode of the discharge was produced by using a transistor switch in series with the discharge. The rise time for the current pulse was 20 μ s, and the pulse duration was about 0.5 ms. It was found that this time was insufficient to get a uniform discharge. In fact, when the discharge was turned on, undesirable transitional processes (for example, discharges on the wall of the tube) were observed. Therefore a weak pilot discharge with 1 mA current was maintained between pulses, which resulted in a fairly uniform volume pulsed discharge. Fig. 15 shows the discharge pulse shape and the time dependence of discharge integral emission (with no shock wave). Clearly, at times near to the middle of the pulse the emission reaches its steady-state value, similar to that of the continuous discharge. The initial peak of intensity is a result of the higher electric field arising in the discharge immediately after the transistor switch is opened (see below).

As shown in Figs. 16 and 17, for the pilot discharge a small acceleration, accompanied by some widening and weakening of the signal can be noticed, but the changes are very small compared to the higher-current continuous discharge. This is no surprise since the electron number density in the pilot discharge is $\sim 10^8$ cm⁻³ only and the measured axial gas temperature is less than 320 K.

Much more important is that schlieren signal obtained from the pulsed discharge, as seen in Figs. 16 and 17, closely matches both no-discharge and pilot-discharge curves, and is very unlike the signal from the continuous discharge. After the transistor switch is turned on, the discharge current reaches its new steady-state value in ~ 20 μ s. This value is almost the same as in continuous discharge. The electric field strength E in the pulse could be found by subtracting cathode drop V_c and voltage drop across the ballast resistor from the power supply voltage. The E values were found to be somewhat larger than in the continuous discharge, but the E/N values are almost identical. Thus, the electron number densities and mean electron energies (electron temperatures) should be very close to those in the continuous discharge. This is confirmed by the behavior of the discharge emission (Fig. 15). It reaches its steady-state value that is very close to that of the continuous discharge. An initial overshoot is related to the over voltage applied to the discharge in the transition period (~ 20 μ s) from small to large current. Higher E/N values in this interval result in efficient excitation of atoms and molecules, including those with radiative lifetime ~ 1 – 10 μ s (e.g., intensive bands of the 1st positive system of the N₂ molecule).

The increase in gas temperature, ΔT , during the pulse for the pulse duration τ_p may be calculated from the simple balance equation $iE\tau_p = c_p m_1 \Delta T$, where c_p is the specific heat, and m_1 is a mass of gas per unit length. Here we ignore heat losses because the pulse duration is a factor of 100 less than the characteristic time for thermal conductivity. For the conditions of Fig. 16, this equation gives $\Delta T = 0.4$ K – 0.6 K. Thus, the pulsed discharge has electron component parameters (E/N , n_e , T_e) the same as in the continuous discharge, but the gas temperature is the same as in the pilot discharge, that is, close to room temperature. Comparing the three schlieren curves of Fig. 16 (and, similarly, those of Fig. 17) definitely shows that changing the electron density by two orders of magnitude does not affect shock wave propagation, while changing gas temperature from $T_g \sim 320$ K to $T_g \sim 500$ – 600 K (from the pilot or pulsed discharge to the continuous discharge) affects the shock dramatically. This result may be considered as a strong evidence of thermal mechanism of shock wave – plasma interaction.

To further illustrate the role of heating in shock dynamics, Fig. 18 shows schlieren signals taken with time delay between turning the discharge on and launching the shock ranging from 1 ms to 200 ms. The 1-ms-delay signal is very close to that in the pilot discharge, while the 200-ms-delay signal is close to that in the continuous discharge. It takes tens and hundreds of milliseconds of the discharge existence for the signal to get close to its steady-state shape. The same point is also illustrated in Fig. 19, showing measured shock speed and schlieren signal width approaching their d.c. discharge values as the discharge is allowed to exist longer. Only gas heating in the discharge takes that long; ionization and excitation processes are many orders of magnitude faster.

As the discharge is turned off, one would expect thermal effects to persist for a long time, tens or even hundreds of milliseconds, when recombination of charged species and quenching of excited states will be long since complete. Indeed, this persistence is clearly seen in Figs. 20 and 21, again supporting the thermal mechanism of shock-plasma interaction.

It should be noted that vibrational temperature, or populations of vibrational states, of nitrogen molecules, could be another parameter (apart from the gas temperature) that is quite different in pulsed and continuous discharges. The vibrational relaxation characteristic time is 1 – 2 orders of magnitude longer than the pulse duration, so the vibrational temperature in the pulsed discharge must be almost the same as in the pilot (1 mA) discharge.

To clarify the role of vibrational relaxation, shock wave propagation through pure argon discharge was also studied at low currents where contraction did not occur. In Fig. 22 schlieren signals for the two gases (Ar and Ar+1%N₂) are compared. The main features of schlieren signals for both cases are similar. For a more detailed comparison, one has to take into account that addition of even 0.1-1% of nitrogen to argon dramatically changes the electron drift velocity for the same E/N.³⁶ Another important factor found in our experiments is that the values of E/N in Ar+1%N₂ are substantially lower than those in pure Ar. Since E/N in the positive column is determined by the local ionization balance,³⁵ ionization and/or recombination rates must be affected by the addition of nitrogen. The exact mechanism of the decrease in E/N with nitrogen addition is not clear at this time, and, being outside the immediate goal of this work, can be investigated in the future. One possible explanation is that metastables, such as N₂(³Σ), and vibrationally excited nitrogen molecules enhance the ionization. In any case, the reduction in E/N is an experimental fact, and it results in lower gas temperature in Ar+1%N₂ even at the same current as in pure Ar. (See, for example, Figs. 5 and 7). For a meaningful comparison of shock propagation data in Ar and Ar+N₂ mixtures, at least one of the parameters – electric current, electron number density, or gas temperature – should be the same in both cases. Data presented in Fig. 22 for Ar+1%N₂ mixture are shown at i=20 mA (the same as for pure argon), at 40 mA, where gas temperatures are close for both discharges, and at 60 mA, where electron densities are almost equal. It is evident that for the condition of almost-equal gas temperatures (40 mA) similarity of the patterns is the best. This eliminates unambiguously the vibrational relaxation effect and supplies one more evidence of the thermal mechanism of shock dispersion.

V. Conclusions

Extensive experimental data on shock propagation in steady-state glow discharges in argon and argon-nitrogen mixtures were found to be in excellent agreement with high-accuracy axisymmetric CFD modeling. This provides compelling evidence that shock acceleration, attenuation, and "broadening" in weakly ionized plasmas can be explained by conventional gas dynamics, with multi-dimensionality (due to transverse temperature gradients) playing a critical role.

Experiments with pulsed discharges allowed us to separate thermal effects from those due to electric fields and charged particles. It turned out that gas heating is necessary for shock velocity and schlieren signal parameters to attain their steady-state values. This provides a direct proof of thermal mechanism of weakly ionized plasma effects on shock propagation.

REFERENCES

- ¹ G.I.Mishin, A.P.Bedin, N.I.Yushchenkova, G.E.Skvortsov, A.P.Ryazin, "Anomalous Relaxation and Instability of Shock Waves in Plasmas," *Sov. Phys. Tech. Phys.* **26**, 1363 (1981).
- ² A.I.Klimov, A.N.Koblov, G.I.Mishin, Yu.L.Serov, and I.P.Yavor, "Shock Wave Propagation in a Glow Discharge," *Sov. Tech. Phys. Lett.* **8**, 192 (1982).
- ³ A.I.Klimov, A.N.Koblov, G.I.Mishin, Yu.L.Serov, K.V.Khodataev, and I.P.Yavor, "Shock Wave Propagation in a Decaying Plasma," *Sov. Tech. Phys. Lett.* **8**, 240 (1982).
- ⁴ I.V.Basargin and G.I.Mishin, "Probe Studies of Shock Waves in the Plasma of a Transverse Glow Discharge," *Sov. Tech. Phys. Lett.* **11**, 535 (1985).
- ⁵ V.A.Gorshkov, A.I.Klimov, G.I.Mishin, A.B.Fedotov, and I.P.Yavor, "Behavior of Electron Density in a Weakly Ionized Nonequilibrium Plasma with a Propagating Shock Wave," *Sov. Phys. Tech. Phys.* **32**, 1138 (1987).
- ⁶ A.P.Ershov, S.V.Klishin, A.A.Kuzovnikov, S.E.Ponomareva, and Y.P.Pyt'ev, "Application of the Reduction Method to the Microwave Interferometry of Shock Waves in Weakly Ionized Plasma," *Sov. Phys. Tech. Phys.* **34**, 936 (1989).
- ⁷ I.V.Basargin and G.I.Mishin, "Precursor of Shock Wave in Glow Discharge Plasma," *Sov. Tech. Phys. Lett.* **15**, 311 (1989).
- ⁸ S.A.Bystrov, I.S.Zaslonko, Y.K.Mukoseev, and P.V.Shugaev, "Precursor Ahead of a Shock Front in an RF Discharge Plasma," *Sov. Phys. – Doklady* **35**, 39 (1990).
- ⁹ G.I.Mishin, A.I.Klimov, and A.Y.Gridin, "Measurements of the Pressure and Density in Shock Waves in a Gas Discharge Plasma," *Sov. Tech. Phys. Lett.* **17**, 602 (1992).

- ¹⁰ A.Y.Gridin, A.I.Klimov, and K.V.Khodataev, "Propagation of Shock Waves in a Nonuniform Transverse Pulsed Discharge," *High Temperature* **32**, 454 (1994).
- ¹¹ A.Y.Gridin, A.I.Klimov, K.V.Khodataev, N.B.Shcherbak, and S.B.Shcherbak, "Two-Dimensional Simulation of Shock Wave Propagation in a Transverse Pulse Glow Discharge with a Heated Cathode layer," *High Temperature* **32**, 755 (1994).
- ¹² B.N.Ganguly, P.Bletzinger, and A.Garscadden, "Shock Wave Damping and Dispersion in Nonequilibrium Low Pressure Argon Plasmas," *Phys. Lett. A* **230**, 218 (1997).
- ¹³ B.N.Ganguly and P.Bletzinger, "Shock Wave Dispersion in Nonequilibrium Plasmas," Paper AIAA-96-4607, 1996.
- ¹⁴ A.Garscadden, P.Bletzinger, and B.N.Ganguly, "Acoustic Shock Interaction in a Positive Column Plasma," Paper AIAA-99-4973, 1999.
- ¹⁵ N.V.Evtyukhin, A.D.Margolin, and V.M.Shmelev, "On the Nature of Shock Wave Acceleration in Glow Discharge Plasma," *Sov. J. Chem. Phys.* **3**(9), 2080 (1986).
- ¹⁶ P.A.Voinovich, A.P.Ershov, S.E.Ponomareva, and V.M.Shibkov, "Propagation of Weak Shock Waves in Plasma of Longitudinal Glow Discharge in Air," *High Temperature* **29**(3), 468 (1991).
- ¹⁷ N.Babaeva, "On the Structure of Shock and Blast Waves in Nonequilibrium Plasma of Gas Discharge," *Russian Journal of Chemical Physics* **12**, 357 (1993) [in Russian].
- ¹⁸ N.Babaeva, A.Mnatsakanyan, and G.Naidis, "Simulation of Shock Wave Propagation in a Gas Discharge Developing in Nitrogen," *High Temperature* **31**, 617 (1993).
- ¹⁹ N.Babaeva and G.Naidis, "Simulation of Shock Wave Propagation in Gas Discharge Plasma Regions," in: *Proceedings of the Workshop "Perspectives of MHD and Plasma Technologies in Aerospace Applications,"* Moscow, March 24-25, 1999, p. 108.
- ²⁰ I.V.Adamovich, V.V.Subramaniam, J.W.Rich, and S.O.Macheret, "Shock Wave Propagation in Weakly Ionized Plasmas," Paper AIAA-97-2499, 1997.
- ²¹ I.V.Adamovich, V.V.Subramaniam, J.W.Rich, and S.O.Macheret, "Phenomenological Analysis of Shock-Wave Propagation in Weakly Ionized Plasmas," *AIAA Journal* **36**, 816 (1998).
- ²² S.O.Macheret, L.Martinelli, and R.B.Miles, "Shock Propagation in Weakly Ionized Plasmas: Mechanisms and Key Problems," *Proceedings of the 1st Weakly Ionized Gases Workshop*, pp. X-11 – X-33, U.S. Air Force Academy, June 9-13, 1997.
- ²³ W.F.Bailey and W.M.Hilbun, "Baseline of Thermal Effects on Shock Propagation in Glow Discharge," *Proceedings of the 1st Weakly Ionized Gases Workshop*, pp. GG3 – GG18, U.S. Air Force Academy, June 9-13, 1997.
- ²⁴ S.O.Macheret, L.Martinelli, and R.B.Miles, "Shock Propagation and Structure in Non-Uniform Gases and Plasmas," Paper AIAA-99-0598, 1999.
- ²⁵ S.M.Aithal and V.V.Subramaniam, "On the Characteristics of a Spark Generated Shock Wave," *Phys. Fluids* **12**, 924 (2000).
- ²⁶ Y.Z.Ionikh, N.V.Chernysheva, A.V.Meshchanov, A.P.Yalin, and R.B.Miles, "Direct Evidence for Thermal Mechanism of Plasma Influence on Shock Wave Propagation," *Phys. Lett. A* **259**, 387 (1999).
- ²⁷ S.O.Macheret, Y.Z.Ionikh, L.Martinelli, P.F.Barker, and R.B.Miles, "External Control of Plasmas for High-Speed Aerodynamics," Paper AIAA-99-4853, 1999.
- ²⁸ J.H.Kiefer and R.W.Lutz, "Simple Quantitative Schlieren Technique of the High Sensitivity for Shock Tube Densitometry," *Phys. Fluids* **8**, 1393 (1965).
- ²⁹ J.A.Bander and G.Sanzone, "An Improved Laser-Schlieren System for the Measurement of Shock-Wave Velocity," *Rev. Sci. Instrum.* **45**, 949 (1974).
- ³⁰ A.P.Yalin and R.B.Miles, "Ultraviolet Filtered Rayleigh Scattering Temperature Measurements with a Mercury Filter," *Optics Lett.* **24**, 590 (1999).
- ³¹ A.P.Yalin, Y.Ionikh, and R.B.Miles, "Temperature Measurements in Glow Discharges with Ultraviolet Filtered Rayleigh Scattering," Paper AIAA-99-3431, 1999.
- ³² N.D.Finkelstein, W.R.Lempert, and R.B.Miles, "Mercury Vapor Filter Technology and Ultraviolet Laser Source for Flowfield Imaging," Paper AIAA-97-0157, 1997.
- ³³ C.A.Kim, A.Jameson, L.Martinelli, and K.Xu, "An Accurate LED-BGK Solver in Unstructured Adaptive Meshes," Paper AIAA 97-0328, 1997.

³⁴ Handbook of Physical Quantities, Ed. by I.S.Grigoriev and E.Z.Meilikhov, CRC Press, Boca Raton, Florida, 1997, Chapters 15 and 16.

³⁵ Yu.P.Raizer, *Gas Discharge Physics*, Springer, 1991, Chapters 4, 10, and 14.

³⁶ S.C.Brown, *Basic Data of Plasma Physics*, M.I.T. Press, Cambridge, MA and London, 1966, p. 94.

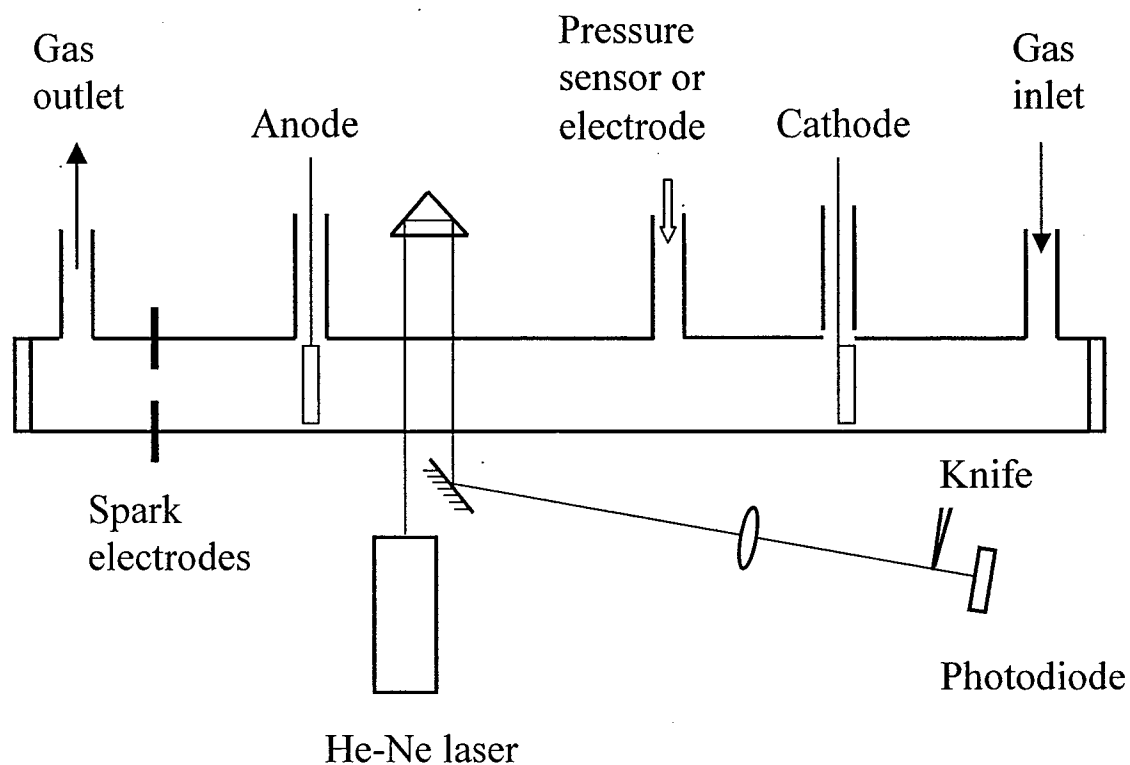


Fig.1. Schematic of the experimental setup for studies of shock propagation in glow discharges

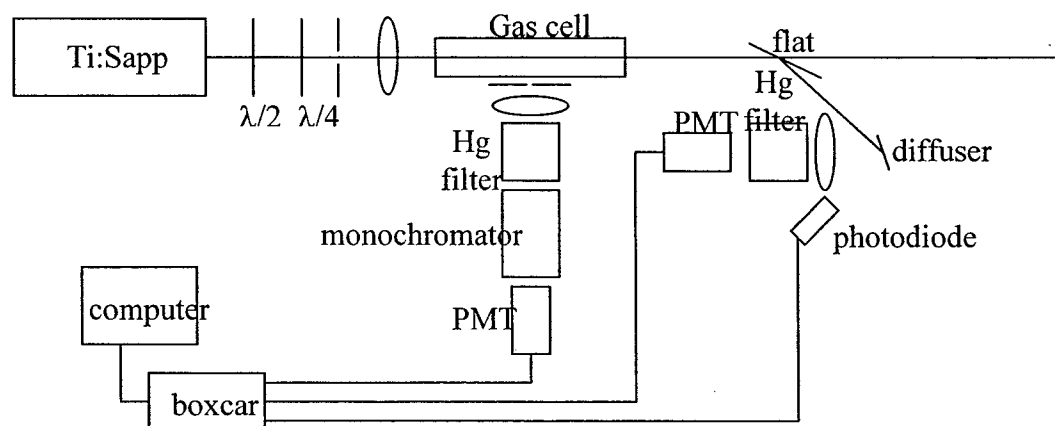


Fig.2. Schematic diagram of experimental setup for UV FRS measurements of temperature profiles.

Modeled UV FRS signal levels for Argon, T=300,...,750 K

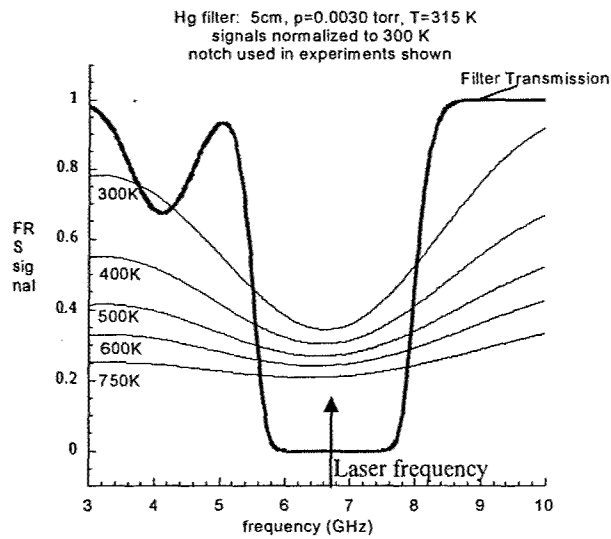


Fig. 3. Modeled FRS signal levels for Argon at a range of temperatures. Mercury has several absorption notches in the 253.7 nm vicinity, however Fig.3 shows the experimentally used (high-frequency) notch.

Conversion Graph: Signal Ratio - Temperature

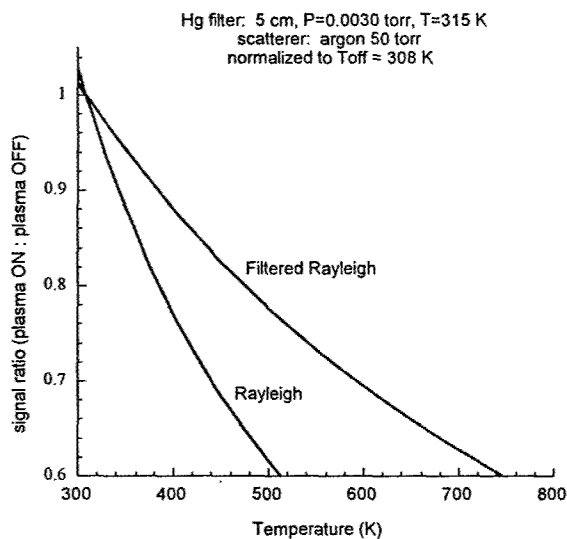


Fig.4. Look-up graph used to convert signal ratio found with discharge ON/OFF to plasma temperature.

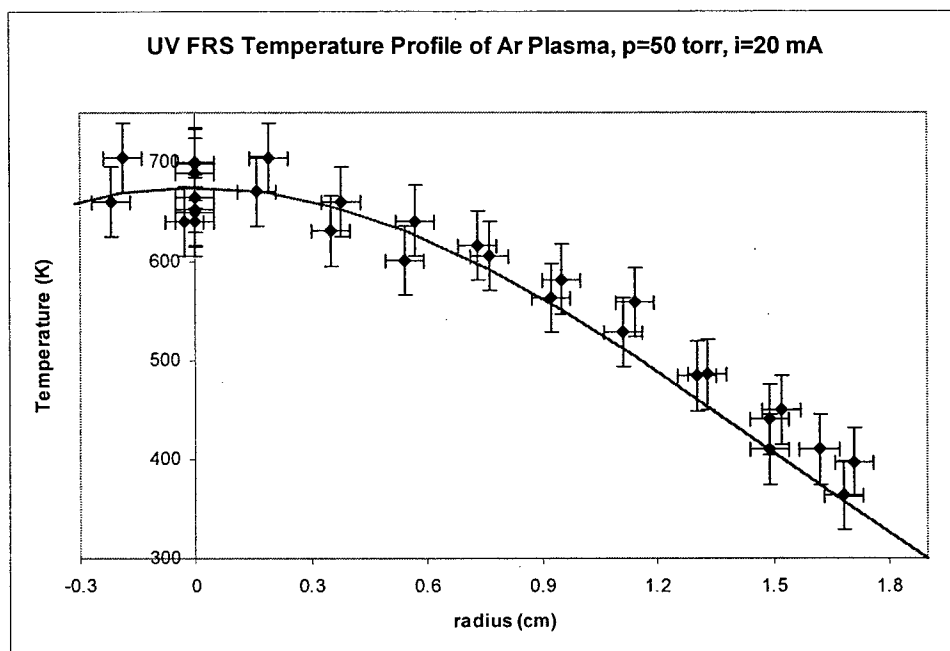


Fig.5. Radial temperature profile in Ar glow discharge tube measured by UV Filtered Rayleigh Scattering. Pressure and electric current are indicated on the plot. Fitting curve – see Eqn. (1).

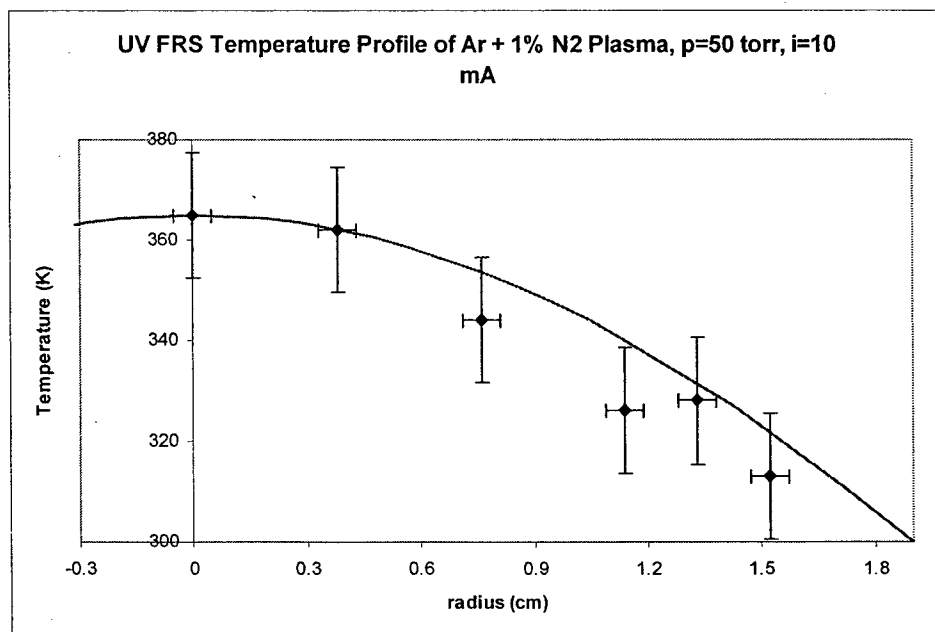


Fig.6. Radial temperature profile in Ar+1%N₂ glow discharge tube measured by UV Filtered Rayleigh Scattering. Pressure and electric current are indicated on the plot. Fitting curve – see Eqn. (1).

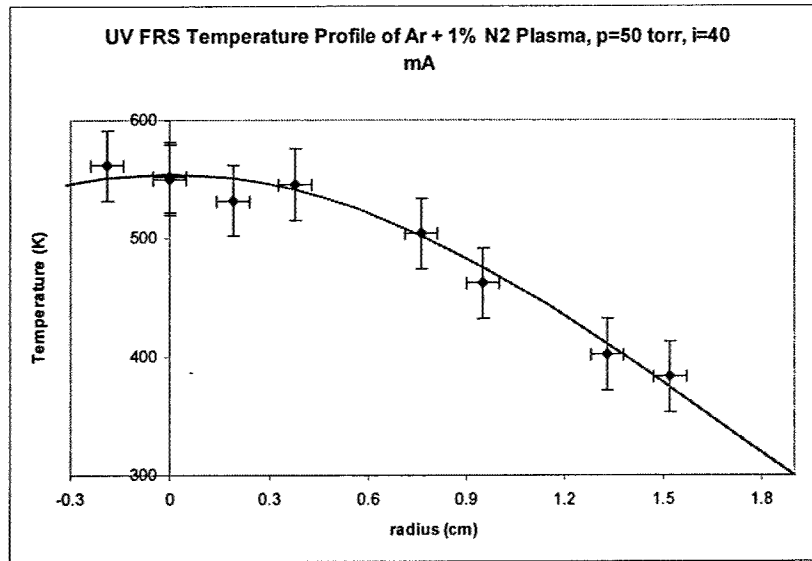


Fig.7. Radial temperature profile in Ar+1%N₂ glow discharge tube measured by UV Filtered Rayleigh Scattering. Pressure and electric current are indicated on the plot. Fitting curve – see Eqn. (1).

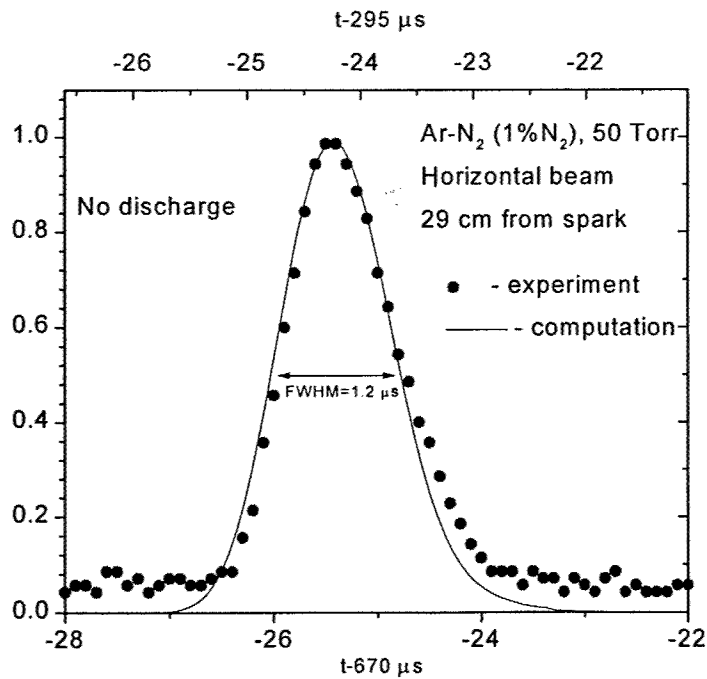


Fig.8. Calibration of the “laser beam width” for CFD modeling against laser schlieren signal with the discharge off. Note: experimental time t was measured from the moment of spark firing, while the computational time t was counted from the moment when the shock was located at a distance of one tube radius to the left of the discharge.

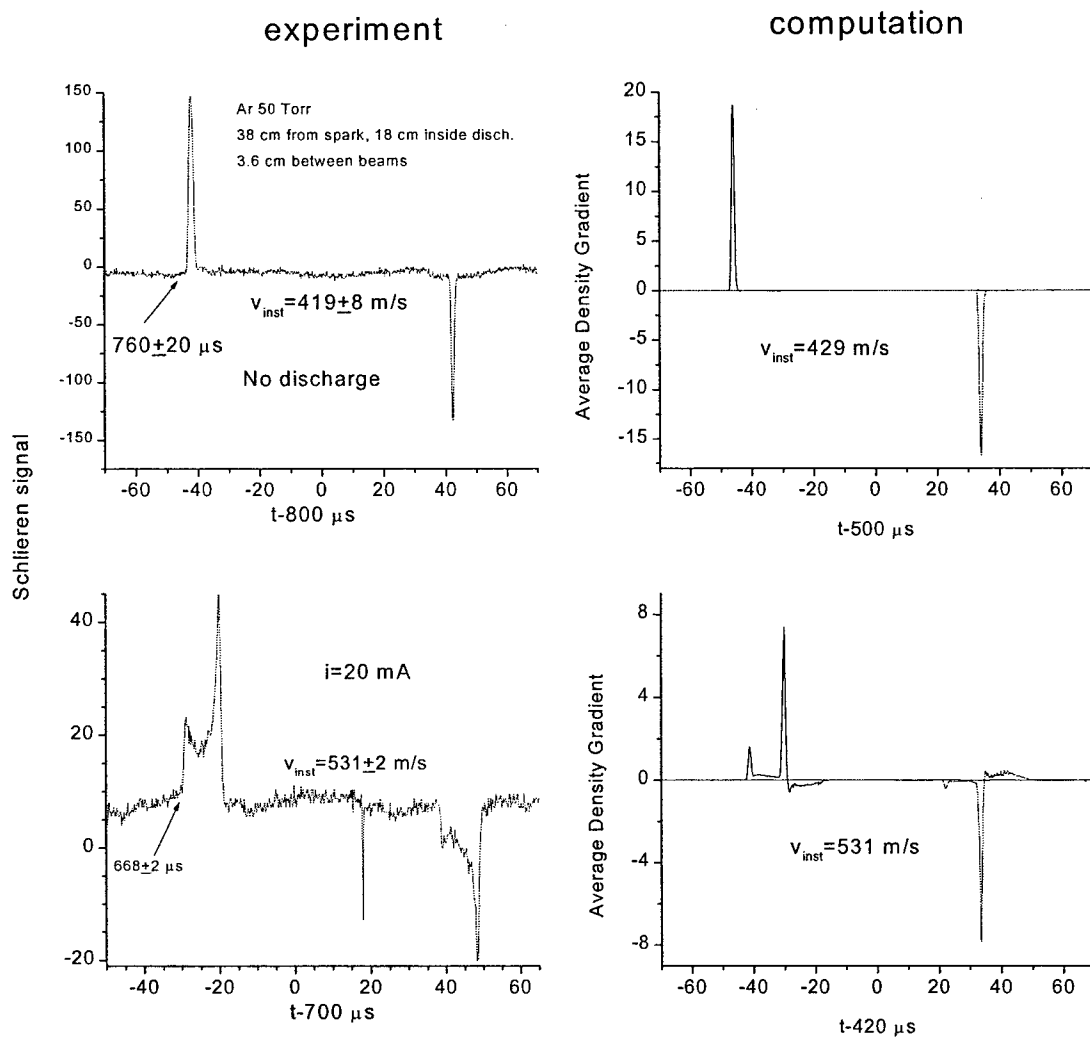


Fig.9. Experimentally measured and simulated laser schlieren signals for shocks propagating in glow discharge in pure Ar at 50 Torr. The discharge current is 20 mA. The first of the two laser beams is located 18 cm from the entrance to the discharge, and the spacing between the two beams is 3.6 cm. The experimentally measured and computed shock velocities are indicated on the figure. Note: experimental time t was measured from the moment of spark firing, while the computational time t was counted from the moment when the shock was located at a distance of one tube radius to the left of the discharge.

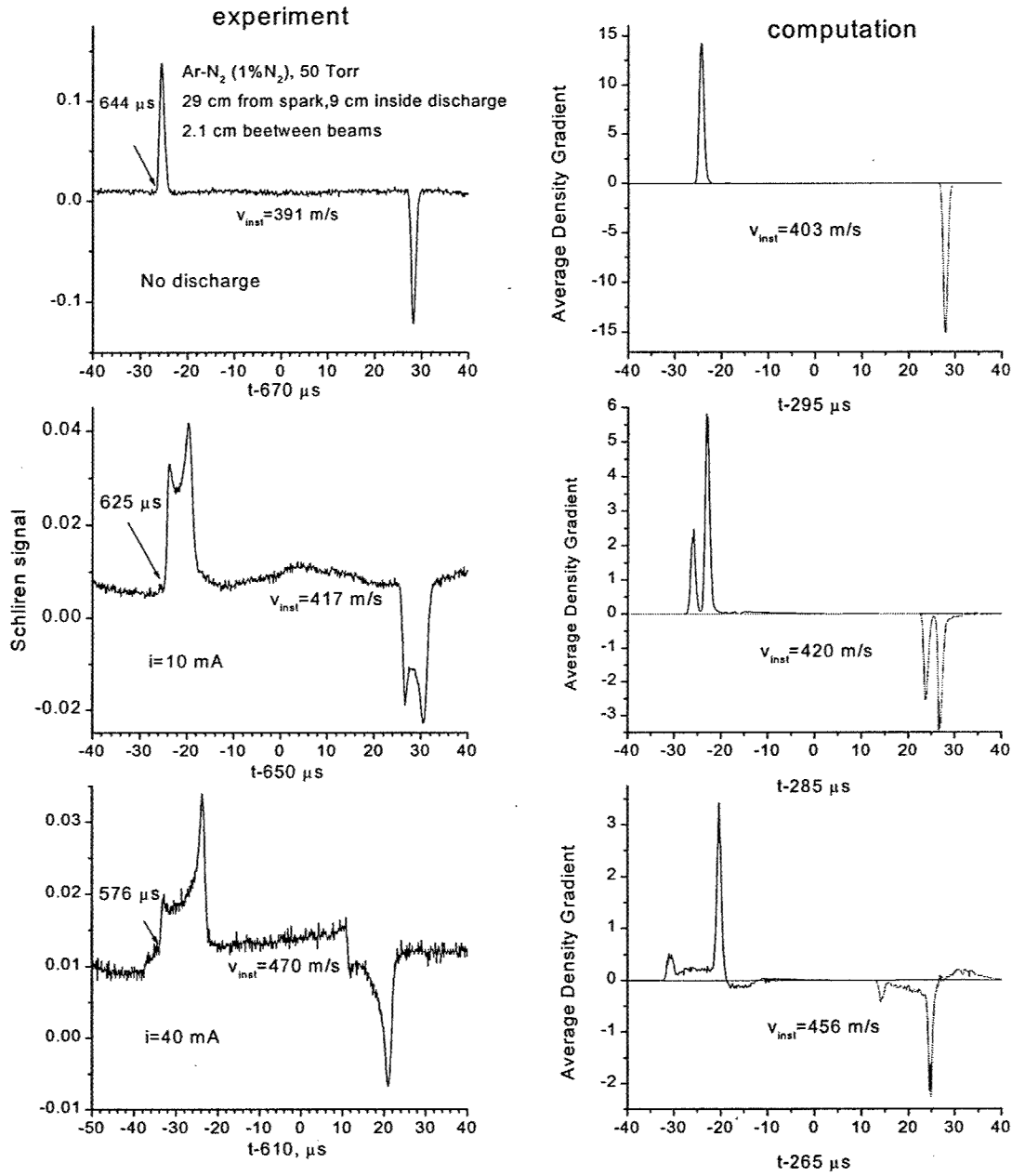


Fig.10. Experimentally measured and simulated laser schlieren signals for shocks propagating in glow discharge in Ar+1%N₂ at 50 Torr. The discharge current values are 10 mA and 40 mA. The first of the two laser beams is located 9 cm from the entrance to the discharge, and the spacing between the two beams is 2.1 cm. The experimentally measured and computed shock velocities are indicated on the figure. Note: experimental time t was measured from the moment of spark firing, while the computational time t was counted from the moment when the shock was located at a distance of one tube radius to the left of the discharge.

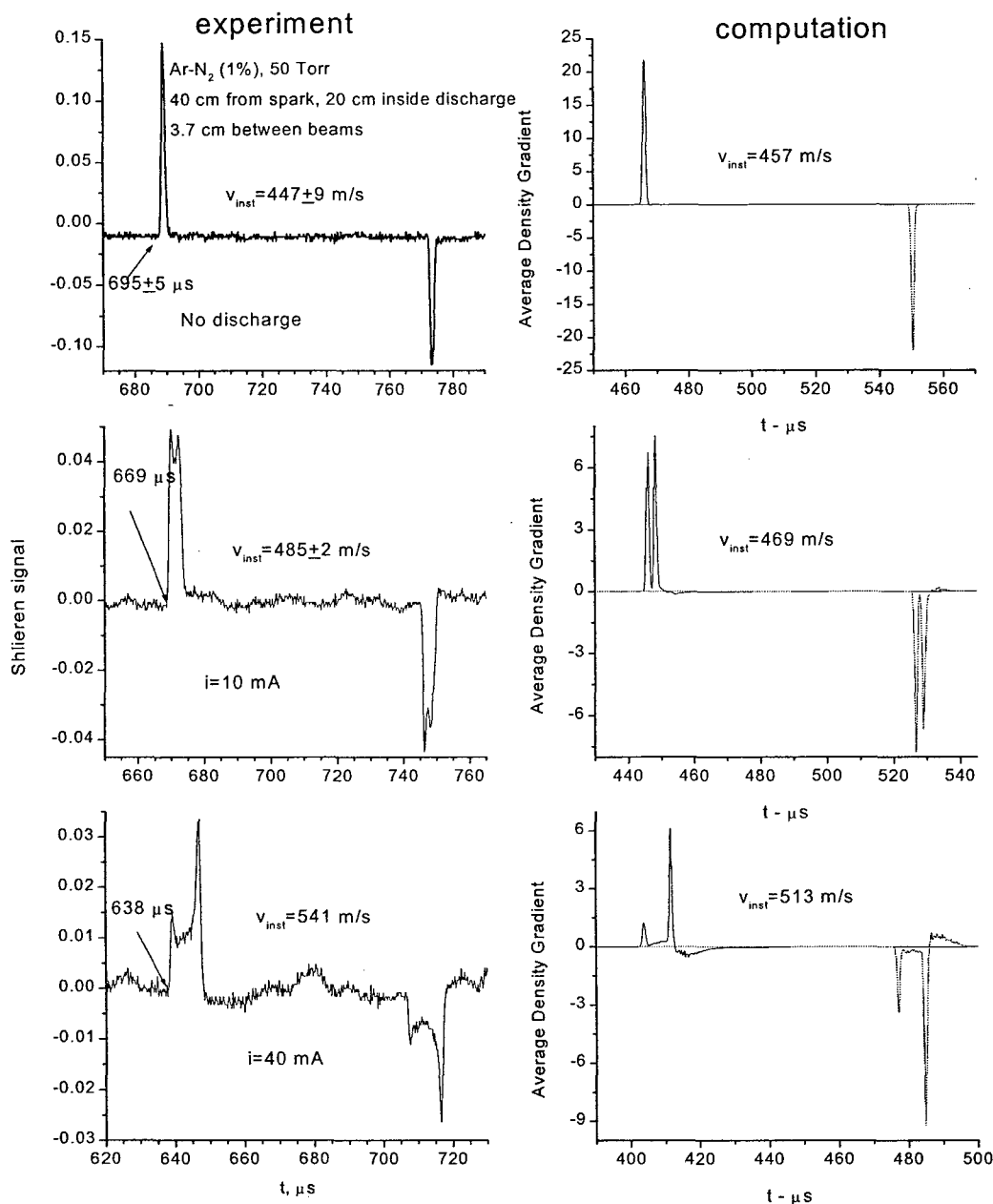


Fig.11. Experimentally measured and simulated laser schlieren signals for shocks propagating in glow discharge in Ar+1%N₂ at 50 Torr. The discharge current values are 10 mA and 40 mA. The first of the two laser beams is located 20 cm from the entrance to the discharge, and the spacing between the two beams is 3.7 cm. The experimentally measured and computed shock velocities are indicated on the figure. Note: experimental time t was measured from the moment of spark firing, while the computational time t was counted from the moment when the shock was located at a distance of one tube radius to the left of the discharge.

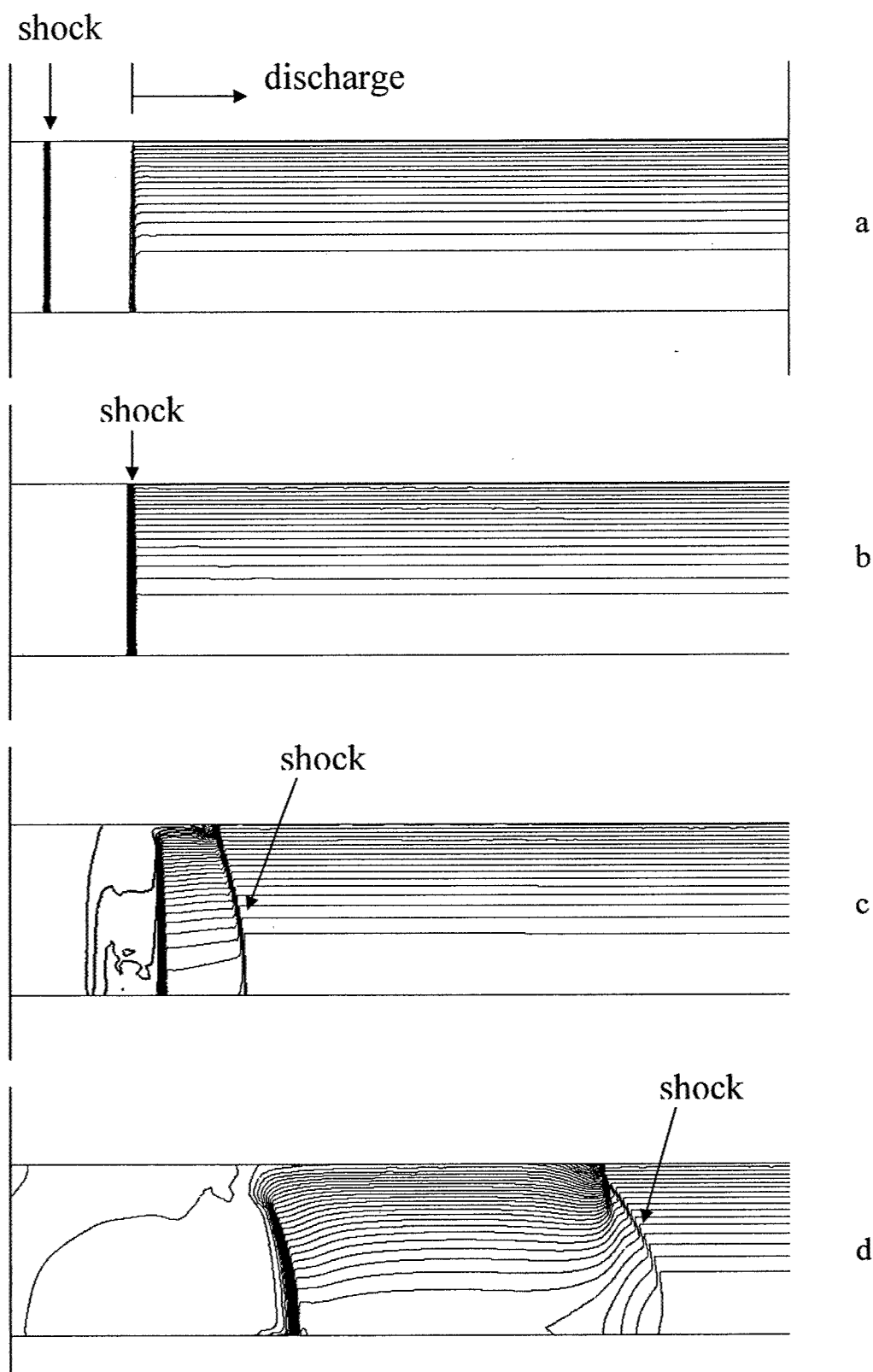


Fig.12. Computed constant-density lines during shock propagation in glow discharge tube (pure Ar, 50 Torr, 20 mA): (a) – $t=21 \mu\text{s}$, prior to shock entry into the discharge; (b) – $t=43 \mu\text{s}$, shock entering the discharge; (c) – $t=60 \mu\text{s}$, shortly after the shock entered the discharge; (d) – $t=123 \mu\text{s}$, shock has penetrated deep inside the discharge. The computational time t was counted from the moment when the shock was located at a distance of one tube radius to the left of the discharge

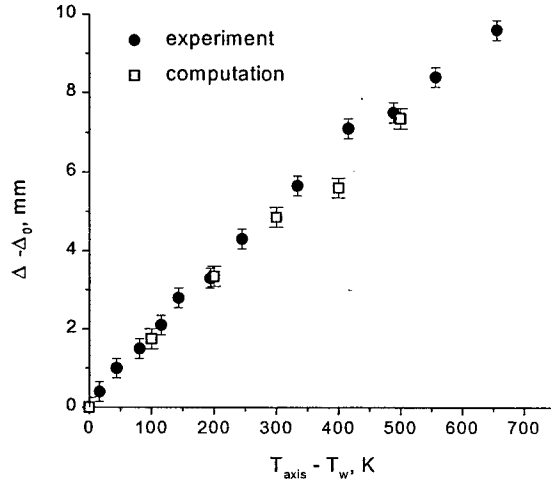


Fig.13. The width of the schlieren signal in the discharge (Δ) minus the signal width with the discharge off (Δ_0) versus temperature difference between the axis and the wall, $T_{axis} - T_w$. Gas mixture Ar+0.16%N₂, pressure 50 Torr; 3 cm spark gap, 15 kV spark voltage; first laser beam is 24.8 cm inside the discharge; spacing between the two beams is 2.9 cm.

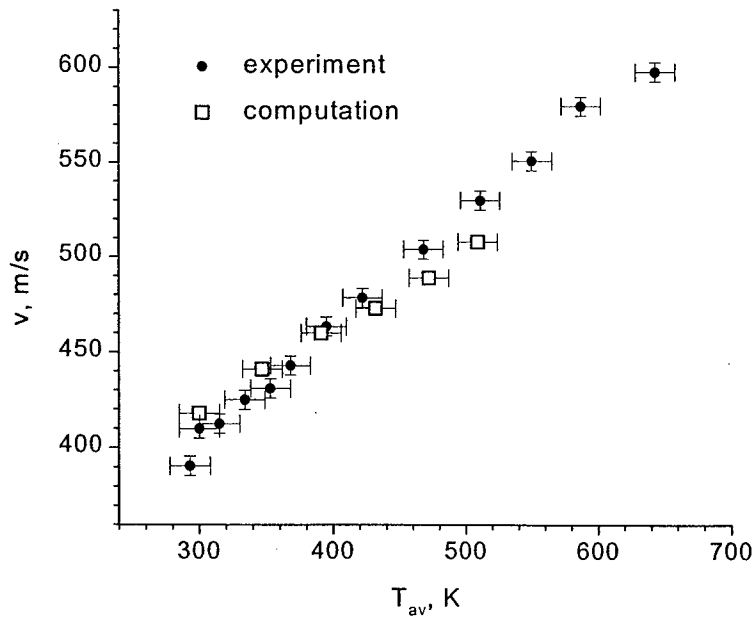


Fig.14. Shock wave velocity versus average temperature [definition – see Eqn. (2)] in the discharge. Gas mixture Ar+0.16%N₂, pressure 50 Torr; 3 cm spark gap, 15 kV spark voltage; first laser beam is 24.8 cm inside the discharge; spacing between the two beams is 2.9 cm.

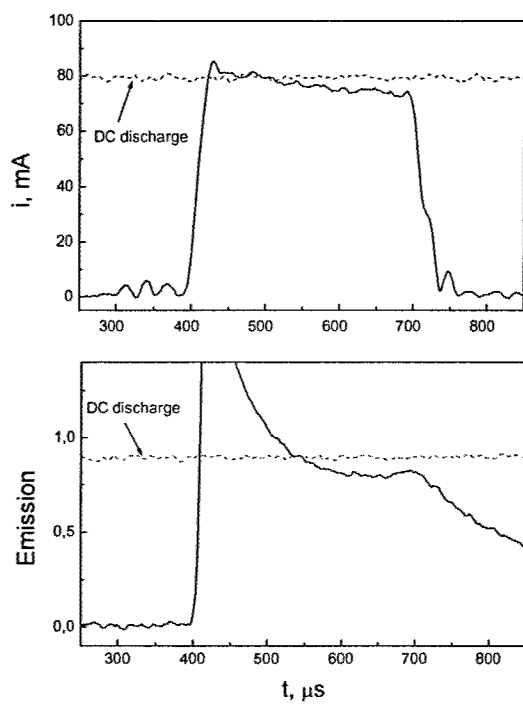


Fig.15. Discharge current and integrated spectral emission versus time during the pulse.

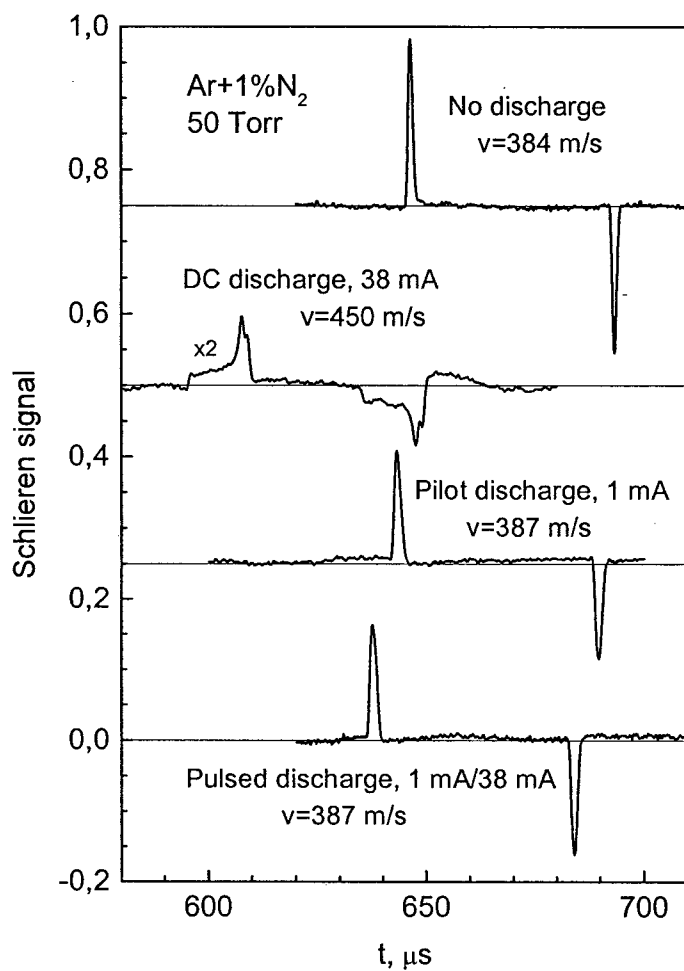


Fig.16. Schlieren signals and shock velocities in glow discharge in Ar+1%N₂ at 50 Torr: the discharge off; 38-mA continuous d.c. discharge, weak (1 mA) pilot discharge, and a pulsed discharge.

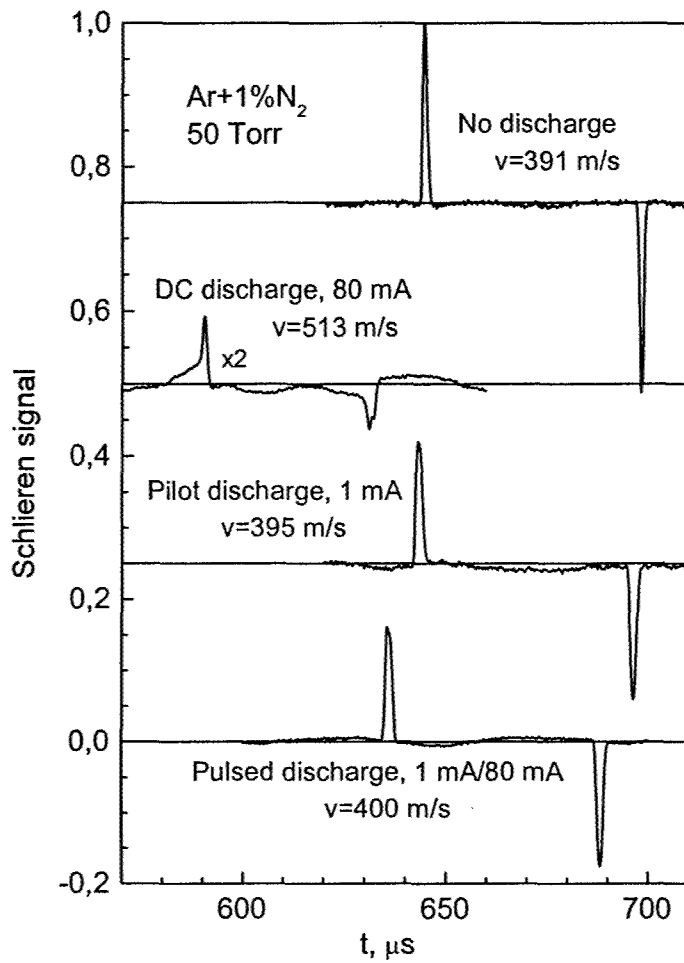


Fig.17. Schlieren signals and shock velocities in glow discharge in Ar+1%N₂ at 50 Torr: the discharge off; 80-mA continuous d.c. discharge, weak (1 mA) pilot discharge, and a pulsed discharge.

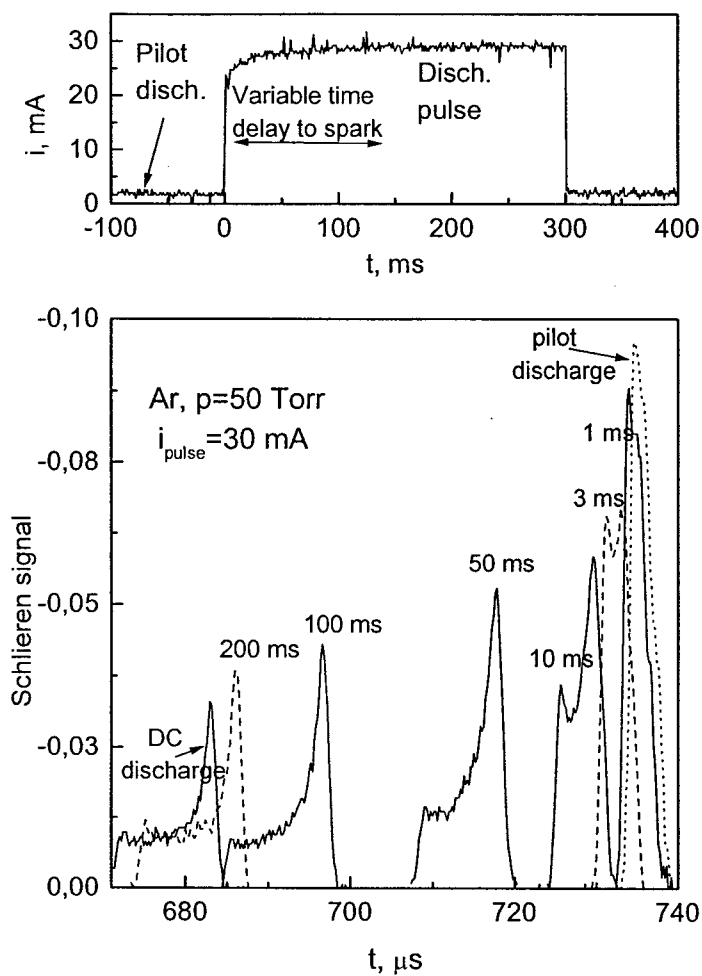


Fig.18. Evolution of the schlieren signal at a fixed location inside the discharge with time delay between the beginning of the discharge and the shock launch

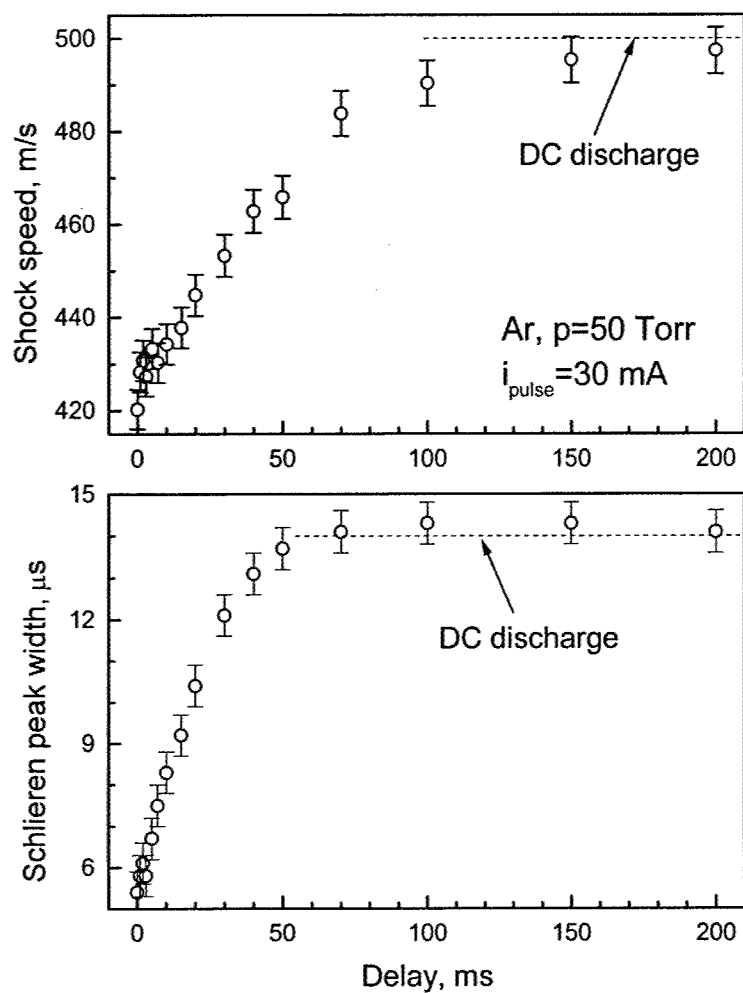


Fig.19. Evolution of shock velocity and the width of the schlieren signal at a fixed location inside the discharge with time delay between the beginning of the discharge and the shock launch

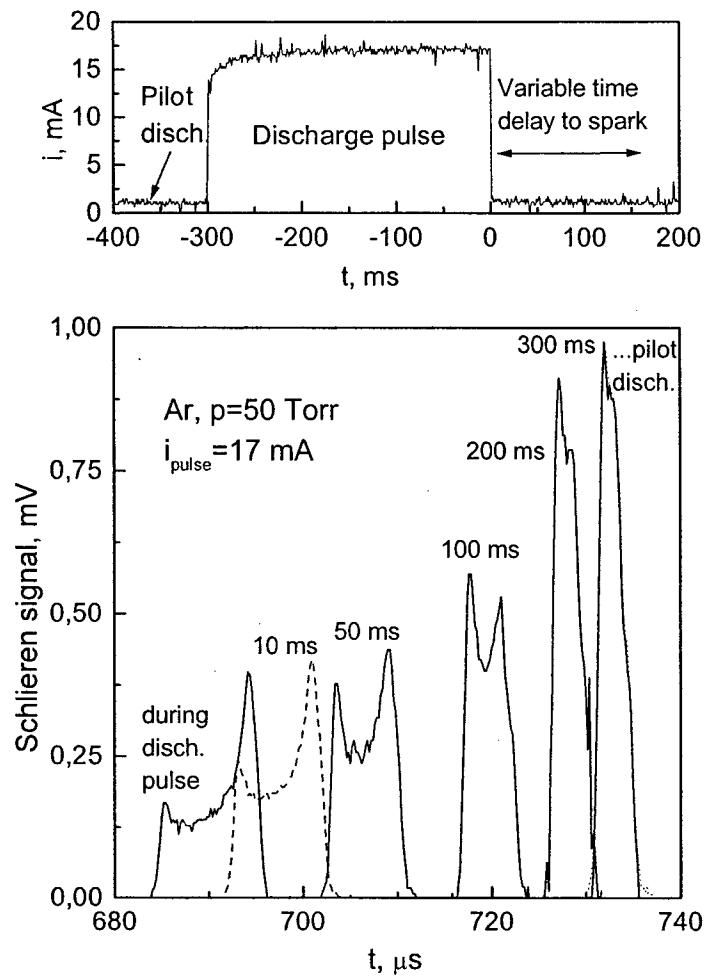


Fig.20. Evolution of the schlieren signal at a fixed location inside the discharge with time delay between the end of the discharge pulse and the shock launch.

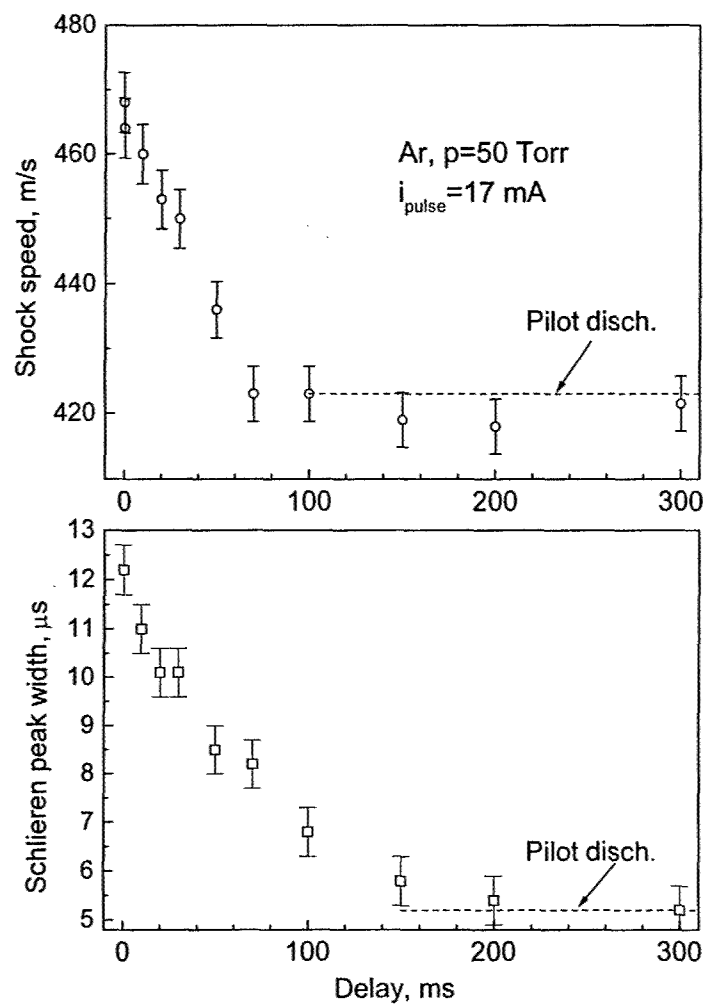


Fig.21. Evolution of shock velocity and the width of the schlieren signal at a fixed location inside the discharge with time delay between the end of the discharge pulse and the shock launch.

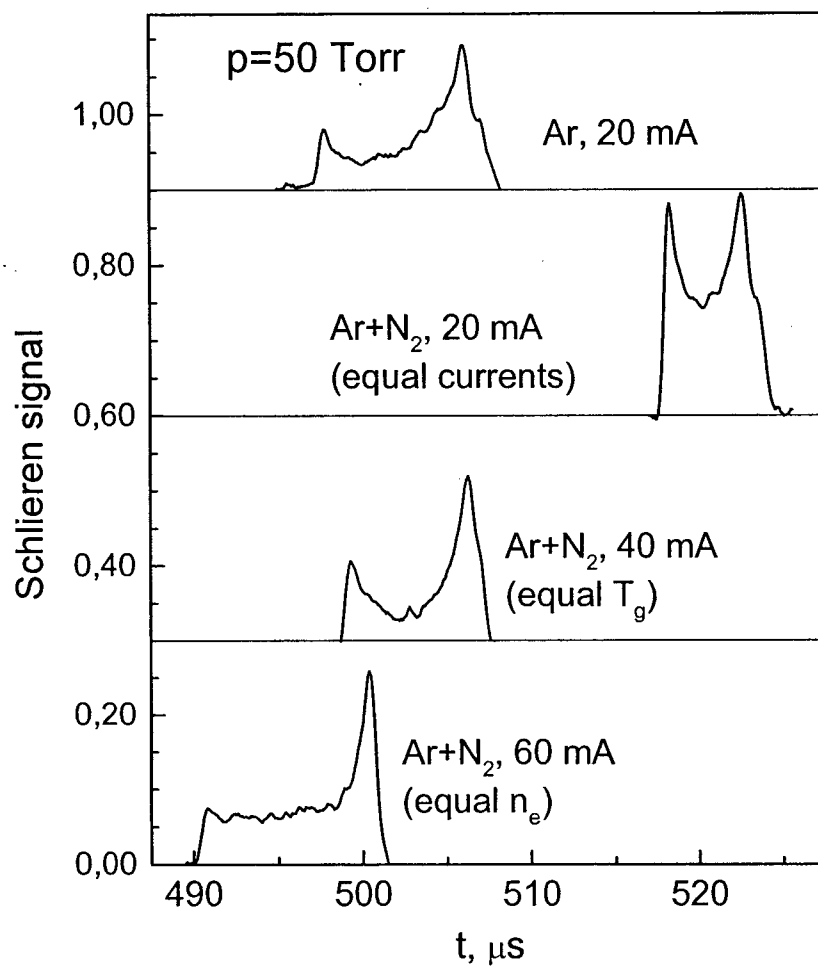


Fig.22. Comparison of shock schlieren signals at a fixed location in Ar and Ar+1%N₂ discharges at 50 Torr and various values of electric current.

CHAPTER 2

THEORETICAL ANALYSIS OF MHD AND EHD EFFECTS IN WEAKLY IONIZED GAS FLOWS

Summary

This chapter focuses on theoretical analysis of fundamental aspects of high-speed flow control using electric and magnetic fields. The principal challenge is that the relatively cold gas is weakly ionized in electric discharges or by electron beams, with ionization fraction ranging from 10^{-8} to 10^{-5} . The low ionization fraction means that, although electrons and ions can interact with electromagnetic fields, transfer of momentum and energy to or from the bulk neutral gas can be quite inefficient. Analytical estimates show that even at the highest values of the electric field that can exist in cathode sheaths of electric discharges, electrohydrodynamic (EHD), or ion wind, effects in a single discharge can be of significance only in low-speed core flows or in laminar sublayers of high-speed flows. Use of multi-element discharges would amplify the single-sheath effect, so that the cumulative action on the flow can conceivably be made significant. However, Joule heating can overshadow the cathode sheath ion wind effects. Theoretical analysis of MHD flow control with electron beam ionization of hypersonic flow shows that the MHD interaction parameter is a steeply increasing function of magnetic field strength and the flow velocity. However, constraints imposed by arcing between electrode segments can reduce the performance and make the maximum interaction parameter virtually independent of Mach number. Estimates also show that the MHD interaction parameter is much higher near the wall (in the boundary layer) than in the core flow, which may have implication for MHD boundary layer and transition control. The paper also considers "electrodeless" MHD turning and compression of high-speed flows. Computations of a sample case demonstrate that the turning and compression of hypersonic flow ionized by electron beams can be achieved; however, the effect is relatively modest due to low ionization level.

Nomenclature

- B - magnetic field
- B_z, B_r - z-component and r-component of the magnetic field
- $B_a(z)$ - local amplitude of B-field on the z-axis
- $B_{a,max}$ - maximum value of the magnetic field
- e - electron charge
- e_{tot} - total energy (internal energy, excluding the energy of vibrational mode, plus kinetic energy) of the gas per unit volume
- c_f - friction drag coefficient
- E_{eff} - effective electric field
- $\vec{E}^* = \vec{E} + \vec{u} \times \vec{B}$ - electric field in the reference frame moving with the gas
- E_ϕ^* - azimuthal electric field component in the reference frame moving with the gas
- E_{cath} - electric field strength at the cathode
- E_a - electric field strength at the anode
- E_c - Hall field corresponding to the arcing threshold
- E_v, E_v^0 - nonequilibrium and equilibrium values of vibrational energy per unit volume
- F_z, F_r - z-component and r-component of the $\vec{j} \times \vec{B}$ force
- f, g - functions defined in Eq. (21)
- h - flight altitude
- \hbar - Planck's constant
- H - column vector in Euler equations
- \dot{H}_{inlet} - total enthalpy entering the inlet per unit time

\bar{j} - electric current density
 j_φ - azimuthal current density component
 j_b - current density of the beam at the injection point
 k - load factor
 k_d - rate coefficient of collisional detachment of electrons from negative ions
 k_{e+} , k_{e-} , k_{en} , k_{+-} , k_{n+} , and k_{n-} - rate coefficients of collisional momentum transfer between different kinds of particles
 L - length of MHD region
 L_R - electron beam relaxation length
 M - Mach number
 M_n - mass of an atom/molecule
 M_+ - positive ion mass
 M_- - negative ion mass
 m - mass of electron
 \dot{m} - mass flow rate
 N - number of consecutive elements (multiple discharges)
 n_+ , n_- , n_e - number densities of positive ions, negative ions, and electrons
 n - number density of gas molecules
 N_O - number density of oxygen atoms
 p - static gas pressure
 p_e - electron gas pressure
 p_+ - positive ion partial pressure
 p_- - negative ion partial pressure
 p_n - partial pressure of neutral particles
 p_E - electric pressure
 $\langle p_{tot} \rangle$ - total pressure averaged over the inlet cross-section
 $p_{tot,0}$ - free-stream total pressure
 q - dynamic pressure
 q_i - ionization rate due to electron beam
 Q_b - total power deposited by the e-beam
 q_b - power density deposited by the e-beam
 Q_J - Joule dissipation rate
 Q_v - power deposited per unit volume into vibrational excitation
 Q_{VT} - heating rate per unit volume due to VT relaxation
 r - coordinate
 r_{inlet} - inlet radius
 R - column vector in Euler equations
 Re_M - magnetic Reynolds number
 Re_x^* - Reynolds number calculated at the reference temperature T^*
 r_{max} - maximal radius of the numerical domain
 S - MHD interaction parameter (Stuart number)
 S_τ - MHD interaction parameter with respect to shear stress at the wall
 T - translational-rotational gas temperature

T_v - vibrational temperature
 T^* - reference temperature
 U - column vector in Euler equations
 \bar{u} - gas velocity
 u_∞ - freestream velocity
 u_z, u_r - z-component and r-component of the gas velocity
 \tilde{u}_r, \tilde{u}_z - effective electron-ion velocity components across magnetic field taking into account ion slip
 u' - characteristic velocity in the near-wall region (friction velocity)
 $\bar{V}_e, \bar{V}_+, \bar{V}_-, \bar{V}_n$ - convective velocities of electrons, positive ions, negative ions, and neutral atoms/molecules
 V_{dr}^+, V_{dr}^- - ion and electron drift velocities
 W_i - energy cost of ionization, i.e. the loss of electron beam energy per each newly generated electron in the plasma
 x - coordinate
 Z - column vector in Euler equations
 z - coordinate
 z_{inlet} - inlet axial location
 z_{max} - maximum length of the numerical domain
 Z_{EHD} - EHD interaction parameter
 Z_{tot} - total interaction parameter
 Z_e - ratio of Joule and viscous dissipation rates
 Z_r - EHD interaction parameter for the boundary layer
 α - Townsend ionization coefficient
 β - electron-ion recombination rate coefficient
 β_{ii} - ion-ion recombination rate coefficient
 γ - specific heat ratio
 $\bar{\Gamma}_e, \bar{\Gamma}_+, \bar{\Gamma}_-$ - fluxes of electrons, positive ions, and negative ions
 ϵ_0 - permittivity of free space
 ϵ_{int} - internal energy (excluding the energy of vibrational mode) per unit mass
 ϵ - work done on an electron by the induced Faraday electric field during the electron's lifetime with respect to dissociative recombination with ions
 ϵ_b - initial energy of beam electrons
 ζ - ratio of the ionization cost to the work done on an electron by the induced Faraday electric field during the electron's lifetime
 η_v - fraction of the Joule dissipation rate spent on vibrational excitation of molecules
 θ - turning angle of the flow
 μ_0 - permeability of free space
 μ - dynamic viscosity
 ν_a - electron attachment frequency (i.e. the number of attachments per unit time)
 ρ - gas density
 ρ_∞ - freestream density
 σ - scalar electrical conductivity
 τ_{VT} - nitrogen vibrational relaxation time
 τ - shear stress at the wall
 ϕ - electric potential

Ω_e - electron Hall parameter

Ω_+ - ion Hall parameter

I. Introduction

There is a growing interest in using weakly ionized gases (plasmas) and electric and magnetic fields in high-speed aerodynamics. Wave and viscous drag reduction, thrust vectoring, reduction of heat fluxes, sonic boom mitigation, boundary layer and turbulent transition control, flow turning and compression, on-board power generation, and scramjet inlet control are among plasma and MHD technologies that can potentially enhance performance and significantly change the design of supersonic and hypersonic vehicles.¹⁻³⁰ Meanwhile, despite many studies devoted to these new technologies, a number of fundamental issues have not been adequately addressed. Any plasma created in gas flow and interacting with electric and magnetic fields would result in gas heating. This heating can certainly have an effect on the flow and, in some cases, can be used advantageously. However, a more challenging issue is whether significant non-thermal effects of plasma interaction with electric and magnetic fields can be used for high-speed flow control.

In conventional magnetohydrodynamics of highly conducting fluid, electric and magnetic effects give rise to ponderomotive force terms $\nabla \frac{\epsilon_0 E^2}{2}$ and $\nabla \frac{B^2}{2\mu_0}$ that can be interpreted as gradients of electric and magnetic field pressures. These ponderomotive forces are successfully utilized for plasma containment in fusion devices and also play an important role in astrophysics. One might hope that these forces can also be used for control of high-speed flow of ionized air. However, the great importance of ponderomotive forces in fusion and astrophysical plasmas is due to the fact that those plasmas are fully, or almost fully, ionized, and, therefore, are highly conductive. In contrast, high-speed air encountered in aerodynamics is not naturally ionized, even in boundary layers and behind shocks if the flight Mach number is below about 12, due to the low static temperature. Therefore, ionization has to be created artificially, using various electric discharges or high-energy particle beams.^{16,18,22-24,26-28,31-34} In most conditions, the artificially created plasmas are weakly ionized, with ionization fraction ranging from 10^{-8} to 10^{-5} . Because of the low ionization fraction and electrical conductivity, interaction of the plasma with electromagnetic fields and transfer of momentum and energy to or from the bulk neutral gas can be quite inefficient.

In the present paper, we derive analytical formulas for the so-called interaction parameters that characterize EHD and MHD effects on gas flows. Numerical estimates based on these formulas are then performed to determine the trends and ranges of conditions where EHD and MHD effects can be significant.

II. Theoretical analysis of MHD and EHD effects in weakly ionized gas flows

2.1. Basic equations

To analyze effects of electric and magnetic forces on weakly ionized gas flows, we denote number densities of electrons, positive and negative ions, and neutrals as n_e , n_+ , n_- , and n , velocities – as \vec{V}_e , \vec{V}_+ , \vec{V}_- , and \vec{V}_n , and pressures – as p_e , p_+ , p_- , and p_n . Rate coefficients of collisional momentum transfer between different kinds of particles will be denoted as k_{e+} , k_{e-} , k_{en} , k_{+-} , k_{n+} , and k_{n-} . Electric and magnetic fields are denoted as usual: \vec{E} and \vec{B} . For simplicity, we will assume that masses of both positive and negative ions are equal to the mass of a neutral molecule, and any of those greatly exceeds the electron mass m : $M_+ = M_- = M_n \gg m$. Equations of motion for four-fluid mixture are then:

$$n_e \frac{d(m\vec{v}_e)}{dt} = -en_e(\vec{E} + \vec{v}_e \times \vec{B}) - \nabla p_e - k_{e+}n_en_+m(\vec{v}_e - \vec{v}_+) - k_{e-}n_en_-m(\vec{v}_e - \vec{v}_-) - k_{en}n_enm(\vec{v}_e - \vec{v}_n) \quad (1)$$

$$n_+ \frac{d(M_n\vec{v}_+)}{dt} = en_+(\vec{E} + \vec{v}_+ \times \vec{B}) - \nabla p_+ - k_{e+}n_en_+m(\vec{v}_+ - \vec{v}_e) - k_{+-}n_+n_-M_n(\vec{v}_+ - \vec{v}_-) - k_{n+}n_+nM_n(\vec{v}_+ - \vec{v}_n) \quad (2)$$

$$n_- \frac{d(M_n\vec{v}_-)}{dt} = -en_-(\vec{E} + \vec{v}_- \times \vec{B}) - \nabla p_- - k_{e-}n_en_-m(\vec{v}_- - \vec{v}_e) - k_{+-}n_+n_-M_n(\vec{v}_- - \vec{v}_+) - k_{n-}n_-nM_n(\vec{v}_- - \vec{v}_n) \quad (3)$$

$$n \frac{d(M_n\vec{v}_n)}{dt} = -\nabla p_n - k_{en}n_enm(\vec{v}_n - \vec{v}_e) - k_{n+}n_+nM_n(\vec{v}_n - \vec{v}_+) - k_{n-}n_-nM_n(\vec{v}_n - \vec{v}_-) + \mu\Delta\vec{v}_n \quad (4)$$

where μ is the dynamic viscosity. Adding these equations, we obtain a single-fluid equation containing the total density ρ , mass velocity \vec{u} , pressure $p = p_n + p_+ + p_- + p_e$, and electric current density $\vec{j} = e(n_+\vec{v}_+ - n_-\vec{v}_- - n_e\vec{v}_e)$:

$$\rho \frac{d\vec{u}}{dt} = -\nabla p + e(n_+ - n_- - n_e)\vec{E} + \vec{j} \times \vec{B} + \mu\Delta\vec{u} \quad (5)$$

Note that the viscous terms in Eqs. (4) and (5) are written for the simplest case of incompressible flow with constant viscosity, because the main focus is on interaction of charged species with electric and magnetic fields and with neutral molecules (the second and third terms in the right-hand side of Eq. (5)). However, the resulting Eq. (5) can be easily written for the general case of compressible flow with variable viscosity: the well-known viscous terms of Navier-Stokes equations should be simply substituted for the last term in the right-hand side of Eq. (5).

2.2. Electrohydrodynamic (EHD), or "ion wind", flow control

Consider EHD effects first. These effects, alternatively referred to as "ion wind",³⁵ are represented by the second term in the right-hand side of Eq. (5). The strength of EHD effect is proportional to the net space charge density. Bulk plasmas are known to be quasineutral, that is, in them, $n_+ \approx n_- + n_e$ with very good accuracy. Substantial EHD effects can be expected only in the presence of a significant space charge, which is the case in cathode sheaths or in space-charge regions of corona discharges. Having those space charge regions or sheaths in mind, in what follows we will neglect n_- and n_e in comparison with n_+ . The change in momentum of a gas element moving along x axis through a space charge region is $d(\rho u) = en_+E \cdot dt = en_+E \cdot dx/u$. Therefore, the relative strength of EHD effects can be characterized by a dimensionless EHD interaction parameter equal to the ratio of EHD push work to the fluid momentum flux:

$$Z_{EHD} = \frac{en_+\Delta\phi}{\rho u^2} \quad (6a)$$

where $\Delta\phi = \int E dx$ is the voltage fall across the space charge region.

An alternative way of expressing EHD effects is to use the Poisson equation, which in a one-dimensional case can be written as $dE/dx = e(n_+ - n_- - n_e)/\epsilon_0$. With the Poisson equation, the second term in the right-hand side of Eq. (5) can be transformed into

$$e(n_+ - n_- - n_e)E = \epsilon_0 E \frac{dE}{dx} = \frac{d}{dx} \left(\frac{\epsilon_0 E^2}{2} \right),$$

which can be interpreted as a gradient of the "electric pressure" $p_E = \frac{\epsilon_0 E^2}{2}$. Therefore, in a one-dimensional flow between the anode and cathode of a glow discharge, the drop of electric pressure between the anode and cathode is

$$\Delta p_E = \frac{\epsilon_0}{2} (E_{cath}^2 - E_a^2),$$

where E_{cath} and E_a are the electric field strengths at the cathode and anode, respectively. In most cases, E_a is negligible compared with E_{cath} .³⁶ Thus, the EHD interaction parameter can be expressed as

$$Z_{EHD} = \frac{en_* \Delta \phi}{\rho u^2} = \frac{\Delta p_E}{\rho u^2} = \frac{\epsilon_0 E_{cath}^2}{2 \rho u^2} \quad (6b)$$

Two principal examples of electric discharge systems that have substantial voltage drops across space charge regions and may be used for EHD flow control are positive corona and the cathode sheath of a glow discharge.

In a positive corona in atmospheric air, n_* can realistically reach about 10^8 cm^{-3} , and $\Delta \phi$ can be from several kilovolts to several tens of kilovolts.³⁶ With $\Delta \phi = 40 \text{ kV}$, the interaction parameter Z_{EHD} will be at least 0.1 only for flows with very low dynamic pressure, 3 Pa or less. For standard sea-level air, this means that the flow velocity should be 2 m/s or lower.

In cathode sheaths of glow discharges, ion density can reach about 10^{11} cm^{-3} .³⁶ Cathode voltage fall in normal (low-current) glow discharges is about 200-300 V, and it can reach about 1 kV in abnormal (high-current) glow discharges.³⁶ Then, to make $Z_{EHD} \geq 0.1$, the dynamic pressure should be less than 80 Pa, corresponding to the maximum flow velocity below 11.3 m/s in standard sea-level air, or below 35.8 m/s in air with 1/10 normal density. Note that effects of surface glow-like discharges with dielectric barrier on low-speed flows have been experimentally demonstrated.^{37,38}

In principle, a stable discharge with electron density on the order of 10^{12} - 10^{13} cm^{-3} can be maintained between the cathode and the anode in longitudinal air flow preheated to 2,000-3,000 K at a pressure of 1 atm.³⁹ In such systems, assuming that the temperature is 2400 K, the charge number density is 10^{12} - 10^{13} cm^{-3} , and the cathode voltage fall is 1 kV, the EHD interaction parameter, according to Eq. (6a), can reach 1 at dynamic pressure of 800-8,000 Pa, corresponding to flow velocities of 23-72 m/s.

An estimate of the maximum EHD effect can also be obtained with Eq. (6b). If thermal emission of electrons from the cathode is insignificant, so that electrons are emitted due to the ion and photon bombardment of the cathode and then multiply in the cathode sheath in Townsend avalanche processes, then the cathode electric field E_c can be very strong: $E_{cath}/n \approx 10^{-14} \text{ V} \cdot \text{cm}^2$.³⁶ Therefore, for the highest value of Z_{EHD} in Eq. (6b), not only the cathode sheath has to be dominated by Townsend processes, but the gas density should be as high as possible. If a Townsend cathode sheath could exist at normal atmospheric density, then the EHD interaction parameter would reach 1 at dynamic pressure of about 1600 Pa, corresponding to a flow velocity of about 50 m/s. At a density of 1/10 of standard sea-level atmospheric density, diffuse glow discharges in air with Townsend cathode sheaths certainly can exist; in that case, $Z \approx 1$ at dynamic pressure of about 160 Pa, corresponding to a flow velocity of about 16 m/s.

Note that, when assessing EHD effects on specific gas flows, the fraction of a gas actually passing through the interaction region (i.e., through the cathode sheath) is as important as the interaction parameter for that fraction of the gas. Since at high pressures, where the interaction parameter can be relatively high, the cathode sheath thickness is micron-scale small, the EHD interaction can affect only a very small portion of the macroscopic flow.

Estimates in the previous paragraphs referred to free stream conditions. However, from Eqs. (6a) and (6b) it is clear that maximum EHD effects will occur where the flow velocity is the slowest, that is, in the boundary layer. For the boundary layer, the interaction parameter can be defined as the ratio of electrostatic and shear (friction) forces:

$$Z_\tau = \frac{en_* \Delta \phi}{\tau} \quad (7)$$

where τ is the shear stress at the wall. This equation is essentially equivalent to Eq. (6a) where u is a characteristic velocity in the near-wall region, also called the friction velocity:⁴⁰ $u = u'$, where $\rho u'^2 = \tau$, or

$$u' = \sqrt{\tau/\rho} \quad (8)$$

The wall shear stress can be related to freestream conditions ρ, u with well-known correlations:⁴¹

$$\tau = \frac{1}{2} \rho u^2 c_f \quad (9)$$

$$c_f = \frac{0.664}{\sqrt{\text{Re}_x^*}} \quad \text{for laminar flow} \quad (10)$$

$$= \frac{0.0592}{(\text{Re}_x^*)^{0.2}} \quad \text{for turbulent flow}$$

where Re_x^* is the Reynolds number calculated at the reference temperature T^* . Therefore,

$$Z_\tau = \frac{en_s \Delta \varphi}{\rho u^2} \times \frac{2}{c_f} \quad (11)$$

and, since $c_f \ll 1$ for high Reynolds number flows, Z_τ greatly exceed Z . For example, in the range $\text{Re}_x^* = 10^5 - 10^7$, the factor $2/c_f \approx 10^3$, so that ion wind effects in the cathode sheath of a glow discharge may affect the boundary layer and skin friction in standard sea-level air flow whose velocity far from the surface is up to 114 m/s. In air with 0.1 normal density, the velocity limit increases to 360 m/s.

The estimates in the preceding paragraphs, using formulas (6a,b) and (7), assumed that a single cathode-anode pair is used for flow control. However, multiple discharges can be conceivably used, so that the cumulative effect of many cathode sheaths would affect the flow. A rough estimate of the number of consecutive elements, N , required to make the total interaction parameter $Z_{\text{tot}} \approx 0.1 - 1$, is simply $N = Z_{\text{tot}}/Z_{\text{EHD}}$ or $N = Z_{\text{tot}}/Z_\tau$, where Z_{EHD} and Z_τ are determined by Eqs. (6a,b) and (7).

Note that the thickness of cathode sheath of a glow discharge is on the order of a few dozen mean free paths. Therefore, only a very thin portion of the laminar sublayer at the cathode would be directly affected. If the cathode is positioned downstream of the anode, the gas in this very thin layer at the cathode would experience ion wind forces directed both towards the surface and in the direction of the flow. What effect these forces would have on flow behavior, such as turbulent transition and heat transfer, remains to be studied.

In assessing ion wind effects, it is important to include the inevitable Joule heating. The ratio of Joule and viscous dissipation rates is:

$$Z_e = \frac{en_s V_{dr}^+ \Delta \varphi}{\tau u'} = Z_\tau \frac{V_{dr}^+}{u'} \quad (12)$$

where V_{dr}^+ is the ion drift velocity. In the cathode sheath, where electric field is extremely strong, ion drift velocity is very high, about $(5-10) \times 10^3$ m/s. Since u' is only several meters a second, Eq. (12) shows that the heating effect in the cathode sheath exceeds the ion wind effect by 3 orders of magnitude. Thermal expansion would push the gas from the wall, thus opposing the cathode-directed ion wind force. The heating would also increase viscosity. Additionally, heating occurs not only in the sheath, but also in the quasineutral plasma region of the discharge, while ion wind is confined to the space charge region. Thus, even if the ion wind force can affect the viscous boundary layer, its action may be accompanied by the strong heating generated by the same electric discharge. With regard to the experiments^{37, 38} where EHD (ion wind) effects of surface glow-like discharges with dielectric barrier on low-speed flows have been demonstrated, it would be interesting to further investigate roles (if any) of viscous and thermal effects versus the EHD action on the inviscid low-speed core flow.

2.3. Basic analysis of MHD flow control

To estimate MHD effects in relatively cold hypersonic flow and boundary layer, Eq. (5) should be analyzed jointly with other appropriate gas dynamic and plasma kinetic equations. The current density can be related to the values of electric and magnetic field through the generalized Ohm's law that is a consequence of Eqs. (1)-(4):⁴¹

$$\vec{j} = \sigma \vec{E}^* + \frac{\Omega_e}{B} \vec{j} \times \vec{B} + \frac{\Omega_e \Omega_i}{B^2} (\vec{j} \times \vec{B}) \times \vec{B} \quad (13)$$

where $\vec{E}^* = \vec{E} + \vec{u} \times \vec{B}$ is the electric field in the reference frame moving with the gas, and Ω_e and Ω_i are the electron and ion Hall parameters:

$$\Omega_e = \frac{eB}{mk_{en}n}; \quad \Omega_i = \frac{eB}{M_n k_{n+} n} \quad (14)$$

The second term in the right-hand side of Eq. (13) represents the Hall effect, and the third term, nonlinear with respect to B , represents the ion slip. In the analysis, we will disregard negative ions and also assume quasineutrality, $n_e = n_+ \approx n_-$.

The MHD interaction parameter, also referred to as the Stuart number, S , is the ratio of ponderomotive (Ampere) and inertia forces. With ion slip correction,

$$S = \frac{\sigma B^2 L}{(1 + \Omega_e \Omega_i) \rho u} \quad (15)$$

where L is the length of MHD region. When ion slip is small, $\Omega_e \Omega_i \ll 1$, the Stuart number increases with magnetic field as B^2 . However, at very strong magnetic fields and in low-density gases, when $\Omega_e \Omega_i \gg 1$, the interaction parameter reaches its asymptotic value independent of B :

$$S \rightarrow (L/u) k_{n+} n_+ \quad (16)$$

The physical meaning of Eq. (16) is that the maximum ion momentum change occurs when they are essentially stopped by the strong transverse magnetic field, and then momentum transfer from the ions to the gas is limited by the number of collisions of a neutral molecule with ions. Indeed, the right-hand side of Eq. (16) is simply the ratio of the flow residence time in the MHD region to the mean time for a molecule to collide with an ion.

As discussed in our earlier work,^{16-18,22-24,26-28} at flight Mach numbers up to about Mach 12, thermal ionization even behind shocks cannot provide an adequate electrical conductivity for MHD flow control and power generation devices. (Above Mach 12, one might achieve adequate ionization near stagnation zones and in the boundary layers, but adequate ionization will not exist in the inviscid flow of slender bodies for Mach numbers much higher than 12.) The ionization must be created and sustained artificially, and the need to spend power on ionization severely limits performance of hypersonic MHD devices.^{16-18,22-24,26-28} Indeed, the work done on an electron by the induced Faraday electric field during the electron's lifetime with respect to dissociative recombination with ions is:

$$\varepsilon = eE V_{dr}^e \frac{1}{\beta n_+} = \frac{(eE)^2}{mk_{en}\beta n n_e} = \frac{(ekuB)^2}{mk_{en}\beta n n_e} \quad (17)$$

where k is the load factor, $E = kuB$ is the induced electric field, $V_{dr}^e = \frac{eE}{mk_{en}n}$ is the electron drift velocity, and β

is the dissociative recombination rate constant. Although in the general problem of MHD flow control one might also be interested in the case where the device is not self-powered, self-powered MHD devices are obviously attractive, since they would not require any on-board power input. In this paper, we limit our analysis to self-powered MHD devices. For efficient self-powered operation of the MHD device, ε must be substantially larger than the energy cost, W_i , of a newly produced electron. Specifically, the ratio

$$\zeta \equiv \frac{W_i}{\varepsilon} = \frac{mk_{en}\beta n n_e W_i}{(ekuB)^2} \quad (18)$$

must be limited to a number less than 1. This obviously limits the electron density n_e and the conductivity

$$\sigma = \frac{e^2 n_e}{mk_{en}n} = \frac{\zeta (e^2 kuB)^2}{(mk_{en}n)^2 \beta W_i} \quad (19)$$

The maximum interaction parameter per unit length is then

$$S/L = \frac{\zeta}{\beta W_i} \times \left(\frac{e^2 k M_n}{k_{en} m} \right)^2 \times \frac{B^4}{1 + \frac{M_n e^2 B^2}{m k_{en} k_{n+} \rho^2}} \times \frac{u}{\rho^3} \quad (20)$$

Hypersonic MHD devices would operate downstream of one or more oblique shocks, and it is convenient to express the interaction parameter in terms of flight velocity, Mach number, and dynamic pressure. Assuming that the MHD device is located downstream of a single oblique shock with flow turning angle θ , we express the density and velocity in terms of the freestream parameters M , u_∞ , ρ_∞ with approximate formulas that can be easily derived for oblique shocks with small turning angles:

$$\rho = \rho_\infty / f; \quad \frac{u}{\rho^3} = \frac{u_\infty}{\rho_\infty^3} \times \frac{f^4}{g};$$

$$f(M, \theta) = \frac{\gamma-1}{\gamma+1} + \frac{32}{(\gamma+1) \left[(\gamma+1) M \tan \theta + \sqrt{(\gamma+1)^2 M^2 \tan^2 \theta + 16} \right]^2}; \quad (21)$$

$$g(M, \theta) = 1 - \frac{4M \tan \theta}{(\gamma+1) M \tan \theta + \sqrt{(\gamma+1)^2 M^2 \tan^2 \theta + 16}}$$

With Eq. (21), and expressing the freestream density in terms of dynamic pressure q and velocity, $\rho_\infty = 2q/u_\infty^2$, we obtain the final expression for the maximum Stuart number per unit length:

$$\frac{S}{L} = \left(\frac{e^2 k M_n}{k_{en} m} \right)^2 \times \frac{\zeta f^4 B^4 u_\infty^7}{8 g \beta W_i q^3} \times \left(1 + \frac{f^2 e^2 M_n B^2 u_\infty^4}{4 k_{en} k_{n+} q^2} \right)^{-1} \quad (22)$$

MHD performance as expressed by Eq. (22) is inversely proportional to the energy cost of producing an electron, W_i . Thus, minimization of W_i is critical. As shown in our earlier work,^{16,18,26,28,32-34} DC, RF, and microwave methods of plasma generation have unacceptably high ionization cost, $W_i \approx 10^4$ eV. Electron beams represent the most efficient nonequilibrium method of ionization,^{16,28,31,33} with $W_i = 34$ eV, and the concept of cold-air hypersonic MHD devices with ionization by electron beams was suggested and developed in our earlier work.¹⁶⁻²⁸ In what follows, we will assume that ionization is done by electron beams, with $W_i = 34$ eV, and that ζ is limited to 0.3.

The maximum MHD interaction parameter (22) increases very rapidly (especially if the ion slip, represented by the last factor in Eq. (22) is not significant) with increasing magnetic field and flight speed, and with decreasing dynamic pressure. The very sharp u_∞^7 dependence is due to both increase in the Faraday e.m.f. with flow velocity and to the decrease in gas density at constant q . Figure 1 shows S/L calculated with Eq. (22) versus flight Mach number at 4 different magnetic field strengths and 2 values of flight dynamic pressure. The load factor value was constant at $k=0.5$.

At low gas density and strong B field that favor MHD performance, Hall effect becomes very significant. If Hall current is allowed to flow, the effective conductivity is reduced by the factor $(1 + \Omega_e^2)$, and the MHD performance decreases. In Faraday MHD devices, Hall current is eliminated by segmenting electrodes.⁴³ However, as the longitudinal Hall electric field increases, arcing between the electrode segments can occur.⁴² The arcing would essentially result in a continuous-electrode Faraday device, with dramatic reduction in performance.

Denoting the value of Hall field corresponding to the arcing threshold as E_c , an additional constraint in assessing the maximum performance is:

$$E_c = (1 - k) \Omega_e u B = \frac{(1 - k) e^2 M_n u B^2}{k_{en} m \rho} \quad (23)$$

This condition limits the allowed B field at high flow velocity and low gas density. With this constraint, the upper limit for the interaction parameter per unit length becomes

$$\frac{S_{\text{lim}}}{L} = \frac{\zeta g e^2 E_c^2 u_\infty}{2\beta W_i q} \times \left(1 + \frac{g e E_c u_\infty}{2(1-k)k_{n,q}} \right)^{-1} \quad (24)$$

This formula does not explicitly depend on B field and has a weak dependence on flight conditions, because at each flight regime, B field is adjusted to satisfy Eq. (23).

Fig. 1 shows the Hall field-limited interaction parameter of Eq. (24) at two values of E_c . While the performance is quite good at $E_c = 50$ kV/m, it is unacceptably low with $E_c = 5$ kV/m. Therefore, determining the threshold field for intersegment arcing is critical for assessing performance of hypersonic MHD devices.

The intersegment arcing in conventional high-temperature MHD generators with thermal ionization was extensively studied both theoretically⁴³⁻⁴⁶ and experimentally.^{47,48} Computational study by Oliver⁴⁵ established 40 V as the intersegment potential drop corresponding to the onset of arcing, and experiments⁴⁸ gave the range of 40-100 V. With centimeter-scale electrode width and intersegment gap, this would correspond to the longitudinal field of 50 V/cm or so. However, experimental^{47,48} and theoretical^{44,46} studies of this thermally induced arcing found that the arcing threshold increases with increasing magnetic field and decreasing electrode surface temperature. Qualitatively, this can be explained by the reduction in electrical conductivity in the boundary layer as the wall gets colder, and by the effective boundary layer conductivity reduction as $(1 + \Omega_e^2)^{-1}$. Thus, even in conventional MHD devices with thermal ionization E_c can be substantially higher than 50 V/cm.

More importantly, the operating conditions and the ionization mechanism in cold-air hypersonic MHD devices differ dramatically from those in conventional thermal systems. In on-ramp MHD shock control and power generation devices,^{17,27} ionization ($n_e \approx 10^{12} \text{ cm}^{-3}$, $\sigma \approx 0.5 \text{ mho/m}$) is sustained by electron beams. The rate of ionization by plasma electrons is very low,¹⁶⁻¹⁸ because the ratio of effective electric field strength to the gas number density, $E_{\text{eff}}/n \approx 10^{-16} \text{ V} \cdot \text{cm}^2$ both in the core flow and in the boundary layer, results in low electron temperature. Since gas temperature in both core flow and, with proper active wall cooling, near electrodes is below 1000 K, thermal ionization is also negligible. Therefore, electron beam-sustained plasmas in hypersonic MHD devices should have higher thresholds of ionization and thermal instabilities than conventional thermally ionized plasma would. We emphasize that the intersegment arcing in cold-air MHD devices with electron beam-controlled ionization was never studied, and it should be studied in the future because of the critical importance of E_c for the performance of those devices.

The analysis in the preceding paragraphs of this subsection was so far focused on MHD interaction parameters in the core flow. Similarly to the EHD analysis in subsection 2.2, one can define an MHD interaction parameter with respect to shear stress at the wall:

$$S_\tau = \frac{\sigma B^2 L}{\rho u'} \quad (25)$$

where u' is the friction velocity defined by Eq. (8). If, for rough estimates, we assume that the conductivity σ and the density ρ near the wall are equal to those in the core flow (this can be ensured by a proper wall cooling and by contouring the profiles of ionizing electron beams), then from Eqs. (25), (8)-(10) we obtain:

$$S_\tau = \sqrt{\frac{2}{c_f}} \times \frac{\sigma B^2 L}{\rho u} = \sqrt{\frac{2}{c_f}} \times S \quad (26)$$

Therefore, in the range $\text{Re}_x^* = 10^5 - 10^7$, the MHD interaction parameter with respect to wall shear stress greatly exceeds S : $S_\tau \approx 30S$. This may have interesting implications for wall friction and transition control.

Of course, MHD effects on the boundary layer would be quite complex. First, if the load factor k is not close to 1 or 0, then the Joule heating is characterized by the same interaction parameters (15) and (25), and the heating effects should be comparable to those of ponderomotive $\vec{j} \times \vec{B}$ forces both in the core flow and near the wall. Second, if the MHD region extends into the core flow, the changes in the core flow would also affect the boundary layer. Thus, evaluation of MHD effects on the boundary layer requires a fully coupled analysis.

III. Electrodeless MHD flow control: a magneto-thermal funnel

Since electrode-related problems like intersegment arcing can potentially reduce performance of MHD flow control devices, it is interesting to consider whether MHD flow turning or compression can be accomplished without electrodes.

Using one of the Maxwell's equations

$$\nabla \times \vec{B} = \mu_0 \vec{j} \quad (27)$$

and the vector identity

$$\frac{1}{2} \nabla B^2 = (\vec{B} \cdot \nabla) \vec{B} + \vec{B} \times (\nabla \times \vec{B}), \quad (28)$$

we obtain from Eq. (5):

$$\begin{aligned} \rho \frac{d\vec{u}}{dt} &= -\nabla p + e(n_+ - n_- - n_e) \vec{E} + \frac{1}{\mu_0} (\vec{B} \cdot \nabla) \vec{B} - \nabla \frac{B^2}{2\mu_0} + \mu \Delta \vec{u} \\ &= -\nabla \left(p + \frac{B^2}{2\mu_0} \right) + \frac{1}{\mu_0} (\vec{B} \cdot \nabla) \vec{B} + e(n_+ - n_- - n_e) \vec{E} + \mu \Delta \vec{u} \end{aligned} \quad (29)$$

Thus, magnetic field energy density, $\frac{B^2}{2\mu_0}$, acts as an additional pressure. The term $\frac{1}{\mu_0} (\vec{B} \cdot \nabla) \vec{B}$ can be interpreted as tension of magnetic field lines due to their curvature. These ponderomotive forces are successfully used for containment of fully ionized plasmas in fusion devices.

With $B=1$ Tesla, the magnetic pressure is about 8 atm, and significant MHD flow turning and compression effects might be expected in hypersonic flow. However, practical applications of the magnetic ponderomotive flow control would be hampered by low ionization level. Indeed, with the conductivity of only 0.1-1 mho/m typical for MHD devices with ionization by electron beams, the magnetic Reynolds number $Re_M = \mu_0 \sigma u L \ll 1$, and the magnetic field is not "frozen" into the plasma. Therefore, ponderomotive forces depend on the conductivity, and their relative strength is characterized by the Stuart number S that, as shown in the previous section, is also less than 1 for an MHD region of a few meters in length. Note the important difference between electric and magnetic pressures in weakly ionized plasmas. While the electric pressure can fully act on even weakly ionized gases (see section 2.2), the magnetic pressure cannot be fully exerted on weakly ionized, low-conductivity media, unless the flow velocity and/or the length scale are extremely large.

Consider a sample case of electrodeless MHD flow control, illustrated in Fig. 2. Gas flow into a cylindrical duct (inlet), and magnetic field lines are coming out of the duct in a pattern similar to that near the edge of a solenoid. Ionizing electron beams form an annular ring coaxial with and adjacent to the duct wall, and are injected upstream, along B field lines. With the plasma moving across the nonuniform magnetic field, induced electric currents form circles coaxial with the inlet. The resulting $\vec{j} \times \vec{B}$ forces decelerate and compress the flow. Additionally, gas heating by the induced currents creates reduced-density region around and upstream of the inlet, deflecting streamlines and causing an increase in compression and mass flow rate into the duct. Thus, both $\vec{j} \times \vec{B}$ forces and heating create what may be called a magneto-thermal funnel.

The calculations were performed for freestream conditions corresponding to Mach 8 flight at the altitude $h=30$ km, with static pressure and temperature of 1197 Pa and 226.5 K, respectively. The cylindrical inlet of radius $r_{inlet} = 1$ m was positioned at axial location $z_{inlet} = 2$ m. The model profile of a solenoid-like stationary magnetic field in the upstream region was:

$$\begin{aligned} \vec{B} &= [B_z(r, z), B_r(r, z), 0]; \quad B_z(r, z) = -\left(B_a^2(z, r) - B_r^2(r, z)\right)^{1/2}; \\ B_a(z) &= B_{a, \max} \exp(-(z - z_{inlet})/4); \quad B_r(r, z) = B_a(z)[1 - \exp(-(r/(0.5 \cdot r_{inlet})))] \end{aligned} \quad (30)$$

with $B_{a, \max} = 7$ T.

The ionizing electron beams are injected in a 1-cm wide ring around the inlet. The energy of beam electrons is $\varepsilon_b \approx 50$ keV, and their relaxation length under the conditions of this case is $L_R \approx 2.5$ m. The current density of the beam at the injection point is very high, $j_b \approx 72$ mA/cm², and the total power of the beam is $Q_b = 4.57$

MW. Power deposition by electron beams was modeled by a 2D profile approximately following magnetic field lines:

$$q_b(z, r) = 3 \times 10^6 \exp\{-(z - 0.7)^2 / 0.45^2 + (r - r_c)^2 / r_{eff}^2(z)\} \text{ W/m}^3, \\ r_c = 1.75 \exp(-z/0.5) + 0.967; \quad r_{eff}(z) = 0.01 + 0.2 \exp(-z/1.05). \quad (31)$$

where z and r are in meters. The profile of both beam-induced ionization rate corresponds to the beam power deposition profile:

$$q_i(z, r) \approx q_b(z, r) / (eW_i), \quad (32)$$

where $W_i = 34$ eV is the energy cost of ionization by high-energy beam electrons.

The generalized Ohm's law (13) in the case $\vec{u} = (u_z, u_r, 0)$, $\vec{B} = (B_z, B_r, 0)$, $\vec{j} = (0, 0, j_\phi)$ is:

$$j_\phi = \frac{\sigma E_\phi^*}{1 + \Omega_e \Omega_i} = \frac{\sigma(u_z B_r - B_z u_r)}{1 + \Omega_e \Omega_i} \quad (33)$$

This azimuthal current produces Joule heating of the gas:

$$Q_J = j_\phi E_\phi^* = \frac{\sigma(u_z B_r - B_z u_r)^2}{1 + \Omega_e \Omega_i} \quad (34)$$

and $\vec{j} \times \vec{B}$ forces:

$$F_z = -j_\phi B_r \text{ and } F_r = j_\phi B_z. \quad (35)$$

The full set of Euler equations in cylindrical coordinates is:

$$\frac{\partial}{\partial t} U + \frac{\partial}{\partial r} R + \frac{\partial}{\partial z} Z = H, \quad (36)$$

$$U = \begin{pmatrix} \rho \\ \rho u_r \\ \rho u_z \\ e_{tot} \\ E_v \end{pmatrix}, \quad R = \begin{pmatrix} \rho u_r \\ \rho u_r^2 + p \\ \rho u_r u_z \\ (e_{tot} + p)u_r \\ E_v u_r \end{pmatrix}, \quad Z = \begin{pmatrix} \rho u_z \\ \rho u_r u_z \\ \rho u_z^2 + p \\ (e_{tot} + p)u_z \\ E_v u_z \end{pmatrix}, \quad (37)$$

$$H = -\frac{1}{r} \begin{pmatrix} \rho u_r \\ \rho u_r^2 \\ \rho u_r u_z \\ (e_{tot} + p)u_r \\ E_v u_r \end{pmatrix} + \begin{pmatrix} 0 \\ -j_\phi B_r \\ j_\phi B_z \\ Q \\ Q_v - Q_{VT} \end{pmatrix}$$

$$p = (\gamma - 1) \rho \varepsilon_{int} \quad (38)$$

$$e_{tot} = \rho \left[\varepsilon_{int} + (u_r^2 + u_z^2) / 2 \right], \quad (39)$$

where ρ and p denote the gas density and pressure, respectively, u_r, u_z are the r and z velocity components, e_{tot} is the total energy (internal energy, excluding the energy of vibrational mode, plus kinetic energy) of the gas per unit volume, and ε_{int} is the internal energy (excluding the energy of vibrational mode) per unit mass.

The source term in the total energy equation is:

$$Q = -Q_v + Q_{VT} + q_b, \quad (40a)$$

where the vibrational excitation term Q_v can be expressed as a fraction η_v of the Joule heating rate: $Q_v = \eta_v j_\phi^2 / \sigma$.

The fraction η_v is a function of the local reduced electric field $E_{eff}/n = |u_z B_r - B_z u_r|/n$. The fraction η_v was taken from Ref. 49, where it was tabulated as a function of E/n on the basis of solution of Boltzmann kinetic equation for plasma electrons. The remaining energy addition and dissipation terms are:

$$Q_{VT} = (E_v - E_v^0(T)) / \tau_{VT}(T), \quad (40b)$$

heating rate per unit volume due to VT-relaxation; and q_b - power deposited per unit volume by the electron beam. Nonequilibrium and equilibrium vibrational energy was expressed through the respective temperatures by the Planck formula, and nitrogen vibrational relaxation time was taken as in Refs. 16-18.

The plasma was modeled as consisting of electrons, positive and negative ions, whose number densities n_e, n_+, n_- obey the quasineutrality: $n_+ \approx n_e + n_-$. The set of equations for kinetics of charge species, accounting for electron beam-induced ionization rate (q_i term), ionization rate due to plasma electrons (with Townsend ionization coefficient α depending on the local reduced electric field, $E_{eff}/n = |u_z B_r - B_z u_r|/n$), attachment of electrons to molecules with formation of negative ions (frequency ν_a), collisional detachment of electrons from negative ions (rate constant k_d), and electron-ion and ion-ion recombination (rate coefficients β and β_{ii} , respectively), is:^{16-18,33,36}

$$\begin{aligned}\frac{\partial n_e}{\partial t} + \text{div} \vec{\Gamma}_e &= \alpha |j_\phi| / e + q_i + k_d N n_- - \nu_a n_e - \beta n_+ n_e, \\ \frac{\partial n_+}{\partial t} + \text{div} \vec{\Gamma}_+ &= \alpha |j_\phi| / e + q_i - \beta_{ii} n_+ n_+ - \beta n_+ n_e, \\ \frac{\partial n_-}{\partial t} + \text{div} \vec{\Gamma}_- &= -k_d N n_- + \nu_a n_e - \beta_{ii} n_- n_+.\end{aligned}\quad (41)$$

In the considered case, there are no drift fluxes along either z or r axes (only azimuthal current, j_ϕ , is present), and, therefore, the fluxes of charged species in (r, z) plane can be written simply as $\vec{\Gamma}_{e,+, -}(r, z) = n_{e,+, -}(\vec{u}_z \cdot \vec{i}_z + \vec{u}_r \cdot \vec{i}_r)$, where $\vec{i}_{r,z}$ are the vectors of unit length in z and r directions; $\vec{u}_{r,z}$ is the effective electron-ion velocity across magnetic field taking into account ion slip,^{17, 18}

$$\vec{u}_{r,z} = \frac{\vec{u}_{r,z}}{1 + \Omega_e \Omega_+} \quad (42)$$

The initial conditions for plasma components are: $n_{e,+, -}(r, z, t = 0) = 0$. The boundary conditions are:

$$\begin{aligned}n_{e,+, -}(z = 0, r, t) &= n_{e,+, -}(z = z_{\max}, r, t) = 0 \\ n_{e,+, -}(z, r = r_{\max}, t) &= 0; \quad dn_{e,+, -}(z, r = 0, t) / dr = 0.\end{aligned}\quad (43)$$

Rate coefficients of electron-ion and ion-ion recombination, and of electron attachment and detachment processes, discussed in Refs. 16-18, 31-34, were taken from Refs. 50 and 51. Since some of those rate coefficients depend on electron temperature T_e , it is important to calculate the electron temperature in the modeling. In our computations, electron temperature was determined from the tabulated data on electron diffusion and mobility coefficients of Ref. 49. In that paper, the diffusion and mobility coefficients are listed as functions of E/N , determined from experimental data and extrapolation based upon solution of Boltzmann kinetic equation for electrons in air.

Results of the calculations are shown in Figs. 3-10. Fig. 3 depicts the magnetic field lines, and Fig. 4 shows the electron beam power deposition profile. The resulting profiles of electron density and azimuthal current are shown in Figs. 5 and 6. Figs. 7-10 show the computed profiles of static and vibrational temperatures, gas density and radial velocity. The formation of magneto-thermal funnel is clearly seen in the figures.

The overall performance of the funnel can be assessed by the mass flow rate and enthalpy flux into the inlet, and by the total pressure coefficient. Without ionization ($q_b = 0$), the mass flow and enthalpy flux into the

inlet are the following: $\dot{m}_{z=z_{\text{inlet}}} = \int_0^{r_{\text{inlet}}} 2\pi r \rho(z, r) u_z dr = 139.6 \text{ kg/s}$, and

$$\dot{H}_{z=z_{\text{inlet}}} = \int_0^{r_{\text{inlet}}} 2\pi r \rho(z, r) u_z [\gamma p / (\gamma - 1) \rho + 0.5(u_z^2 + u_r^2)] dr = 438.5 \text{ MW}.$$

The total pressure coefficient, that is, the total pressure averaged over the inlet cross-section divided by the freestream total pressure, is $\langle p_{\text{tot}} \rangle / p_{\text{tot},0} = 1$. When the electron beam is turned on, but in the absence of any magnetic field ($B=0$, $q_b \neq 0$), gas heating by the beam and streamline deflection result in a barely noticeable

increase in mass and enthalpy fluxes, and a slight decrease in total pressure: $\dot{m}_{z=z_{inlet}} = 139.9$ kg/s; $\dot{H}_{z=z_{inlet}} = 439.4$ MW; $\langle p_{tot} \rangle / p_{tot,0} = 0.997$. With both ionization and magnetic field on ($\vec{B} = \vec{B}(r, z)$, $q_b \neq 0$), the increased mass and enthalpy fluxes and the decreased total pressure coefficient are: $\dot{m}_{z=z_{inlet}} = 146$ kg/s; $\dot{H}_{z=z_{inlet}} = 457.8$ MW; $\langle p_{tot} \rangle / p_{tot,0} = 0.93$. The maximum flow turning induced in the flowfield is about 2.5° .

The computations were performed with 2nd order MacCormack method⁵² on a rectangular 310×250 grid. Computations with a finer grid, 465×375, show that the mass and enthalpy fluxes and the total pressure are within 0.1% from those computed with 310×250 grid, thus confirming the accuracy of computations.

Thus, magneto-thermal funnel can indeed increase mass capture and total enthalpy flux into the inlet. However, because of gas heating, the total pressure would decrease. In the sample case, the beam and magnetic field parameters were not optimized, and the effects are quite modest, despite the very high current density of the beam. The mass flow rate increase can be made stronger by using stronger magnetic fields and higher beam currents. Practicality of this method of flow control, with advantages weighted against flaws (strong magnetic fields, high electron beam currents, and losses of total pressure) should be a subject of a systems study.

IV. Conclusions

The principal difficulty in high-speed flow control using electric and magnetic fields is that the relatively cold gas has to be ionized in electric discharges or by electron beams, which requires large power inputs and results in low ionization fraction and electrical conductivity. The low ionization fraction means that, although electrons and ions can interact with electromagnetic fields, transfer of momentum and energy to or from the bulk neutral gas can be small compared with momentum and energy carried by the high-speed flow.

Even at the highest values of the electric field that can exist in cathode sheaths of electric discharges, electrohydrodynamic (EHD), or ion wind, effects in a single discharge can be of significance only in low-speed core flows or in laminar sublayer of the boundary layer. Cumulative action of multi-element discharges would conceivably amplify the single-sheath effect. However, Joule heating can overshadow the cathode sheath ion wind effects.

Theoretical analysis of MHD flow control with electron beam ionization of hypersonic flow shows that the MHD interaction parameter is a steeply increasing function of magnetic field strength and the flow velocity. However, constraints imposed by arcing between electrode segments can reduce the performance and make the maximum interaction parameter virtually independent of Mach number. Thus, the value of critical Hall field corresponding to the onset of arcing between electrode segments is extremely important in designing and evaluating performance of hypersonic MHD devices, and the arcing instability should be investigated theoretically and experimentally.

Estimates of MHD interaction parameter with respect to shear stress show that the relative strength of MHD effects can be higher near the wall (in the boundary layer) than in the core flow, which may have implications for MHD boundary layer and transition control. Overall, one of the qualitative conclusions from this work is that large-scale bulk MHD effects on the overall hypersonic flow field are quite difficult (although not impossible) to achieve, whereas small and/or localized MHD effects such as those for small-angle flow turning or boundary layer control may be useful for significant flow field manipulation.

In this work, we also suggested a magneto-thermal funnel concept that would accomplish and electrodeless MHD turning and compression of high-speed flows. Computations of a sample case demonstrate that the turning and compression of hypersonic flow ionized by electron beams can be achieved; however, the effect is relatively modest due to low ionization level.

REFERENCES

- ¹ Fraishtadt, V.L., Kuranov, A.L., and Sheikin, E.G., "Use of MHD Systems in Hypersonic Aircraft," *Technical Physics*, Vol. 43, No. 11, 1998, pp.1309-1313.
- ² Gurijanov, E.P., and Harsha, P.T., "AJAX: New Directions in Hypersonic Technology," AIAA Paper 96-4609, 1996.

- ³ Bityurin, V.A., Lineberry, J.T., Potebnia, V.G., Alferov, V.I., Kuranov, A.L., and Sheikin, E.G., "Assessment of Hypersonic MHD Concepts," AIAA Paper 97-2323, 1997.
- ⁴ Bityurin, V.A., Klimov, A.I., Leonov, S.B., Bocharov, A.N., and Lineberry, J.T., "Assessment of a Concept of Advanced Flow/Flight Control for Hypersonic Flights in Atmosphere," AIAA Paper 99-4820, 1999.
- ⁵ Brichkin, D.I., Kuranov, A.L., and Sheikin, E.G., "MHD Technology for Scramjet Control," AIAA Paper 98-1642, 1998.
- ⁶ Kuranov, A.L. and Sheikin, E.G., "The Potential of MHD Control for Improving Scramjet Performance," AIAA Paper 99-3535, 1999.
- ⁷ Brichkin, D.I., Kuranov, A.L., and Sheikin, E.G., "The Potentialities of MHD Control for Improving Scramjet Performance," AIAA Paper 99-4969, 1999.
- ⁸ Kuranov, A.L., and Sheikin, E.G., "MHD Control on Hypersonic Aircraft under AJAX Concept: Possibilities of MHD Generator," AIAA Paper 2002-0490, 2002.
- ⁹ Chase, R.L., Mehta, U.B., Bogdanoff, D.W., Park, C., Lawrence, S., Aftosmis, M., Macheret, S.O., and Shneider, M.N., "Comments on an MHD Energy Bypass Engine Powered Spaceliner," AIAA Paper 99-4965, November 1999.
- ¹⁰ Park, C., Mehta, U.B., and Bogdanoff, D.W., "Real Gas Calculation of MHD-Bypass Scramjet Performance," AIAA Paper 2000-3702, 2000.
- ¹¹ Golovachev, Yu.P., and Sushikh, S.Yu., "Supersonic Air-Scoop Flows of a Weakly Ionized Gas in External Electromagnetic Field," *Technical Physics*, Vol. 45, No. 2, 2000, p.168.
- ¹² Golovachev, Yu.P., Sushikh, S.Yu., and Van Wie, D., "Numerical Simulation of MGD Flows in Supersonic Media," AIAA Paper 2000-2666, 2000.
- ¹³ Vatazhin, A., Kopchenov, V., and Gouskov, O., "Some Estimations of Possibility to Use the MHD Control for Hypersonic Flow Deceleration," AIAA Paper 99-4972, 1999.
- ¹⁴ Kopchenov, V., Vatazhin, A., and Gouskov, O., "Estimation of Possibility of Use of MHD Control in Scramjet," AIAA Paper 99-4971, 1999.
- ¹⁵ Vatazhin, A., Kopchenov, V., and Gouskov, O., "Numerical Investigation of Hypersonic Inlets Control by Magnetic Field," *The 2nd Workshop on Magneto- and Plasma Aerodynamics in Aerospace Applications*, Moscow, 5-7 April 2000, pp. 56-63.
- ¹⁶ Macheret, S. O., Shneider, M. N., Miles, R. B., and Lipinski, R. J., "Electron Beam Generated Plasmas in Hypersonic Magnetohydrodynamic Channels," *AIAA Journal*, 2001, Vol. 39, No. 6, pp. 1127-1136.
- ¹⁷ Macheret, S. O., Shneider, M. N., and Miles, R. B., "Magnetohydrodynamic Control of Hypersonic Flow and Scramjet Inlets Using Electron Beam Ionization," *AIAA Journal*, Vol. 40, No. 1, 2002, pp. 74-81.
- ¹⁸ Macheret, S. O., Shneider, M. N., and Miles, R. B., "MHD Power Extraction from Cold Hypersonic Air Flow with External Ionizers," *Journal of Propulsion and Power*, Vol. 18, No. 2, 2002, pp. 424-431.
- ¹⁹ Macheret, S. O., Miles, R. B., and Nelson, G. L., "Feasibility Study of a Hybrid MHD/Radiatively Driven Facility for Hypersonic Ground Testing," AIAA Paper 97-2429, 1997.
- ²⁰ Macheret, S. O., Shneider, M. N., Miles, R. B., Lipinski, R. J., and Nelson, G. L., "MHD Acceleration of Supersonic Air Flows Using Electron Beam-Enhanced Conductivity," AIAA Paper 98-2922, 1998.
- ²¹ Shneider, M. N., Macheret, S. O., and Miles, R. B., "Electrode Sheaths and Boundary Layers in Hypersonic MHD Channels," AIAA Paper 99-3532, 1999.
- ²² Macheret, S. O., Shneider, M. N., and Miles, R. B., "Electron Beam Generated Plasmas in Hypersonic MHD Channels," AIAA Paper 99-3635, 1999.
- ²³ Macheret, S. O., Shneider, M. N., and Miles, R. B., "MHD Power Extraction from Cold Hypersonic Air Flow with External Ionizers," AIAA Paper 99-4800, 1999.
- ²⁴ Macheret, S. O., Ionikh, Y. Z., Martinelli, L., Barker, P. F., and Miles, R. B., "External Control of Plasmas for High-Speed Aerodynamics," AIAA Paper 99-4853, 1999.
- ²⁵ Simmons, G. A., Nelson, G. L., Cambier, J.-L., Macheret, S. O., Shneider, M. N., Lipinski, R. J., and Reed, K. W., "Electron Beam Driven MHD for the RDHWT/MARIAH II Hypersonic Wind Tunnel," AIAA Paper 2000-2277, 2000.
- ²⁶ Macheret, S. O., Shneider, M. N., and Miles, R. B., "Potential Performance of Supersonic MHD Power Generators," AIAA Paper 2001-0795, 2001.
- ²⁷ Macheret, S. O., Shneider, M. N., and Miles, R. B., "External Supersonic Flow and Scramjet Inlet Control by MHD with Electron Beam Ionization," AIAA Paper 2001-0492, 2001.

- ²⁸ Macheret, S. O., Shneider, M. N., and Miles, R. B., "Energy-Efficient Generation of Nonequilibrium Plasmas and Their Applications to Hypersonic MHD Systems," AIAA Paper 2001-2880, 2001.
- ²⁹ Girgis, I., Shneider, M., Macheret, S., Brown, G., and Miles, R., "Creation of Steering Moments in Supersonic Flow by Off-Axis Plasma Heat Addition," AIAA Paper 2002-0129, 2002.
- ³⁰ Miles, R., Martinelli, L., Macheret, S., Shneider, M., Girgis, I., Zaidi, S., Mansfield, D., Siclari, M., Smereczniak, O., Kashuba, R., and Vogel, P., "Suppression of Sonic Boom by Dynamic Off-Body Energy Addition and Shape Optimization," AIAA Paper 2002-0150, 2002.
- ³³ Macheret, S. O., Shneider, M. N., and Miles, R. B., "Modeling of Air Plasma Generation by Electron Beams and High-Voltage Pulses," AIAA Paper 2000-2569, 2000.
- ³⁴ Macheret, S. O., Shneider, M. N., and Miles, R. B., "Modeling of Plasma Generation in Repetitive Ultra-Short High-Power DC, Microwave, and Laser Pulses," AIAA Paper 2001-2940, 2001.
- ³⁵ El-Khabiry, S., and Colver, G.M., "Drag Reduction by DC Corona Discharge Along an Electrically Conductive Flat Plate for Small Reynolds Number Flow," *Physics of Fluids*, Vol. 9, No. 3, 1997, pp. 587 – 599.
- ³⁶ Raizer, Yu.P., "Physics of Gas Discharges," Springer, Berlin, 1991, Chapters 14 and 17.
- ³⁷ Roth, J.R., Sherman, D.M., and Wilkinson, S.P., "Boundary Layer Flow Control With a One Atmosphere Uniform Glow Discharge Surface Plasma," AIAA Paper 98-0328, 36th AIAA Aerospace Sciences Meeting & Exhibit, Jan. 12-15, 1998, Reno, NV.
- ³⁸ Roth, J., Sin, H., Madhan, R., and Wilkinson, S., "Flow Re-attachment and Acceleration by Paraelectric and Peristaltic Electrohydrodynamic (EHD) Effects," AIAA Paper 2003-531, 41st AIAA Aerospace Sciences Meeting and Exhibit, Jan. 6-9, 2003, Reno, NV.
- ³⁹ Yu, L., Laux, C.O., Packan, D.M., and Kruger, C.H., "Direct-Current Glow Discharges in Atmospheric Pressure Air Plasmas," *Journal of Applied Physics*, Vol. 91, Issue 5, March 1, 2002, pp. 2678 – 2686.
- ⁴⁰ Henoch, C., and Stace, J., "Experimental Investigation of a Salt Water Turbulent Boundary Layer Modified by an Applied Streamwise Magnetohydrodynamic Body Force," *Physics of Fluids*, Vol. 7, No. 6, 1995, pp. 1371 – 1383.
- ⁴¹ Anderson, J.D., Jr., "Hypersonic and High Temperature Gas Dynamics," McGraw-Hill, New York, 1988, pp. 286, 287.
- ⁴² Cowling, T.G., "Magnetohydrodynamics," Interscience, New York, 1957, Chap. 3.
- ⁴³ Rosa, R.J., "Magnetohydrodynamic Energy Conversion," McGraw-Hill, 1968, Chap. 3, 4.
- ⁴⁴ Nedospasov, A.V., and Khait, V.D., "Fundamentals of Physics of Processes in Devices with Low Temperature Plasmas" ("Osnovy Fiziki Protessov v Ustroistvakh s Nizkotemperaturnoi Plazmoi"), Energoatomizdat, Moscow, 1991, Chap. 6 (in Russian).
- ⁴⁵ Oliver, D.A., in: Proceedings of 14th Symposium on Engineering Aspects of MHD, University of Tennessee Space Institute, Tullahoma, Tennessee, 1974, pp. VIII.6.1 – VIII.6.7.
- ⁴⁶ Nedospasov, A.V., Paramonov, A.A., and Khait, V.D., in: Proceedings of 8th International Conference on MHD Energy Conversion, Moscow, 1983, Vol. 1, pp. 264-276.
- ⁴⁷ Heydt, R.P., and Eustis, R.H., in: Proceedings of 21st Symposium on Engineering Aspects of MHD, Argonne National Laboratory, Argonne, Illinois, 1983, Supplemental Volume, pp. 11 – 15.
- ⁴⁸ Zalkind, V.I., Kirillov, V.V., Tikhotskii, A.S., et. al., *Teplofizika Vysokikh Temperatur (High Temperature)*, Vol. 19, No. 5, 1981, pp. 1050 – 1060.
- ⁴⁹ Aleksandrov, N.L., Vysikailo, F.I., Islamov, R.Sh., Kochetov, I.V., Napartovich, A.P., and Pevgov, V.G., "Electron distribution function in 4:1 N₂-O₂ mixture," *High Temperature*, Vol. 19, No. 1, 1981, pp. 17-21.
- ⁵⁰ Kosy, I.A., Kostinsky, A.Yu., Matveyev, A.A., and Silakov, V.P., "Kinetic scheme of the non-equilibrium discharge in nitrogen-oxygen mixtures," *Plasma Sources Science and Technology*, Vol. 1, No. 3, 1992, pp. 207-220.
- ⁵¹ Bazelyan, E.M., and Raizer, Yu.P., "Spark Discharge," CRC Press, Boca Raton, Florida, 1997, Chap. 2.
- ⁵² Anderson D.A., Tannehill J.C., Pletcher R.H., Computational Fluid Mechanics and Heat Transfer, Hemishpere Publishing Corporation, 1984, Chapter 4.

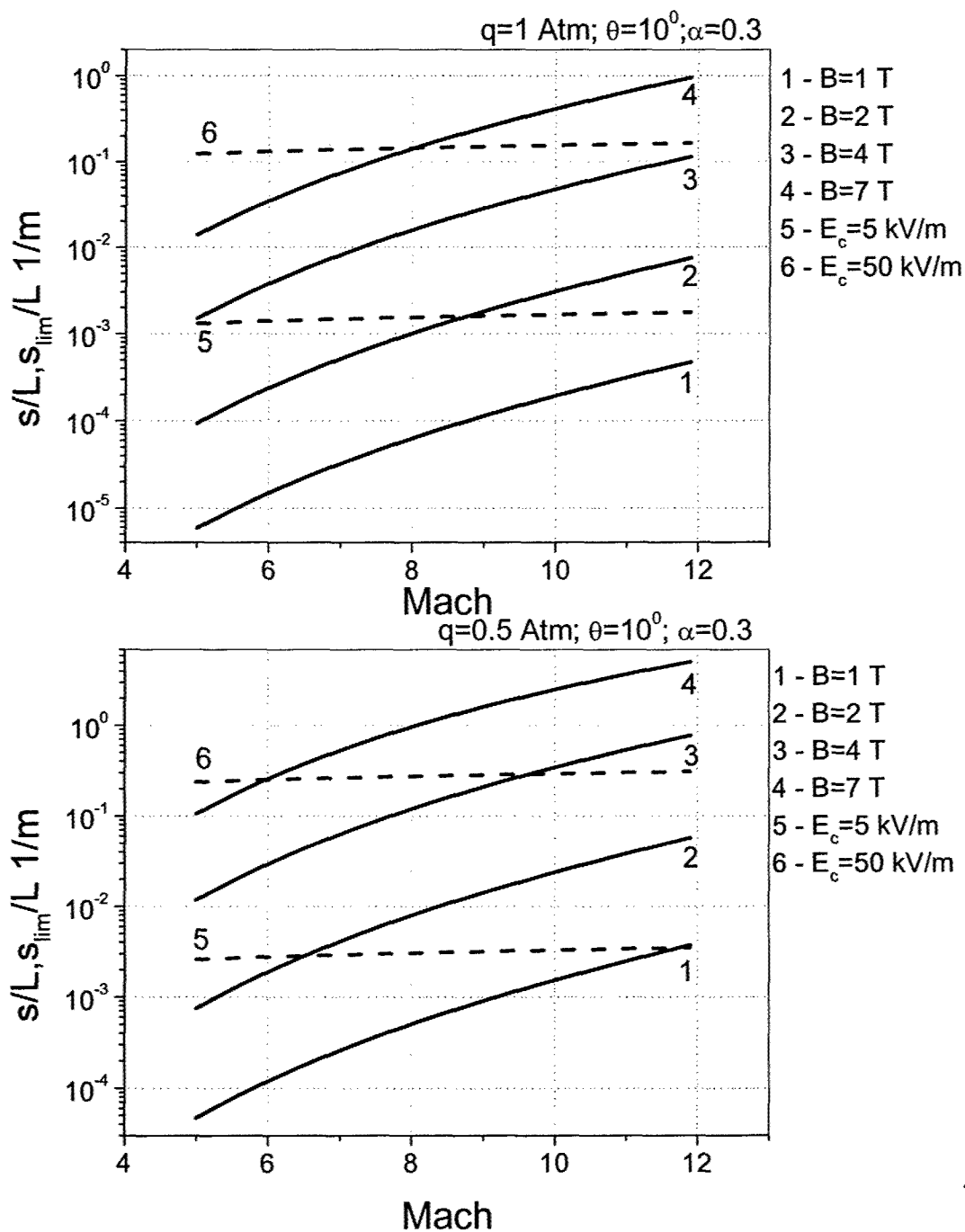


Fig. 1. Maximum MHD interaction parameter per unit length versus flight Mach number. Solid lines – interaction parameter at different values of magnetic field, with no constraint on Hall field; dashed lines – upper limit of interaction parameter imposed by constraint on maximum allowed Hall field.

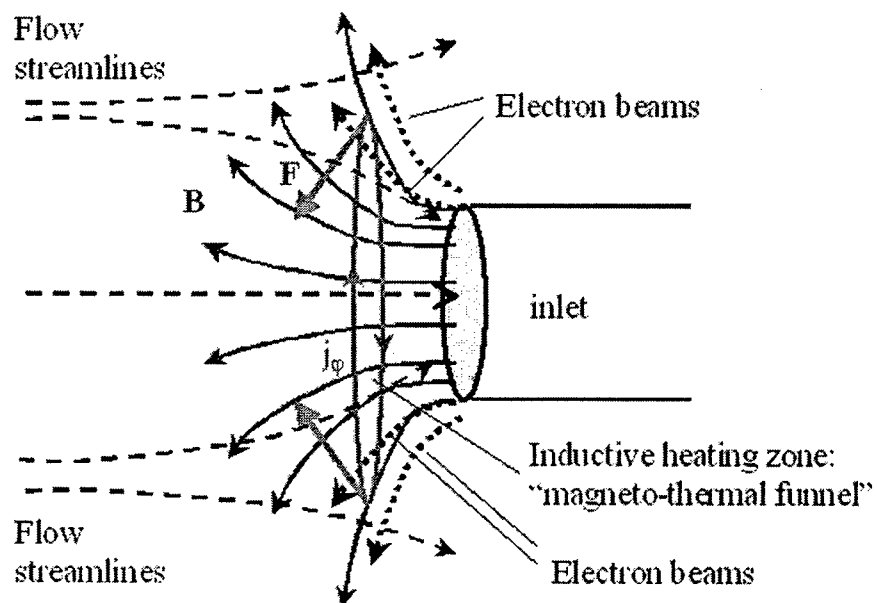


Fig. 2. Schematic illustration of the magneto-thermal funnel concept.

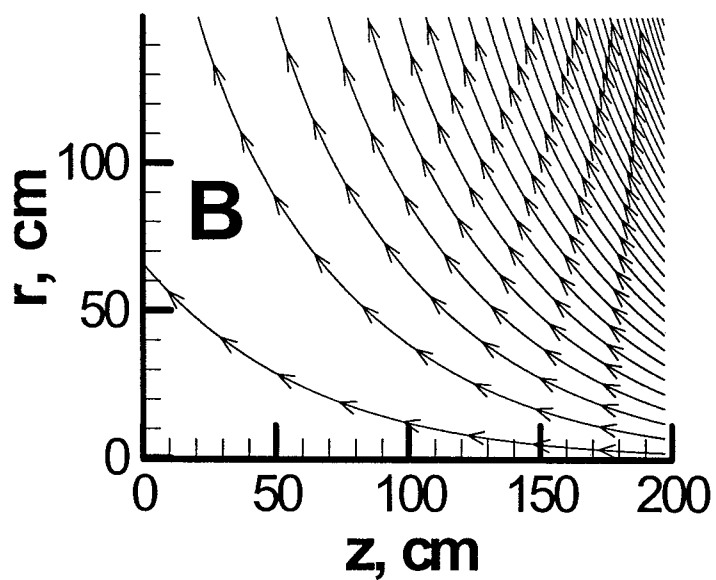


Fig. 3. Magnetic field lines in the computed case.

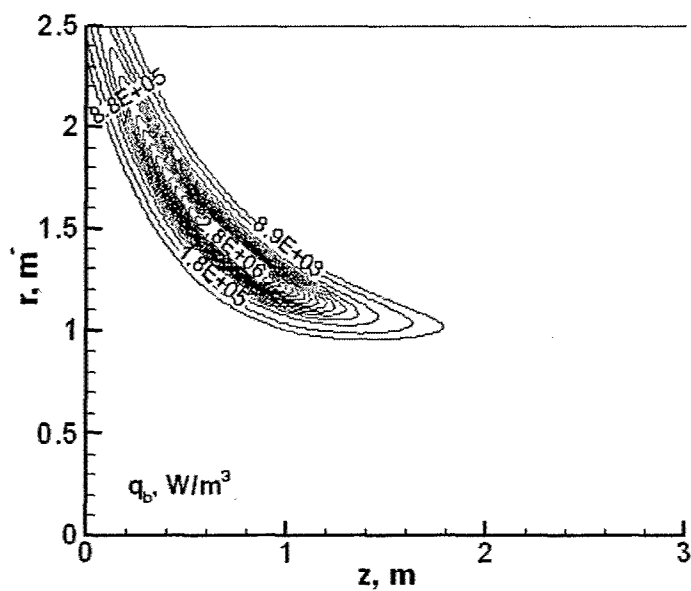


Fig. 4. Electron beam power deposition contour lines in the computed case

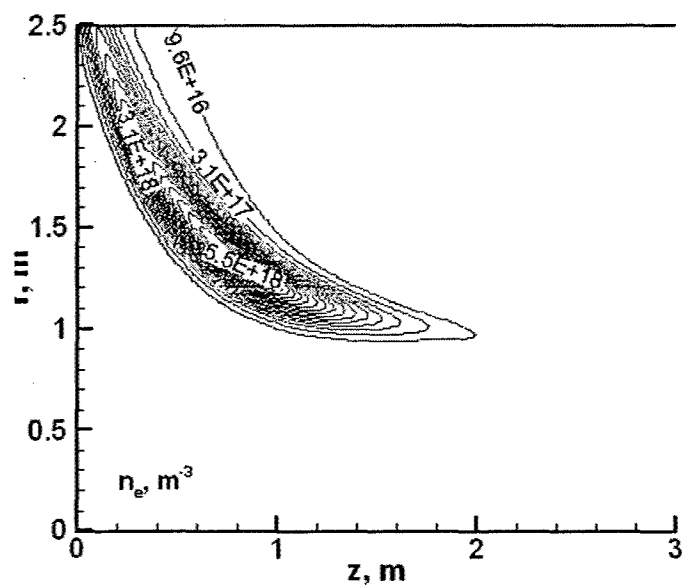


Fig. 5. Electron number density contours in the computed case.

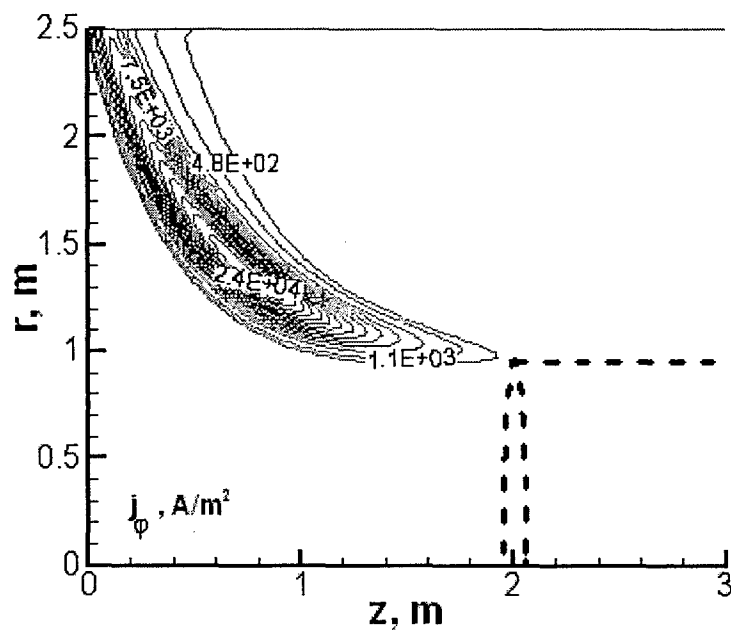


Fig. 6. Azimuthal current density contour lines in the computed case

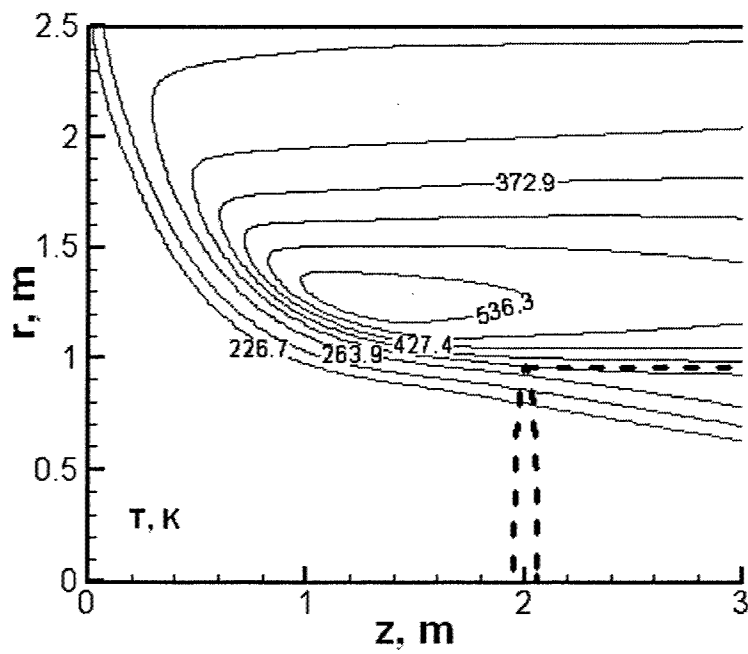


Fig. 7. Static temperature contours in the computed case.

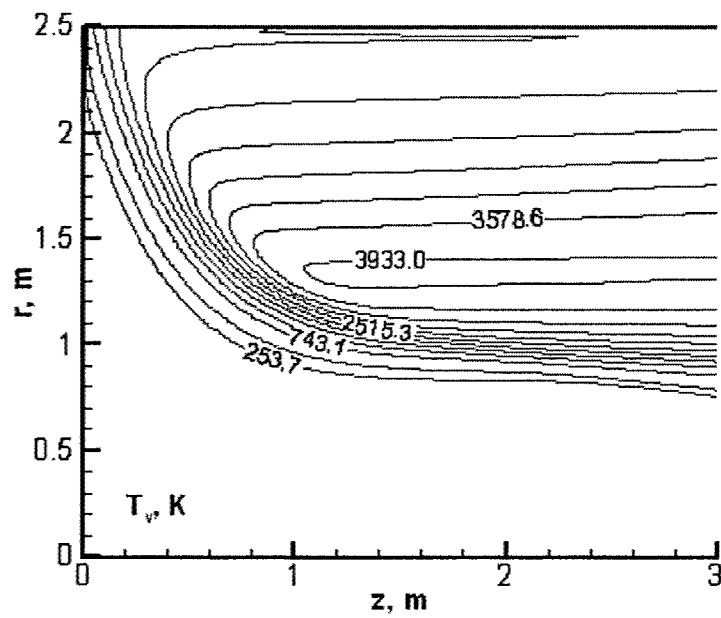


Fig. 8. Vibrational temperature contour lines in the computed case

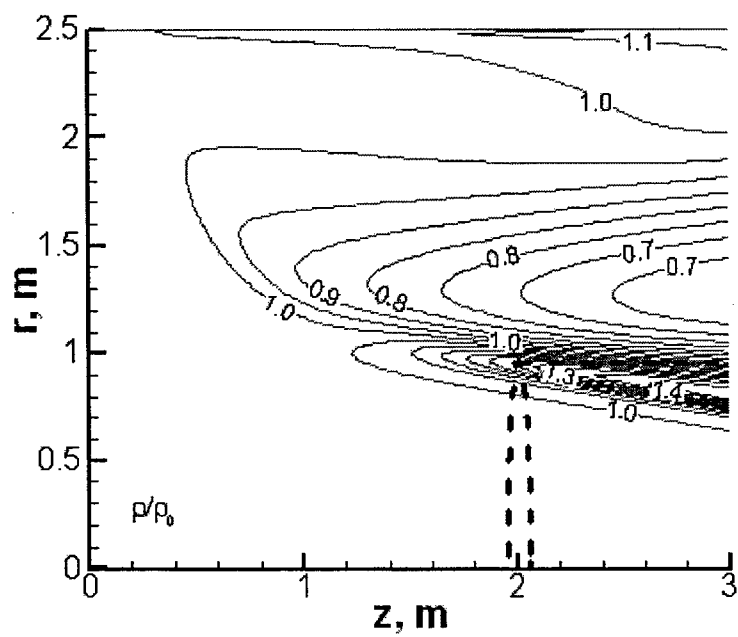


Fig. 9. Density contours in the computed case.

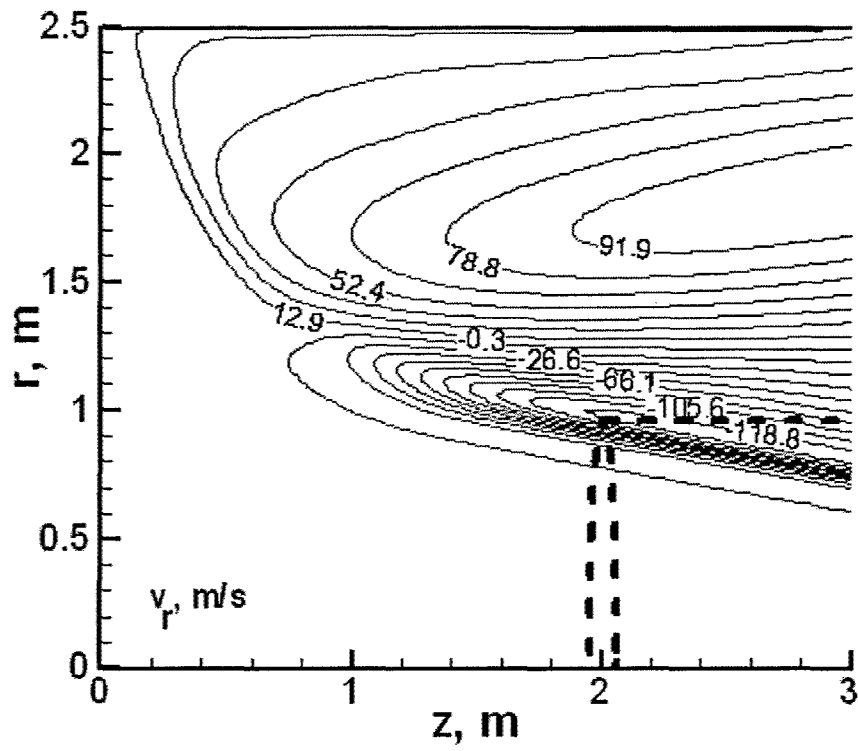


Fig. 10. Radial velocity contour lines in the computed case

CHAPTER 3

NONEQUILIBRIUM MHD CONTROL OF SCRAMJET INLETS

Summary

This chapter is devoted to theoretical analysis of magnetohydrodynamic (MHD) control of forebody flow compression and air mass capture in scramjet inlets for vehicles that would fly at Mach 6-10. Due to the low static temperature, nonequilibrium air ionization and electrical conductivity are created by electron beams injected into the gas along magnetic field lines. Two-dimensional inviscid steady-state flow equations are solved jointly with equations describing electron beam-induced ionization profiles, plasma kinetics, and MHD equations. Several scenarios are considered. At flight Mach numbers 8 and 10, with forebody and inlet geometry designed for Mach 6, the shocks that would enter the inlet can be moved back on the cowl lip by placing an MHD generator at the first compression ramp. In addition to controlling the shocks, the MHD device would generate electric power; however, Joule heating would result in losses of total pressure. Another scenario is an on-ramp MHD accelerator that should increase mass capture at Mach 6 or 8 for a vehicle designed for Mach 10. Calculations show that this scenario has only disadvantages, as the MHD device consumes high power, reduces total pressure, and actually decreases mass capture due to Joule heating and thermal expansion of the gas. A modest increase in mass capture can be in principle accomplished in an MHD generator mode, if the magnetic field has components both parallel and orthogonal to the flow. However, this scenario requires unrealistically large volumes of strong magnetic fields, and the mass capture increase is due mostly to a nonuniform gas heating. A new concept of a virtual inlet is proposed, where a localized off-body energy addition is used to increase mass capture, while not reducing (and even increasing) total pressure at the inlet.

I. Introduction

The geometry, size, and weight of scramjet-powered hypersonic vehicles are largely dictated by the need to compress the ambient low-density air upstream of the combustor. The optimum geometry corresponds to the well-known shock-on-lip (SOL) condition (Fig. 1): the compression ramp shocks converge on the cowl lip, and the reflected shock impinges on the upper boundary of the inlet. Since shock angles are determined by the flight Mach number, the SOL condition cannot be met at Mach numbers higher or lower than the design Mach number. At Mach numbers higher than the design one, the shocks move inside the inlet (Fig. 2), causing multiple reflected shocks, loss of stagnation pressure, possible boundary layer separation, and engine unstart. At Mach numbers lower than the design one, the so-called spillage occurs, and the air mass capture decreases (Fig. 3).

To avoid performance penalties at off-design Mach numbers, a variable geometry inlet can be used. However, the mechanical variable geometry system would be quite heavy, weighing perhaps tens of metric tons. An alternative approach is to optimize inlets using energy addition to or extraction from the flow. Plasmas and various magnetohydrodynamic devices may offer a viable optimization scheme.

One method that was analyzed by several groups,¹⁻⁸ is to design the vehicle for a relatively low Mach number (for example, Mach 6), and move the shocks from inside the inlet back to the cowl lip by an MHD generator device placed at one of the compression ramps (Fig. 4). The advantages of this method are the following: 1) reduction in vehicle size and weight due to both absence of mechanically variable inlet and the shortening of compression ramps because of the reduction of design Mach number; the weight savings may more than offset the weight of the magnet and other MHD-related hardware; 2) no net power is required to run the MHD device, since the generator mode is used, and the power requirements for air ionization can be minimized with electron beams as ionizers; 3) flexibility of flow control. An important disadvantage of this approach is that the inevitable Joule heating and other dissipative processes result in substantial stagnation pressure losses.

Another method of MHD control is to design the vehicle for a high Mach number (for example, Mach 10), and to decrease or eliminate the flow spillage by an MHD accelerator device placed at one of the compression ramps (Fig. 5). A substantial disadvantage of this method compared with the MHD generator method shown in Fig. 4 is that an

accelerator requires a substantial amount of power. Meanwhile, the accelerator method would still result in considerable stagnation pressure losses.

Yet another, recently suggested,⁵ method of MHD inlet control is to operate an on-ramp MHD device in generator mode, but use a magnetic field configuration with B field components both parallel and orthogonal to the flow. According to Ref. 5, air mass capture at Mach numbers lower than the design one can be increased with this method.

In this paper, we perform computational and qualitative analysis of all the three methods of MHD flow and shock control at off-design Mach numbers. We also propose a new method of inlet control: a virtual inlet.

An important factor in the analysis is that in the flight regime of interest, static temperature is too low for thermal ionization of air. Therefore, nonequilibrium ionization in MHD devices must be done. The energy cost of ionization imposes very rigid constraints on the choice of ionization methods: only the most energetically efficient ionization method can be used in these devices. Our earlier work showed that electron beams injected into the gas along magnetic field lines constitute the most efficient way of creating nonequilibrium ionization. However, even with the most efficient ionizer, the very existence of ionization cost does not allow the ionization degree and the conductivity in hypersonic MHD devices to be high. This makes the task of using MHD for hypersonic flow control and power generation quite challenging.

II. The model

We consider hypersonic gas flow along the two ramps with 10° and 20° angles upstream of the inlet with forward-shifted cowl lip, as shown in Figs. 1-6. The flow is two-dimensional in (x, z) plane. Cases both without and with MHD influence on the flow are computed. In MHD cases, both magnetic field and ionizing electron beam are directed parallel to z -axis. Because the entire flow region is hypersonic, steady state solution using x as marching coordinate can be found.

The set of Euler equations in Cartesian coordinates, together with an ideal gas equation of state, a simple model of an ideal Faraday MHD generator, vibrational relaxation, and a plasma kinetic model are those of Refs. 7 and 8. In the present paper, we solve steady-state problems only, so that all time derivatives in the equations of Ref. 8 were equated to zero. Additionally, in MHD accelerator cases, the load factor $k > 1$, so that in the equations of Ref. 8, $(1-k)$ should be substituted by $(k-1)$, and the power P dissipated in the external load per unit gas volume should be taken with the sign opposite to its sign in Eq. (5) of Ref. 8. In the cases with B field with both B_x and B_y components, the corresponding components of $\vec{j} \times \vec{B}$ force, as well as both contributions to the Faraday e.m.f., were included in the equations, similar to Ref. 5.

Power deposition and ionization by the electron beams have to be coupled with gas dynamic and plasma kinetic equations. In our earlier work,⁹⁻¹³ we used the so-called "forward-backward" approximation¹⁴ for electron beam propagation along magnetic field lines into gases and beam-generated ionization. This method is quite accurate, and it can be (and, in fact, was^{9, 10}) coupled with Navier-Stokes and MHD equations. However, computational demands of the full "forward-back" method, when coupled with gas dynamic and MHD equations, are prohibitive. Therefore, a simple but accurate way to predict ionization profiles should be found.

Having analyzed physics of ionization processes, we concluded that in a uniform gas the ionization rate profile has to be close to a truncated Gaussian. Indeed, ionization of molecules by electron impact is inefficient both at low and high (above 1 keV) electron energies.^{15, 16} The maximum of the ionization cross section corresponds to electron energy of several hundred electronvolts.^{15, 16} In this energy range, and even above it, the probability of back scattering is substantial, and there are both forward and backward electron fluxes exchanging electrons between them. The resulting motion is very much like diffusion. Thus, energy deposition (Q_b) and ionization profiles computed with both "forward-back" method and CYLTRAN Monte Carlo Calculations (MCC)^{9, 13} are very close to

Gaussian profiles:^{7,8} $Q_b(\xi) = a + \frac{b}{w} \exp(-2(\xi - z_m)^2 / w^2)$

(1)

where $\xi = z_b(x) - z$; $z_m \approx L_R / 3.21$, $w \approx 1.64 z_m$; $L_R(\varepsilon_b, N)$ is the beam relaxation length. There are two additional conditions for determining the constants a and b :

$$Q_b(L_R) = 0 \text{ and } \int_0^{L_R} Q_b(\xi) d\xi = |j_b| \varepsilon_b / e; \quad (2)$$

ε_b and j_b are the beam electron energy and current density at the injection point.

The use of a loss function^{7,8} or the direct solution of kinetic equation for electrons in the "forward-back" approximation give a relaxation length overestimated by a factor of 1.5-2. This is because lateral electron scattering and the loss of an additional energy equal to the energy of the secondary electron were neglected in those approximations. In the present paper, an empirical approximation formula for the electron beam relaxation length that effectively includes those two effects is used.

Assuming that the empirical approximation¹⁷ for the beam relaxation length in a gas with uniform number density, $N = \text{const}$, is also valid for nonuniform neutral gas density, but with the average number density along the beam direction, \bar{N} , and that the relaxation length along magnetic field in dense gases is the same as without the magnetic field, we have for the relaxation length:

$$L_R = 1.1 \cdot 10^{21} \varepsilon_b^{1.7} / \bar{N}, \text{ m} \quad (3)$$

where ε_b is in keV, \bar{N} is in m^{-3} , and L_R is in meters. At each location along x , with the L_R in this location, we can find $\bar{N}(x)$ and $\varepsilon_b(x)$:

$$\bar{N}(x) = \frac{1}{L_R} \int_0^{L_R} N(\xi, x) d\xi; \quad \varepsilon_b(x) = (L_R \bar{N} / 1.1 \cdot 10^{21})^{1/1.7}, \text{ keV}. \quad (4)$$

Equations (1)-(4) fully determine both beam-induced profiles: energy deposition, Q_b and ionization rate:

$$q_i(x, \xi) \approx Q_b(x, \xi) / (e W_i), \quad (5)$$

where $W_i = 34 \text{ eV}$ is the energy cost of ionization by high-energy beam.

In Fig. 7, Q_b obtained with Eqs. (1)-(4) is compared with results of CYLTRAN Monte Carlo calculations (MCC).^{9,13} Note that when the Gaussian approximation (1) uses the same relaxation length as that given by the MCC, the agreement is very good.

III. Computed cases

a. MHD control at $M > M_{\text{design}}$

The inlet geometry was first optimized for Mach 6: the location of the cowl lip was chosen so that both oblique shocks would together reach the lip, and the reflected shock would fall right on the corner between the second ramp and the engine. This configuration is shown in Fig. 8. The freestream conditions correspond to the altitude of 26 km. The shocks inside the inlet are weak, as can be seen from the streamline pattern.

Next, the flow velocity was increased to Mach 8 for the same geometry. To keep the freestream dynamic pressure about the same as at Mach 6, the flight altitude has to be increased, and all Mach 8 cases were run for an altitude of 30 km, and Mach 10 cases – for 33 km. As seen in Fig. 9, the shock would now make contact with the cowl farther downstream, producing strong multiple reflected shocks. Although in this work, shock-boundary layer interactions and unsteady processes were not studied, flow separation and unstart can be expected in this case.

To find out if an MHD system could bring the flow closer to the design point, an ideal Faraday generator system with the loading parameter $k = 0.5$ was put near the surface of the first ramp. Both the magnetic field and the

electron beam were directed downward along z -axis. Both the B field and the beam were assumed uniform along x within the region $2.75 \text{ m} \leq x \leq 10.8 \text{ m}$, and to be equal to zero elsewhere. The presumed MHD configuration in (x, z) and (y, z) planes is shown schematically in Fig. 6. The B field profile along the z -axis was Gaussian

$$B = B_{\max} \exp\left(-\frac{(z_b(x) - z)^2}{(0.75 \text{ m})^2}\right) \text{ with the maximum of } B_{\max} = 4 \text{ Tesla at the wall. Electron beam energy and current}$$

density were adjusted so as to move the shocks at Mach 8 back to the cowl lip. In this case and throughout this paper, the electron beam current was set at $j_b = 1 \text{ mA/cm}^2$.

As seen in Fig. 10, with the MHD generator on, both shocks can be moved back to the lip, and streamlines in the inlet duct become much more parallel to the walls. However, their angles of incidence are slightly different from those in the Mach 6 case, so that the reflected shock would not exactly follow the design line. Perhaps an additional adjustment with an internal MHD or other control system would be required.

Details of charged species and vibrational temperature profiles in the computed MHD case are shown in Fig. 11. As seen in the figure, inside the MHD region with electron beam ionization, electron density is of the order of 10^{12} cm^{-3} , controlled by beam-induced ionization and electron-ion recombination. Attachment is insignificant, and the negative ion density is small. Downstream of the beam-ionized MHD region, electrons disappear almost immediately, but the wake of about $5 \times 10^8 \text{ cm}^{-3}$ negative ions persists and enters the inlet. Vibrational temperature (Fig. 11) does exceed the gas temperature (Fig. 10), but the degree of nonequilibrium and the enthalpy content of the vibrational mode are not high.

At Mach 10, $h=33 \text{ km}$ (design regime $M=6$, $h=26 \text{ km}$) (Fig. 12a, b), return of the shocks back to the cowl lip requires, with the same electron beam current density and energy and the same maximum B field, an adjustment to the length and location of the MHD region compared with that in the Mach 8 case. The MHD region is now positioned at $4 \text{ m} \leq x \leq 12.25 \text{ m}$. Note that in principle a change of MHD region location and size can be achieved by controlling the electron beam profile, without moving or changing the magnets. In Fig. 13, electron beam energy at the injection point is plotted versus distance along the MHD generator region in the cases of Fig. 10, 11, and 12, with $L_R = 2.3 \text{ m} = \text{const}$.

Table 1 lists some important parameters in the computed cases at the inlet entrance cross section (at the location corresponding to the corner at the end of the last ramp): mass (\dot{m}) and total enthalpy flow rate (\dot{H}) into the inlet, and averaged over the inlet cross section compression ratio, total pressure recovery coefficient, translational temperature, and mass capture. As seen in the Table, MHD operation is accompanied by substantial losses of total pressure. Table 2 lists MHD generator parameters: extracted power, P_{MHD} , electron beam input power, P_b , power of the $\vec{j} \times \vec{B}$ force, $P_{j \times B}$, Joule dissipation rate, P_j , the difference between the MHD-generated electric power and the beam power, $(P_{MHD} - P_b)$, and enthalpy extraction ratio (i.e., the MHD-generated electric power as a percentage of the total enthalpy entering the inlet per unit time), χ .

The enthalpy extraction ratio in both MHD cases is about 2-4%. The power cost of ionization is quite low compared with other power budget components, including the generated electric power. Therefore, the ionizing beams can be powered by a fraction of generated power, and a substantial portion of that power can be used for other purposes. The losses of total pressure seen in Table 1 are due to entropy-generating Joule dissipation.

All the computed cases were inviscid. We have performed a preliminary uncoupled estimate of the boundary layers for design Mach 6, $h=26 \text{ km}$ and off-design Mach 8, $h=30 \text{ km}$ cases with and without the MHD at $x=10 \text{ m}$ downstream from the nose. The boundary layer was modeled as that for viscous flow along the flat plate, using the steady state core flow profiles of pressure, velocity, temperature and current density (in the MHD case) computed

with the inviscid model as boundary conditions. In the MHD case, the $\vec{j} \times \vec{B}$ body force acting on the flow in the upstream direction, $f = -|j_y(x)B_z|\cos\theta$, was included in the momentum equation, and power extraction, $-|j_y(x)u(x,z)B_z|k\cos\theta$ – in the energy equation. Here $k = 0.5$ is the load factor, $u(x,z)$ is the flow velocity in the boundary layer, and $\theta = 10^\circ$ is the ramp angle. The wall temperature was assumed to be $T_{\text{wall}} = 600$ K. The boundary layer structure was computed with of the standard set of equations for steady-state compressible turbulent flat-plate flow¹⁸ developed by Cebeci and Smith.¹⁹ The results are shown in Fig. 14 and Table 3. In Fig. 14 and Table 3, δ_{dis} is the displacement thickness, δ_u is the boundary layer thickness corresponding to the velocity of 0.99 freestream velocity, and δ_T is the thermal boundary layer thickness defined as the distance from the wall where static temperature is 1.01 of its freestream value.

b. MHD control at $M < M_{\text{design}}$: accelerator regime

Consider the scenario when the inlet and the forebody are designed for shock-on-lip condition at a high Mach number, and flow spillage occurs when flying at lower Mach numbers (Fig. 3). The task of a plasma or MHD device is to increase the mass capture.

The specific design we consider is SOL at Mach 10, $h = 33$ km, as shown in Fig. 15 (Case 1 in Table 4). At off-design $M = 6$, $h = 26$ km, spillage occurs (Fig. 16 and Case 2 in Table 4). The first method of mass capture increase is to use an on-ramp MHD accelerator (Fig. 5). Presumably, the accelerator would increase the compression ratio and mass capture. Figs. 17 and 18 show results in 2 accelerator cases (Cases 3 and 4 in Table 4). In the first one (Case 3), the magnetic field profile was identical to that in the MHD generator case, and ionization by electron beams was realistic with finite relaxation length $L_R = 2.9$ m and Gaussian power deposition profile (Fig. 17). In the second, ideal, case (Case 4 in Table 4), both ionization profile and magnetic field profile were uniform across a semi-infinite slab (Fig. 18). The load factor in both cases was $k = 1.15$. (Calculations with other values of k give qualitatively similar results).

Results in both cases show that the MHD accelerator increases the flow velocity, but due to heating, local Mach numbers decrease. Also, because of heating, mass capture and total pressure actually decrease. Thus, the use of MHD accelerator is only detrimental. Table 4 lists the key parameters in all the cases with geometry designed for $M = 10$.

c. MHD control at $M < M_{\text{design}}$: generator regime

As suggested recently, mass capture can be increased by an on-ramp MHD generator with a magnetic field that has components both parallel and orthogonal to the flow.⁵ Figs. 19-21 illustrate the results of our computations for three versions of such a device for $M = 6$, $h = 26$ km, off-design regime (the design regime is $M = 10$, $h = 33$ km). The key computed parameters are listed in Table 4 as Cases 5, 6, and 7. For all three versions, the MHD region was placed between $x = 22.3$ m and $x = 23.3$ m, the magnetic field components were $B_x = B_z = -2$ T (the negative sign, of course, means that the component's direction is opposite to that of the coordinate axis), and the load factor was $k = 0.5$.

In the first version (Fig. 19), an electron beam power deposition of $Q_b = 10^6$ W/m³ was assumed uniform through a "slab" region that extends vertically down from the ramp and does not reach the cowl level. In the second version (Fig. 20), a Gaussian distribution of beam power across the "slab" in the vertical direction was assumed. The results, as seen in Table 4, show that both versions give results that are close to each other and quite negative: mass capture, total pressure coefficient, and compression ratio all decrease. The negative performance is due to Joule heating and power introduced by the beam, resulting in entropy generation and thermal expansion. The positive effect of the compressing force $(\vec{j} \times \vec{B})_z = -j_y B_x$ is too weak to overcome the thermal expansion; no less important is that this force does not act on the gas below the ionized "slab".

In the third version of MHD generator with flow compression, a uniform electron beam power deposition of $Q_b=10^6$ W/m³ was assumed through a "slab" region that extends vertically down to infinity (Fig. 21). In this case, mass capture and compression ratio did increase slightly, although stagnation pressure decreases in about the same proportion as the mass capture increase. Note that practical realization of this version would be very problematic. First, a strong and reasonably uniform magnetic field has to extend several meters down from the ramp. Second, electron beams can reach the intended MHD region only along magnetic field lines, so that configuration like that depicted in Fig. 22 should be created. In this configuration, ionization and heat addition would also occur outside the intended "slab", resulting in stagnation pressure and mass capture losses. Third, electric current collection may be problematic.

As is clear from comparison of the modestly successful third version (Fig. 21) that has a very long "slab" MHD region with the versions of Figs. 19 and 20, where MHD regions are shorter, most of the ionized region in the "slab" in Fig. 21 is useless or even detrimental for the task of mass capture increase. It is only the combined effect of heating and $(\vec{j} \times \vec{B})_x = -j_y B_x$ force on the gas region at the cowl lip level and below it that deflects streamlines and increases mass capture.

IV. . Mass capture increase by off-body energy addition: a virtual cowl

We propose a new method of decreasing flow spillage and increasing mass capture at Mach numbers lower than the design one. The essence of the method is to create a heated region upstream of and somewhat below the cowl lip (Figs. 23 and 24). The incoming flow would be deflected by the elevated-temperature and/or elevated pressure region, causing an increased mass flow into the inlet. In other words, a thermal funnel, or a virtual cowl, would be used to increase mass capture.

The heated region may be generated by supplying microwave or RF energy to a volume pre-ionized by a focused laser or electron beam. Other possible means include plasma or hot-air jets, and external combustion. Both off-body (Fig. 23) and on-lip (Fig. 24) variants can be suggested.

An advantage of this method of inlet control as compared with the MHD accelerator method is its relative simplicity and the absence of problems with electron beams and their transmission windows, massive superconducting magnets, high-voltage hardware, and interelectrode arcing due to high Hall fields that characterize hypersonic MHD devices in cold air.⁷⁻¹³ Another advantage of the new method is that the air entering the inlet would have experienced little or no Joule heating, thus minimizing stagnation pressure losses. The virtual cowl method can have additional advantages of increased lift and decreased drag.

Preliminary results of two-dimensional inviscid modeling of mass capture increase by off-body heat addition are shown on the Fig. 25 and listed in Table 4. The freestream conditions were those at Mach 6, $h=26$ km, and the geometry corresponded to shock-on-lip condition at Mach 10. A heat source was placed upstream and below the inlet. The heating was distributed in a Gaussian stretched ellipsoidal shape (Fig. 25). The key parameters are listed in Table 4 for 2 cases: heat addition rate of $Q=5$ MW and $Q=10$ MW per meter in the transverse direction (these power levels are equal to ~1% and ~2% of total enthalpy entering the inlet in 1 second).

Mass capture in the two cases increases by 4-8%. Interestingly, both total pressure recovery and compression ratio also improve. The reason for such favorable behavior of total pressure is that the angle at which gas enters the inlet becomes shallower due to interaction between the deflected flow and the weak shock wave produced by the heat source, on one side, and the ramp compression shocks and the flow downstream of the second ramp on the other side.

In the computed cases, the location, shape, and power of the heat addition were not optimized. These issues should be investigated in future work.

V. Conclusions

Among the various scenarios of scramjet inlet control investigated in this paper, two appear attractive. One is the on-ramp MHD generator that would bring the shocks back on lip at Mach numbers greater than the design one. Despite the weight of magnets and other components, overall weight savings may in principle result from avoiding a mechanical system of variable geometry inlet, and from shorter forebody designed for lower Mach numbers. The MHD device is self-powered, with ionization cost substantially lower than the generated power. Two serious issues associated with this method are: electron beam transmission windows, and losses of stagnation pressure due to Joule heating. Note that the stagnation pressure losses can be partially compensated with energy bypass: the generated electricity can be used for MHD acceleration of the flow in the combustor or downstream of it.

Another inlet control method that appears interesting is the virtual cowl concept: mass capture increase at Mach numbers lower than the design one by off-body energy addition. While working with fixed-geometry inlet and avoiding difficulties with electron beams, magnets, and electrodes associated with MHD devices, the virtual cowl method not only increases mass capture, but it also increases total and static pressure at the inlet. The virtual cowl method does require power input. Although the required power may be only a small fraction of the enthalpy flux in the inlet, the absolute power, as typical for hypersonic regime, can be high. One scenario that can be explored in future work is extraction of a small fraction of flow enthalpy with an MHD generator downstream of the combustor and using this power to increase mass capture and compression at the inlet by virtual cowl.

REFERENCES

- ¹ Vatazhin, A., Kopchenov, V., and Gouskov, O., "Some Estimations of Possibility to Use the MHD Control for Hypersonic Flow Deceleration," AIAA Paper 99-4972, 1999.
- ² Kopchenov, V., Vatazhin, A., and Gouskov, O., "Estimation of Possibility of Use of MHD Control in Scramjet," AIAA Paper 99-4971, 1999.
- ³ Vatazhin, A., Kopchenov, V., and Gouskov, O., "Numerical Investigation of Hypersonic Inlets Control by Magnetic Field," *The 2nd Workshop on Magneto- and Plasma Aerodynamics in Aerospace Applications*, Moscow, 5-7 April 2000, pp. 56-63.
- ⁴ Brichkin, D.I., Kuranov, A.L., and Sheikin, E.G., "The Potentialities of MHD Control for Improving Scramjet Performance," AIAA Paper 99-4969, 1999.
- ⁵ Kuranov, A.L., and Sheikin, E.G., "MHD Control on Hypersonic Aircraft under AJAX Concept: Possibilities of MHD Generator," AIAA Paper 2002-0490, 2002.
- ⁶ Bityurin, V.A., Klimov, A.I., Leonov, S.B., Bocharov, A.N., and Lineberry, J.T., "Assessment of a Concept of Advanced Flow/Flight Control for Hypersonic Flights in Atmosphere," AIAA Paper 99-4820, 1999.
- ⁷ Macheret, S. O., Shneider, M. N., and Miles, R. B., "External Supersonic Flow and Scramjet Inlet Control by MHD with Electron Beam Ionization," AIAA Paper 2001-0492, 2001.
- ⁸ Macheret, S. O., Shneider, M. N., and Miles, R. B., "Magnetohydrodynamic Control of Hypersonic Flow and Scramjet Inlets Using Electron Beam Ionization," *AIAA Journal*, Vol. 40, No. 1, 2002, pp. 74-81.
- ⁹ Macheret, S. O., Shneider, M. N., Miles, R. B., Lipinski, R. J., and Nelson, G. L., "MHD Acceleration of Supersonic Air Flows Using Electron Beam-Enhanced Conductivity," AIAA Paper 98-2922, 1998.
- ¹⁰ Macheret, S. O., Shneider, M. N., and Miles, R. B., "Electron Beam Generated Plasmas in Hypersonic MHD Channels," AIAA Paper 99-3635, 1999.
- ¹¹ Macheret, S. O., Shneider, M. N., and Miles, R. B., "MHD Power Extraction from Cold Hypersonic Air Flow with External Ionizers," AIAA Paper 99-4800, 1999.
- ¹² Macheret, S. O., Shneider, M. N., and Miles, R. B., "MHD Power Extraction from Cold Hypersonic Air Flow with External Ionizers," *Journal of Propulsion and Power*, Vol. 18, No. 2, 2002, pp. 424-431.
- ¹³ Macheret, S. O., Shneider, M. N., Miles, R. B., and Lipinski, R. J., "Electron Beam Generated Plasmas in Hypersonic Magnetohydrodynamic Channels," *AIAA Journal*, 2001, Vol. 39, No. 6, pp. 1127-1136.
- ¹⁴ Raizer, Y.P., and Shneider, M.N., "Simplified Kinetic Equation for Electrons in Nonuniform Fields of Arbitrary Strength in Connection with the Cathode Sheath of a Glow Discharge," *Soviet Journal of Plasma Physics*, Vol. 15, No. 3, 1989, pp. 184-189.

- ¹⁵ Berger, M.J., and Seltzer, S.M., "Tables of Energy Losses and Ranges of Electrons and Positrons," NASA SP-3012, 1964.
- ¹⁶ Bychkov, Y.I., Korolev, Y.D., and Mesyats, G.A., *Injection Gaseous Electronics (Inzheksionnaia Gazovaia Elektronika)*, Nauka, Moscow, 1982, Chap. 2 (in Russian).
- ¹⁷ Bychkov, V.L., Vasilev, M.N., and Zuev, A.P., "An Experimental and Theoretical Investigation of the Properties of Surface Electron-Beam Nitrogen Plasma," *High Temperature*, Vol. 32, No. 3, 1994, pp. 303-312.
- ¹⁸ Anderson, D.A., Tannehill, J.C., and Pletcher, R., *Computational Fluid Mechanics and Heat Transfer*, Hemisphere, New York, 1984, Chap. 5.
- ¹⁹ Cebeci, T., and Smith, A.M.O., *Analysis of Turbulent Boundary Layers*, Academic Press, New York, 1974, Chaps. 5, 6, and 9.

Table 1. Principal inlet parameters in design and off-design cases with and without MHD generator control. Design conditions: $M=6$, $h=26$ km, 0.546 atm freestream dynamic pressure. Off-design conditions: $M=8$, $h=30$ km, 0.53 atm freestream dynamic pressure, and $M=10$, $h=33$ km, 0.527 atm freestream dynamic pressure. \bar{p} , \bar{p}_t , and \bar{T} are the pressure, total pressure and translational temperature, averaged over the inlet entrance cross section.

Case	\dot{m} , kg/(m ² s)	\dot{H} , MW/m	Compression ratio: \bar{p}/p_∞	Total pressure recovery: $\bar{p}_t/p_{t,\infty}$	\bar{T} , K	Mass capture
M=6, h=26 km design	395.1	721	49.8	0.589	785	1
M=8, h=30 km no MHD	284.4	883	64.9	0.432	916.8	1
M=8, h=30 km with MHD	284.4	872	75.6	0.223	1235	1
M=10, h=33 km no MHD	224.6	1070	81.6	0.305	1128	1
M=10, h=33 km with MHD	224.6	1030	108.7	0.098	1832	1

Table 2. MHD generator characteristics for the cases of Table 1. Electron beam current density is $j_b = 1$ mA/cm², the beam relaxation length is $L_R = 2.3$ m, and the MHD load factor is $k=0.5$.

Case	P_{MHD} , MW/m	P_b , MW/m	$P_{j \times B}$, MW/m	P_J , MW/m	$\chi = P_{MHD}/\dot{H}$, %
M=8, h=30 km	20.9	5.42	41.9	16.8	2.4
M=10, h=33 km	42.9	4.43	85.8	29.3	4.16

Table 3. Estimated displacement thickness, 99% velocity thickness, and thermal boundary layer thickness in Mach 6 design and Mach 8 off-design (with and without MHD) cases.

Results at $x=10$ m downstream from vehicle nose	δ_{dis} , cm	δ_T , cm	δ_u , cm
M=6; h=26 km; design	5.08	12.0	7.01
M=8; h=30 km; no MHD	6.08	13.42	7.674
M=8; h=30 km; with MHD	5.71	13.46	10.4

Table 4. Performance of various methods of inlet control at Mach number lower than the design one. Design conditions: $M=10$, $h=33$ km. All other, off-design, regimes: $M=6$, $h=26$ km. \bar{p} , \bar{p}_t , and \bar{T} are the static pressure, total pressure, and translational temperature, averaged over the inlet cross section; Q is the heat addition rate per unit length in the transverse direction, with heat source located upstream and below the cowl lip

Case number	Case description	\dot{m} , kg/(m's)	\dot{H} , MW/m	Compression ratio: \bar{p}/p_∞	Total pressure recovery: $\bar{p}_t/p_{t,\infty}$	\bar{T} , K	Mass capture
1	M=10, h=33 km design	261	1270	131.6	0.31	1245	1
2	no MHD; $Q=0$	274.9	504	46.1	0.607	758.6	0.585
3	MHD accelerator, "short slab" Gaussian ionization profile	237.9	458	43.0	0.494	835.4	0.497
4	MHD accelerator, "infinite slab" uniform ionization	264.9	502	47.53	0.549	818	0.554
5	MHD generator, "infinite slab" uniform ionization	283.9	519	48.81	0.592	773.2	0.593
6	MHD generator, "short slab" uniform ionization profile	266.4	487	45.1	0.578	763	0.557
7	MHD generator, "short slab" Gaussian ionization profile	266.2	487	45.2	0.572	769	0.556
8	Virtual cowl, $Q=5$ MW/m	289.4	530	47.9	0.632	760.9	0.605
9	Virtual cowl, $Q=10$ MW/m	302.5	554	50.2	0.642	772	0.632

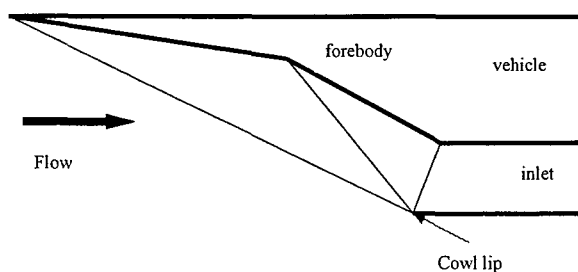


Fig. 1. Design forebody and inlet geometry with shock-on-lip condition.

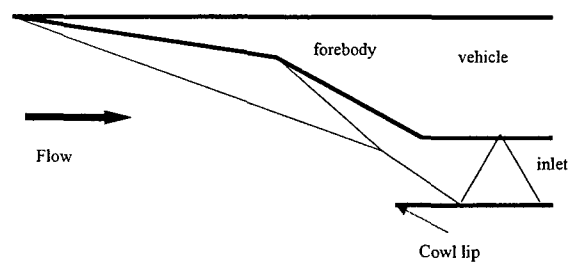


Fig. 2. Flow and shock geometry at Mach number higher than the design one, with no MHD control.

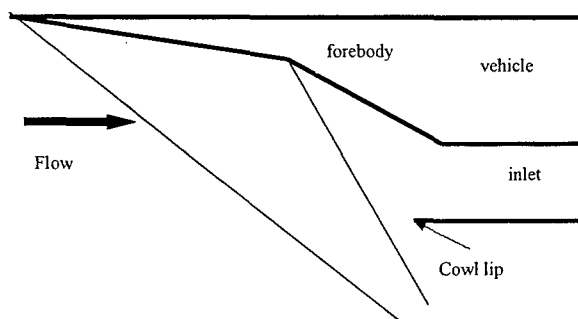


Fig. 3. Flow and shock geometry at Mach number lower than the design one, with no MHD control.

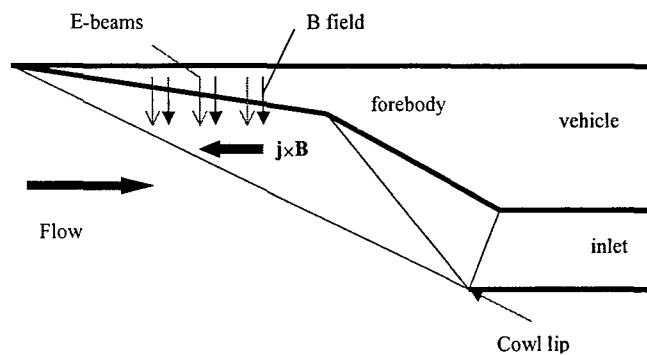


Fig. 4. Flow and shock geometry at Mach number higher than the design one, with MHD generator control.

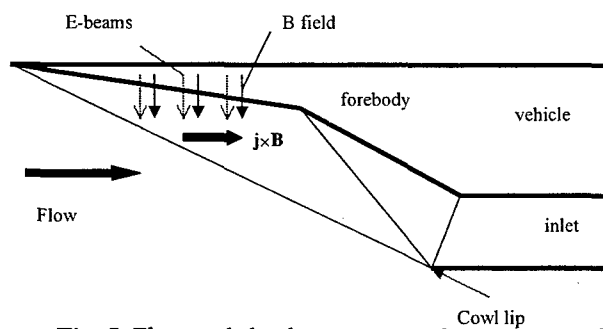


Fig. 5. Flow and shock geometry at Mach number lower than the design one, with MHD accelerator control.

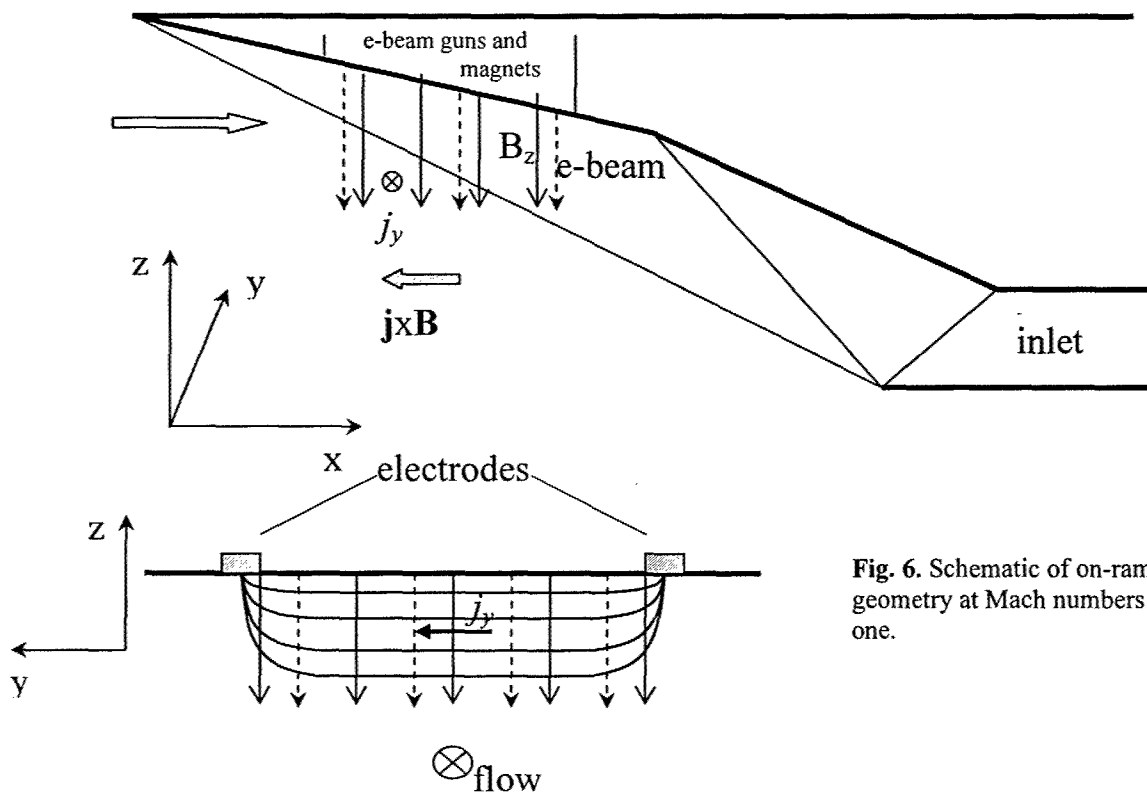


Fig. 6. Schematic of on-ramp MHD generator control geometry at Mach numbers greater than the design one.

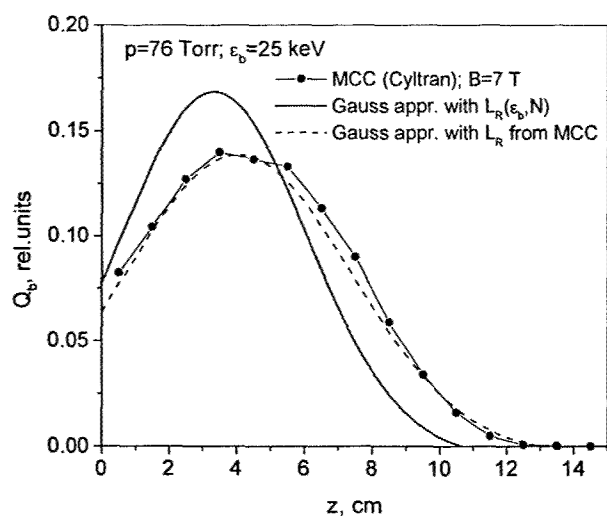


Fig. 7. Comparison of electron beam power deposition profiles predicted by Monte-Carlo calculations (MCC) with CYLTRAN, Gaussian approximation with empirical relaxation length $L_R(\epsilon_b, N)$,¹⁷ and Gaussian approximation with the $L_R(\epsilon_b, N)$ given by the MCC.

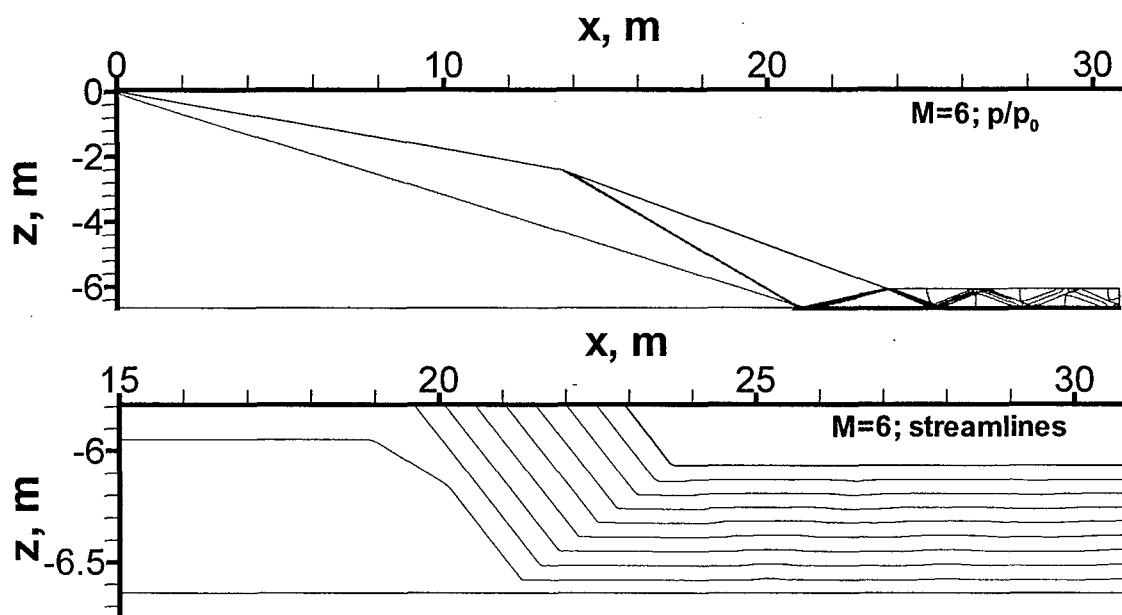


Fig. 8. Shock pattern (upper plot) and flow streamlines (lower plot) in the $M=6$, $h=26$ km, design regime.

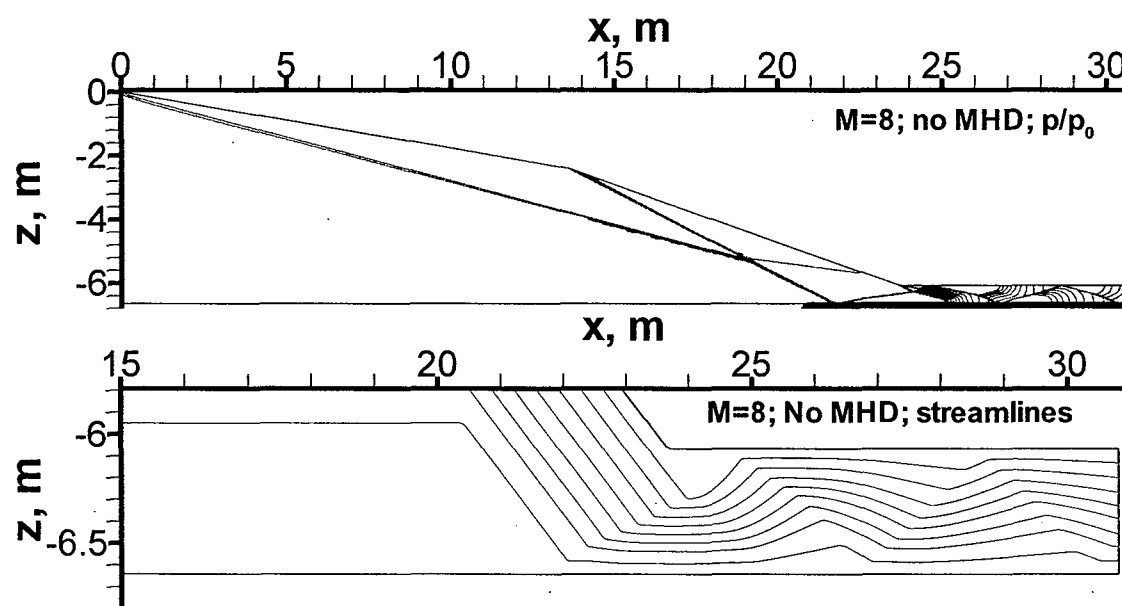


Fig. 9. Shock pattern (upper plot) and flow streamlines (lower plot) in $M=8$, $h=30$ km, off-design regime, without MHD control, for the geometry of Fig. 8.

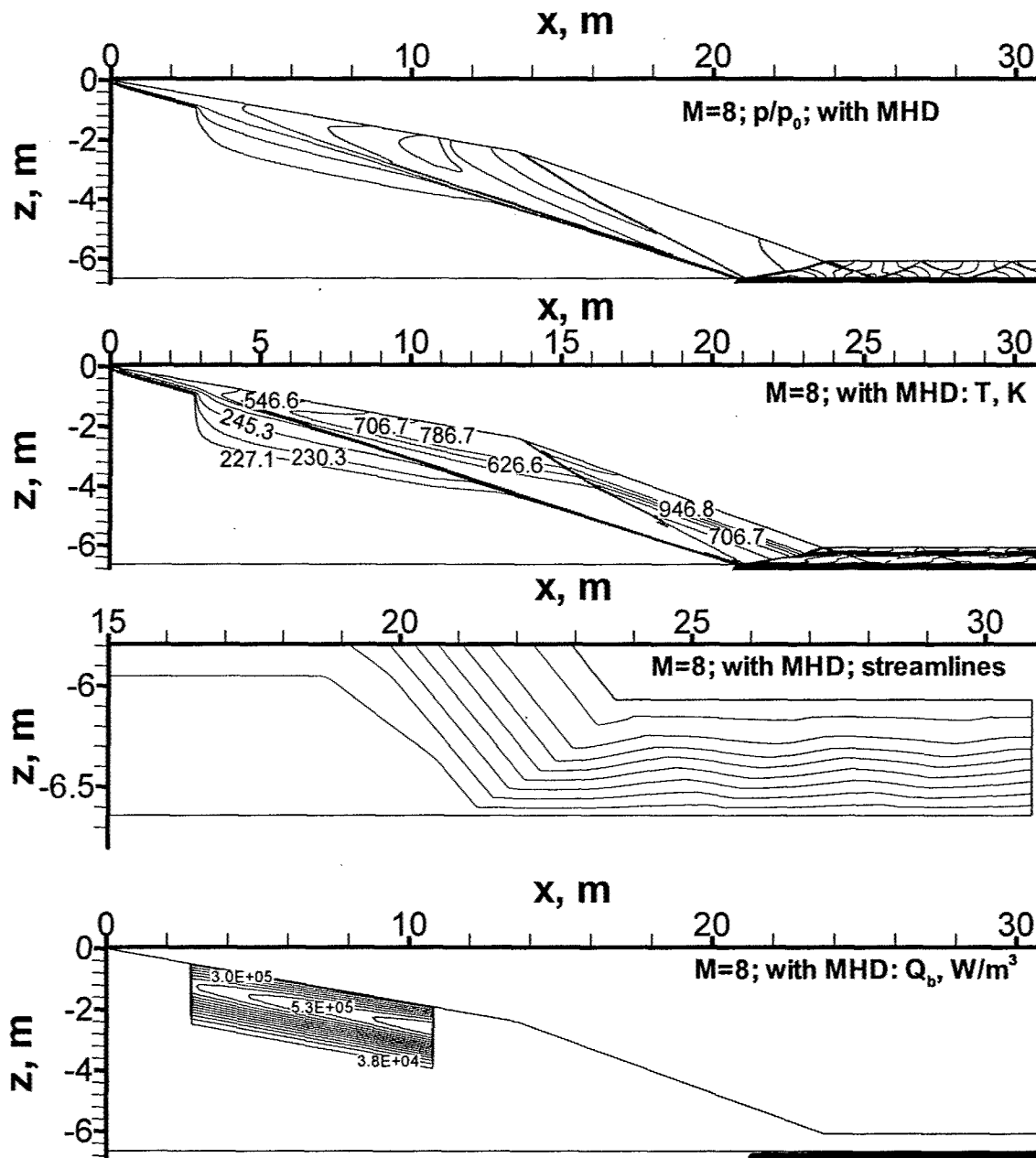


Fig. 10. Pressure contours, temperature contours, flow streamlines, and electron beam power deposition contours in Mach 8, $h=30$ km, case with MHD generator control, for the geometry of Fig. 8.

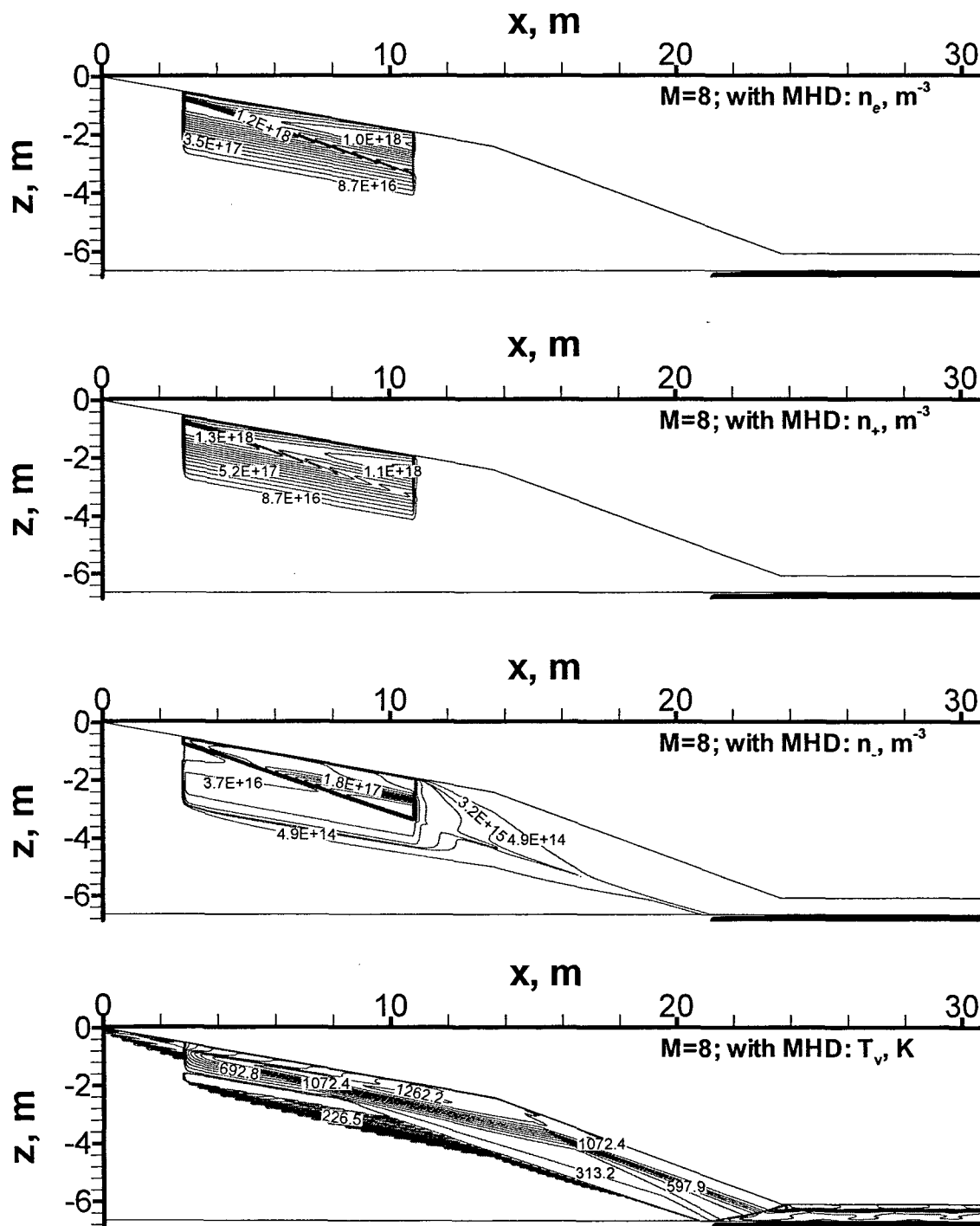


Fig. 11. Contour lines of number densities of electrons and positive and negative ions, and vibrational temperatures contour lines in Mach 8, $h=30$ km, case with MHD generator control, for the geometry of Fig. 8.

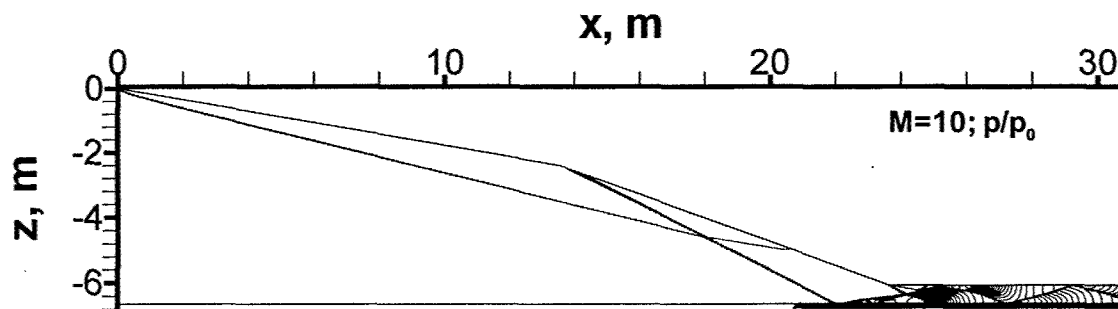


Fig. 12a. Pressure contours at Mach 10, $h=33$ km, without MHD control, for the geometry of Fig. 8.

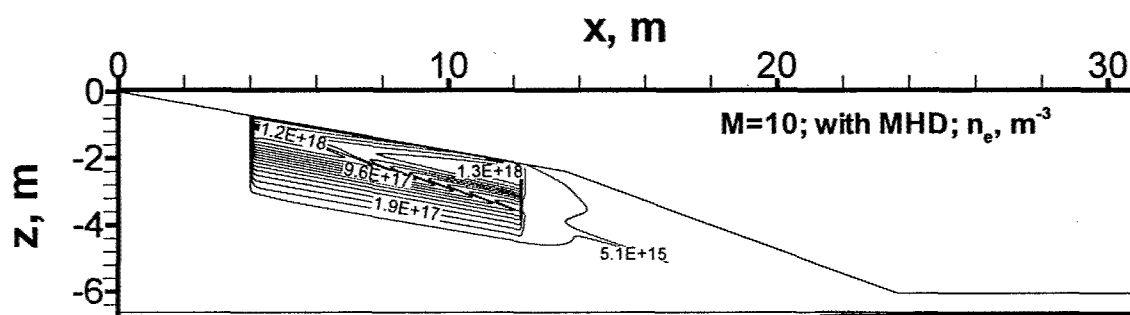
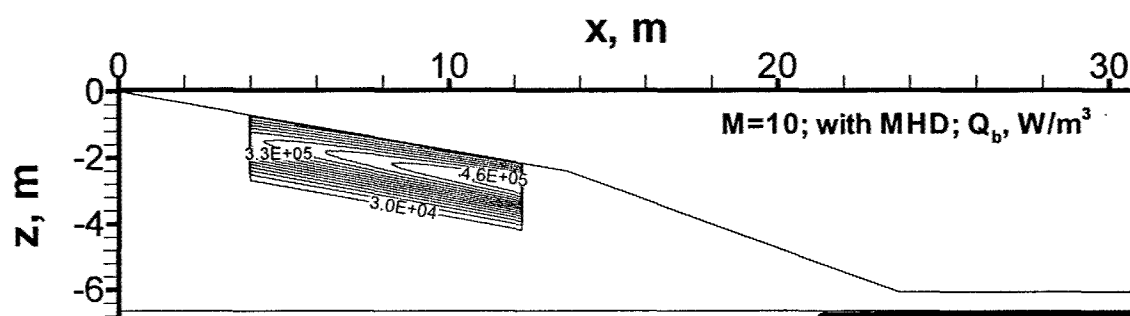
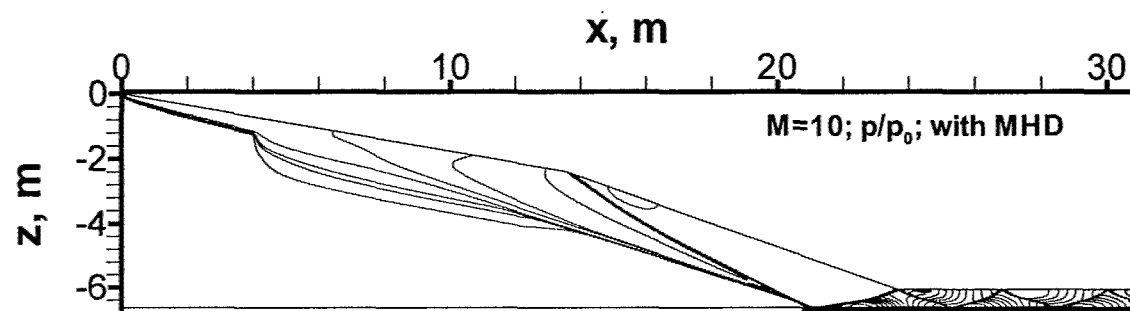


Fig. 12b. Contour lines of pressure, electron beam power deposition, and electron number density at Mach 10, $h=33$ km, with MHD generator control, for the geometry of Fig. 8.

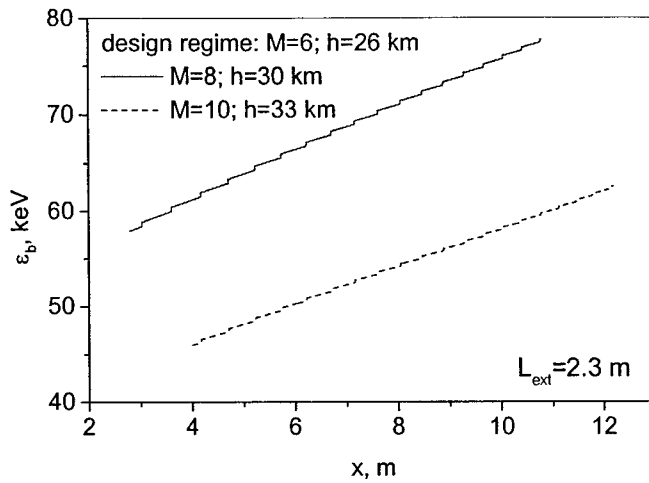


Fig. 13. Electron beam energy at the injection point versus coordinate along the MHD generator channel in the cases of Figs. 10 and 11 and Fig. 12, with $L_R = 2.3$ m = const.

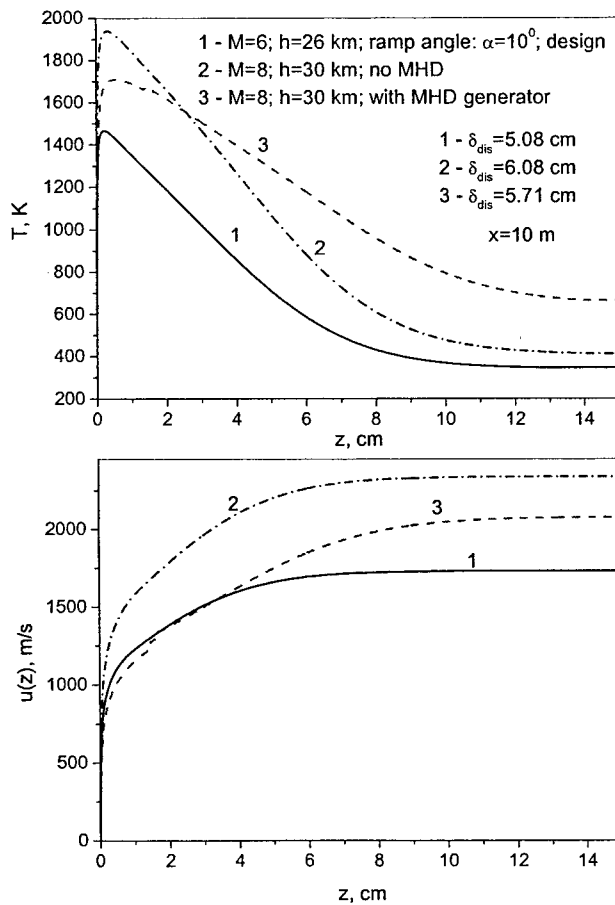


Fig. 14. Computed temperature and velocity profiles in the boundary layer at $x=10$ m downstream of the vehicle nose in design regime of Mach 6, $h=26$ km (the case of Fig. 8), and off-design regime $M=8$, $h=30$ km, without (the case of Fig. 9) and with MHD (the case of Figs. 10 and 11).

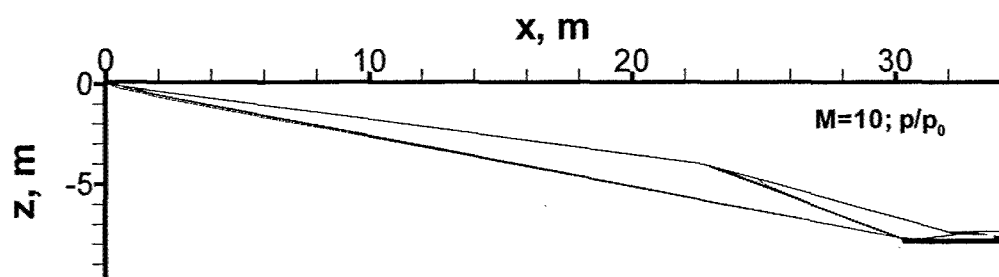


Fig. 15. Pressure contours at $M=10$, $h=33$ km, in the design regime, with shock-on-lip condition.

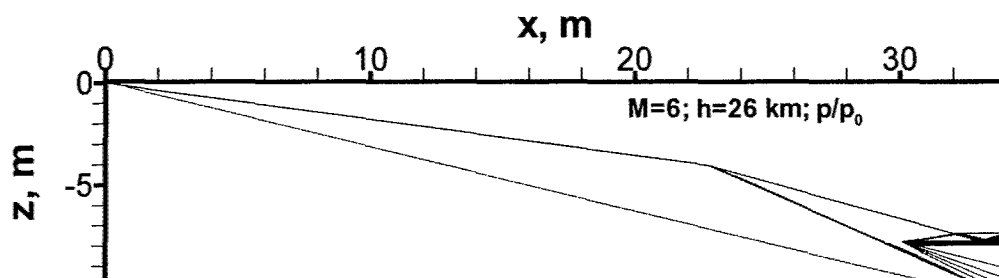


Fig. 16. Pressure contours at $M=6$, $h=26$ km, off-design regime for the geometry of Fig. 15.

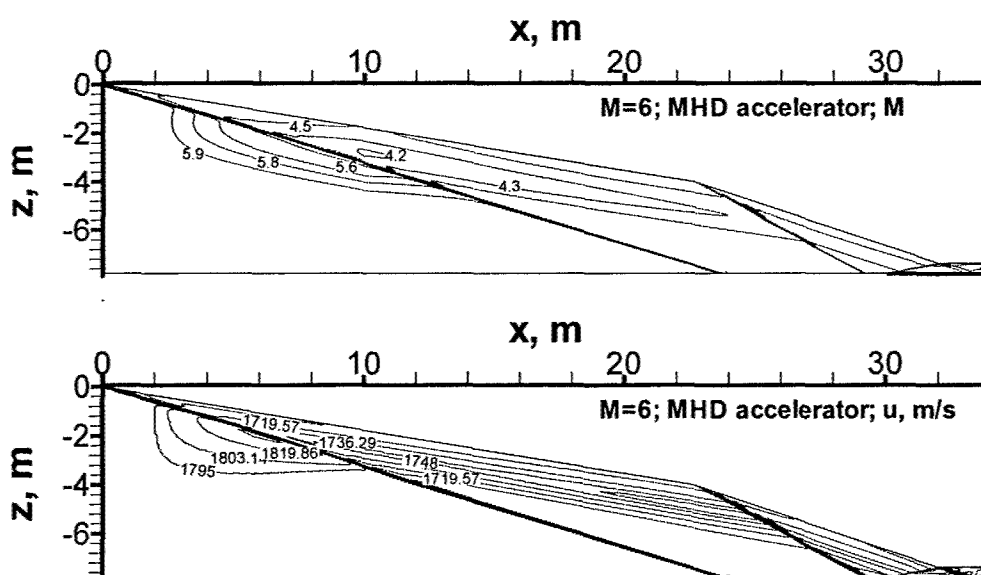


Fig. 17. Local Mach number and horizontal flow velocity contours in $M=6$, $h=26$ km, off-design regime (geometry of Fig. 15), with MHD accelerator parameters: $B=4$ T, $k=1.15$, and $L_R=2.9$ m.

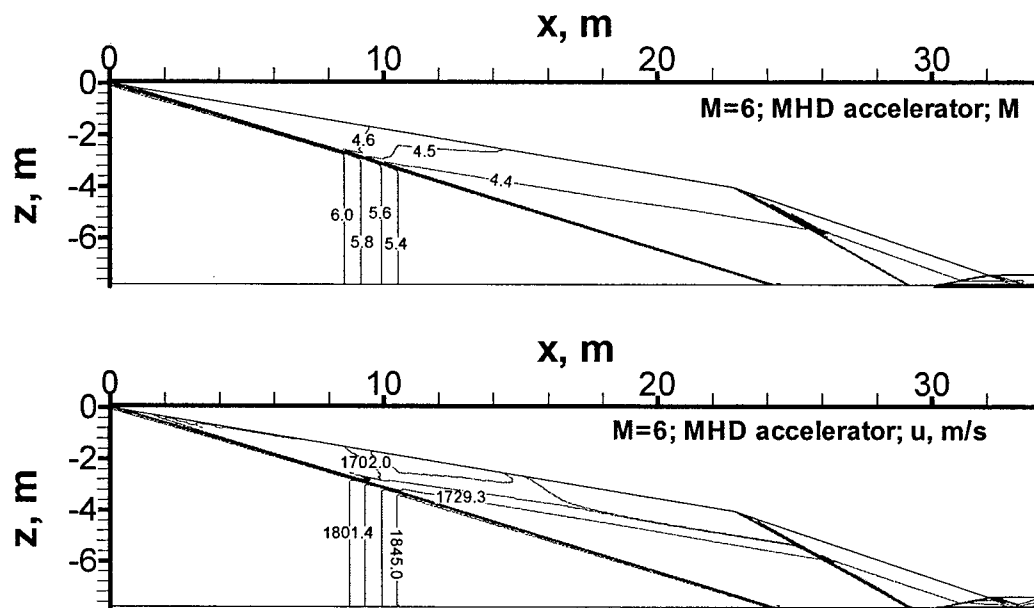


Fig. 18. Local Mach number and horizontal flow velocity contours in $M=6$, $h=26$ km, off-design regime (geometry of Fig. 15), with MHD accelerator at $B=4$ T, $k=1.15$, and with uniform electron beam power deposition of $Q_b=10^6$ W/m³ in semi-infinite "slab" located from $x=8.5$ to $x=10.5$ m.

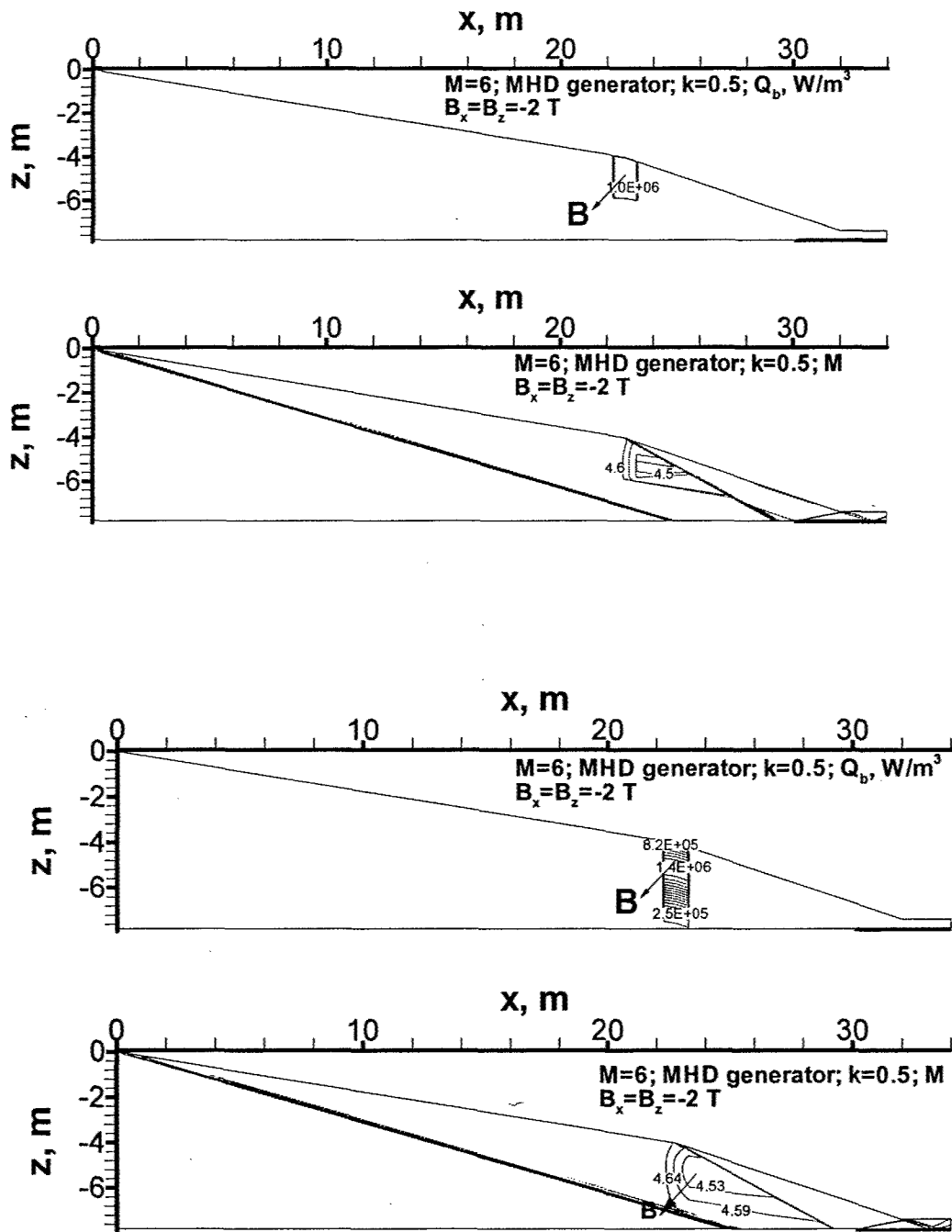


Fig. 19. Electron beam power deposition and local Mach number contours in MHD generator with flow compression case $M=6$, $h=26$ km, off-design regime (geometry of Fig. 15). Load factor $k=0.5$; magnetic field components $B_x=B_z=-2$ T. Beam power deposition of $Q_b=10^6 \text{ W/m}^3$ is uniform in "short slab" from $x=22.3$ up to $x=23.3$ m.

Fig. 20. Electron beam power deposition and local Mach number contours in MHD generator with flow compression case $M=6$, $h=26$ km, off-design regime (geometry of Fig. 15). Load factor $k=0.5$; magnetic field components $B_x=B_z=-2$ T. Beam power deposition along z is Gaussian in "short slab" from $x=22.3$ up to $x=23.3$ m.

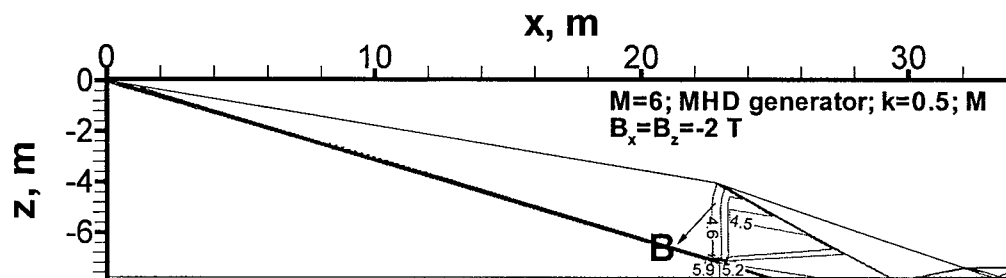


Fig. 21. Local Mach number contours in MHD generator with flow compression case $M=6$, $h=26$ km, off-design regime (geometry of Fig. 15). Load factor $k=0.5$; magnetic field components $B_x=B_z=-2$ T. Beam power deposition of $Q_b=10^6$ W/m³ is uniform in semi-infinite "slab" from $x=22.3$ up to $x=23.3$ m.

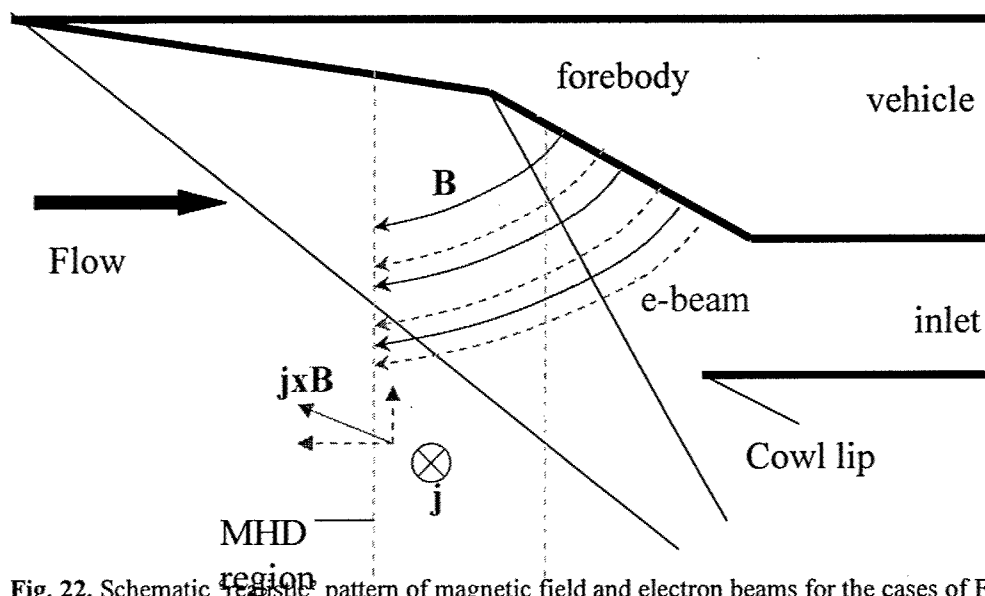


Fig. 22. Schematic pattern of magnetic field and electron beams for the cases of Figs. 19-21.

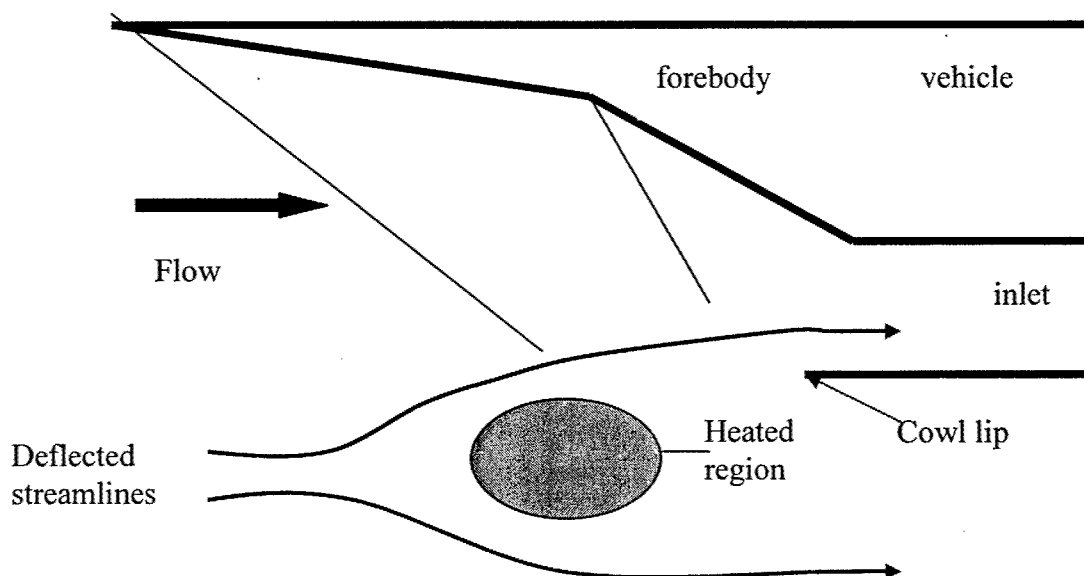


Fig. 23. Schematic diagram of the virtual cowl concept: off-body heat addition increases mass capture.

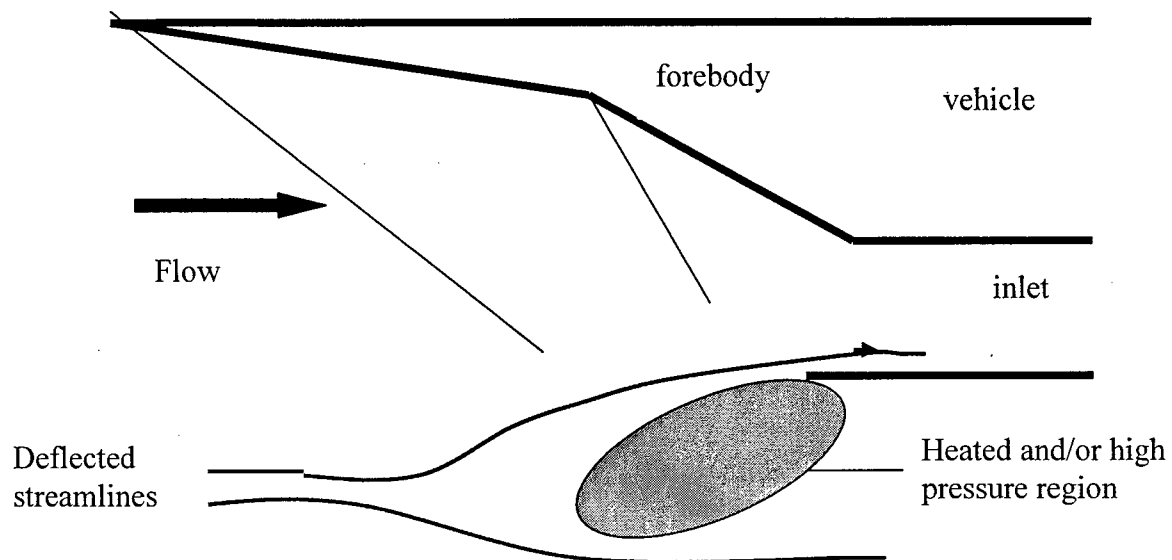


Fig. 24. Schematic diagram of the virtual cowl concept: heat addition at the cowl lip increases mass capture.

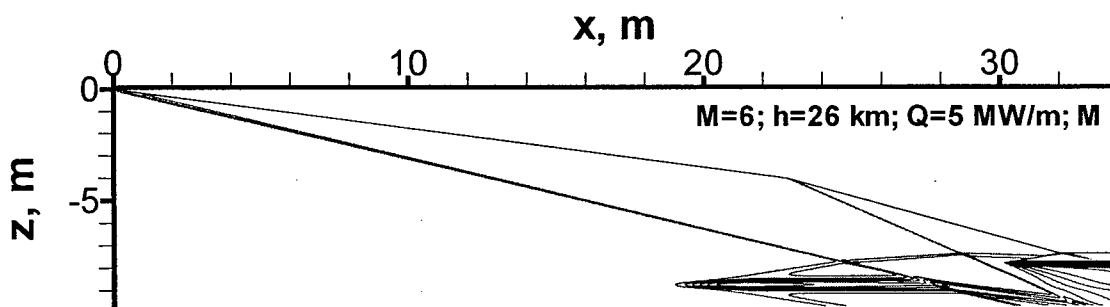


Fig. 25. Mach number contour lines in virtual cowl case. Freestream conditions: Mach 6, $h=26 \text{ km}$. Geometry is that of Fig. 15. Heat addition rate of $Q=5 \text{ MW}$ per 1 meter in the transverse direction is distributed as a stretched ellipsoidal Gaussian function of (x, z) .

CHAPTER 4

DEVELOPMENT OF A SUPERSONIC PLASMA WIND TUNNEL

ABSTRACT

The study of controlled plasma discharges in supersonic air has become an area of increasing interest. These discharges may be used for flow control, drag reduction, combustion initiation and stabilization, as well as for power extraction and plasma shielding applications. In order to study the formation of such discharges and their impact on the flow, proper testing facilities are required. This chapter details the work done in the design, construction, and testing of a supersonic plasma wind tunnel.

I. Introduction

Over the past decade, research into the interaction of plasma with a gas flow has yielded some results which have not yet been fully explained¹⁻⁵. For example, changes in shock wave strength and shock standoff distance caused by the presence of plasma have been observed experimentally, but cannot be fully explained with present theoretical models. A better understanding of these interactions, as well as the potential applications for the controlled modification of shock structure, motivates the present work.

II. Wind Tunnel Design

The basic configuration of the wind tunnel is controlled by the need to create a plasma in the region of supersonic flow. A schematic of the facility is shown in Figure 1 below.

A plasma is created with a 50 kW, 1 ms pulse of microwave radiation at 2.45 GHz, which induces electric breakdown of the air in the region of supersonic flow. Microwaves are introduced into the plenum through an EM window mounted over a port on one wall. The direction of propagation is then turned 90° by an aluminum reflector, so the microwaves travel coaxially with the flow through the plenum chamber and nozzle section. The aluminum reflector is made with a dense array of 1/4" holes in it to allow passage of air while simultaneously reflecting the microwaves. The breakdown location is controlled by two factors: a reduced static pressure in the high speed section, and an increased field intensity downstream of the throat.

Microwave discharges occur more easily at low pressure due to the reduced collision frequency. Thus, introducing microwaves through the plenum where the air is at high pressure avoids the risk of parasitic breakdown near the window housing and window surface.

As shown in Figure 1, the waveguide walls are tapered to create an enhancement of the electric field as the microwaves propagate downstream. The nozzle contours within the taper are made of dielectric material so as to transmit the microwave radiation. The taper continues down to and slightly beyond the cutoff dimension for radiation at 2.45 GHz. This generates a reflection, reversing the propagation direction as the microwaves reach the cutoff point. This taper is used as one end of a microwave resonator. The other end of the resonator is formed by a triple stub tuner on the generator side of the entrance window. This arrangement allows for the build up of a standing wave in the wind tunnel. In order to provide a further field enhancement at the intended breakdown location, and to provide for spatial localization of the plasma, two 1 cm long metal pins are mounted opposite each other on the inside walls of the wind tunnel. The magnetron is protected from spurious reflections by a circulator and dummy load.

The flow of air proceeds from the plenum, through the nozzle, and into the 2"x2" test section. The air is then discharged into a vacuum tank. The nozzle is contoured to achieve Mach 3 flow in the test section. Flow conditions in the test section are 20 Torr static pressure, 110 K static temperature, and a Mach number of 3.

III. Microwave Field Distribution

The microwave field distribution was measured along the centerline of the wind tunnel from the reflector plate to the wind tunnel exit plane. For these measurements, the microwave field was generated

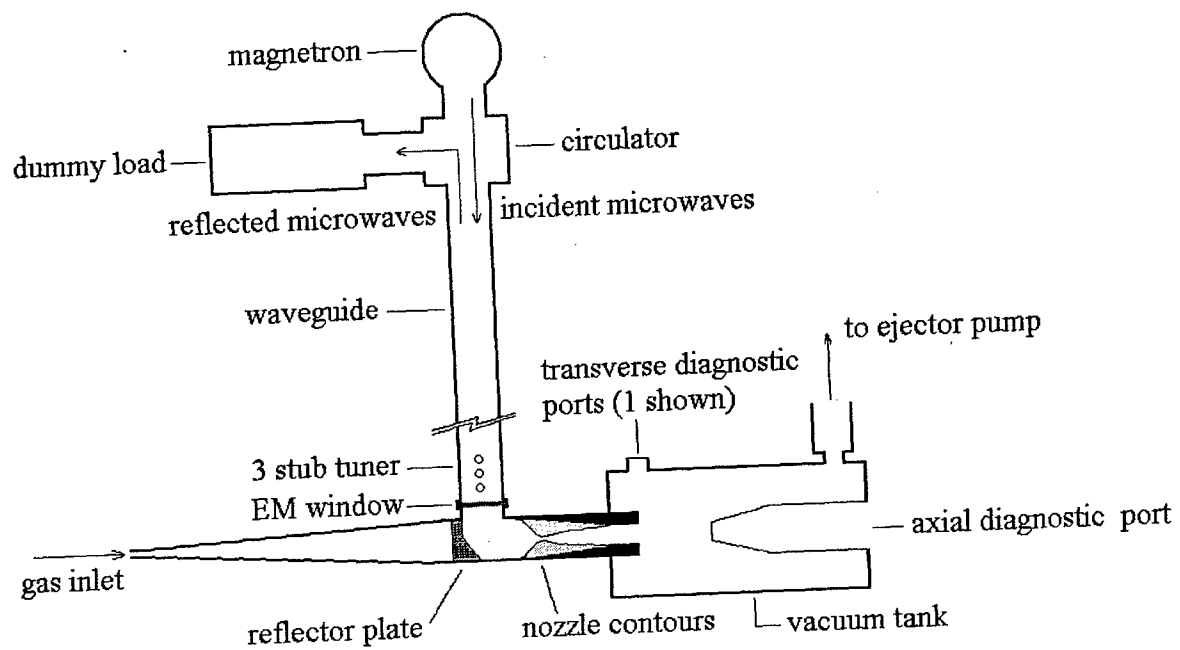


FIGURE 1: FACILITY SCHEMATIC

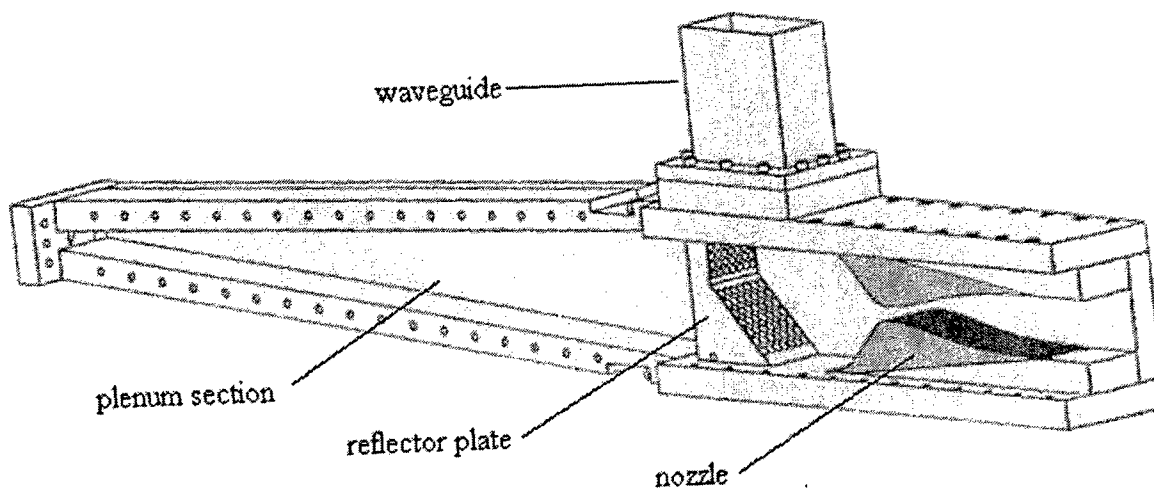


FIGURE 2: PLENUM AND NOZZLE CUTAWAY DRAWING

using a 100 mw source operating in a continuous mode at 2.45 GHz. This source was coupled into the wind tunnel with the same triple stub tuner and window arrangement used for the 50 kW, 1 ms pulse breakdown experiments. The measurements were made with a probe consisting of a 1 cm antenna protruding from a length of semi-rigid coaxial cable. This probe was introduced into the wind tunnel from the downstream end and traversed through the wind tunnel in increments. The 2.45 GHz signal obtained with the probe was attenuated and rectified with a crystal diode before being recorded on a digital oscilloscope. An average of several such traverse measurements is shown in Figure 3.

IV. Numerical Simulations

To complement the measurements described above, as well as to permit parametric studies of the effect of changes in the electrical properties of the wind tunnel, a commercial finite element code was used to simulate the electric field standing wave pattern.

The code used was the High Frequency Structure Simulator package from Hewlett Packard, which was run on a UNIX based workstation. The results of several case studies, including a comparison with the measurements described above, are presented in Figures 4 through 8.

In the above simulations, incident wave phase is chosen to show the standing wave pattern at its maximum intensity. For the cases shown in Figures 4 and 5 the region of highest field intensity remains localized at the same point throughout each cycle of the incident wave propagation. For the cases shown in Figures 6 and 7, due to the lossy dielectric, deviations from a perfect standing wave pattern occur. In particular, the region of highest field intensity changes dramatically as the incident wave goes through one cycle. The field can be seen to be strongly dependent on dielectric material properties, which has important implications for the generation of plasma inside the wind tunnel.

V. Breakdown Measurements

Using the G-10 nozzle breakdown can occur in either of two locations, depending upon conditions. Under static conditions below about 30 Torr, breakdown occurs upstream of the throat, slightly below the centerline of the wind tunnel. Above 30 Torr under static conditions breakdown occurs downstream of the throat at the intended location. These two positions correspond with the two peaks in field intensity in the simulation. Note that under flow conditions, with higher pressure upstream of the throat than downstream, the breakdown will also occur in the downstream location.

Breakdown in the wind tunnel was recorded with photodiodes and high speed photographic equipment. The pressure was chosen for the static case so as to match gas density with the flow conditions. Measurements of the plasma luminosity were made both with flow and under static conditions. In all cases the tests were performed in air with a microwave pulse duration of 1 ms. The results indicate the initiation of the plasma within 10 μ s after the start of the microwave pulse without flow, and within 20 μ s after the start of the pulse with flow. A brighter plasma was observed with flow than without flow, as shown in Figures 9 and 10.

The photographs shown in Figure 11 were made with a grated, intensified CCD camera. The view is through the axial diagnostic port shown in Figure 1, looking upstream through the wind tunnel. Images were taken of the plasma both with the wind tunnel running and under static conditions at 60 Torr and room temperature. The pressure was chosen for static conditions to match the density with the Mach 3 flow for comparison. In all cases the camera gate was maintained at 3 μ s. The images show the plasma generated while the wind tunnel was running to be brighter and more contracted than the plasma generated under static conditions. The location of the plasma within the tunnel appears to be stable for the duration of the 1 ms pulse. Note that each image represents a separate instance of plasma generation.

VI. Conclusions

A Mach 3 wind tunnel with integrated microwave plasma generating capability has been designed and tested. The importance of the electrical properties of the wind tunnel for microwave propagation and breakdown has been shown. Self induced plasma generation has been achieved with a microwave pulse length of 1 ms. A stable, well localized plasma has been maintained in the wind tunnel with flow. Measurements of the plasma indicate a brighter and more filamentary discharge with flow than without flow.

REFERENCES

1. W. Beaulieu, V. Bytyrin, A. Klimov, S. Leonov, A. Pashina, and B. Timofeev, "Plasma Aerodynamic Wind Tunnel Tests with 1/6 Scale Model of Nose Part of F-15," 3rd Weakly Ionized Gases Workshop, Norfolk, VA, November 1-5, 1999.
2. A. Klimov, S. Leonov, A. Pashina, V. Skvortsov, T. Cain, and B. Timofeev, "Influence of a Corona Discharge on the Supersonic Drag of an Axisymmetric Body," 3rd Weakly Ionized Gases Workshop, Norfolk, VA, November 1-5, 1999.
3. S. Merriman, I. Adamovich, and J.W. Rich, "Studies of Oblique Shock Waves in Weakly Ionized Nonequilibrium Plasmas," 3rd Weakly Ionized Gases Workshop, Norfolk, VA, November 1-5, 1999.
4. R. Yano, V. Contini, E. Ploenjes, P. Palm, S. Merriman, I. Adamovich, W. Lempert, V. Subramaniam, and J.W. Rich, "Flow Visualization in a Supersonic Nonequilibrium Plasma Wind Tunnel," 30th Plasmadynamics and Lasers Conference, Norfolk, VA, June, 1999.
5. V. Soloviev, V. Krivstov, A. Konchakov, N.D. Malmuth, "Mechanisms of Shock Wave Dispersion and Attenuation in Weakly Ionized Cold Discharge Plasmas," Perspectives of MHD and Plasma Technologies in Aerospace Applications Conference, IVTAN, Moscow, Russia, March 24-25, 1999.
6. S. Macheret, L. Martinelli, and R. Miles, "Shock Wave Propagation in Non-Uniform Gases and Plasmas," 37th AIAA Aerospace Sciences Meeting and Exhibit, Reno, NV, January 11-14, 1999.
7. A. Yalin, Y. Ionikh, R. Miles, "Temperature Measurements in Glow Discharges with Ultraviolet Filtered Rayleigh Scattering," 30th AIAA Plasmadynamics and Lasers Conference, Norfolk, VA, June 28-July 1, 1999.
8. P. Harsha and E. Gurjanov, "AJAX: New Directions in Hypersonic Technology," 8th Aerospace Planes and Hypersonic Technologies Meeting, Norfolk, VA, April, 1996.
9. A.D. MacDonald, *Microwave Breakdown in Gases*, Wiley, 1966.
10. R. Collin, *Foundations for Microwave Engineering*, McGraw-Hill, 1966.
11. G. Matthaei, L. Young, E. Jones, *Microwave Filters, Impedance Matching Networks, and Coupling Structures*, McGraw-Hill, 1964.

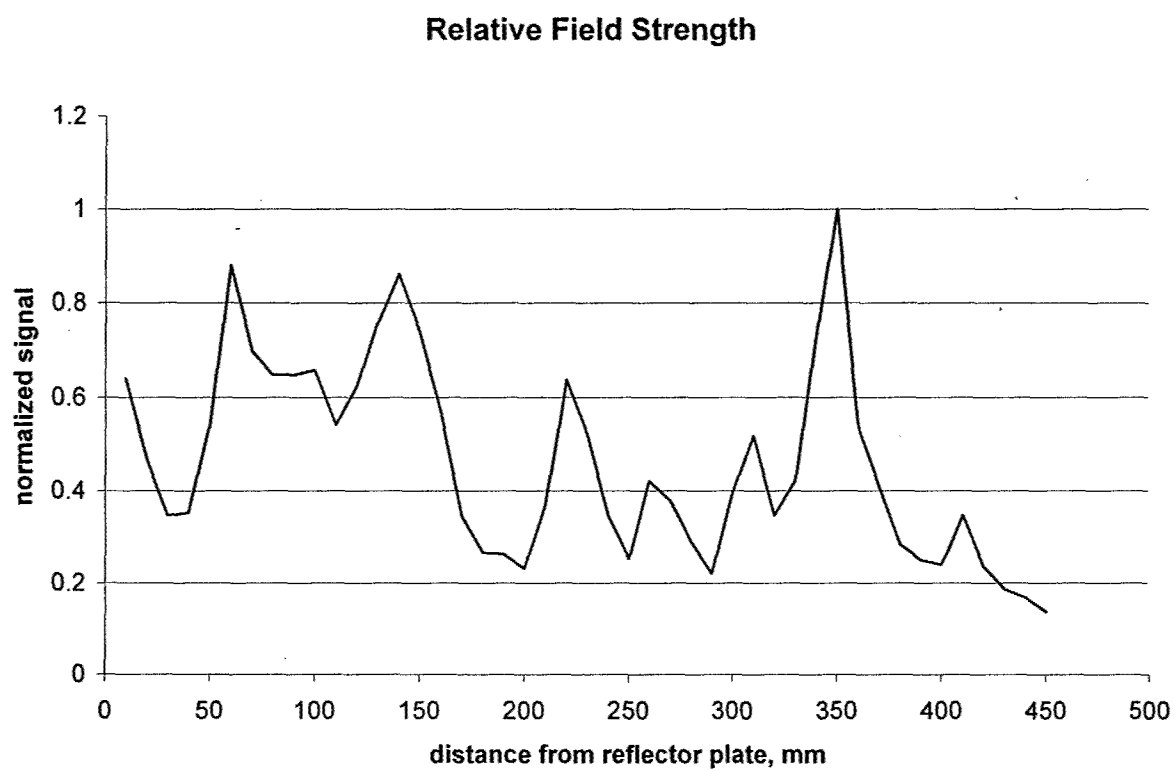


FIGURE 3: MEASURED ELECTRIC FIELD ALONG WIND TUNNEL CENTERLINE

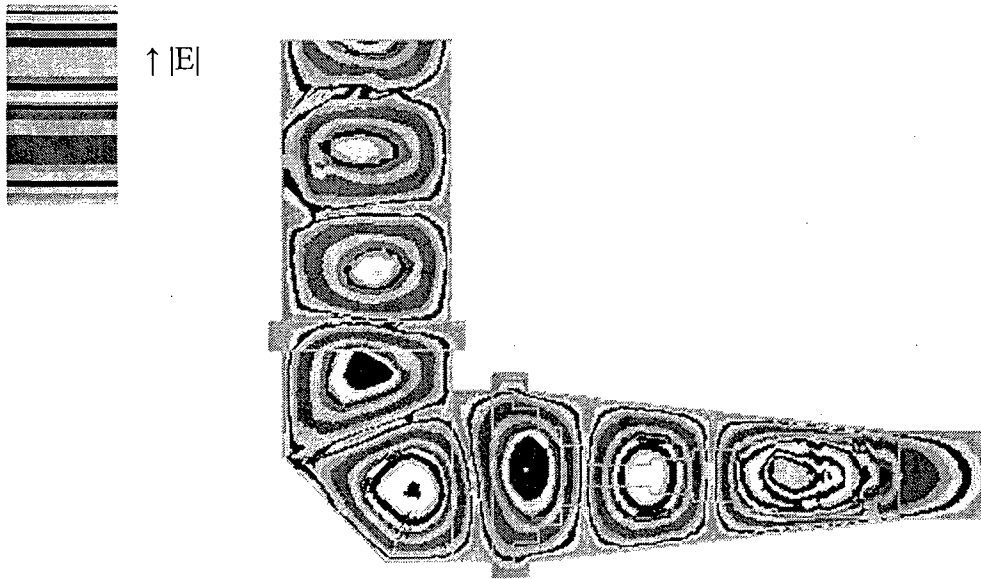


FIGURE 4: ELECTRIC FIELD MAGNITUDE WITH AIR FILLED WAVEGUIDE (NO DIELECTRIC)

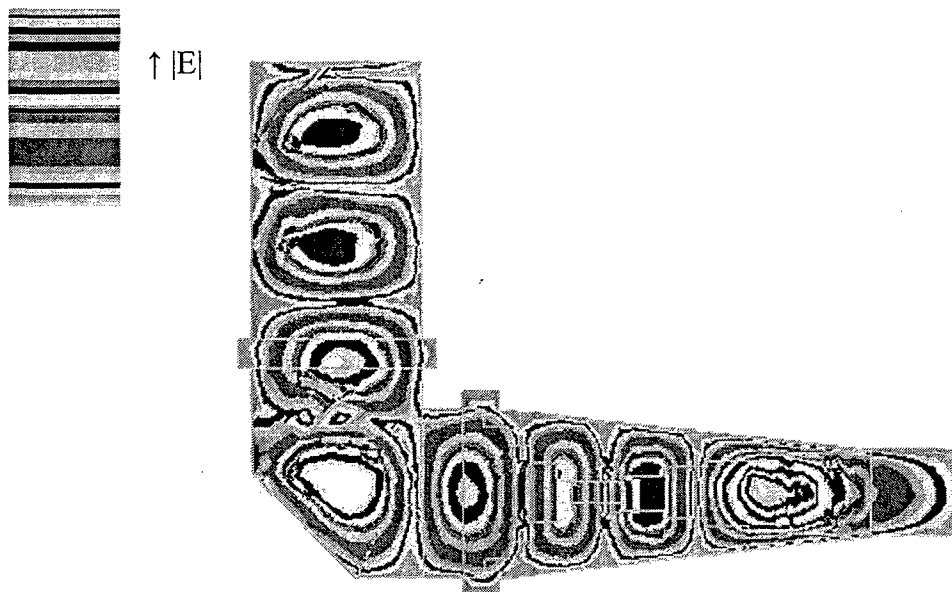


FIGURE 5: ELECTRIC FIELD MAGNITUDE WITH TEFLON NOZZLE
Relative permittivity = 2.08 Dielectric loss tangent = 0.00037

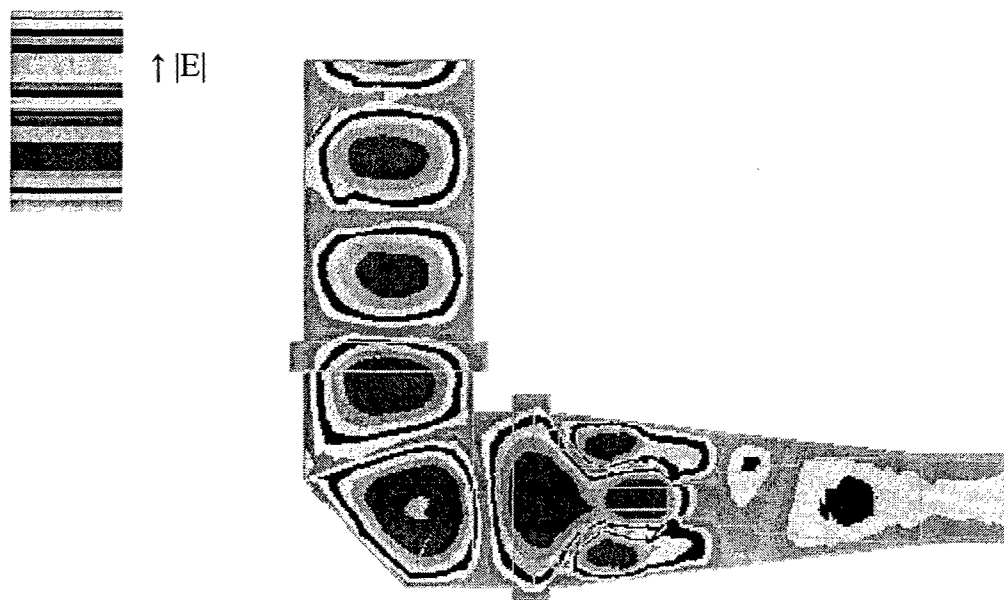


FIGURE 6: ELECTRIC FIELD MAGNITUDE WITH G-10 NOZZLES
 Relative permittivity = 5.0 Dielectric loss tangent = 0.019
 Incident wave phase = 157°

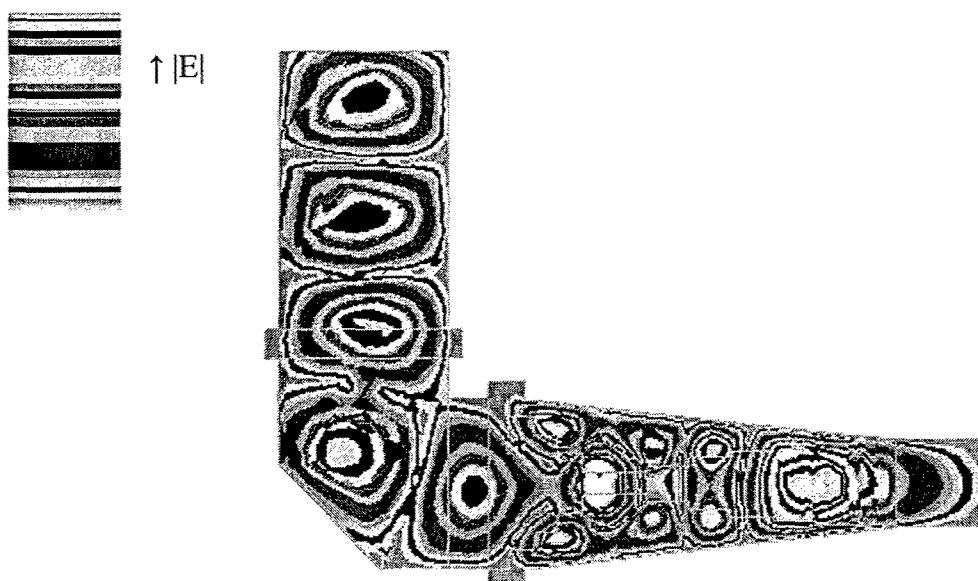


FIGURE 7: ELECTRIC FIELD MAGNITUDE WITH G-10 NOZZLES
 Relative permittivity = 5.0 Dielectric loss tangent = 0.019
 Incident wave phase = 70°

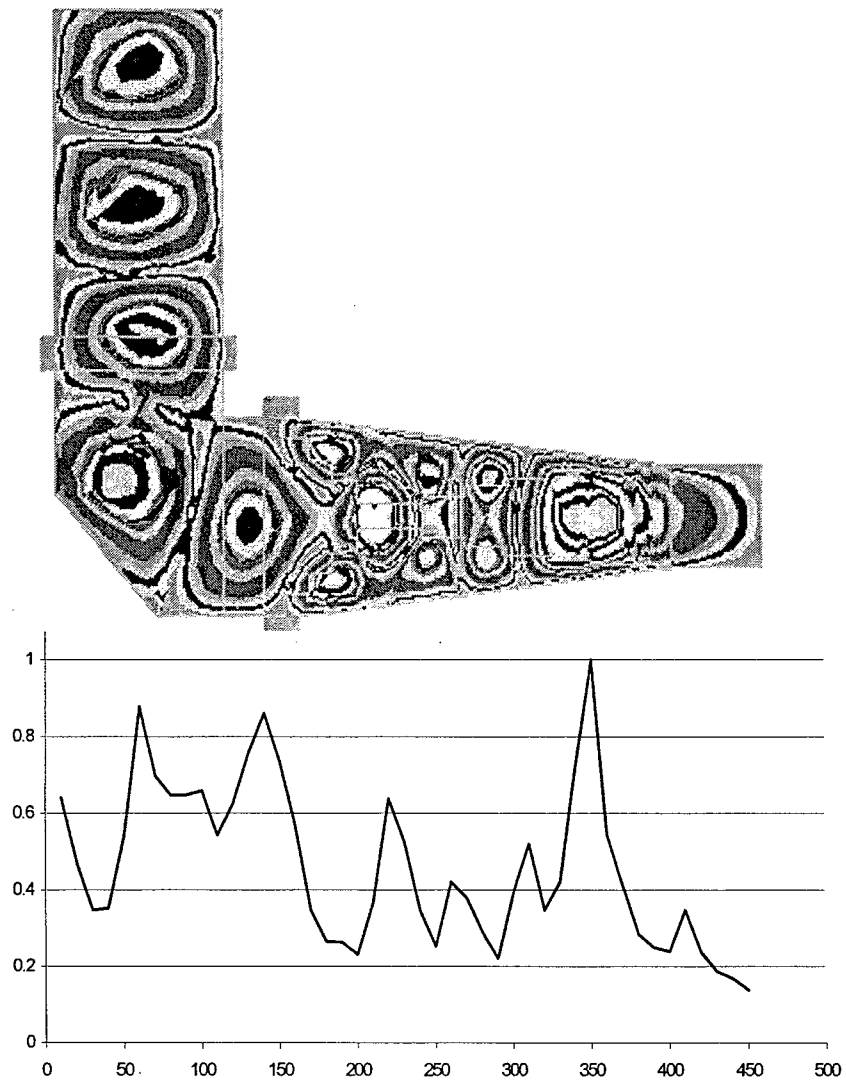


FIGURE 8: COMPARISON BETWEEN SIMULATION AND MEASUREMENT USING G-10 NOZZLES

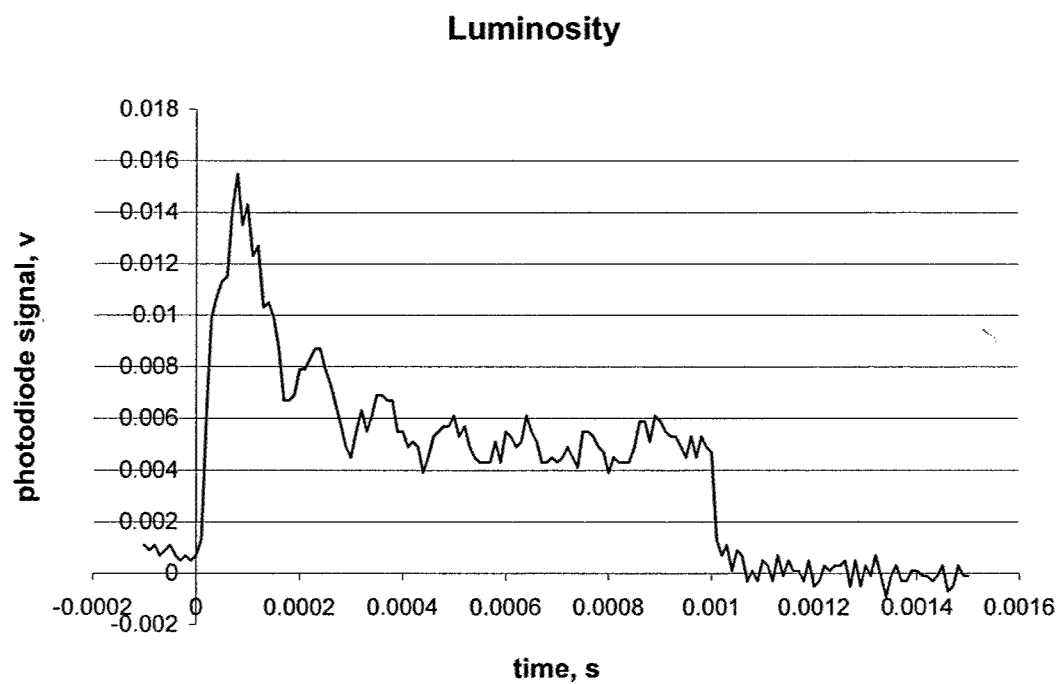
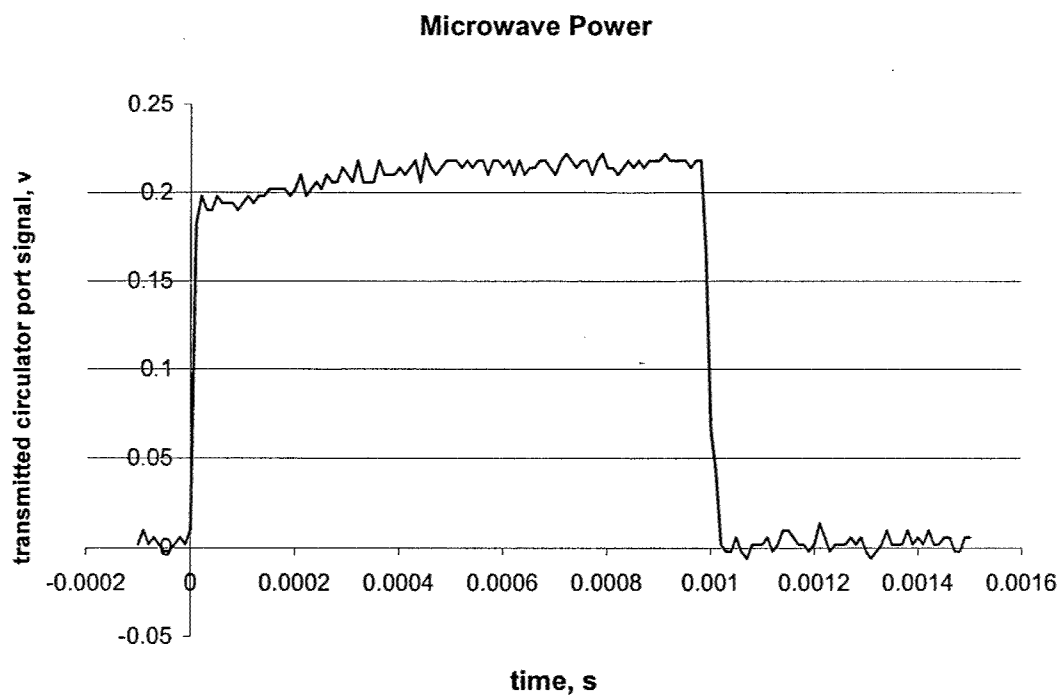


FIGURE 9: PLASMA LUMINOSITY WITHOUT FLOW (60 TORR, 300 K)

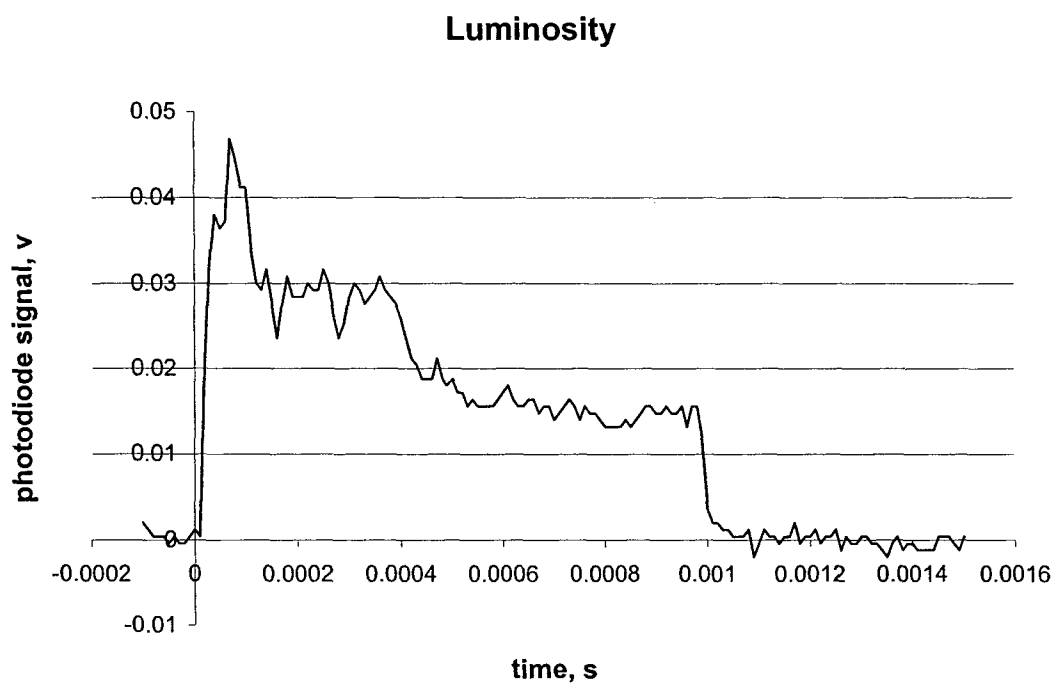
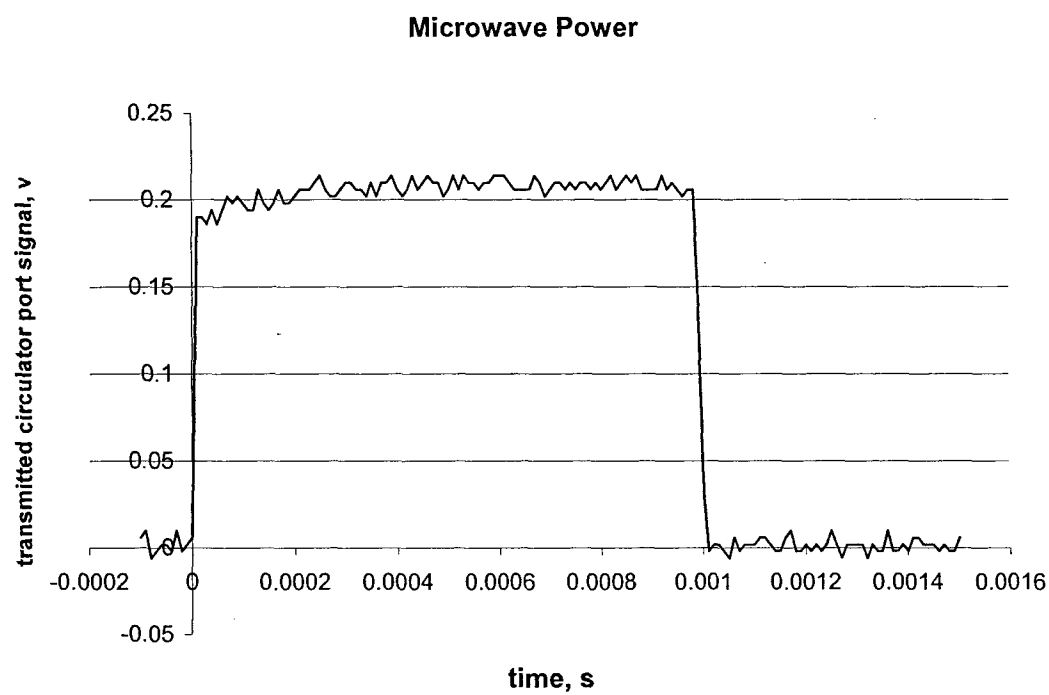


FIGURE 10: PLASMA LUMINOSITY WITH FL

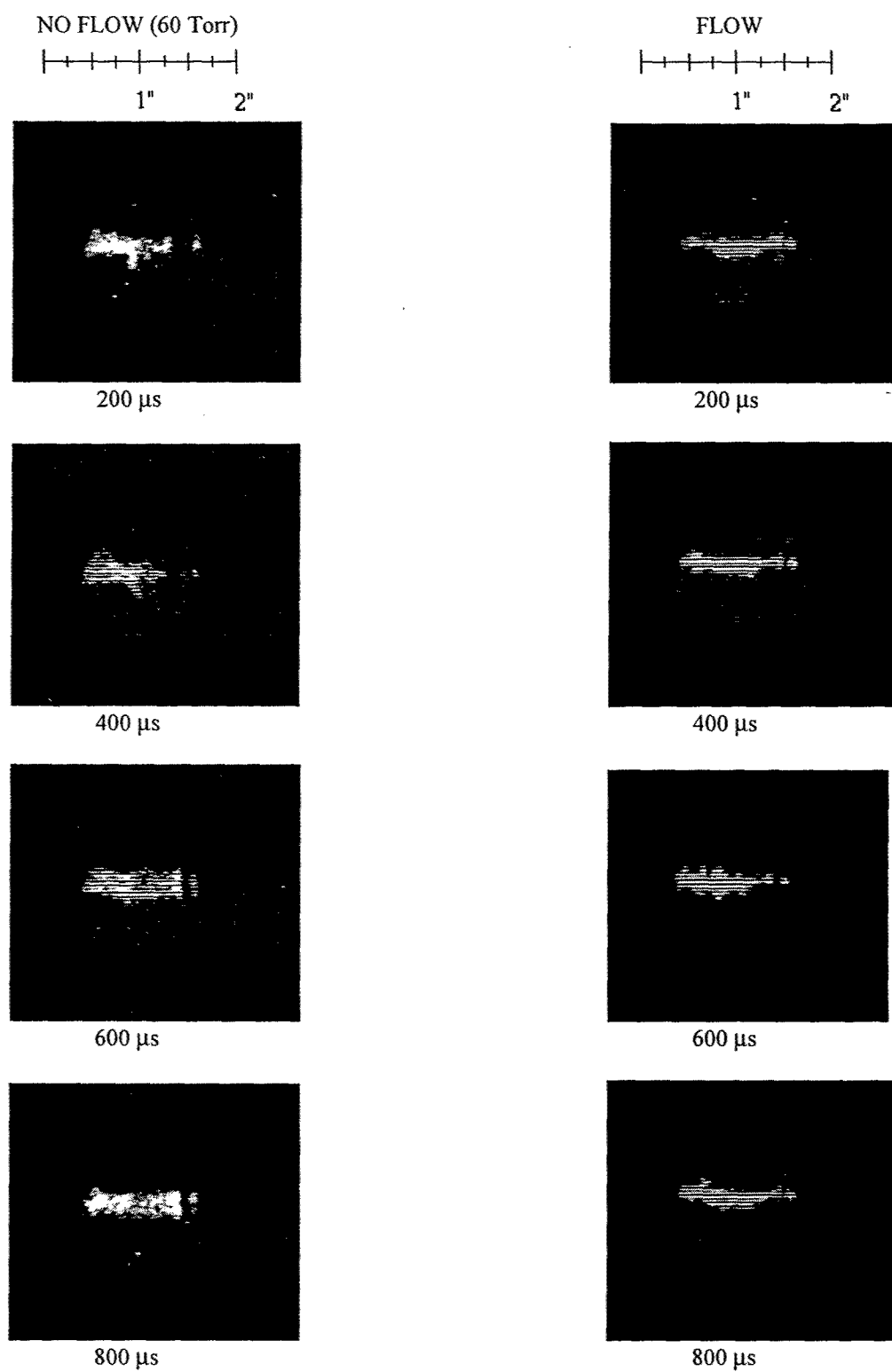


FIGURE 11: COMPARISON OF PLASMA WITH AND WITHOUT FLOW

CHAPTER 5

STUDIES OF ELECTRON BEAM-INITIATED, MICROWAVE DRIVEN PLASMA DISCHARGES FOR AERODYNAMIC CONTROL

ABSTRACT

Control of supersonic vehicles by means of heat addition is possible using off body heat addition by microwave breakdown in air. The resulting changes in temperature and shock structure alter the pressure distribution around a body downstream of the heat addition region. In the present work, a controlled microwave driven discharge in a small scale Mach 3 wind tunnel is studied to investigate its potential use as a means of vehicle control. The location of the discharge is controlled by the microwave power, the geometry of the wind tunnel, and a low power electron beam injected into the wind tunnel. The electron beam was found to reduce the microwave power required for breakdown, and to provide a means of modulating the plasma in time.

I. Introduction

Localized heat addition upstream of a moving body can affect the lift, drag, and moments about the body by altering the pressure distribution over the surface. This has several potential advantages over conventional aerodynamic controls. Unlike conventional control surfaces, this type of control may be implemented without the use of moving parts, and thus has reduced time response and increased frequency range as compared to conventional control surfaces. This type of control is also inherently more flexible. The pressure distribution may be altered anywhere on the body, rather than along control surfaces at fixed points on the body.

The heat addition profile creates a corresponding perturbation in temperature, Mach number, and stagnation pressure encountered by the body. Shock waves produced by the expanding gas in the heat addition region change the flow properties in adjacent regions, and can also be made to impinge on the body itself. The exact manner in which the flow is perturbed is determined by the size, heat deposition profile, and spatial location of the heat addition region relative to the body, and also by the way in which these parameters are varied in time. CFD simulations showing detailed flow structure and optimization of the heat deposition region for flow around a conical model, similar to the model used in the present experiments, can be found in reference 2.

The present work involved experiments performed in a Mach 3 wind tunnel with heat deposited in the test section by a microwave driven discharge. The control of this discharge is accomplished by adjustment of the microwave power, the wind tunnel geometry, and modulation of a 20 kV electron beam injected into the wind tunnel.

II. Apparatus

The wind tunnel used in this work is of the indraft type, drawing air at atmospheric conditions into the plenum and exhausting to a vacuum line maintained at 150 torr. This facility has been described in some detail in a previous publication¹. The tunnel is comprised of a plenum section, a rectangular nozzle with a Mach 3 expansion ratio, a 2.15"x2.166" rectangular test section, and a 5.5° half angle diffuser. An air ejector pump connected through a vacuum line to the diffuser exit maintains the overall pressure drop through the wind tunnel. A schematic of the wind tunnel is shown in Figure 1.

Microwaves are used to provide local energy addition in the tunnel by creating a microwave driven discharge in the test section. The microwaves are generated externally by a 6 kW, 2.45 GHz magnetron and are introduced via a waveguide into the plenum of the wind tunnel through a port in the top wall. The waveguide has a 4.3"x2.15" cross section and transmits the microwaves in the TE₁₀ mode. The plenum is made of aluminum and is of the same dimensions as the waveguide, allowing the microwaves to propagate in the same TE₁₀ mode. A three stub tuner near the waveguide entrance is used to match the impedance of the waveguide to that of the tunnel, minimizing reflections back toward the source. Upstream of the microwave port, a reflector plate perforated with an array of 1/4" holes reflects microwaves in the downstream direction and prevents microwaves from leaking out of the wind tunnel upstream of the plenum. The holes in the reflector plate serve as an air inlet to the plenum, but do not allow the passage of microwaves since the diameter of the holes is much smaller than the cutoff dimension for 2.45 GHz radiation. Adding microwaves through the plenum rather than directly to the test section aids in avoiding

parasitic breakdown around the entrance port because the higher pressure in the plenum relative to that in the test section suppresses breakdown in the plenum.

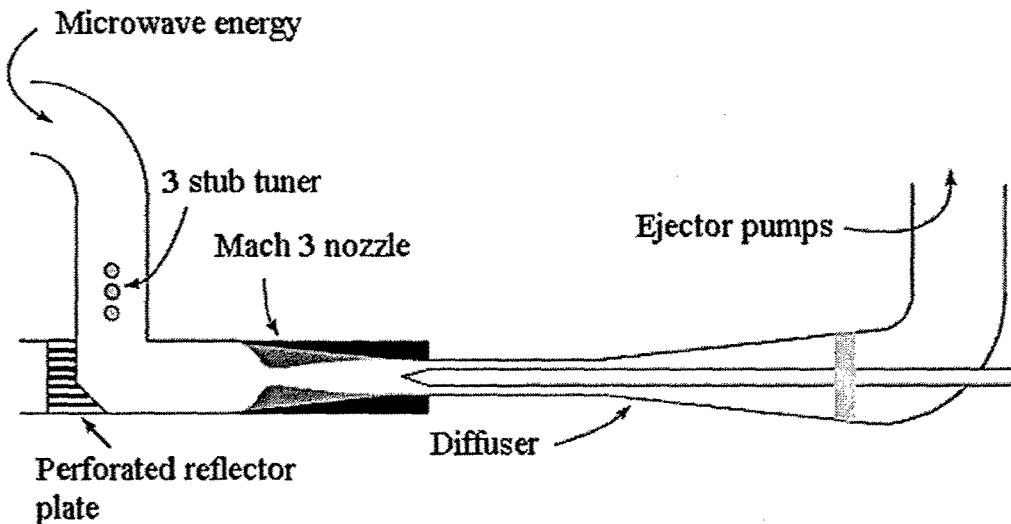


Figure 1: Wind tunnel schematic

Two identical contoured blocks of virgin electrical grade Teflon, along with two flat aluminum walls, form the nozzle. Teflon was chosen as the nozzle material due to its excellent electrical characteristics, being nearly transparent to microwaves. The Teflon is mounted on angled aluminum plates, which form a taper toward the test section. This taper is extended to be slightly beyond the microwave cutoff dimension. As the microwaves approach cutoff, the group velocity approaches zero and the electric field intensity increases. The cutoff taper also reflects the incident microwave power back upstream. With a properly adjusted three stub tuner, the wind tunnel can be made to act as a microwave cavity resonator. A standing wave is formed between the tuner and the cutoff taper. Incident microwave energy is stored in the standing wave, and the electric field strength inside the tunnel becomes much stronger than the field in the waveguide, with the field near the cutoff point being the strongest. This is the region where the discharge forms.

The test section is constructed of aluminum and has a 2.15"x2.166" rectangular cross section, with 1.5" diameter quartz windows in the side walls. Aluminum tubes smaller than the cutoff dimension are mounted over the windows to prevent microwave leakage but still allow optical access. The cutoff taper, containing the region of highest electric field strength, is just upstream of the windows in the test section.

The diffuser used downstream of the test section is made up of two parts. The first part is a 6" long aluminum shock duct of the same cross section as the test section. The second part transitions along the axial direction gradually from the rectangular test section cross section to the circular vacuum line cross section and expands through a 5.5° half angle to form a smooth transition to the 6" diameter vacuum line. It is made of stainless steel sheet metal, and contains a 1" diameter stainless steel sting used for mounting models in the wind tunnel. The sting, which also extends through the shock duct, reduces the area for the flow. Together with the attached model, this arrangement produces a converging area for the flow at the entrance to the shock duct. The shock waves from the model become the initial stage of compression for the diffuser, improving the pressure recovery. The sting also acts as a central conductor, so microwaves that leak beyond the cutoff portion of the test section can propagate along the sting into the diffuser. A close fitting section of aluminum honeycomb near the downstream end of the diffuser prevents microwaves from passing into the vacuum line, while still allowing air to flow through.

The electron beam assembly is located adjacent to the wind tunnel. The beam is generated by a small electron gun, similar to the gun in a television picture tube, housed inside a vacuum line. A custom power supply allows for the independent setting of all grid and filament voltages on the gun, and for switching the beam on and off at various frequencies. The electron beam is directed out of the vacuum line via two pairs of steering magnets through a thin silicon nitride window, and then into the wind tunnel. The beam is directed parallel to the electric field of microwaves and perpendicular to the flow velocity. However, the beam diverges through a large angle after

passing through the window due to scattering collisions. A simplified schematic of the electron beam assembly is shown below in Figure 2.

The electron beam window is made from a 500nm thick film of silicon nitride coated on a silicon wafer. An etching process is performed to remove a 1x1 mm square of silicon from the wafer, leaving only the thin silicon nitride film. This film can hold one atmosphere of pressure across its surface at room temperature, although heating caused by the electron beam reduces its strength. Thus the required pressure that must be held across the window limits the amount of electron beam current which can be transmitted through it. The window is recessed from the inner wall of the wind tunnel by one tenth of an inch to provide some protection from aerodynamic forces.

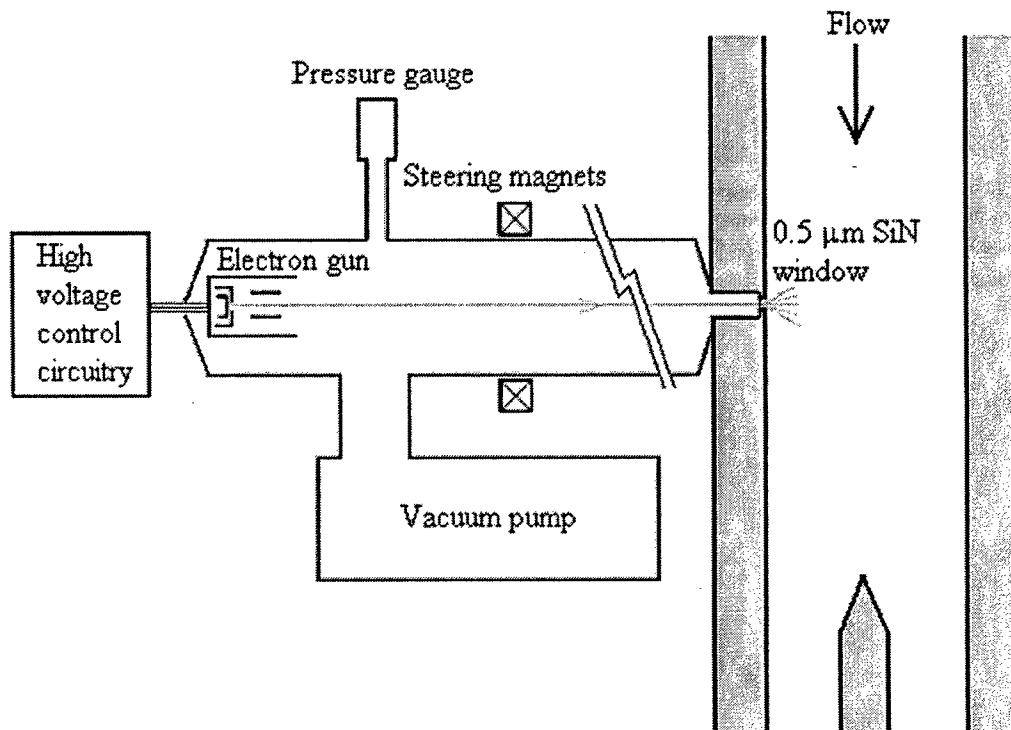


Figure 2: Electron beam assembly

III. Experiment

The experiments performed in the wind tunnel were all done using one of two models in the test section: a 1" diameter 15° half angle steel cone and a similar cone made of Teflon. It was found that with the steel cone, a visible corona had a tendency to form at the tip, as can be seen in Figure 3. The steel cone was replaced with a Teflon cone of the same dimensions to prevent the corona from forming and to determine how that might change the electron beam control of the plasma. The majority of experiments involved microwave power levels near the breakdown threshold, ranging from approximately 900 to 2400 watts of transmitted power. Once initiated, the plasma absorbed about 60% of the transmitted power. Data was collected using an RF crystal mounted on the reflected power port of the isolator to measure reflected power, a photodiode to determine the light emission intensity, and a fast shutter CCD camera to obtain images of the plasma.

Three distinct types of discharge control experiments were undertaken: the first type was simply to establish the breakdown threshold both with and without the electron beam, the second was to investigate the response of the plasma to frequency modulation of the electron beam, and the third was an attempt at using the electron beam to move the plasma to a new location.

For the breakdown tests, the electron beam was first turned off and microwave power reduced from a value well above threshold to a value somewhat below threshold for breakdown. These tests were then repeated with the electron beam set to various current levels. The electron beam was maintained at a constant 20 kV for these tests. Due to a power ripple present in the output of the magnetron, fluctuations in the plasma at 60 Hz and higher

frequencies were present in most of these experiments. This is particularly apparent near the breakdown threshold, where the plasma is alternately initiated and extinguished as the magnetron power fluctuates. This is also where the electron beam had its greatest effect on the plasma, so the data presented in the results reflect this unintentional fluctuation.

Frequency modulation of the electron beam was performed at microwave power levels for which the beam was required to initiate breakdown, as determined by the breakdown tests described above. Various frequencies were used, and the response of the plasma was determined by reflected microwave power and light emission measurements.

The final set of experiments to control the discharge location were done by inserting a metal pin into the wind tunnel on the opposite side from the electron beam. The pin acts to initiate breakdown on its side of the wind tunnel. Due to its strong effect on initiation as compared to the electron beam, the discharge showed a high degree of sensitivity to the pin insertion depth. Because of this, the pin was inserted a variable depth into the wind tunnel by means of a translation stage which could be adjusted in small increments. Experiments were first conducted with the electron beam off, and the pin inserted incrementally until the plasma began to form on the side with the pin only. This was then repeated with the electron beam on to move the plasma over to the other side of the tunnel.

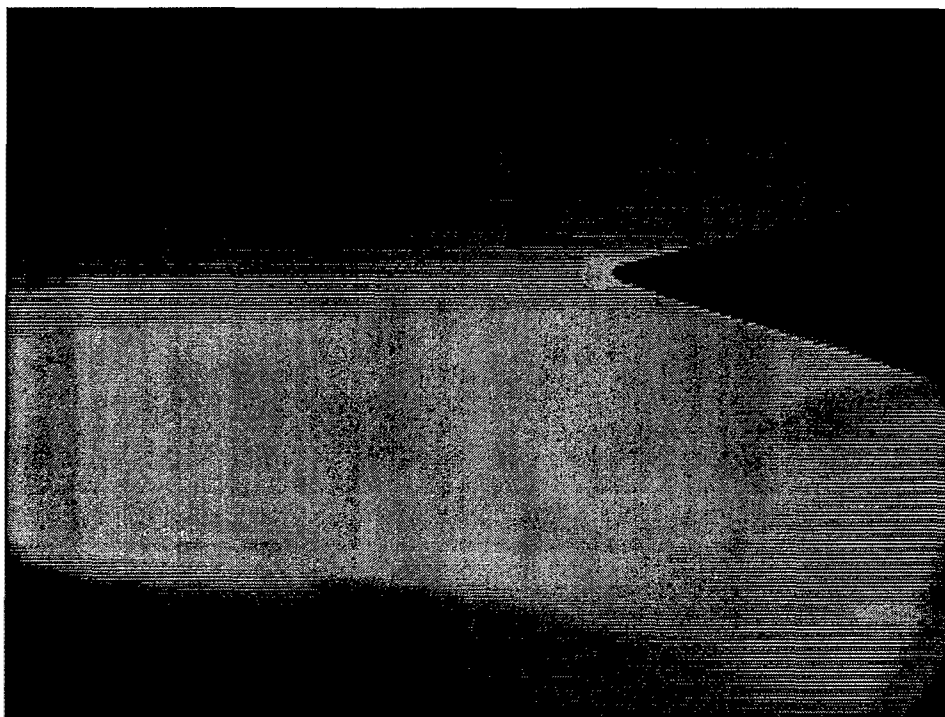


Figure 3: Plasma over a steel cone in Mach 3 flow

IV. Results

The breakdown threshold was significantly reduced by the presence of the electron beam. Self initiated breakdown occurred at about 1700 watts of transmitted microwave power. Using the electron beam, the power level required for breakdown dropped from 1700 watts to 1100 watts, a reduction of 35%. This change in breakdown threshold is not a strong

function of the beam current, at least in the range tested; there was no significant change in the threshold at beam currents ranging from 0.25 A to 40 A. The lower limit of this range represents the practical lower limit for which beam current can be controlled with the present facility, and the upper limit is the maximum current obtainable without damage to the electron gun. No changes in the plasma due to the electron beam were observed at microwave power levels above that required for self initiated breakdown.

At power levels between 1100 and 1700 watts, the electron beam was used to modulate the plasma in time. The electron beam was cycled on and off at known frequencies, and the plasma luminosity was recorded with a photodiode. The plots presented in Figures 4a, 4b, and 4c show the results of these tests at 5, 10, and 20 Hz. At 20

Hz, the ripple in the microwave power noticeably interferes with the modulation, as an additional 60 Hz frequency from the microwave power supply is overlaid on top of the electron beam modulation frequency.

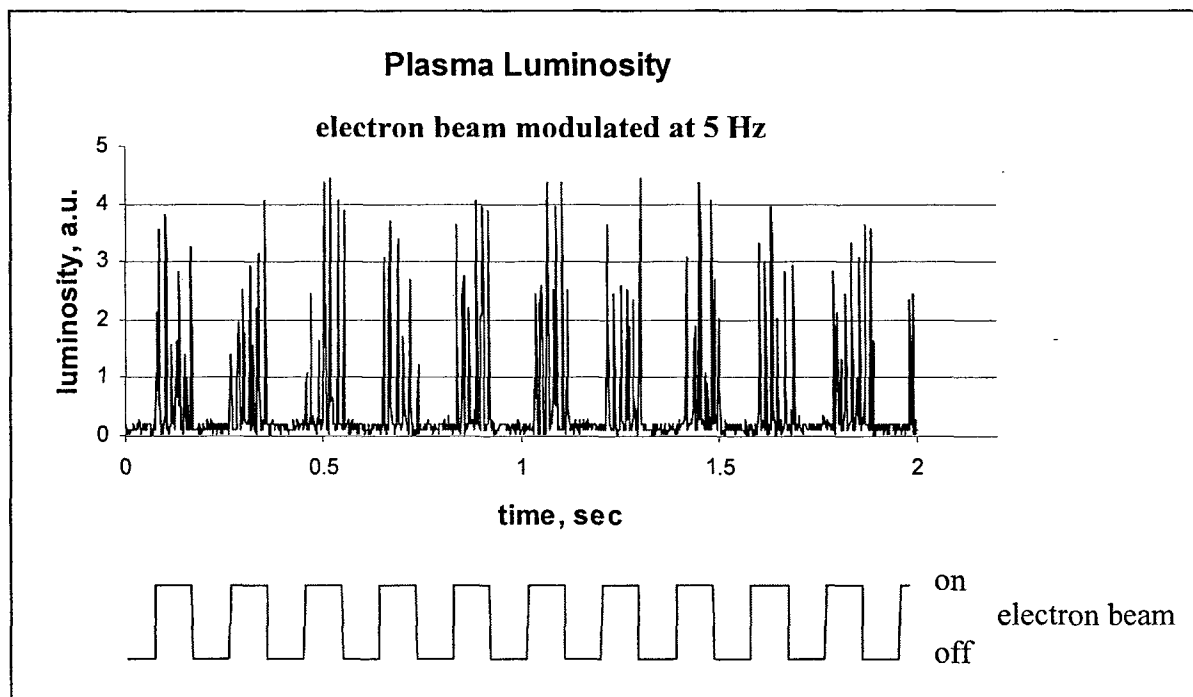


Figure 4a: Electron beam modulated at 5 Hz

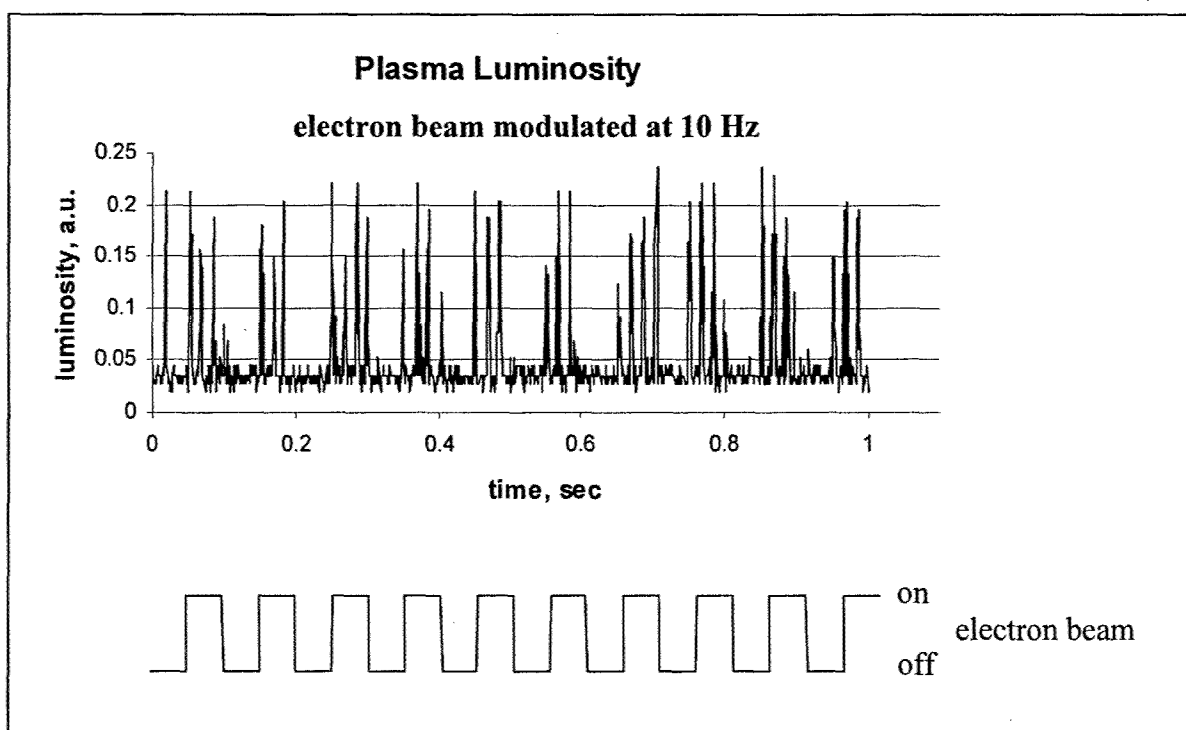


Figure 4b: Electron beam modulated at 10 Hz

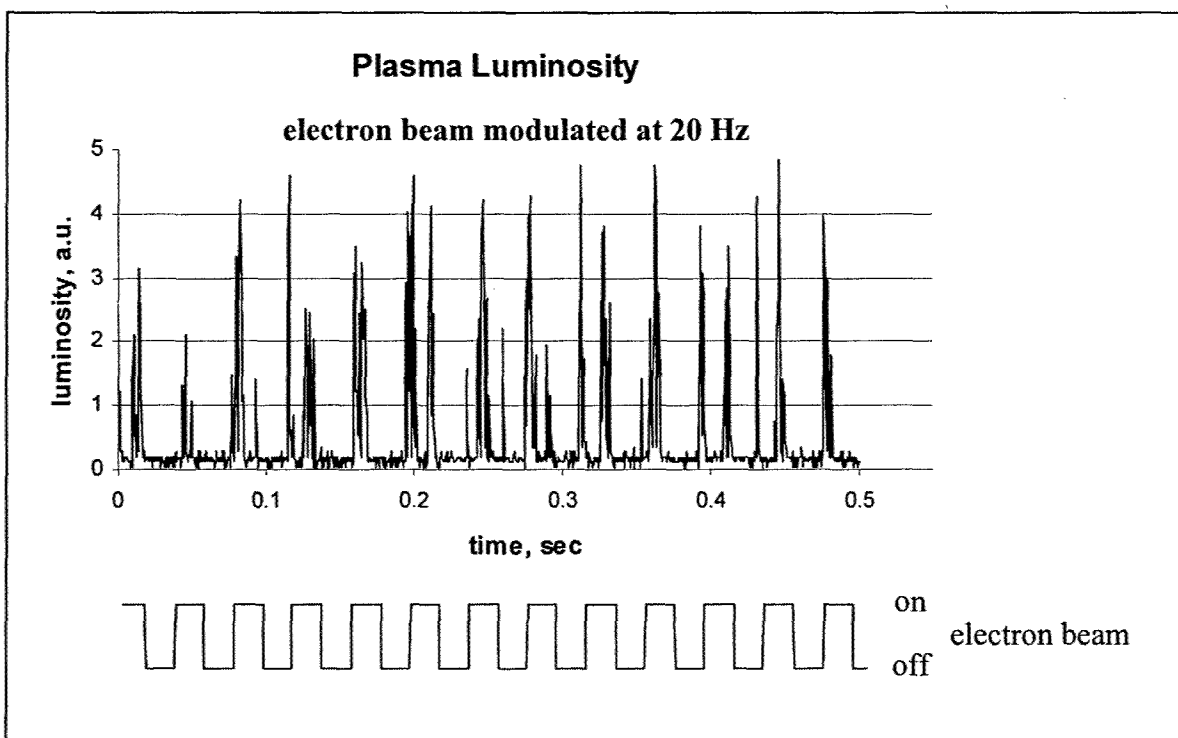


Figure 4c: Electron beam modulated at 20 Hz

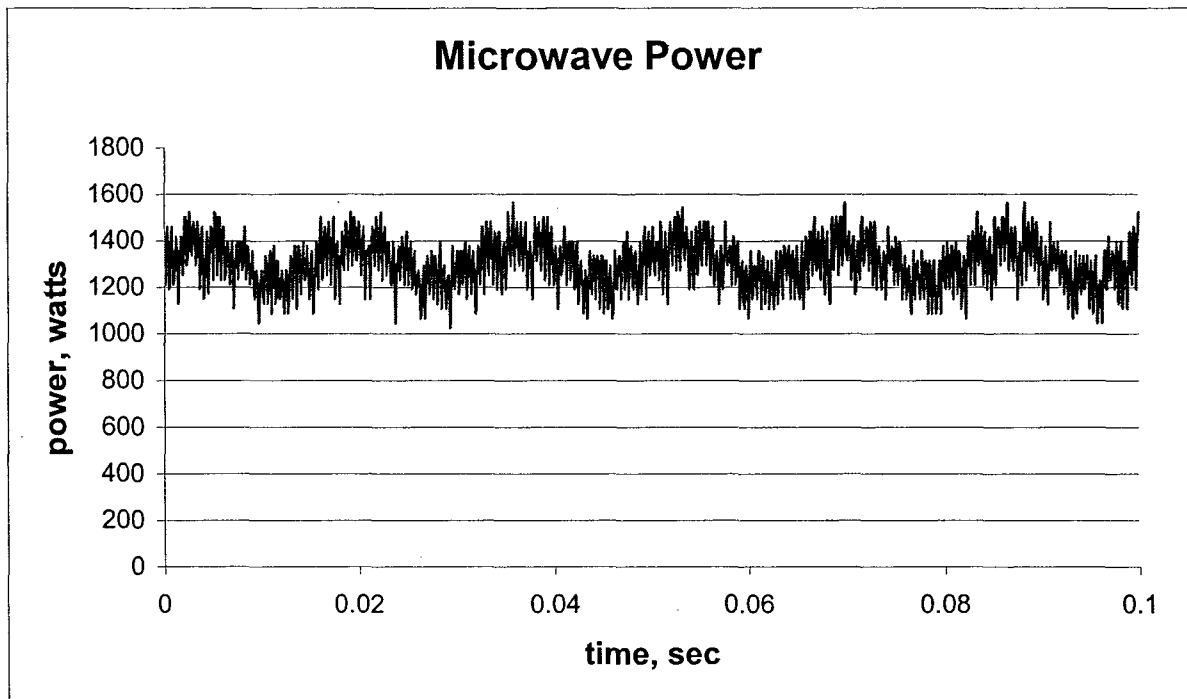


Figure 5: Transmitted microwave power

The power supply ripple is characterized in Figure 5, showing a relatively large power fluctuation of $\pm 20\%$. Four frequencies at 60 Hz, 360 Hz, 2.3 kHz, and 27.6 kHz were identified from the data. A portion of a typical plot of plasma luminosity is shown in Figure 6, with fluctuations at 60 Hz and 360 Hz also apparent in the plasma.

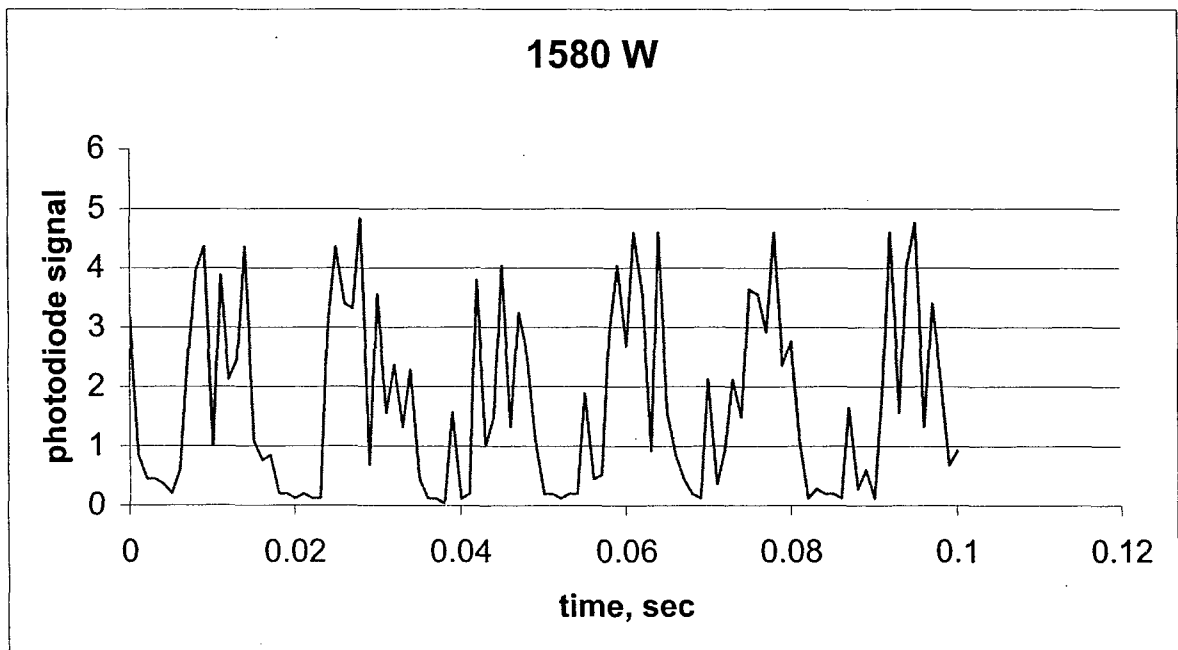


Figure 6: Plasma fluctuations due to power supply ripple

The results of third type of experiment to control discharge location with the electron beam were inconclusive. As described in the previous section, a pin was placed in the wind tunnel along the opposite wall from the electron beam window. This provided a means to initiate the discharge on the pin side of the wind tunnel. The electron beam was then turned on in an attempt to extend the discharge over to the other wall. However, whenever the pin was inserted far enough to reliably initiate the discharge, the electron beam had no effect. Conversely, when the pin was retracted from this point, the discharge had a tendency to jump between the two side walls whether the electron beam was present or not. This could be due to vibration in the pin while the wind tunnel is running.

All experiments were repeated for both a steel cone in the test section and a Teflon cone of the same dimensions. The results were found to be essentially the same for both materials, despite the formation of a corona on the tip of the steel cone, which did not occur with the Teflon cone.

V. Conclusions

A stable microwave driven discharge was maintained in a small scale wind tunnel against a Mach 3 flow. A 20 kV electron beam injected into the wind tunnel reduced the breakdown threshold by 35% from 1700 to 1100 watts. Within this range of microwave power the discharge was controlled in time by modulating the electron beam. The discharge behavior was not a strong function of beam current between 0.25 A and 40 A, and the electron beam did not alter the discharge behavior at microwave power levels above that required for self initiated breakdown.

REFERENCES

1. B. McAndrew, R. Murray, M. Shneider, J. Fox, J. Kline, P. Efthimion, and R. Miles, "Comparison of Numerical and Experimental Results from Localized, Microwave Driven Plasma Energy Addition into a Mach 3 Flow", AIAA paper #2001-3061.
2. I. Girgis, M. Shneider, S. Macheret, G. Brown, and R. Miles, "Creation of Steering Moments in Supersonic Flow by Off-Axis Plasma Heat Addition", AIAA paper #2002-0129.
3. Riddle, L., "Electron Beams for Control of Microwave Generated Plasma", Sarnoff Corporation technical report, March 3, 2000.
4. Ghose, R. N., Microwave Circuit Theory and Analysis. McGraw-Hill Book Co., Inc., 1963.
5. B. McAndrew, P. Barker, and R. Miles, "Development of a Supersonic Plasma Wind Tunnel", AIAA paper #2000-0533.

CHAPTER 6

EFFICIENT PLASMA GENERATION BY REPETITIVE HIGH-VOLTAGE NANOSECOND PULSES FOR MHD FLOW CONTROL

I. INTRODUCTION

An important factor in MHD flow control is that in the flight regime of interest, static temperature is too low for thermal ionization of air. Therefore, nonequilibrium ionization in MHD devices must be done, and, because of high recombination rates, the ionization must be sustained throughout the MHD region. The energy cost of ionization imposes very rigid constraints on the choice of ionization methods: only the most energetically efficient ionization method can be used in these devices. Our earlier work [3-10] showed that electron beams injected into the gas along magnetic field lines constitute the most efficient way of creating nonequilibrium ionization.

An alternative method is to generate high-energy ionizing electrons inside the plasma by applying a very high (super-breakdown) voltage for a very short (nanosecond-scale) time, and to repeat such pulses at a rate matching the recombination rate [10-12]. Theoretical analysis [10-12] demonstrated that the repetitive-pulse method is much more efficient than is ionization by a steady-state DC or RF field, but less efficient than the ionization by electron beams. The repetitive-pulse method is, however, free from window problems associated with electron beams. Fig. 1 shows that energy cost per newly generated electron as a function of the reduced electric field, and Fig. 2 shows

theoretical prediction of power budget required to sustain an average electron density of 10^{12} cm^{-3} in room-temperature air at a pressure of 10 Torr, and of the required pulse repetition rate [10-12].

A custom-developed pulser that produces 1-3 nanosecond pulses with 30 kV peak voltage at up to 100 kHz repetition rate, with average power of 500-800 W, has been purchased and installed. Fig. 3 is a photograph of the plasma produced with this pulser between two flat-plate electrodes in air at 10 Torr at 50 kHz repetition rate. This plasma generator has been integrated with a Mach 4 nozzle and 2.5 inch working section of a 6.5 Tesla superconducting magnet purchased earlier. Experiments on MHD effects in supersonic cold air with nonequilibrium ionization have begun.

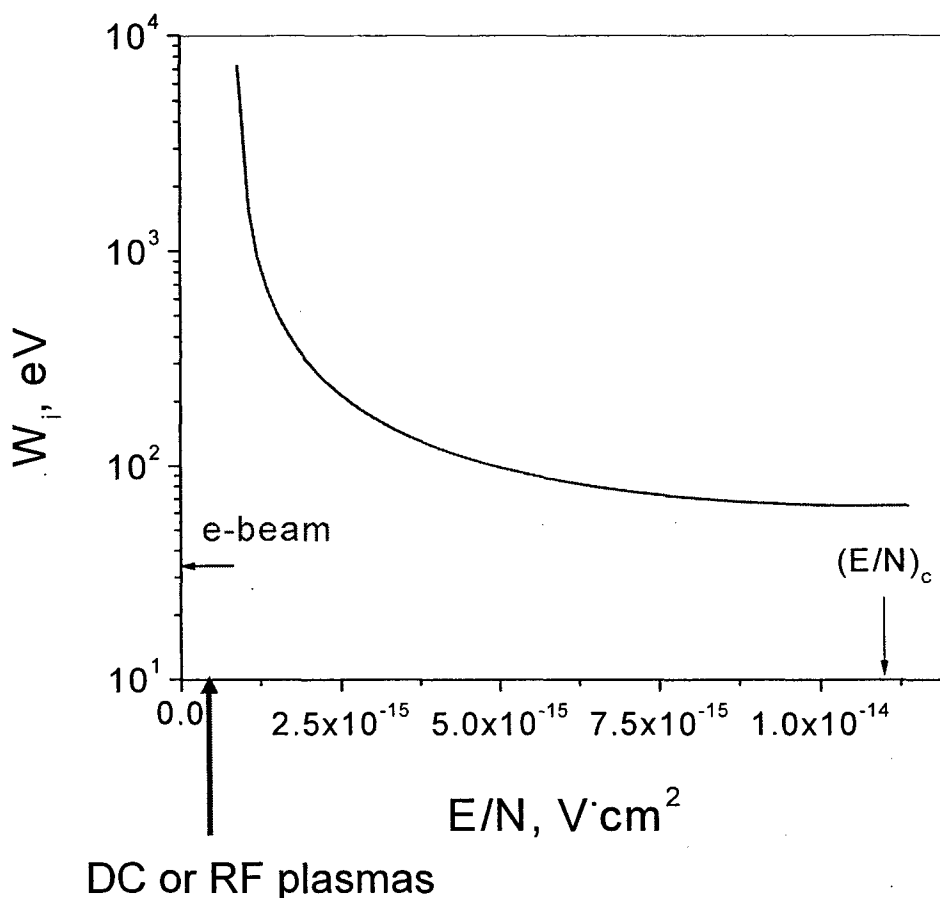


Fig. 1. Energy cost, in eV per newly produced electron in weakly ionized air plasmas versus ratio of electric field strength E to the gas number density N . Values of E/N corresponding to bulk DC and RF plasmas and to the cathode sheath of glow discharges are indicated by vertical arrows. The energy cost of ionization by high-energy electron beams is indicated by a horizontal arrow.

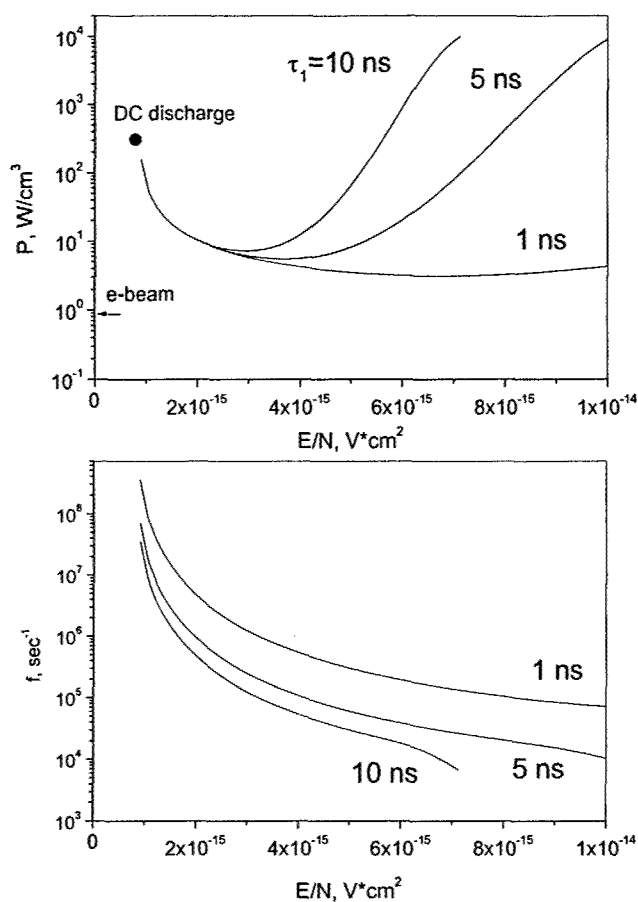


Fig. 2. Power input (upper plot) and pulse repetition rate (lower plot) required to sustain a time-averaged electron number density of 10^{12} cm^{-3} in air at 10 Torr, 300 K, by repetitive pulses, as functions of E/N at various pulse lengths τ_i . Power inputs required to sustain the same electron density at steady state by DC discharge and high-energy electron beams are indicated in the upper plot.

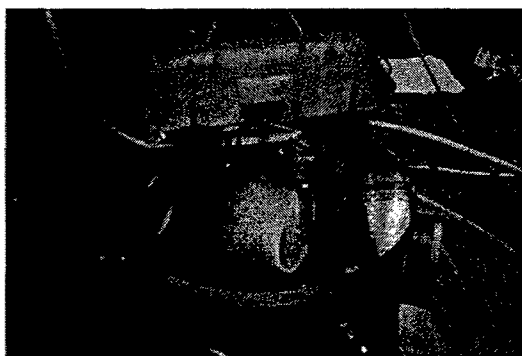


Fig. 8. Plasma produced between flat-plate electrodes in air at 10 Torr by 1 ns, 30 kV pulses at 50 kHz repetition rate.

References

1. S. O. Macheret, M. N. Shneider, and R. B. Miles, "Magnetohydrodynamic and Electrohydrodynamic Control of Hypersonic Flows of Weakly Ionized Plasmas," Paper AIAA 2002-2249.
2. S. O. Macheret, M. N. Shneider, and R. B. Miles, "Nonequilibrium Magnetohydrodynamic Control of Scramjet Inlets," Paper AIAA 2002-2251.
3. S. O. Macheret, M. N. Shneider, and R. B. Miles, "Modeling of Discharges Generated by Electron Beams in Dense Gases: Fountain and Thunderstorm Regimes", *Physics of Plasmas*, 2001, Vol. 8, No. 5, pp. 1518-1528.
4. S. O. Macheret, M. N. Shneider, and R. B. Miles, "External Supersonic Flow and Scramjet Inlet Control by MHD with Electron Beam Ionization," Paper AIAA 2001-0492, 2001.
5. S. O. Macheret, M. N. Shneider, and R. B. Miles, "Potential Performance of Supersonic MHD Power Generators," Paper AIAA 2001-0795.
6. S. O. Macheret, M. N. Shneider, and R. B. Miles, "Energy-Efficient Generation of Nonequilibrium Plasmas and Their Applications to Hypersonic MHD Systems," Paper AIAA 2001-2880.
7. S. O. Macheret, M. N. Shneider, and R. B. Miles, "Magnetohydrodynamic Control of Hypersonic Flow and Scramjet Inlets Using Electron Beam Ionization," *AIAA Journal*, Vol. 40, No. 1, 2002, pp. 74-81.
8. S. O. Macheret, M. N. Shneider, and R. B. Miles, "MHD Power Extraction from Cold Hypersonic Air Flow with External Ionizers", *Journal of Propulsion and Power*, Vol. 18, No. 2, 2002, pp. 424-431.
9. S. O. Macheret, M. N. Shneider, R. B. Miles, and R. J. Lipinski, "Electron Beam Generated Plasmas in Hypersonic Magnetohydrodynamic Channels", *AIAA Journal*, 2001, Vol. 39, No. 6, pp. 1127-1136.
10. S.O. Macheret, M.N. Shneider, and R.B. Miles, "Modeling of Air Plasma Generation by Electron beams and High-Voltage Pulses," Paper AIAA-2000-2569.
11. S. O. Macheret, M. N. Shneider, and R. B. Miles, "Modeling of Plasma Generation in Repetitive Ultra-Short High-Power DC, Microwave, and Laser Pulses," Paper AIAA 2001-2940.
12. S. O. Macheret, M. N. Shneider, and R. B. Miles, "Modeling of Air Plasma Generation by Repetitive High-Voltage Nanosecond Pulses," *IEEE Transactions on Plasma Science*, June 2002.

CHAPTER 7

SEMICLASSICAL MODELING OF STATE-SPECIFIC DISSOCIATION RATES IN DIATOMIC GASES

I. Introduction

The vibration-dissociation coupling is of key importance to hypersonic reentry, significantly affecting aerodynamics, radiative and convective heat fluxes, and spectral signatures of vehicles flying at sub-orbital to super-orbital velocities in rarefied atmosphere. Over the last four decades, high-temperature dissociation and vibrational relaxation was a subject of a number of experimental and theoretical studies, reviewed by Park,¹ and, more recently, by Macheret.² A number of models, such as those suggested by Marrone and Treanor,³ Losev,⁴ and Park,^{1,6} have been used with some success to describe experimental data on nonequilibrium dissociation. Those models, however, are empirical or semiempirical, using adjustable parameters found from a fit to a limited number of experimental data, which cannot guarantee their validity outside of the calibration range.

Most models of vibrational relaxation, until recently, relied upon a first-order perturbation (FOP) method,⁷ such as that used in SSH theory,^{7,8} with some modifications.^{7,9} Despite a reasonable agreement of the calculated overall relaxation times with experiments, FOP methods cannot pretend to adequately describe state-specific relaxation rates at high collision energies and temperatures typical of hypersonic bow shocks.

Recently, the authors and their colleagues have developed new theories of high-temperature relaxation¹⁰⁻¹⁴ and dissociation^{2,15,16}, especially well suited for high-temperature environment. The principal idea of these theories is that at high energy of colliding particles a molecule can jump over many vibrational quantum states. These jumps can be both bound-bound (vibrational relaxation) and bound-free (dissociation), and they must be correctly accounted for even in the first approximation. For the relaxation problem, correct and convenient framework is provided by the Forced Harmonic Oscillator (FHO) model,¹⁷⁻²⁰ which naturally and consistently includes multi-quantum jumps. With relatively simple corrections for anharmonicity and enforcement of detailed balance, this model has been demonstrated to agree very well with both experimental data and sophisticated state-of-the-art quantum computations. The FHO approach was also used to model dynamics of populations of vibrational levels during relaxation, and to resolve a long-debated "bottleneck" problem.¹² Most recently, the approach was extended to explicitly account for three-dimensional motion of colliding particles and molecular rotation, resulting in a fully analytical, without adjustable parameters, non-perturbative theory of multi-quantum vibrational energy transfer.^{13,14} The important role of rotation and non-collinear collisions was clearly demonstrated, and the calculated rates agree well with experiments as well as with close-coupled quantum and semiclassical computations using full potential energy surfaces for N_2 -He,²¹⁻²³ N_2 - N_2 ,²⁴ and O_2 - O_2 .²⁵⁻²⁹

The recently developed dissociation model^{2,15,16} also argued that because of availability of high kinetic energies of particles in the post-shock environment molecules can dissociate even from low vibrational states in a single collision. The model used classical impulsive (sudden) approximation to calculate both dissociation thresholds and probabilities to find the colliding pair near its optimum configuration. Vibrational state-specific and rotational energy dependent dissociation rates have been derived in closed analytical form. However successful, the model^{2,15,16} is not free from problems. The impulsive approximation should certainly be correct as a high-energy asymptotic, but it is not clear if a real dissociating system is close to this limit. Additionally, the calculated probability factors¹⁶ turned out to have singularities at certain energies, which calls for more sophisticated methods of evaluating the probabilities.

In the present chapter, we suggest a theory of state-specific dissociation rates of simple diatomic molecules. The approach is essentially a modified FHO model that allows to calculate probabilities of jumps across many quantum states, if an energy transferred to a classical initially non-vibrating oscillator can be determined. The latter value is derived for three-dimensional collisions of rotating molecules in two cases: free-rotation approximation and impulsive (sudden) limit. As a result, both state-specific and thermally-averaged dissociation rates are calculated, and roles of various degrees of freedom can be quantified.

II. The FHO-based dissociation model

Consider collisions of diatomic molecules AB with atoms M in the course of which the molecule changes its vibrational quantum state from i to f :



If the molecule is modeled as a harmonic oscillator, and the collision's effect is treated as exerting a perturbing force on the oscillator, then the probability of the process (1) is:^{7, 10, 11, 18}

$$P_{VRT}(i \rightarrow f, Q) = i!f!Q^{i+f} \exp(-Q) \left| \sum_{r=0}^n \frac{(-1)^r}{r!(i-r)!(f-r)!} \frac{1}{Q^r} \right|^2 \quad (2)$$

where $n = \min(i, f)$, and $Q = \Delta E / \hbar \omega$ is the dimensionless energy (i.e. the average number of quanta) transferred to the initially non-vibrating classical oscillator in an AB-M collision.

The Forced Harmonic Oscillator (FHO) method is a consistent and convenient scaling tool, allowing close-coupled calculations of transitions across an arbitrary number of vibrational levels. This method reduces the complexity of the quantum problem to classical calculations of collisional energy transfer to an initially non-vibrating oscillator. The principal drawbacks of the FHO method are: i) anharmonicity of real molecules-oscillators, and ii) neglect of the reverse effect of the oscillator on the perturbing classical trajectory. The simplest way to account for the anharmonicity is to correct only frequency, and not the wavefunctions: for each transition $i \rightarrow f$, the quantity $\omega = |E_i - E_f| / (\hbar|i - f|)$, where E_i and E_f are the energies of the respective levels, is used as the effective oscillator frequency. To account for the oscillator feedback effect on the classical trajectory, a symmetrization procedure is commonly used whereby the effective initial velocity of the colliding pair is taken as an arithmetic average between the actual velocity and that calculated with the kinetic energy reduced by the oscillator energy increase, $E_i - E_f$.³⁰⁻³² These two simple corrections have proved to be successful in bringing the FHO-calculated vibrational energy transfer rates^{10, 11, 13} into an excellent agreement with more sophisticated quantum calculations^{21, 22, 24-26}.

To model dissociation, we need to calculate probabilities of bound-free transitions. The original FHO theory, strictly speaking, cannot describe such transitions. First of all, the discrete energy spectrum of harmonic oscillator extends to infinity. Secondly, even for a truncated oscillator, calculating probabilities of bound-free transitions is difficult and is not done directly by the FHO theory. In this paper, we will make use of the fact that, when molecular vibrations are modeled by a Morse oscillator with the lowest vibrational quantum and the anharmonicity constant equal to their known spectroscopic values, the depth of the resulting potential well exceeds the experimental value of the molecule's dissociation energy. This fact, of course, means that the Morse oscillator model is inaccurate at high vibrational levels, but it also gives an opportunity to formally model dissociation as a bound-bound transition. Specifically, we will consider transitions to any of the Morse oscillator quantum levels with energy equal to or above the experimental bond energy of the molecule to be dissociative. Obviously, transitions to the quantum levels with energies below the experimental bond energy, also approximated by the same Morse oscillator throughout the present paper, are still interpreted as bound-bound transitions. The choice of the 'cutoff' bond energy is assumed to be independent of the rotational energy of the molecules. The parameters of the intermolecular Morse potential used are listed in Table I.

Table 1. Morse potential parameters

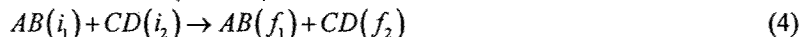
	Nitrogen	Oxygen
ω_e, cm^{-1}	2359.6	1580.3
x_e	$6.1265 \cdot 10^{-3}$	$7.639 \cdot 10^{-3}$
$D = \omega_e^2 / 4x_e, \text{cm}^{-1}$	96,287	51,718
$D_{\text{exp}}, \text{cm}^{-1}$	78,672	41,268
Total number of vibrational levels, $v_D = 1/2x_e$	81	65
Number of bound vibrational levels ($E_v < D_{\text{exp}}$)	46	35

The total probability of collisional dissociation from vibrational level i is, therefore, a sum over all final "dissociative" Morse vibrational levels:

$$P_{\text{diss}}(i) = \sum_{E_f \geq D} P_{VRT}(i \rightarrow f) \quad (3)$$

where D is the molecule's dissociation (bond) energy, and the subscript "VRT" denotes vibration-rotation-translation energy transfer.

Similarly, for molecule-molecule (AB-CD) collisions:



the dissociation probability can be defined as:

$$P_{diss}(i_1) = \sum_{E_{f_1} \geq D_{AB}} P_{VRT}(i_1 \rightarrow f_1) \quad (5)$$

As demonstrated earlier,^{11, 12} in calculating probabilities of vibrational transitions in AB molecule at high kinetic energies or temperatures, vibration-vibration (VV) exchange between AB and CD can be neglected. Since this work is devoted to high-temperature dissociation processes, we will adopt this approximation. Additionally, summing over all possible vibrational states of CD molecule can be performed. The FHO transition probability scaling^{11, 12} is then similar to that in the molecule-atom case:

$$P_{VRT}(i, \text{all} \rightarrow f, \text{all}; Q_1) = i! f! Q_1^{i+f} \exp(-Q_1) \left| \sum_{r=0}^n \frac{(-1)^r}{r!(i-r)!(f-r)!} \frac{1}{Q_1^r} \right|^2 \quad (6)$$

$$= P_{VRT}(i \rightarrow f; Q_1)$$

Here $n = \min(i, f)$, and $Q_1 = \Delta E / \hbar \omega_1$ is the dimensionless energy (i.e. the average number of quanta) transferred to the initially non-vibrating classical oscillator AB in an AB-CD collision.

Note that in Refs. 13 and 14, the exact FHO probabilities of Eqs. (2) and (6) have been reduced to the approximate analytic expressions using the asymptotic behavior of the series in the right-hand-sides of Eqs. (2) and (6) (e.g., see Ref. 11). This permitted straightforward analytic integration of the transition probabilities over the collision energies and obtaining the closed-form analytic expressions for the state-specific rate coefficients for vibrational energy transfer. Since developing a fully analytic dissociation model is beyond the scope of the present paper, we are using the exact FHO scaling expressions.

Energy transfer to a classical rotating oscillator in 3D collisions: free-rotation and impulsive approximations

From the previous section, it is clear that to evaluate probabilities of vibrational transitions, including dissociation, an energy transferred to a classical initially non-vibrating oscillator has to be calculated. For this, an adequate potential energy surface should be determined, and then classical equations of motion should be integrated for the three- or four-atom system. We will use 2 approximations permitting analytic solutions.

III.1 Free-rotation approximation

Consider collisions between a rotating symmetric diatomic molecule and an atom. For the pairwise atom-to-atom interaction described by repulsive exponential functions, the atom-molecule interaction potential can be written as follows:^{13, 21-23}

$$U(R, r, \vartheta, \varphi) = 2Ae^{-\alpha R} \cosh\left(\frac{\alpha r}{2} \cos \vartheta \cos \varphi\right) \quad (7)$$

where R is the center-of-mass distance, r is the separation of atoms in a molecule, ϑ is the rotation angle (i.e. the angle between R and r), and φ is the angular momentum vector (i.e. the angle between the plane of rotation and the radius vector R). As in earlier work¹³, we will assume that the rotation is free, that is, neither the magnitude nor the direction of the angular momentum vector change in a collision. Then the classical trajectory can be found analytically, and it is essentially an exponential function of $R(t)$ modulated by the periodic rotational factor. The resulting expression for the Q in Eq. (2) is:¹³

$$Q(E, \varepsilon, y, \vartheta, \varphi) = \frac{\theta' \xi}{4\theta} \frac{\cos^2 \vartheta \cos^2 \varphi}{\sinh^2 \left[\frac{\pi \omega}{\alpha y \gamma(\varepsilon, \vartheta, \varphi, y)} \right]} \quad (8)$$

where $E = E_{tr} + E_{rot}$ is the total collision energy, $\varepsilon = E_{rot}/E$, $y = b^2/R_m^2$, b is the impact parameter, $R_m = 2.5$ Å is the hard-sphere diameter, $s = |i-f|$ is the number of quanta transferred, $\omega = |E_f - E_i|/s \hbar$ is the average vibrational quantum for

the transition $i \rightarrow f$, $\theta' = \frac{4\pi^2 \omega^2 m}{\alpha^2 k}$, $\theta = \frac{\hbar \omega}{k}$, $u = \sqrt{2E/m}$, m is the collision reduced mass, m_o is the oscillator reduced mass, $2\xi = m/m_o$ is the ratio of the collision and oscillator reduced masses, and

$$\gamma(\varepsilon, \vartheta, \varphi, y) = \max \left[0, -\frac{\sin 2\vartheta \cos \varphi}{2} \sqrt{\xi \varepsilon} + \sqrt{(1-\varepsilon)(1-y)} \right] \quad (9)$$

The range of applicability of the free-rotation approximation was discussed in the earlier paper.¹³ In the same paper, the FHO vibrational transition probabilities calculated with this approximation were found to agree very well with the full semiclassical modeling using full potential energy surface.²³

An extension to 3D molecule-molecule collisions with rotation is straightforward.¹⁴ The potential energy can be written as:

$$U(R, r, \vartheta_1, \varphi_1, \vartheta_2, \varphi_2) = 4Ae^{-\alpha R} \cosh \left(\frac{\alpha r}{2} \cos \vartheta_1 \cos \vartheta_2 \right) \cosh \left(\frac{\alpha r}{2} \cos \vartheta_2 \cos \varphi_2 \right) \quad (10)$$

where R is the center-of-mass distance, r is the separation of atoms in the molecules, ϑ_i are the rotation angles (i.e., the angles between R and each r), and φ_i are the angular momentum vectors (i.e. the angles between the planes of rotation and the radius vector R). Having calculated the classical trajectory in this potential, assuming the free rotation, the energy transfer parameter Q turns out to be:¹⁴

$$Q_k(E, \varepsilon_1, \varepsilon_2, \vartheta_1, \varphi_1, \vartheta_2, \varphi_2, y) = \frac{\theta'_k}{4\theta_k} \frac{\cos^2 \vartheta_k \cos^2 \varphi_k}{\sinh^2 \left[\frac{\pi \omega_k}{\alpha u \gamma(\varepsilon_1, \varepsilon_2, \vartheta_1, \varphi_1, \vartheta_2, \varphi_2, y)} \right]} ; k=1, 2 \quad (11)$$

Here $E = E_{tr} + E_{rot,1} + E_{rot,2}$ is the total collision energy, $\varepsilon_k = E_{rot,k}/E$, $y = b^2/R_m^2$, b is the impact parameter, $R_m = 2.5$ Å is the hard sphere diameter, $s_k = |i_k - f_k|$ is the number of quanta transferred, $\omega_k = |E_{f,k} - E_{i,k}|/s_k \hbar$ is the average vibrational quantum for the transition $i_k \rightarrow f_k$, $\theta'_k = \frac{4\pi^2 \omega_k^2 m}{\alpha^2 k}$, $\theta_k = \frac{\hbar \omega_k}{k}$, $u = \sqrt{2E/m}$, m is the collision reduced mass, and

$$\gamma(\varepsilon_1, \varepsilon_2, \vartheta_1, \varphi_1, \vartheta_2, \varphi_2, y) = \max \left[0, -\frac{\sin 2\vartheta_1 \cos \varphi_1}{2} \sqrt{\varepsilon_1} - \frac{\sin 2\vartheta_2 \cos \varphi_2}{2} \sqrt{\varepsilon_2} + \sqrt{(1-\varepsilon_1)(1-\varepsilon_2)} \right] \quad (12)$$

III.2 Impulsive (sudden) approximation

In this approximation, AB is modeled by two hard spheres, A and B, connected by an initially non-deformed spring. Collision with an atom C, also modeled as a hard sphere, reduces to a hard-sphere collision of B and C. The center-of-mass kinetic energy, AB rotational energy, and the set of orientation angles at the moment of collision fully define the outcome of the collision. Applying energy and momentum conservation, the post-collision component of the velocity of B atom along the A-B axis can be determined, and the post-collision vibrational energy of the AB molecule calculated. Similarly, AB-CD collisions can be analyzed in the assumption that only hard spheres B and C collide directly.

The hard-sphere collision of B and C atoms can be treated as being either "smooth-sphere", where the collision is elastic along the line connecting centers of B and C, with no forces normal to that line, or "rough-sphere" one, where the collision is elastic along the line connecting B and C centers and fully inelastic perpendicular to that line.

When, in a collision, B atom receives a velocity increment Δv along the A-B axis, the initially non-vibrating AB molecule acquires vibrational energy

$$\Delta E = 2 \cdot \frac{1}{2} m \left(\frac{\Delta v}{2} \right)^2 = \frac{1}{4} m (\Delta v)^2, \quad (13)$$

where m is the mass of each of the atoms A and B. Since, in the present model, B collides directly only with C, it is convenient to introduce B velocity increments along the B-C axis, Δv_{\parallel} , and perpendicular to the B-C axis and parallel to the A-B-C plane, Δv_{\perp} , so that

$$\Delta v = \Delta v_{\parallel} \cos \theta + \Delta v_{\perp} \sin \theta. \quad (14)$$

Here θ is the angle between the A-B molecular axis and the B-C axis; $\theta \in [0, \pi/2]$. Note that the B atom velocity increment component perpendicular to both B-C axis and A-B-C plane does not contribute to Δv .

Consider now an AB-C collision in the AB-C center-of-mass system. Translational velocities of the colliding atoms B and C, $v_{B,tr}$ and $v_{C,tr}$, antiparallel to each other, are related to the center-of-mass kinetic energy, E_t , of the colliding pair by the momentum and energy equations:

$$2mv_{B,tr} = Mv_{C,tr}; 2 \cdot \frac{1}{2}mv_{B,tr}^2 + \frac{1}{2}Mv_{C,tr}^2 = E_t, \quad (15)$$

where M is the mass of C atom. The direction of $v_{B,tr}$ and $v_{C,tr}$ can be characterized by α , the angle between the velocity of the C atom (in the AB-C center-of-mass system) and the B-C axis, and by φ , the angle between $v_{B,tr}$ or $v_{C,tr}$ and the straight line parallel to the A-B-C plane and normal to the B-C axis. The intervals of variation of these angles are: $\alpha \in [0, \pi/2]$ and $\varphi \in [\pi/2 - \alpha, \pi - \alpha]$.

Additionally, atom B has a rotational velocity, $v_{B,rot}$, whose magnitude can be expressed in terms of the initial rotational energy of AB, E_r :

$$2 \cdot \frac{1}{2}mv_{B,rot}^2 = E_r, \quad (16)$$

and whose direction (obviously, normal to the A-B axis) can be characterized by the angle β between $v_{B,rot}$ and the B-C axis; $\beta \in [\pi/2 - \theta, \pi/2 + \theta]$.

Considering an elastic collision of B and C atoms along the B-C line, from the energy and momentum conservation equations we obtain:

$$\Delta v_0 = \frac{2M}{M+m} \left[(v_{B,tr} + v_{C,tr}) \cos \alpha + v_{B,rot} \cos \beta \right] = \frac{2M}{M+m} \left[\sqrt{\frac{(M+2m)E_t}{Mm}} \cos \alpha + \sqrt{\frac{E_r}{m}} \cos \beta \right] \quad (17)$$

Here we expressed velocities $v_{B,rot}$, $v_{B,tr}$, and $v_{C,tr}$ through the energies E_r and E_t according to equations (15) and (16). Since in the smooth spheres case $\Delta v_\perp = 0$, substituting Eqn. (17) into Eqn. (14), and inserting the result into Eqn. (13), we obtain the energy transferred to the initially non-vibrating oscillator in the **smooth spheres, molecule-atom** case:

$$\Delta E = \left[\frac{M}{M+m} \left(\sqrt{\frac{(M+2m)E_t}{M}} \cos \alpha + \sqrt{E_r} \cos \beta \right) \cos \theta \right]^2 \quad (18)$$

In the rough spheres case, one needs to calculate projections of all velocities of B and C atoms onto an axis perpendicular to the B-C line and parallel to the A-B-C plane. Then, from the energy and momentum equations for an absolutely inelastic collision of B and C atoms along that axis, one obtains:

$$\Delta v_\perp = \frac{M}{M+m} \left[(v_{B,tr} + v_{C,tr}) \cos \varphi - v_{B,rot} \cos \beta \cos \theta / \sin \theta \right] \quad (19)$$

Expressing velocities $v_{B,rot}$, $v_{B,tr}$, and $v_{C,tr}$ through the energies E_r and E_t according to equations (15) and (16), then substituting Eqns. (17) and (19) into Eqn. (14), and inserting the resulting formula for Δv into Eqn. (13), we obtain the energy transferred to the initially non-vibrating oscillator in the **rough spheres, molecule-atom** case:

$$\Delta E = \left\{ \frac{1}{2} \cdot \frac{M}{M+m} \cdot \left[\sqrt{\frac{(M+2m)E_t}{M}} (2 \cos \alpha \cos \theta + \cos \varphi \sin \theta) + \sqrt{E_r} \cos \beta \cos \theta \right] \right\}^2. \quad (20)$$

Similar derivations can be performed for molecule-molecule collisions. When writing energy and momentum conservation equations for B-C collisions, additional (compared with the molecule-atom case) C atom velocity components, corresponding to rotational and vibrational motion of CD molecule, have to be included, leading to additional terms in equations.

In the **molecule-molecule, smooth spheres** case:

$$\Delta E = \left[\frac{M}{M+m} \left(\sqrt{\frac{(M+m)E_t}{M}} \cos \alpha + \sqrt{E_r} \cos \beta + \sqrt{\frac{m}{M}} E'_v \cos \eta \cos \gamma_1 + \sqrt{\frac{m}{M}} E'_r \cos \gamma_2 \right) \cos \theta \right]^2 \quad (21)$$

Here, of course, we consider AB-CD collisions, with B and C atoms actually colliding. The mass of each of the atoms C and D equals M . E'_v and E'_r are the pre-collision vibrational and rotational energies of the CD molecule.

Arguments of the new cosines are: η - the phase of CD oscillations in the moment of collision, γ_1 - the angle between B-C and C-D axes, and γ_2 - the angle between the rotational velocity of C atom and the B-C axis. The intervals of variation of the new arguments are:

$$\begin{aligned} \eta &\in [0, 2\pi]; \gamma_1 \in [0, \pi]; \\ \gamma_2 &\in [\pi/2 - \gamma_1, \pi/2 + \gamma_1], \text{ if } \gamma_1 \in [0, \pi/2], \\ &\in [\gamma_1 - \pi/2, 3\pi/2 - \gamma_1], \text{ if } \gamma_1 \in (\pi/2, \pi]. \end{aligned} \quad (22)$$

In the molecule-molecule, rough spheres case:

$$\begin{aligned} \Delta E = & \left\{ \frac{1}{2} \cdot \frac{M}{M+m} \left[\sqrt{\frac{(M+m)E_t}{M}} (2\cos\alpha\cos\theta + \cos\varphi\sin\theta) \right. \right. \\ & + \sqrt{E_r} \cos\beta\cos\theta + \sqrt{\frac{m}{M}} E_v' \cos\eta (2\cos\gamma_1\cos\theta + \cos\varphi_1\sin\theta) \\ & \left. \left. + \sqrt{\frac{m}{M}} E_v' (2\cos\gamma_2\cos\theta + \cos\varphi_2\sin\theta) \right] \right\}^2 \end{aligned} \quad (23)$$

The new angles, φ_1 and φ_2 , are the angles between vectors of vibrational and rotational velocity, respectively, of C atom and the straight line parallel to the A-B-C plane and perpendicular to the B-C axis. The intervals of their variation are:

$$\begin{aligned} \varphi_1 &\in [\pi/2 - \gamma_1, \pi/2 + \gamma_1], \text{ if } \gamma_1 \in [0, \pi/2], \\ &\in (\gamma_1 - \pi/2, 3\pi/2 - \gamma_1], \text{ if } \gamma_1 \in (\pi/2, \pi] \\ \text{and} \\ \varphi_2 &\in [\pi/2 - \gamma_2, \pi/2 + \gamma_2], \text{ if } \gamma_2 \in [0, \pi/2], \\ &\in (\gamma_2 - \pi/2, 3\pi/2 - \gamma_2], \text{ if } \gamma_2 \in (\pi/2, \pi] \end{aligned} \quad (24)$$

Dissociation probabilities, cross sections, and rate coefficients

Formulas (8), (9), (11), (12), and (18)-(24) for Q and ΔE , when inserted into FHO scaling formulas (2) and (6), give sets of state-to-state transfer probabilities. Summing over the final states according to Eqs. (3) and (5), dissociation probabilities are found as functions of vibrational, rotational, and translational energies, and of the set of angles. Integrating over the angles, and assuming rotational-translational equilibrium with temperature T , gives the dissociation cross section as a function of vibrational quantum number i , total (translational plus rotational) collision energy E , and the temperature T .

The dissociation cross-section for molecule-atom collisions in the free-rotation approximation is:³¹

$$\begin{aligned} \sigma_{diss}(i, E, T) = & \frac{\pi \hbar^2}{2mT} \frac{\hbar^2}{2IT} \frac{1}{\pi^2} \int_0^{J_{max}} dJ (2J+1) \int_0^{J_{max}} dj \int_{|j-j|}^{J+j} dl \int_0^\pi d\vartheta \int_0^\pi d\varphi \cdot \sum_f P_{if} \\ & \approx \pi R_m^2 \left(\frac{E}{T} \right)^2 \frac{1}{\pi^2} \int_0^1 dy \int_0^1 d\varepsilon \int_0^\pi d\vartheta \int_0^\pi d\varphi \cdot \sum_f P_{if}(E, \varepsilon, \vartheta, \varphi, y) \end{aligned} \quad (25)$$

where I is the moment of inertia of the AB molecule. For molecule-molecule collisions in the free-rotation approximation:³²

$$\begin{aligned}
\sigma_{diss}(i, E, T) &= \frac{\pi \hbar^2}{2mT} \frac{\hbar^2}{2I_1 T} \frac{\hbar^2}{2I_2 T} \int_0^{l_{max}} dl (2l+1) \int_0^{j_{1max}} dj_1 (2j_1+1) \int_0^{j_{2max}} dj_2 (2j_2+1) \\
&\quad \cdot \frac{1}{\pi^4} \int_0^\pi d\vartheta_1 \int_0^\pi d\varphi_1 \int_0^\pi d\vartheta_2 \int_0^\pi d\varphi_2 \cdot \sum_f P_{if} \\
&\approx \pi R_m^2 \left(\frac{E}{T} \right)^3 \frac{1}{\pi^4} \int_0^1 dy \int_0^1 d\varepsilon_1 \int_0^1 d\varepsilon_2 \int_0^\pi d\vartheta_1 \int_0^\pi d\varphi_1 \int_0^\pi d\vartheta_2 \int_0^\pi d\varphi_2 \\
&\quad \cdot \sum_f P_{if}(E, \varepsilon_1, \varepsilon_2, \vartheta_1, \varphi_1, \vartheta_2, \varphi_2, y)
\end{aligned} \tag{26}$$

where I_1 and I_2 are the moments of inertia of AB and CD molecules, respectively. Similar formulas can be written for the impulsive approximation. In Eqs. (25) and (26), the rigid rotor approximation has been used. The limits of integration over the angular momenta in Eqs. (25) and (26) are determined from the condition that the cross section is evaluated at the constant total energy E of the classical degrees of freedom (i.e. the sum of translational energies of the radial and the orbital motion and the rotational energies, $E = E_{rad} + E_{orb} + E_{rot,k}$).^{31, 32} The approximate integration forms in the right-hand sides of Eqs. (25) and (26) are obtained by replacing integration over the rotational and orbital angular momenta by integration over the dimensionless rotational energies, $\varepsilon_k = E_{rot,k}/E$, and the dimensionless impact parameter $y = b^2/R_m^2$. In this procedure, replacing the appropriate integration limits for ε_k and y by unity does not significantly affect the integration accuracy since the dissociation cross section, σ_{diss} , was found to steeply drop both at the high values of rotational energies and the impact parameter (i.e. at the low values of the translational energy of the radial motion).

In this work, cross-sections were calculated at 60 values of total collision energy in the range 10^3 - 10^6 cm⁻¹. For each total collision energy E , 1000 randomly picked phase space points were used for evaluation of multi-dimensional cross-section integral. Previous calculations using this approach by Billing^{24, 25} showed that the use of only 100-400 phase space points is sufficient to obtain a 20-30% confidence in the averaged cross sections. In the present calculations, the use of 1000 phase space points allows about 10-20% accuracy in the cross sections. To account for the oscillator reaction on the classical trajectory, or, in other words, to enforce the detailed balance, a symmetrization procedure^{31, 32} was used, whereby the effective energy U was substituted for E , corresponding to the arithmetically averaging velocity before and after collision:

$$U = E + \frac{\Delta E_{if}}{2} + \frac{(\Delta E_{if})^2}{16E}; \quad E_{min} = \Delta E_{if}/4 \tag{27}$$

Averaging the dissociation flux over Maxwellian energy distribution gives vibrational state-specific dissociation rate coefficient (v is the vibrational quantum number):^{31, 32}

$$k_{diss}(v, T) = \left(\frac{8kT}{\pi m} \right)^{1/2} \int_0^\infty \sigma_{diss}(v, U, T) \exp\left(-\frac{U}{T}\right) d\left(\frac{U}{T}\right) \tag{28}$$

The integral in Eq. (28) is evaluated numerically by the RATECONS procedure³¹ using all 60 values of the cross sections given by Eqs. (25) and (26). The estimated accuracy of numerical integration is about 10%. Further averaging of the state-specific rate coefficients over the vibrational energy mode distribution function would give the total dissociation rate coefficient. In the present paper, this is done for both nonequilibrium and equilibrium vibrational mode energy distributions. In both cases, the energy distributions are assumed to be Boltzmann with vibrational temperature T_v and the gas temperature T , respectively. In the latter case, the thermal dissociation rate constant is obtained.

III. Results and discussion

To check the difference between vibrational energy transfer predicted by free-rotation and impulsive approximations, the parameter $Q = \Delta E / \hbar \omega$, averaged over collision angles, was calculated for O₂-Ar and O₂-O₂ collisions and plotted in Fig. 1 (a, b) as a function of the total (translational plus rotational) collision energy. In all free-rotation calculations done in this work, the parameters of the exponential repulsive potential of Eq. (7) were taken to be $\alpha = 4.0 \times 10^8$ cm⁻¹, which is the commonly accepted number for nitrogen and oxygen,^{10-13, 23, 24} and $A = 1730$ eV.²⁴ As seen in Fig. 1 (a, b), there is virtually no difference between smooth and rough sphere impulsive approximations. At very high energies, free-rotation and impulsive approximations converge to close asymptotics, which is physically reasonable and provides a consistency check. At moderate and low energies, the impulsive

approximation is seen to overpredict the energy transfer by orders of magnitude. Again, this could be expected, since in the impulsive approximation collision duration is assumed to be much shorter than the vibrational period, while low-velocity collisions last much longer than the period of vibrations, thus reducing the efficiency of energy transfer.

Fig. 2 (a, b) shows the dissociation probability from ground vibrational state versus total collision energy. Similar to Fig. 1, free-rotation and impulsive results are close to each other at high energies, while at low energies impulsive approximation predicts an excessively high dissociation probability.

An important step in validating any dissociation model is to compare predicted dissociation rates in thermal equilibrium with experimental data. Strictly speaking, this would require full master equation modeling, with dissociation, recombination, and energy transfer processes all taken into account. Such modeling can be done using the newly derived dissociation rates and FHO-based vibrational energy transfer rates,^{10, 11, 13, 14, 16} similar to the modeling performed earlier.^{11, 12, 16} However, such modeling is beyond the scope of this paper. For the first-cut comparison, in this work we calculated thermal dissociation rates for nitrogen and oxygen assuming the equilibrium Boltzmann vibrational energy distribution function. Of course, if atom-atom recombination is weak, the irreversible dissociation would depopulate very high vibrational states, reducing the dissociation rate by perhaps a factor of 2-3.^{1, 7, 33} If, on the other hand, recombination is significant, highly excited states would be close to equilibrium. Thus, a caution is needed when comparing computed thermal dissociation rates with experiments, as the degree to which highly excited states were close to thermal equilibrium in a specific experiment is often not clear.

In Fig. 3, a comparison with the dissociation rate inferred from shock tube measurements is shown for O₂-Ar collisions. Both free-rotation and impulsive energy transfer models in conjunction with FHO scaling give an excellent agreement with experiments in a very wide temperature range, especially considering that the experimental fit has an uncertainty range within a factor of 2-3. The agreement of the impulsive model with both experimental data and free-rotation predictions may seem somewhat surprising. The explanation lies in the fact that at thermal equilibrium the dissociation proceeds chiefly from very high vibrational levels, close to the dissociation threshold. This is well known from the literature,⁷ and is confirmed in our calculations (see below). Since spacing between vibrational levels is very small near the dissociation threshold, the Massey parameter,⁷ that is, the product of vibrational frequency and the collision duration, is small even for particles moving with mean thermal velocity. This means that most dissociative collisions at thermal equilibrium can be adequately described in the impulsive approximation.

Figure 4 shows calculated and experimental thermal dissociation rate coefficients in oxygen. One can see that both models somewhat underpredict the dissociation rate compared to the experimental data, $2.2 \times 10^{16} \exp(-59380/T) [1 - \exp(-2240/T)] \text{ cm}^3 / (\text{mole} \cdot \text{s})$.^{38, 39} The impulsive model, which provides for more efficient rotational energy transfer into the dissociating bond than the free-rotation model does, appears to be closer to experiments in this case. It is also instructive to consider the ratio of thermal dissociation rate coefficients in O₂-O₂ and O₂-Ar collisions. Both free-rotation and impulsive models predict the ratio to be about 3 and to depend on temperature very weakly. That molecule-molecule collisions are more effective than molecule-atom ones demonstrates the role of rotational energy in dissociation and is qualitatively consistent with theoretical expectations.⁷ Nikitin⁷ argued that the vibrational energy E^* , that approximately separates the regions of single-quantum and multiquantum (including bound-free) transitions is determined by the criterion that the Massey parameter calculated with vibrational frequency at the energy level E^* be of the order of unity. On the basis of this criterion, Nikitin⁷ estimated reduction in E^* due to efficient transfer of rotational energy of the non-dissociating molecule into vibrational mode of the highly-excited dissociating molecule and predicted the ratio of thermal dissociation rate coefficients in O₂-O₂ and O₂-Ar collisions to be about 10-20, independent of temperature. Experimental data quoted by Stupochenko, Losev, and Osipov,³³ specifically, O₂-O₂ data³⁴⁻³⁶ and O₂-Ar data³⁷ seem to indicate that the dissociation rate ratio decreases from 30-40 at 3500 K to about 5-10 at 7000 K. Since at thermal equilibrium dissociation in both O₂-O₂ and O₂-Ar collisions is determined by the processes at very high vibrational states, one possible reason for the less than perfect agreement between our predictions and the experiment could be an error introduced by modeling the highly excited states by Morse oscillator. Further refinement of the theoretical model, especially with regard to the energy spectrum at high vibrational levels, would clarify the issue. However, experimental data of different authors also have to be treated with caution. For example, Losev *et al.*,^{4, 5, 38} based on experimental data of Losev and Shatalov,³⁹ recommend the dissociation rate value of $2.2 \times 10^{16} \exp(-59380/T) [1 - \exp(-2240/T)] \text{ cm}^3 / (\text{mole} \cdot \text{s})$ for O₂-O₂ collisions. Together with the O₂-Ar rate $6.0 \times 10^{13} (59380/T) \exp(-59380/T) \text{ cm}^3 / (\text{mole} \cdot \text{s})$ of Camac and Vaughan,³⁷ this would give the ratio of thermal dissociation rate coefficients in O₂-O₂ and O₂-Ar collisions of about 10, weakly dependent on temperature (see Fig.

4). Considering the fact that both rates are known within a factor of 3 at best, this would mean a reasonably good agreement between our model and experiments. A detailed analysis of the experiments quoted, as well as further shock-tube experimental studies, could be helpful in developing a better understanding of dissociation processes.

Figures 5 and 6 depict calculated and experimental thermal dissociation rate coefficients for N_2 -Ar and N_2 - N_2 collisions. As seen from the figures, the agreement, within a factor of 2-3 experimental uncertainty, is uniformly excellent over the wide temperature range. Interestingly, the calculated ratio of the thermal dissociation rate coefficients for N_2 - N_2 and N_2 -Ar collisions is about 3, weakly changing with temperature, which is in a very good agreement with experiments.

As is well known,^{1, 3, 4, 33} rotational relaxation behind shocks is quite fast, while vibrational relaxation is much slower. Thus, dissociation rate coefficient as a function of vibrational energy and translational-rotational temperature is quite useful for shock modeling. When averaged over nonequilibrium vibrational distribution, such vibrational energy-dependent rate coefficient could be converted into a two-temperature rate coefficient $k(T_v, T)$. The calculated vibrational energy-dependent rates normalized by the dissociation rate from the uppermost vibrational level at several temperatures are shown in Fig. 7 for N_2 -Ar collisions. Very steep exponential increase of the rates with vibrational energy is clearly seen. Perhaps more informative is Fig. 8, where the rates from Fig. 7 have been multiplied by the equilibrium Boltzmann factor $f_v = \exp(-E_v/T)$. The plotted quantity, therefore, represents contributions of various vibrational states to the total thermal dissociation rate. As expected from theory,⁷ the principal contribution to thermal dissociation comes from states with vibrational energy close to the dissociation threshold.

The plot in Fig. 8 is helpful in understanding the degree of preferentiality of dissociation. The well-known Marrone-Treanor model³ assumes that the probability of dissociation from vibrational state with energy E_v becomes non-zero when translational collision energy exceeds the threshold $(D - E_v)$, and that there is an additional exponential increase of the probability with vibrational energy, so that the vibrational energy-dependent rate is proportional to

$$k_{MT}(E_v, T) \propto \exp\left(-\frac{D - E_v}{T}\right) \cdot \exp\left(-\frac{D - E_v}{U_{MT}}\right) \quad (29)$$

where the empirical parameter U_{MT} is a measure of preferentiality of the dissociation from higher vibrational states. The smaller U_{MT} , the more preferential dissociation is, while $U_{MT} = \infty$ corresponds to non-preferential dissociation.

Multiplying the Marrone-Treanor rate [Eq. (29)] by the Boltzmann factor $\exp(-E_v/T)$, normalizing, and plotting the product in a semi-logarithmic scale would give a linear function of vibrational energy, with the slope determining the preferentiality parameter. In Fig. 8 that shows such a plot, the free-rotation approximation is seen to predict dissociation rates that are very preferential towards higher vibrational states. However, interpreting the rates in terms of a single constant parameter U_{MT} is quite difficult. First, the functions plotted in a semi-logarithmic scale in Fig. 8 deviate substantially from linearity. Second, slopes of the curves at each vibrational energy seem to decrease with increasing temperature, so that the effective parameter U_{MT} would increase with temperature, making dissociation less preferential at higher temperatures. The impulsive model, as seen in Fig. 8, gives rates that are less preferential than those given by the free-rotation model, so that at very high temperatures the impulsive-model rates are virtually non-preferential.

Finally, the new model was tested against experimental data on nonequilibrium dissociation of nitrogen. Losev *et al.*^{4, 5, 38, 42} have measured both vibrational and translational-rotational temperatures, and the nonequilibrium factor $k(T_v, T)/k(T)$, i.e. the ratio of nonequilibrium and thermally-equilibrium dissociation rates, has been inferred from shock-tube experiments. In Ref. 38, the best fit to the measured nonequilibrium factor is obtained using a two-temperature dissociation model^{4, 5},

$$\frac{k(T_v, T)}{k(T)} = \frac{1 - \exp(-\theta/T_v)}{1 - \exp(-\theta/T)} \cdot \exp\left[-\frac{D - \beta kT}{k} \left(\frac{1}{T_v} - \frac{1}{T}\right)\right], \quad (30)$$

with $\beta=3$. In Eq. (30), $\theta=3353$ K is the characteristic vibrational temperature of N_2 . As shown in Fig. 9, the present model agrees well with the data inferred from the experiments (Eqn. (30) with $\beta=3$), considering that the latter are known within a factor of 2-3. The theoretical two-temperature dissociation rate $k(T_v, T)$ shown in Fig. 9 is obtained by averaging the state-specific rates $k(E_v, T)$ over the nonequilibrium Boltzmann distribution over the vibrational mode energy, with the vibrational temperature T_v . Note that Figs. 8 and 9 plot two essentially different characteristics of the dissociation process. Particularly, Fig. 8 shows the relative contribution of each vibrational level into the overall dissociation rate at thermal equilibrium, $k(E_v, T)f_{eq}(E_v, T)/k(T)$, where $f_{eq}(E_v, T)$ is the

equilibrium relative population. On the other hand, Fig. 9 shows *the sum of contributions of all vibrational levels* into the overall dissociation rate at nonequilibrium conditions, at $T_v < T$. In fact, only the asymptotic limit of the ratio $k(T_v, T)/k(T)$ at $T_v \rightarrow 0$, plotted in Fig. 9 shows the relative contribution of vibrational level $v=0$ alone, i.e. $k(E_v=0, T)/k(T)$.

IV. Conclusions

The new semiclassical theory of dissociation of diatomic molecules, suggested in this paper, is based upon an anharmonicity-corrected and energy-symmetrized Forced Harmonic Oscillator (FHO) quantum scaling in conjunction with free-rotation or impulsive energy-transfer models. Although the theory is not fully analytical, it is computationally simple, and it can predict both state-specific and thermal dissociation rates, explicitly accounting for molecular rotation and three-dimensional collisions, without any adjustable parameters.

Calculated thermal dissociation rates of nitrogen and oxygen are in excellent agreement with shock-tube data over a wide temperature range. Agreement with experimental data on nonequilibrium dissociation of nitrogen is also quite good.

Predicted vibrational energy-dependent rates show that dissociation from very high vibrational states is strongly favored in the free-rotation approximation. However, the preferential nature of dissociation is difficult to interpret in terms of a single Marrone-Treanor parameter U_{MT} , as this parameter would be vibrational energy dependent and increase with temperature. The impulsive approximation for energy transfer results in dissociation rates with relatively little preference for high vibrational states.

A possible future refinement of the theory would involve using a more sophisticated and precise energy spectrum of highly vibrationally excited molecules. For practical application in CFD or DSMC analyses, the theory could be used to either generate a set of tabulated rates or to develop simple interpolation formulas.

REFERENCES

- ¹ C.Park, *Nonequilibrium Hypersonic Aerothermodynamics* (Wiley, N.Y., 1990).
- ² S.O.Macheret, Paper AIAA 97-2501, 1997.
- ³ P.V.Marrone and C.E.Treanor, *Phys. Fluids* **6**, 1215 (1963).
- ⁴ S.A.Losev, Paper AIAA 96-2026, 1996.
- ⁵ A.L.Sergievskaya, E.A.Kovach, S.A.Losev, and N.M.Kuznetsov, Paper AIAA 96-1895, 1996.
- ⁶ C.Park, *J. Thermophys. and Heat Transfer* **2**, 8 (1988); *ibid.*, **3**, 233 (1989).
- ⁷ E.E.Nikitin, *Theory of Elementary Atomic and Molecular Processes in Gases* (Clarendon Press, Oxford, 1974), Chap. 7.
- ⁸ R.N.Schwartz, Z.I.Slawsky, and K.F.Herzfeld, *J. Chem. Phys.* **22**, 767 (1954).
- ⁹ S.P.Sharma, W.Huo, and C.Park, Paper AIAA 88-2714, 1988.
- ¹⁰ I.V.Adamovich, S.O.Macheret, J.W.Rich, and C.E.Treanor, *AIAA Journal* **33**, 1064 (1995).
- ¹¹ I.V.Adamovich, S.O.Macheret, C.E.Treanor, and J.W.Rich, *J. Thermophys. and Heat Transfer* **12**, 57 (1998).
- ¹² I.V.Adamovich, J.W.Rich, and S.O.Macheret, *J. Thermophys. and Heat Transfer* **11**, 261 (1997).
- ¹³ I.V.Adamovich and J.W.Rich, *J. Chem. Phys.* **109**, 7711 (1998).
- ¹⁴ I.V.Adamovich and J.W.Rich, Paper AIAA 99-3565, 1999.
- ¹⁵ S.O.Macheret and J.W.Rich, *Chem. Phys.* **174**, 25 (1993).
- ¹⁶ a) S.O.Macheret, A.A.Fridman, I.V.Adamovich, J.W.Rich, and C.E.Treanor, Paper AIAA 94-1984, 1994; b) I.V.Adamovich, S.O.Macheret, J.W.Rich, C.E.Treanor, and A.A.Fridman, "Vibrational Relaxation, Nonequilibrium Chemical Reactions, and Kinetics of NO Formation Behind Strong Shock Waves", in M. Capitelli (ed.) "Molecular Physics and Hypersonic Flows", NATO Advanced Study Institute Series, vol. 482, Kluwer, 1996, p. 85-104.
- ¹⁷ E.H.Kerner, *Can. J. Phys.* **36**, 371 (1958).
- ¹⁸ C.E.Treanor, *J. Chem. Phys.* **43**, 532 (1965).
- ¹⁹ A.Zelechow, D.Rapp, and T.E.Sharp, *J. Chem. Phys.* **49**, 286 (1968).
- ²⁰ J.D.Kelley, *J. Chem. Phys.* **56**, 6108 (1972).
- ²¹ A.J.Banks, D.C.Clary, and H.-J.Werner, *J. Chem. Phys.* **84**, 3788 (1986).
- ²² G.D.Billing, *Chem. Phys.* **107**, 39 (1986).
- ²³ M.M.Maricq, E.A.Gregory, C.T.Wickham-Jones, D.J.Cartwright, and C.J.S.M.Simpson, *Chem. Phys.* **75**, 347 (1983).
- ²⁴ G.D.Billing and E.R.Fisher, *Chem. Phys.* **43**, 395 (1979).

- ²⁵ G.D.Billing and R.E.Kolesnick, Chem. Phys. Lett. **200**, 382 (1992).
²⁶ R.Hernandez, R.Toumi, and D.C.Clary, J. Chem. Phys. **102**, 9544 (1995).
²⁷ J.M.Price, J.A.Mack, C.A.Rogaski, and A.M.Wodtke, Chem. Phys. **175**, 83 (1993).
²⁸ H.Park and T.G.Slanger, J. Chem. Phys. **100**, 287 (1994).
²⁹ M.Klatt, I.W.M.Smith, R.P.Tuckett, and G.N.Ward, Chem. Phys. Lett. **224**, 253 (1994).
³⁰ G.D.Billing, in *Nonequilibrium Vibrational Kinetics*, ed. by M.Capitelli (Springer, Berlin, 1986), p. 85.
³¹ G.D.Billing, Computer Physics Communications **32**, 45 (1984).
³² G.D.Billing, Computer Physics Communications **44**, 121 (1987).
³³ Ye.V.Stupochenko, S.A.Losev, and A.I.Osipov, *Relaxation in Shock Waves* (Springer-Verlag, New York, 1967).
³⁴ S.A.Losev, Doklady Acad. Sci. SSSR **141**, 894 (1961).
³⁵ D.L.Matthews, Phys. Fluids **2**, 170 (1959).
³⁶ S.R.Byron, J. Chem. Phys. **30**, 1380 (1959).
³⁷ M.Camac and A.Vaughan, J. Chem. Phys. **34**, 460 (1961).
³⁸ S.A.Losev and G.G.Chernyi, eds., "Analysis of Russian Experimental Investigations for Validation of Kinetic Models for Hypersonic Flows in Thermal Nonequilibrium," Final Report on the Research Grant No. 93-0987-01 by and between the North Carolina State University and Avogadro Center of Institute of Mechanics (Moscow State University, 1993).
³⁹ S.A.Losev and O.P.Shatalov, Doklady Acad. Nauk SSSR **185**, 293 (1969) [Russian].
⁴⁰ J.P.Appleton, M.Steinberg, and D.J.Liquornik, J. Chem. Phys. **48**, 599 (1968).
⁴¹ S.Byron, J. Chem. Phys. **44**, 1378 (1966).
⁴² S.A.Losev and M.S.Yalovik, Khimiia Vysokikh Energii (High Energy Chemistry) **4**, 202 (1970) [Russian].

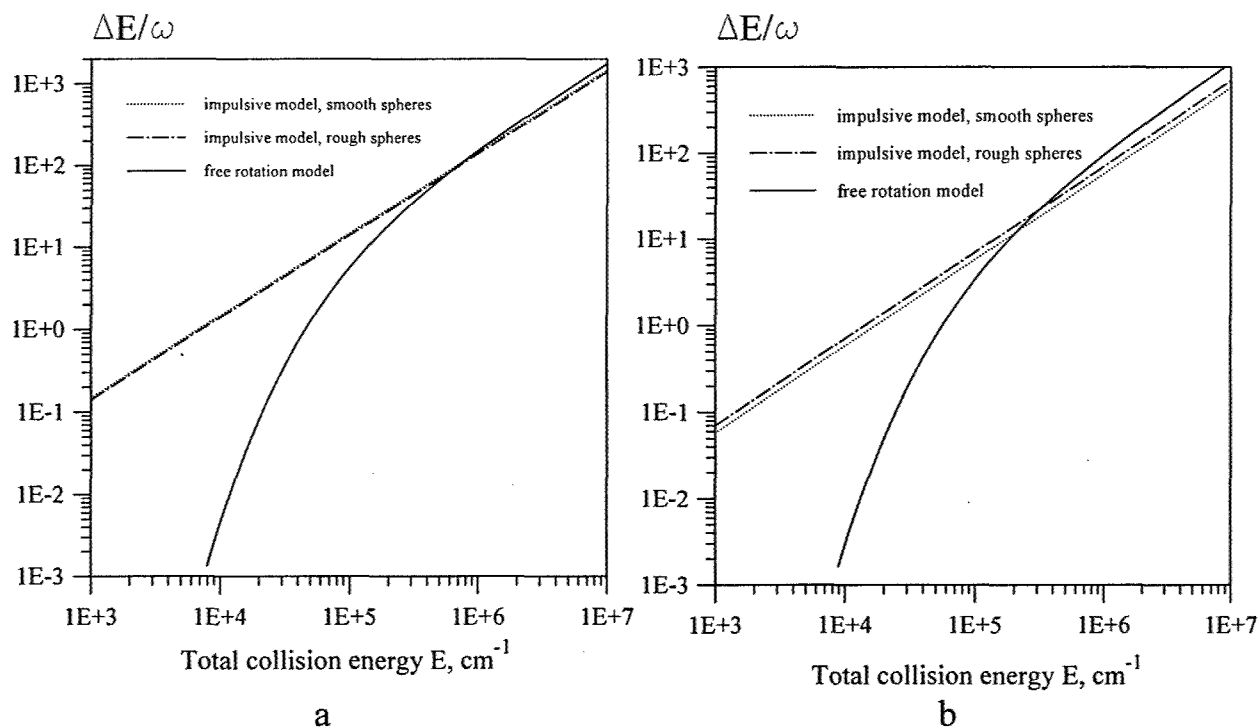


Fig.1a, b. Average number of quanta transferred to initially non-vibrating oxygen molecule versus total collision energy, as given by impulsive and free-rotation models. (a) O_2 -Ar collisions; (b) O_2 - O_2 collisions

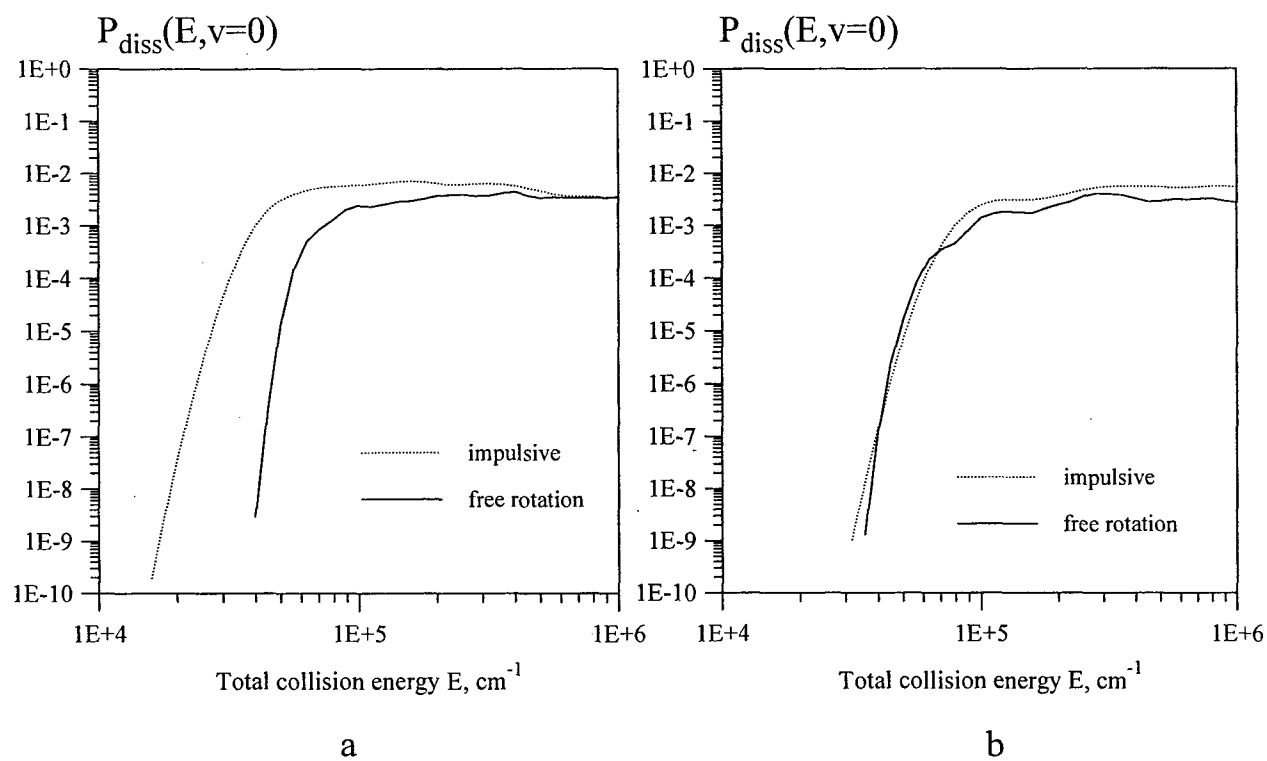


Fig. 2 a, b. Probability of oxygen molecule dissociation from the ground vibrational state versus total collision energy, as calculated with impulsive and free-rotation models. (a) $\text{O}_2\text{-Ar}$ collisions; (b) $\text{O}_2\text{-O}_2$ collisions

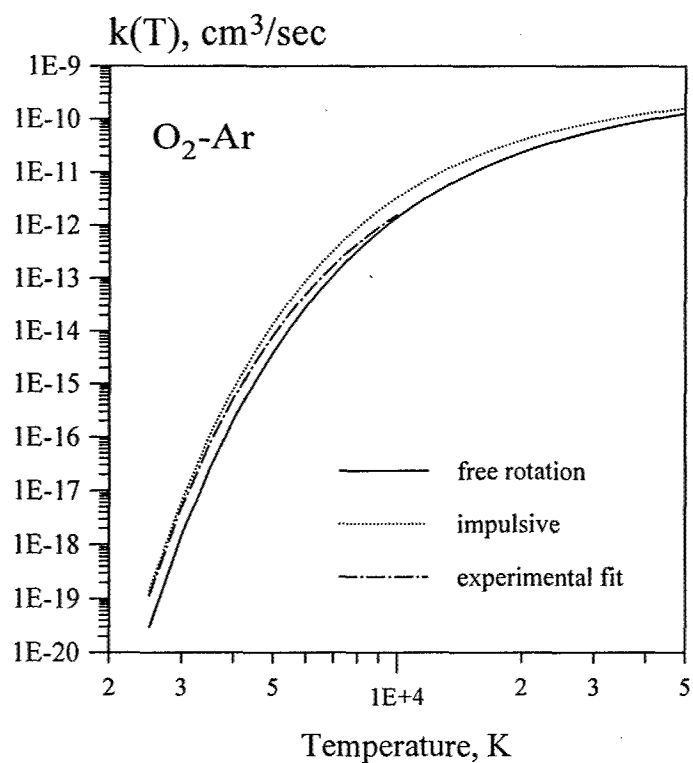


Fig. 3. Computed and inferred from experiments³⁷ thermal dissociation rate constant for oxygen diluted in argon

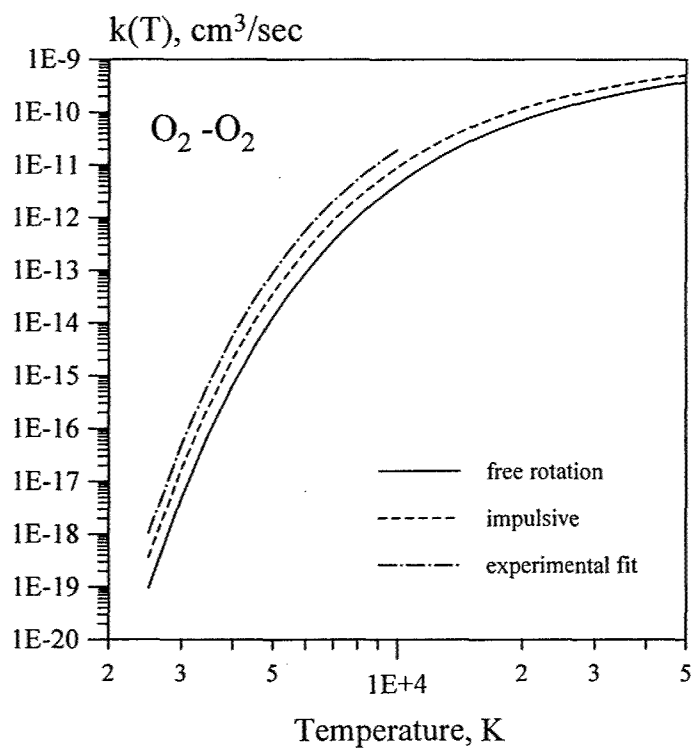


Fig. 4. Computed and inferred from experiments³⁴⁻³⁶ thermal dissociation rate constant for oxygen

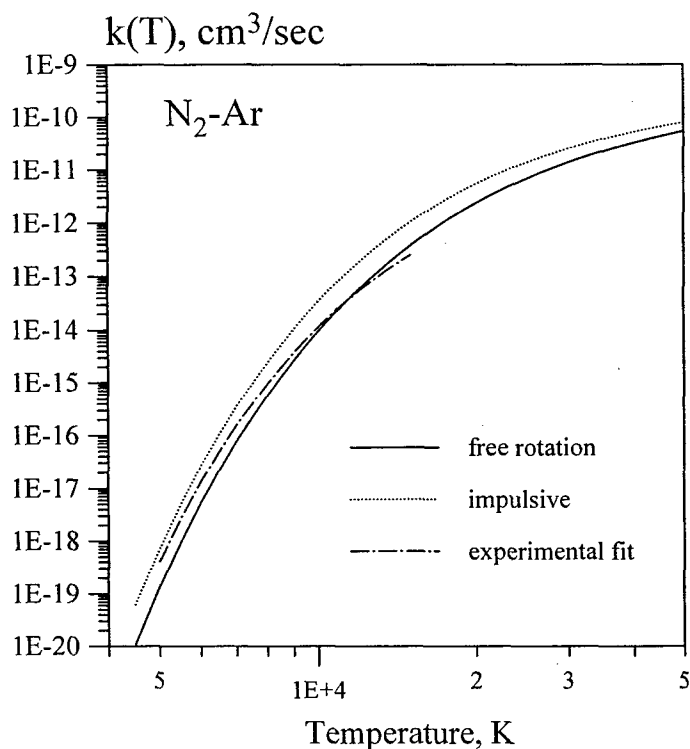


Fig. 5. Calculated and experimental⁴⁰ nitrogen thermal dissociation rates in N_2 -Ar collisions versus temperature.

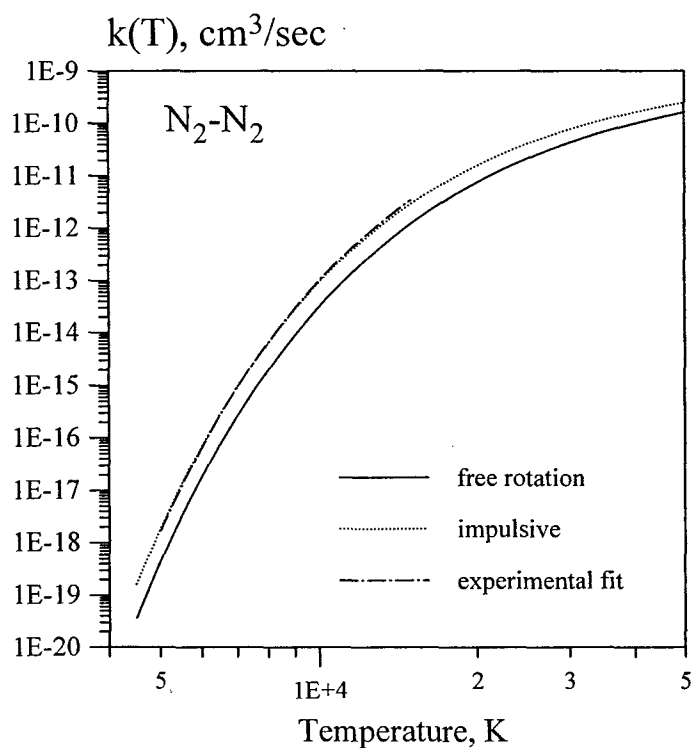


Fig. 6. Calculated and experimental⁴¹ thermal dissociation rate of nitrogen in N_2 - N_2 collisions versus temperature.

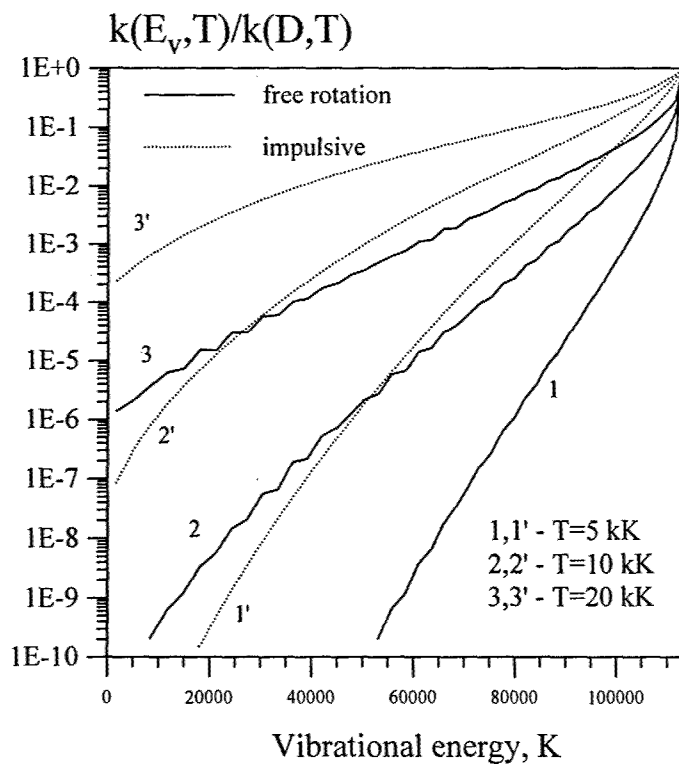


Fig. 7. Calculated state-specific dissociation rates in N_2 -Ar collisions, normalized by the dissociation rate from the uppermost vibrational level.

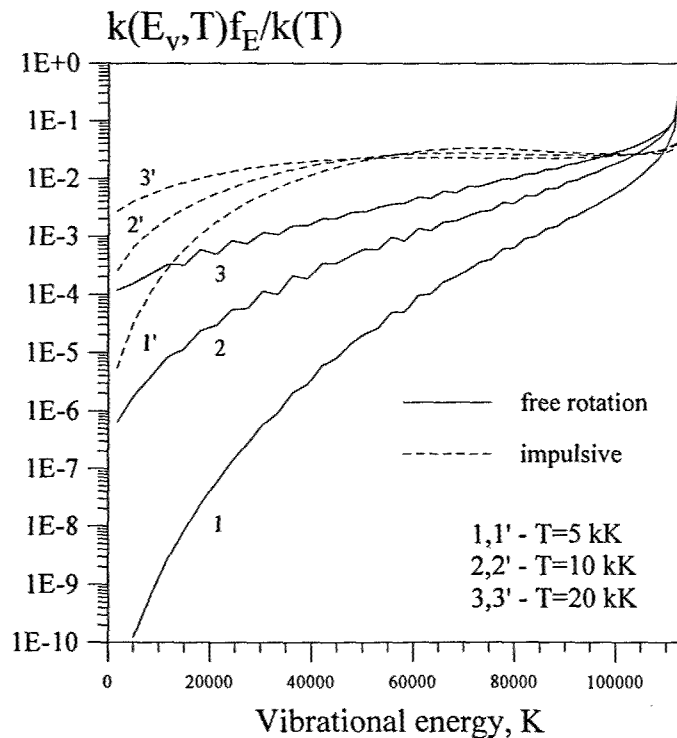


Fig. 8. Calculated state-specific dissociation rates in N_2 -Ar collisions, multiplied by the Boltzmann population factor and normalized by the thermal dissociation rate.

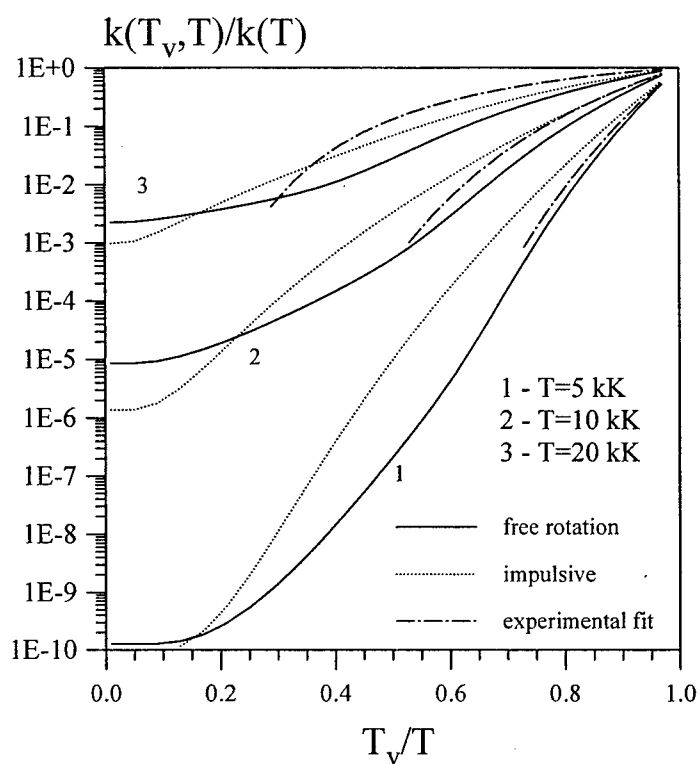


Fig. 9. Comparison of calculated and experimental^{4, 5, 38, 42} nonequilibrium factors, i.e., the ratios of nonequilibrium and equilibrium dissociation rates, in pure nitrogen versus the ratio of vibrational and translational-rotational temperatures.

Personnel Supported

Richard Miles, Professor, Co-Principal Investigator
Sergey Macheret, Research Scientist, Co-Principal Investigator
Mikhail Shneider, Research Staff
Philip Efthimion, Principal Scientist (Princeton Plasma Physics Laboratory)
Sohail Zaidi, Research Staff
Yury Ionikh, Visiting Researcher
Philip Howard, Technical Staff
Azer Yalin, Ph.D. student
Brendan McAndrew, Ph.D. Student
Xingguo Pan, Ph.D. student
Lipeng Qian, Ph.D. student
Richard P. Clark, undergraduate student

Publications

Books and Book Chapters

1. G. G. Chernyi, S. A. Losev, S. O. Macheret, and B. V. Potapkin, *Physical and Chemical Processes in Gas Dynamics, Vol. I: Cross Sections and Rate Constants*, Progress in Astronautics and Aeronautics, Volume 196, AIAA, 2002.
2. Richard B. Miles, "Planar Laser Imaging," Chapter 5, pp. 93-122 in "Flow Visualization--Techniques and Examples," Edited by A.J. Smits and T.T. Lim, Imperial College Press, London, November 2000.
3. Richard B. Miles, "Flow Field Diagnostics," Chapter 7, in Applied Combustion Diagnostics, Edited by Katharina Kohse-Hoeinghaus and Jay Jeffries, Taylor & Francis, New York, 2002.

Journal papers

1. A.P. Yalin and R.B. Miles, "Ultraviolet Filtered Rayleigh Scattering Temperature Measurements with a Mercury Filter," *Optics Letters*, Vol. 24, No. 9, May 1, 1999, pp. 590-592.
2. Y.Z. Ionikh, N.V. Chernysheva, A.V. Meshchanov, A.P. Yalin, and R.B. Miles, "Direct Evidence for Thermal Mechanism of Plasma Influence on Shock Wave Propagation," *Physics Letters A*, Vol. 259, No. 5, August 23, 1999, pp. 387-392.
3. P.F. Barker, J.H. Grinstead, and Richard B. Miles, "Single-Pulse Temperature Measurement in Supersonic Air Flow with Predissociated Laser-Induced Thermal Gratings," *Optics Communications*, Vol. 168, Sept. 1, 1999, pp. 177-182.
4. P. Wu, W.R. Lempert, and R.B. Miles, "MHz Pulse-Burst Laser and Visualization of Shockwave/Boundary Layer Interaction," *AIAA Journal J.*, Vol. 38, No. 4, April 2000, pp. 672-679.
5. A.P. Yalin, R.B. Miles, "Temperature Measurements by Ultraviolet Filtered Rayleigh Scattering Using a Mercury Filter," *J. Thermophysics and Heat Transfer*, Vol. 14, No. 2, April-June 2000, pp. 210-215.
6. P. Wu and R.B. Miles, "High Energy, Pulse-Burst Laser System for MHz-Rate Flow Visualization," *Optics Letters*, Vol. 25, No. 22, Nov. 15, 2000, pp. 1639-1641.
7. S.O. Macheret and I.V. Adamovich, "Semiclassical Modeling of State-Specific Dissociation Rates in Diatomic Gases," *J. Chem. Phys.*, 2000, Vol. 113, No. 17, p. 7351.

8. S. O. Macheret, M. N. Shneider, R. B. Miles, and R. J. Lipinski, "Electron Beam Generated Plasmas in Hypersonic Magnetohydrodynamic Channels", *AIAA Journal*, 2001, Vol. 39, No. 6, pp. 1127-1136.
9. S. O. Macheret, M. N. Shneider, and R. B. Miles, "Modeling of Discharges Generated by Electron Beams in Dense Gases: Fountain and Thunderstorm Regimes", *Physics of Plasmas*, 2001, Vol. 8, No. 5, pp. 1518-1528.
10. S. O. Macheret, Yu. Z. Ionikh, N. V. Chernysheva, A. P. Yalin, L. Martinelli, and R. B. Miles, "Shock Wave Propagation and Dispersion in Glow Discharge Plasmas," *Physics of Fluids*, Vol. 13, No. 9, 2001, pp. 2693-2705.
11. R.B. Miles, W. Lempert, and J. Forkey, "Laser Rayleigh Scattering," *J. of Measurement Science & Technology*, Vol. 12, (May 2001) R33-R51 **Invited** (Published by the Institute of Physics Publishing, Bristol, England).
12. S. O. Macheret, M. N. Shneider, and R. B. Miles, "Magnetohydrodynamic Control of Hypersonic Flow and Scramjet Inlets Using Electron Beam Ionization," *AIAA Journal*, Vol. 40, No. 1, 2002, pp. 74-81.
13. S. O. Macheret, M. N. Shneider, and R. B. Miles, "MHD Power Extraction from Cold Hypersonic Air Flow with External Ionizers", *Journal of Propulsion and Power*, Vol. 18, No. 2, 2002, pp. 424-431.
14. S. O. Macheret, M. N. Shneider, and R. B. Miles, "Modeling of Air Plasma Generation by Repetitive High-Voltage Nanosecond Pulses," *IEEE Transactions on Plasma Science*, Vol. 30, No. 3, June 2002, pp. 1301-1314.
15. G. V. Candler, J. D. Kelley, S. O. Macheret, M. N. Shneider, and I. V. Adamovich, "Effects of Vibrational Relaxation, Thermal Non-Uniformities, and Unsteady Phenomena on Supersonic Blunt Bodies," *AIAA Journal*, Vol. 40, No. 9, September 2002, pp. 1803-1810.
16. X. Pan, P.F. Barker, A. Meschanov, J.H. Grinstead, M.N. Shneider, and R.B. Miles, "Temperature Measurements by Coherent Rayleigh Scattering," *Optics Letters*, Vol. 27, No. 3, February 1, 2002, pp. 161-163.
17. S.H. Zaidi, Z. Tang, A.P. Yalin, P. Barker, R.B. Miles, "Filtered Thomson Scattering in an Argon Plasma," *AIAA Journal*, Vol. 40, No. 6, June 2002, pp. 1087-1093.
18. A.P. Yalin, Y.Z. Ionikh, and R.B. Miles, "Gas Temperature Measurements in Weakly Ionized Glow Discharges with Filtered Rayleigh Scattering," *Applied Optics*, Vol. 41, No. 18, June 20, 2002, pp. 3753-3762.
19. X. Pan, M.N. Shneider, and R.B. Miles, "Coherent Rayleigh-Brillouin Scattering," *Physical Review Letters*, Vol. 89, No. 18 (article #183001), Oct. 28, 2002.

AIAA papers and other published conference proceedings

1. A. Yalin, Y. Ionikh, and R. Miles, "Ultraviolet Filtered Rayleigh Scattering Temperature Measurements Using a Mercury Filter," Paper #AIAA-99-0642, 37th AIAA Aerospace Sciences Meeting, Reno, NV, Jan. 11-14, 1999.
2. P.F. Barker, J.H. Grinstead, and R.B. Miles, "Temperature Measurement in a Supersonic Air Flow with Resonant Laser-Induced Thermal Gratings," Paper #AIAA-99-0644, 37th AIAA Aerospace Sciences Meeting, Reno, NV, Jan. 11-14, 1999.
3. S. Macheret, L. Martinelli, and R. Miles, "Shock Wave Propagation and Structure in Nonuniform Gases and Plasmas," Paper #AIAA-99-0598, 37th AIAA Aerospace Sciences Meeting, Reno, NV, Jan. 11-14, 1999.
4. S. O. Macheret and I. V. Adamovich, "Nonequilibrium Dissociation at High Temperature: the Role of Vibrational and Rotational Energy," Paper #AIAA 99-0351, 37th AIAA Aerospace Sciences Meeting, Reno, NV, Jan. 11-14, 1999.

5. M.N. Shneider, S.O. Macheret, and R.B. Miles, "Electrode Sheaths and Boundary Layers in Hypersonic MHD Channels," Paper #AIAA-99-3532, 30th AIAA Plasmadynamics & Lasers Conference, Norfolk, VA, June 28-July 1, 1999.
6. A. Yalin, Y. Ionikh, and R. Miles, "Temperature Measurements in Glow Discharges with Ultraviolet Filtered Rayleigh Scattering," Paper #AIAA-99-3431, 30th AIAA Plasmadynamics and Lasers Conference, Norfolk, VA, June 28-July 1, 1999.
7. S.O. Macheret, M.N. Shneider, and R.B. Miles, "New Types of Electron Beam Generated Electric Discharges in Dense Gases: A "Fountain" and a "Thunderstorm," Paper #AIAA-99-3721, 30th AIAA Plasmadynamics & Lasers Conference, Norfolk, VA, June 28-July 1, 1999.
8. S.O. Macheret, M.N. Shneider, and R.B. Miles, "Electron Beam Generated Plasmas in Hypersonic MHD Channels," Paper #AIAA-99-3635, 33rd AIAA Thermophysics Conference, Norfolk, VA, June 28-July 1, 1999. **(Invited)**
9. S.O. Macheret, P.F. Barker, K. Waichman, R.B. Miles, E. Ploenjes, P. Palm, I.V. Adamovich, W.R. Lempert, and J.W. Rich, "Optically Pumped and Controlled Electric Discharges, Paper #AIAA-99-3636, 33rd AIAA Thermophysics Conference, Norfolk, VA, June 28-July 1, 1999.
10. S.O. Macheret, Y.Z. Ionikh, L. Martinelli, P.F. Barker, and R. B. Miles, "External Control of Plasmas for High-Speed Aerodynamics," Paper #AIAA-99-4853, AIAA 9th International Space Planes and Hypersonic Systems and Technologies Conference and 3rd Weakly Ionized Gases Workshop, Norfolk, VA, Nov. 1-5, 1999.
11. R. L. Chase, U. B. Mehta, D. W. Bogdanoff, C. Park, S. Lawrence, M. Aftosmis, S. O. Macheret, and M. N. Shneider, "Comments on an MHD Energy Bypass Engine Powered Spaceliner", Paper AIAA-99-4965, AIAA 9th International Space Planes and Hypersonic Systems and Technologies Conference and 3rd Weakly Ionized Gases Workshop, Norfolk, VA, Nov. 1-5, 1999.
12. S.O. Macheret, M.N. Shneyder, and R. B. Miles, "MHD Power Extraction from Cold Hypersonic Air Flow with External Ionizers," Paper #AIAA-99-4800, AIAA 9th International Space Planes and Hypersonic Systems and Technologies Conference and 3rd Weakly Ionized Gases Workshop, Norfolk, VA, Nov. 1-5, 1999.
13. A.P. Yalin, Y. Ionikh, A. Meshchanov, and R.B. Miles, "2-D Temperature Fields in Glow Discharges Measured with Ultraviolet Filtered Rayleigh Scattering," Paper #AIAA-2000-0375, 38th AIAA Aerospace Sciences Meeting and Exhibit, Reno, NV, January 10-13, 2000.
14. Y. Ionikh, N.V. Chernysheva, A.P. Yalin, S.O. Macheret, L. Martinelli, and R.B. Miles, "Shock Wave Propagation Through Glow Discharge Plasmas: Evidence of Thermal Mechanism of Shock Dispersion," Paper #AIAA-2000-0714, 38th AIAA Aerospace Sciences Meeting and Exhibit, Reno, NV, January 10-13, 2000.
15. B. McAndrew, P. Barker, and R.B. Miles, "Development of a Supersonic Plasma Wind Tunnel," Paper #AIAA-2000-0533, 38th AIAA Aerospace Sciences Meeting and Exhibit, Reno, NV, January 10-13, 2000.
16. S.O. Macheret, M.N. Shneider, and R.B. Miles, "MHD Power Generation and Control of Hypersonic Flows Ionized by Electron Beams," Second Workshop on Magneto- and Plasma Aerodynamics for Aerospace Applications, Institute Of High Temperatures, Russian Academy of Sciences, Moscow, Russia, April 5-7, 2000.
17. S.O. Macheret, Yu.Z. Ionikh, N.V. Chernysheva, A.P. Yalin, L. Martinelli, B. McAndrew, P.F. Barker, M.N. Shneider, and R.B. Miles, "Shock Propagation in Weakly Ionized Gases and Plasma Control of High-Speed Flows," Second Workshop on Magneto- and Plasma Aerodynamics for Aerospace Applications, Institute Of High Temperatures, Russian Academy of Sciences, Moscow, Russia, April 5-7, 2000.
18. R.B. Miles, "Flow Control by Energy Addition into High-Speed Air," AIAA-2000-2324, Fluids 2000, Denver, CO, June 19-22, 2000. **(Invited)**

19. S.O. Macheret, M.N. Shneider, and R.B. Miles, "Modeling of Air Plasma Generation by Electron beams and High-Voltage Pulses," AIAA-2000-2569, 31st AIAA Plasmadynamics and Lasers Conference, Denver, CO, June 19-22, 2000.
20. S. Zaidi, Z. Tang, A. Yalin, P. Barker, and R. Miles, "Filtered Thomson Scattering in an Argon Plasma," Paper #AIAA-2001-0415, 39th AIAA Aerospace Sciences Meeting & Exhibit, Reno, NV, Jan. 8-11, 2001.
21. S. Macheret, M. Shneider, and R. Miles, "MHD Control of External Supersonic Flow with Electron Beam Ionization," Paper #AIAA-2001-0492, 39th AIAA Aerospace Sciences Meeting & Exhibit, Reno, NV, Jan. 8-11, 2001.
22. P. Barker, A. Meschanov, and R. Miles, "Temperature Measurements in Plasmas Using Coherent Rayleigh Scattering," Paper #AIAA-2001-0416, 39th AIAA Aerospace Sciences Meeting & Exhibit, Reno, NV, Jan. 8-11, 2001.
23. S. Macheret, M. Shneider, and R. Miles, "Potential Performance of Supersonic MHD Power Generators," Paper #AIAA-2001-0795, 39th AIAA Aerospace Sciences Meeting & Exhibit, Reno, NV, Jan. 8-11, 2001.
24. G. V. Candler, S. O. Macheret, M. N. Shneider, I. V. Adamovich, and J. D. Kelley, "Modeling of RF Plasma Kinetics and Aerodynamics of the AEDC Ballistic Range Experiments," Paper AIAA 2001-0494, 39th AIAA Aerospace Sciences Meeting & Exhibit, Reno, NV, Jan. 8-11, 2001.
25. S.O. Macheret, M.N. Shneider, and R.B. Miles, "MHD Control of Scramjet Inlets and On-Board Power Generation," Third Workshop on Magneto- and Plasma Aerodynamics for Aerospace Applications, Institute Of High Temperatures, Russian Academy of Sciences, Moscow, Russia, April 25-27, 2001.
26. S.O. Macheret, M.N. Shneider, and R.B. Miles, "Efficient Generation of Nonequilibrium Plasmas by High-Energy Electrons," Third Workshop on Magneto- and Plasma Aerodynamics for Aerospace Applications, Institute Of High Temperatures, Russian Academy of Sciences, Moscow, Russia, April 25-27, 2001.
27. S.O. Macheret, M.N. Shneider, L. Martinelli, R. Murray, B. McAndrew, R.B. Miles, J. Fox, and J. Kline, "Plasma Control of Shock Waves in Aerodynamics and Sonic Boom Mitigation," Third Workshop on Magneto- and Plasma Aerodynamics for Aerospace Applications, Institute Of High Temperatures, Russian Academy of Sciences, Moscow, Russia, April 25-27, 2001.
28. S.O. Macheret, M.N. Shneider, and R.B. Miles, "Energy-Efficient Generation of Nonequilibrium Plasmas and their Applications to hypersonic MHD Systems," Paper AIAA-2001-2880, 32nd AIAA Plasmadynamics and Lasers Conference and 4th Weakly Ionized Gases Workshop, Anaheim, CA, June 11-14, 2001.
29. S.O. Macheret, M.N. Shneider, and R.B. Miles, "Modeling of Plasma Generation in Repetitive Ultra-short DC, Microwave, and Laser Pulses," Paper AIAA-2001-2940, 32nd AIAA Plasmadynamics and Lasers Conference and 4th Weakly Ionized Gases Workshop, Anaheim, CA, June 11-14, 2001.
30. R.B. Miles, S.O. Macheret, L. Martinelli, R. Muray, M. Shneider, Yu.Z. Ionikh, J. Kline and J. Fox, "Plasma Control of Shock Waves in Aerodynamics and Sonic Boom Mitigation," Paper AIAA-2001-3062, AIAA Plasmadynamics and Lasers Conference and 4th Weakly Ionized Gases Workshop, Anaheim, CA, June 11-14, 2001.
31. B. McAndrew, R. Murray, M. Shneider, R. Miles, J. Kline and J. Fox, "Comparison of Numerical and Experimental Results from Localized Microwave-Driven Plasma Energy Addition into a Mach 3 Flow," Paper AIAA-2001-3061, AIAA Plasmadynamics and Lasers Conference and 4th Weakly Ionized Gases Workshop, Anaheim, CA, June 11-14, 2001.
32. R.B. Miles, S.O. Macheret, and M.N. Shneider, "High Efficiency, Nonequilibrium Air Plasmas Sustained by High Energy Electrons," Paper #869, PPS-2001, ICOPS 2001, Las Vegas, NV, June 17-22, 2001.
33. S.O. Macheret, M.N. Shneider, and R.B. Miles, "Dynamics of Plasmas Sustained by Repetitive Ultrahigh

Voltage DC or Subpicosecond Laser Pulses," Paper #766, PPS-2001, ICOPS 2001, Las Vegas, NV, June 17-22, 2001.

- 34. S. Zaidi, Z. Tang, and R.B. Miles, "Rubidium Filtered Thomson Scattering Measurement in an Atmospheric Pressure Argon Arc," Paper #339, PPS-2001, ICOPS 2001, Las Vegas, NV, June 17-22, 2001.
- 35. M.N. Shneider, S.O. Macheret, and R.B. Miles, "Properties of Electron Beam Generated, Steady-State, Weakly Ionized Plasmas in Air," Paper #682, PPS-2001, ICOPS 2001, Las Vegas, NV, June 17-22, 2001.

Interactions/Transitions

a. Presentations at meetings, conferences, seminars, etc.

- 36. A. Yalin, Y. Ionikh, and R. Miles, "Ultraviolet Filtered Rayleigh Scattering Temperature Measurements Using a Mercury Filter," Paper #AIAA-99-0642, 37th AIAA Aerospace Sciences Meeting, Reno, NV, Jan. 11-14, 1999.
- 37. P.F. Barker, J.H. Grinstead, and R.B. Miles, "Temperature Measurement in a Supersonic Air Flow with Resonant Laser-Induced Thermal Gratings," Paper #AIAA-99-0644, 37th AIAA Aerospace Sciences Meeting, Reno, NV, Jan. 11-14, 1999.
- 38. S. Macheret, L. Martinelli, and R. Miles, "Shock Wave Propagation and Structure in Nonuniform Gases and Plasmas," Paper #AIAA-99-0598, 37th AIAA Aerospace Sciences Meeting, Reno, NV, Jan. 11-14, 1999.
- 39. S. O. Macheret and I. V. Adamovich, "Nonequilibrium Dissociation at High Temperature: the Role of Vibrational and Rotational Energy," Paper AIAA 99-0351, 37th AIAA Aerospace Sciences Meeting, Reno, NV, Jan. 11-14, 1999.
- 40. M.N. Shneider, S.O. Macheret, and R.B. Miles, "Electrode Sheaths and Boundary Layers in Hypersonic MHD Channels," Paper #AIAA-99-3532, 30th AIAA Plasmadynamics & Lasers Conference, Norfolk, VA, June 28-July 1, 1999.
- 41. A. Yalin, Y. Ionikh, and R. Miles, "Temperature Measurements in Glow Discharges with Ultraviolet Filtered Rayleigh Scattering," Paper #AIAA-99-3431, 30th AIAA Plasmadynamics and Lasers Conference, Norfolk, VA, June 28-July 1, 1999.
- 42. S.O. Macheret, M.N. Shneider, and R.B. Miles, "New Types of Electron Beam Generated Electric Discharges in Dense Gases: A "Fountain" and a "Thunderstorm," Paper #AIAA-99-3721, 30th AIAA Plasmadynamics & Lasers Conference, Norfolk, VA, June 28-July 1, 1999.
- 43. S.O. Macheret, M.N. Shneider, and R.B. Miles, "Electron Beam Generated Plasmas in Hypersonic MHD Channels," Paper #AIAA-99-3635, 33rd AIAA Thermophysics Conference, Norfolk, VA, June 28-July 1, 1999. (Invited)
- 44. S.O. Macheret, P.F. Barker, K. Waichman, R.B. Miles, E. Ploenjes, P. Palm, I.V. Adamovich, W.R. Lempert, and J.W. Rich, "Optically Pumped and Controlled Electric Discharges, Paper #AIAA-99-3636, 33rd AIAA Thermophysics Conference, Norfolk, VA, June 28-July 1, 1999.
- 45. S.O. Macheret, Y.Z. Ionikh, L. Martinelli, P.F. Barker, and R. B. Miles, "External Control of Plasmas for High-Speed Aerodynamics," Paper #AIAA-99-4853, AIAA 9th International Space Planes and Hypersonic Systems and Technologies Conference and 3rd Weakly Ionized Gases Workshop, Norfolk, VA, Nov. 1-5, 1999.
- 46. R. L. Chase, U. B. Mehta, D. W. Bogdanoff, C. Park, S. Lawrence, M. Aftosmis, S. O. Macheret, and M. N. Shneider, "Comments on an MHD Energy Bypass Engine Powered Spaceliner", Paper AIAA-99-4965, AIAA 9th International Space Planes and Hypersonic Systems and Technologies Conference and 3rd Weakly Ionized Gases

Workshop, Norfolk, VA, Nov. 1-5, 1999.

47. S.O. Macheret, M.N. Shneyder, and R. B. Miles, "MHD Power Extraction from Cold Hypersonic Air Flow with External Ionizers," Paper #AIAA-99-4800, AIAA 9th International Space Planes and Hypersonic Systems and Technologies Conference and 3rd Weakly Ionized Gases Workshop, Norfolk, VA, Nov. 1-5, 1999.
48. A.P. Yalin, Y. Ionikh, A. Meshchanov, and R.B. Miles, "2-D Temperature Fields in Glow Discharges Measured with Ultraviolet Filtered Rayleigh Scattering," Paper #AIAA-2000-0375, 38th AIAA Aerospace Sciences Meeting and Exhibit, Reno, NV, January 10-13, 2000.
49. Y. Ionikh, N.V. Chernysheva, A.P. Yalin, S.O. Macheret, L. Martinelli, and R.B. Miles, "Shock Wave Propagation Through Glow Discharge Plasmas: Evidence of Thermal Mechanism of Shock Dispersion," Paper #AIAA-2000-0714, 38th AIAA Aerospace Sciences Meeting and Exhibit, Reno, NV, January 10-13, 2000.
50. B. McAndrew, P. Barker, and R.B. Miles, "Development of a Supersonic Plasma Wind Tunnel," Paper #AIAA-2000-0533, 38th AIAA Aerospace Sciences Meeting and Exhibit, Reno, NV, January 10-13, 2000.
51. S.O. Macheret, M.N. Shneider, and R.B. Miles, "MHD Power Generation and Control of Hypersonic Flows Ionized by Electron Beams," Second Workshop on Magneto- and Plasma Aerodynamics for Aerospace Applications, Institute Of High Temperatures, Russian Academy of Sciences, Moscow, Russia, April 5-7, 2000.
52. S.O. Macheret, Yu.Z. Ionikh, N.V. Chernysheva, A.P. Yalin, L. Martinelli, B. McAndrew, P.F. Barker, M.N. Shneider, and R.B. Miles, "Shock Propagation in Weakly Ionized Gases and Plasma Control of High-Speed Flows," Second Workshop on Magneto- and Plasma Aerodynamics for Aerospace Applications, Institute Of High Temperatures, Russian Academy of Sciences, Moscow, Russia, April 5-7, 2000.
53. R.B. Miles, "Flow Control by Energy Addition into High-Speed Air," AIAA-2000-2324, Fluids 2000, Denver, CO, June 19-22, 2000. (Invited)
54. S.O. Macheret, M.N. Shneider, and R.B. Miles, "Modeling of Air Plasma Generation by Electron beams and High-Voltage Pulses," AIAA-2000-2569, 31st AIAA Plasmadynamics and Lasers Conference, Denver, CO, June 19-22, 2000.
55. S. Zaidi, Z. Tang, A. Yalin, P. Barker, and R. Miles, "Filtered Thomson Scattering in an Argon Plasma," Paper #AIAA-2001-0415, 39th AIAA Aerospace Sciences Meeting & Exhibit, Reno, NV, Jan. 8-11, 2001.
56. S. Macheret, M. Shneider, and R. Miles, "MHD Control of External Supersonic Flow with Electron Beam Ionization," Paper #AIAA-2001-0492, 39th AIAA Aerospace Sciences Meeting & Exhibit, Reno, NV, Jan. 8-11, 2001.
57. P. Barker, A. Meschanov, and R. Miles, "Temperature Measurements in Plasmas Using Coherent Rayleigh Scattering," Paper #AIAA-2001-0416, 39th AIAA Aerospace Sciences Meeting & Exhibit, Reno, NV, Jan. 8-11, 2001.
58. S. Macheret, M. Shneider, and R. Miles, "Potential Performance of Supersonic MHD Power Generators," Paper #AIAA-2001-0795, 39th AIAA Aerospace Sciences Meeting & Exhibit, Reno, NV, Jan. 8-11, 2001.
59. G. V. Candler, S. O. Macheret, M. N. Shneider, I. V. Adamovich, and J. D. Kelley, "Modeling of RF Plasma Kinetics and Aerodynamics of the AEDC Ballistic Range Experiments," Paper AIAA 2001-0494, 39th AIAA Aerospace Sciences Meeting & Exhibit, Reno, NV, Jan. 8-11, 2001.
60. S.O. Macheret, M.N. Shneider, and R.B. Miles, "MHD Control of Scramjet Inlets and On-Board Power Generation," Third Workshop on Magneto- and Plasma Aerodynamics for Aerospace Applications, Institute Of High Temperatures, Russian Academy of Sciences, Moscow, Russia, April 25-27, 2001.
61. S.O. Macheret, M.N. Shneider, and R.B. Miles, "Efficient Generation of Nonequilibrium Plasmas by High-

Energy Electrons," Third Workshop on Magneto- and Plasma Aerodynamics for Aerospace Applications, Institute Of High Temperatures, Russian Academy of Sciences, Moscow, Russia, April 25-27, 2001.

62. S.O. Macheret, M.N. Shneider, L. Martinelli, R. Murray, B. McAndrew, R.B. Miles, J. Fox, and J. Kline, "Plasma Control of Shock Waves in Aerodynamics and Sonic Boom Mitigation," Third Workshop on Magneto- and Plasma Aerodynamics for Aerospace Applications, Institute Of High Temperatures, Russian Academy of Sciences, Moscow, Russia, April 25-27, 2001.
63. S.O. Macheret, M.N. Shneider, and R.B. Miles, "Energy-Efficient Generation of Nonequilibrium Plasmas and their Applications to hypersonic MHD Systems," Paper AIAA-2001-2880, 32nd AIAA Plasmadynamics and Lasers Conference and 4th Weakly Ionized Gases Workshop, Anaheim, CA, June 11-14, 2001.
64. S.O. Macheret, M.N. Shneider, and R.B. Miles, "Modeling of Plasma Generation in Repetitive Ultra-short DC, Microwave, and Laser Pulses," Paper AIAA-2001-2940, 32nd AIAA Plasmadynamics and Lasers Conference and 4th Weakly Ionized Gases Workshop, Anaheim, CA, June 11-14, 2001.
65. R.B. Miles, S.O. Macheret, L. Martinelli, R. Muray, M. Shneider, Yu.Z. Ionikh, J. Kline and J. Fox, "Plasma Control of Shock Waves in Aerodynamics and Sonic Boom Mitigation," Paper AIAA-2001-3062, AIAA Plasmadynamics and Lasers Conference and 4th Weakly Ionized Gases Workshop, Anaheim, CA, June 11-14, 2001.
66. B. McAndrew, R. Murray, M. Shneider, R. Miles, J. Kline and J. Fox, "Comparison of Numerical and Experimental Results from Localized Microwave-Driven Plasma Energy Addition into a Mach 3 Flow," Paper AIAA-2001-3061, AIAA Plasmadynamics and Lasers Conference and 4th Weakly Ionized Gases Workshop, Anaheim, CA, June 11-14, 2001.
67. R.B. Miles, S.O. Macheret, and M.N. Shneider, "High Efficiency, Nonequilibrium Air Plasmas Sustained by High Energy Electrons," Paper #869, PPPS-2001, ICOPS 2001, Las Vegas, NV, June 17-22, 2001.
68. S.O. Macheret, M.N. Shneider, and R.B. Miles, "Dynamics of Plasmas Sustained by Repetitive Ultrahigh Voltage DC or Subpicosecond Laser Pulses," Paper #766, PPPS-2001, ICOPS 2001, Las Vegas, NV, June 17-22, 2001.
69. S. Zaidi, Z. Tang, and R.B. Miles, "Rubidium Filtered Thomson Scattering Measurement in an Atmospheric Pressure Argon Arc," Paper #339, PPPS-2001, ICOPS 2001, Las Vegas, NV, June 17-22, 2001.
70. M.N. Shneider, S.O. Macheret, and R.B. Miles, "Properties of Electron Beam Generated, Steady-State, Weakly Ionized Plasmas in Air," Paper #682, PPPS-2001, ICOPS 2001, Las Vegas, NV, June 17-22, 2001.
71. I.G. Girgis, M.N. Shneider, S.O. Macheret, G.L. Brown, and R.B. Miles, "Creation of Steering Moments in Supersonic Flow by Off-Axis Plasma Heat Addition," Paper AIAA-2002-0129, 40th AIAA Aerospace Sciences Meeting & Exhibit, Reno, NV, Jan. 14-17, 2002.
72. B. McAndrew, J. Fox, J. Kline, M.D. Bowie, and R. Miles, "Supersonic Flow Control by Microwave-Driven Plasma Discharges," I. Girgis, M. Shneider, S. Macheret, G. Brown, and R. Miles, "Creation of Steering Moments in Supersonic Flow by Off-Axis Plasma Heat Addition," Paper AIAA-2002-0354, 40th AIAA Aerospace Sciences Meeting & Exhibit, Reno, NV, Jan. 14-17, 2002.
73. M.N. Shneider, S.O. Macheret, and R.B. Miles, "Nonequilibrium Magnetohydrodynamic Control of Scramjet Inlets," Paper #AIAA-2002-2251, 33rd AIAA Plasmadynamics and Lasers Conference, Maui, Hawaii, May 20-23, 2002.
74. S.O. Macheret, M.N. Shneider, and R.B. Miles, "Magnetohydrodynamic and Electrohydrodynamic Control of Hypersonic Flows of Weakly Ionized Plasmas," Paper #AIAA-2002-2249, 33rd AIAA Plasmadynamics and Lasers Conference, Maui, Hawaii, May 20-23, 2002.
75. S.H. Zaidi, M.N. Shneider, D.K. Mansfield, Y.Z. Ionikh, and R.B. Miles, "Influence of Upstream Pulsed

Energy Deposition on a Shockwave Structure in Supersonic Flow," Paper #AIAA-2002-2703, 22nd AIAA Aerodynamic Measurement Technology and Ground Testing Conference, St. Louis, MO, June 24-26, 2002.

76. X. Pan, M.N. Shneider, and R.B. Miles, "Coherent Rayleigh-Brillouin Scattering in Monatomic Gases in the Kinetic Regime," Paper #AIAA-2002-3235, 22nd AIAA Aerodynamic Measurement Technology and Ground Testing Conference, St. Louis, MO, June 24-26, 2002.

Invited presentations and seminars

- R.B. Miles, "MHD Effects to Optimize Shock Position for Off-Design Scramjet Conditions," Reusable Launch Vehicle/Space Operations Vehicle (RLV/SOV) Airframe Technology Review, NASA Langley, Hampton, VA, Nov. 21, 2002
- R.B. Miles, presentation at DARPA "Joint Supersonic Technology Exchange Meeting," Chicago, IL, June 10-13, 2002
- S.O. Macheret and R.B. Miles, "Magnetohydrodynamic Control of Hypersonic Flows: Potential Performance and Critical Problems," Defense Scientific Research Council (DSRC), Washington, DC, April 18, 2002
- R.B. Miles, "Breakthrough Technologies for Space Access with Air-Breathing Vehicles," Invited MAE Departmental Seminar, Princeton, University, Princeton, NJ, April 5, 2002
- R.B. Miles, "Novel Trends in Nonlinear Laser Spectroscopy and Optical Diagnostics," XVII International Conference on Coherent and Nonlinear Optics (ICONO), Belarus Cultural Center, Minsk, Belarus, June 26-July 1, 2001 (Invited Keynote Speaker).
- R.B. Miles, "Flow Field Diagnostics by Filtered Rayleigh and Raman Scattering," Georgia Tech, Atlanta, Georgia, April 27, 2001
- S.O. Macheret, "Novel Hypersonic MHD Concepts," Tokyo Institute of Technology, Yokohama, Japan, October 31, 2001
- S.O. Macheret, "Energy-Efficient Generation of Nonequilibrium Plasmas by Electron Beams and Ultrashort Pulses," Tokyo Institute of Technology, Yokohama, Japan, October 29, 2001
- S.O. Macheret, "Gases and Plasmas in Vibrational Nonequilibrium: Fundamental Processes and Engineering Applications," University of Southern California, Department of Aerospace Engineering, October 22, 2001
- S.O. Macheret, "Magnetohydrodynamic Control of Hypersonic Flows, Optimization of Engine Inlets, and On-Board Power Generation," Pratt & Whitney, East Hartford, CT, August 18, 2001
- S.O. Macheret, "The Case for Electron Beam-Sustained MHD Applications to Hypersonic Aerodynamics," NASA Marshall Space Flight Center, July 31, 2001
- S.O. Macheret, "High-Energy Molecules and Electrons in Nonequilibrium Fluids: Fundamental Kinetics and Engineering Applications," Invited seminar at Princeton University, April 17, 2001
- S.O. Macheret, "Nonequilibrium Processes in Gases and Plasmas and Their Applications," Vanderbilt University, Nashville, TN, April 12, 2001
- R.B. Miles and S.O. Macheret, "Microwave-Driven Air Plasma Studies for Drag Reduction and Power Extraction in Supersonic Air," AFOSR 2000 Contractors' Meeting in Unsteady Aerodynamics & Hypersonics, Monterey, CA, Sept. 6-7, 2000
- R.B. Miles, "Flow Control by Energy Addition into High-Speed Air," Fluids 2000, Denver, CO, June 19-20, 2000
- S.O. Macheret, "Perspectives of Plasma and MHD Hypersonic Aerodynamic Control and Power Generation," Briefing to the U.S. Air Force Science Advisory Board (SAB) Study Team "Why and Whither Hypersonics Research in the USAF," Arlington, VA, March 28, 2000
- R.B. Miles, "MHD--Air Plasma Processes for Hypersonics," Briefing to the USAF Scientific Advisory Board Study Team "Why and Whither Hypersonics Research in the USAF," Arlington, VA, March 28, 2000
- S.O. Macheret, "Shock Propagation in Weakly Ionized Gases and Plasma Control of High-Speed Flows," 2nd Workshop on Magneto- and Plasma Aerodynamics for Aerospace Applications, 5-7 April 2000, Moscow, Russia
- S.O. Macheret, "MHD Power Generation and Control of Hypersonic Flows Ionized by Electron Beams," 2nd Workshop on Magneto- and Plasma Aerodynamics for Aerospace Applications, 5-7 April 2000, Moscow, Russia
- S.O. Macheret, "New Types of Electron Beam Generated Discharges in Dense Gases: a "Fountain" and a "Thunderstorm" ", 30th AIAA Plasmadynamics and Lasers Conference, Norfolk, June 1999

- S.O. Macheret, "*Electron Beam Generated Plasmas in Hypersonic MHD Channels*", 33rd AIAA Thermophysics Conference, Norfolk, June 1999

b. Consultative and advisory functions

R.B. Miles and S.O. Macheret performed consultative and advisory functions for Boeing (St. Louis, MO), Plasma Tec., Inc. (Princeton, NJ), MSE Technology Applications, Inc. (Butte, MT), and DARPA Defense Science Research Council (Arlington, VA)

c. Transitions

The physical models and concepts of plasma/MHD control of hypersonic flows and scramjet inlets developed at Princeton University in this program were used by AFRL researchers (D. Gaitonde and J. Poggie) and were also transitioned to Boeing (P. Smereczniak and J. Silkey).

New discoveries, inventions, and patent disclosures

- C. E. Albright, J. W. Rich, R. B. Miles, W. R. Lempert, and S. O. Macheret, "Method and Apparatus for Initiating, Directing, and Constricting Electrical Discharge Arcs", U.S. Patent #6,191,386, Feb. 20, 2001
- C. E. Albright, J. W. Rich, R. B. Miles, W. R. Lempert, and S. O. Macheret, "Method and Apparatus for Initiating, Directing, and Constricting Electrical Discharge Arcs", U.S. Patent #6,483,077, Nov. 19, 2002
- R. B. Miles, S. O. Macheret, K. V. Khodataev, L. P. Grachev, and I. I. Esakov, "Laser Stabilized, Microwave-Driven, Filamentary X-Ray Source", Invention Disclosure, filed March 18, 1999
- S. O. Macheret, M. N. Shneyder, and R. B. Miles, "Optimization of Scramjet Inlets by Energy Addition off the Cowl Lip (Virtual Cowl)", Invention Disclosure, filed April 2002

Honors/Awards

- R.B. Miles was elected Fellow of the American Institute of Aeronautics and Astronautics
- S.O. Macheret was elected Associate Fellow of the American Institute of Aeronautics and Astronautics

Acknowledgement/Disclaimer

This work was sponsored, in large part, by the Air Force Office of Scientific Research, USAF, under grant/contract number F49620-00-1-0034. The views and conclusions contained herein are those of the authors and should not be interpreted as necessarily representing the official policies or endorsements, either expressed or implied, of the Air Force Office of Scientific Research or the U.S. Government.